

**NASA CONTRACTOR  
REPORT**

**NASA CR-1587**



**NASA CR-1587**

NASA  
CR  
1586  
v.2  
c.1

0060919



TECH LIBRARY KAFB, NM

LOAN COPY: RETURN TO  
AFWL (WLOL)  
KIRTLAND AFB, N MEX

# **POTASSIUM TURBOALTERNATOR PRELIMINARY DESIGN STUDY**

## **II - Refinement of Selected Turboalternator Layout (Phase II)**

*Prepared by*  
**GENERAL ELECTRIC COMPANY**  
Cincinnati, Ohio  
*for Lewis Research Center*



0060919

1. Report No. NASA CR-1587	2. Government Accession No.	3. Recipient's Catalog No.	
4. Title and Subtitle POTASSIUM TURBOALTERNATOR PRELIMINARY DESIGN STUDY. II - REFINEMENT OF SELECTED TURBOALTERNATOR LAYOUT (PHASE II)		5. Report Date June 1970	
		6. Performing Organization Code	
7. Author(s)		8. Performing Organization Report No. GESP-297	
9. Performing Organization Name and Address  General Electric Company Cincinnati, Ohio 45215		10. Work Unit No.	
		11. Contract or Grant No. NAS 3-10933	
12. Sponsoring Agency Name and Address  National Aeronautics and Space Administration Washington, D.C. 20546		13. Type of Report and Period Covered  Contractor Report	
		14. Sponsoring Agency Code	
15. Supplementary Notes  Edited by E. Schnetzer			
16. Abstract  The preliminary design selected from the Phase I study of a potassium turboalternator for space has been established as part of a nuclear Rankine cycle space power system of 2 MW <sub>th</sub> reactor power. The rating is 660 KVA, 450 kw <sub>e</sub> , 480 V (L-N), 1600 Hz. Potassium is the 2-phase turbine working fluid. Liquid potassium is the lubricant and the coolant. The turbine is all refractory metal. Design life is 3 years with growth potential to 5 years. Performance and design feasibility have been established. Remaining problems are turbine erosion, long term creep behavior of turbine rotor materials, and the alternator bore seal.  <div style="text-align: center;"><i>Rankine Cycle Turbo generators</i></div>			
17. Key Words (Suggested by Author(s)) Nuclear Rankine power systems Potassium turboalternator Condensing vapor turbine High temperature alternator		18. Distribution Statement Unclassified - unlimited	
19. Security Classif. (of this report) Unclassified	20. Security Classif. (of this page) Unclassified	21. No. of Pages 380	22. Price* \$3.00

\*For sale by the Clearinghouse for Federal Scientific and Technical Information  
Springfield, Virginia 22151



## FOREWORD

The work described in this report was performed by the Nuclear Systems Programs Department of the General Electric Company in Cincinnati, Ohio, under NASA contract NAS 3-10933. The Project Manager at General Electric was Mr. E. Schnetzer, and the NASA Project Manager was Mr. J. P. Joyce, of the Lewis Research Center Space Power Systems Division.

The study was performed in two phases, Phase I to provide basic analysis of components and conceptual KTA designs for various design conditions (volume I), and Phase II to establish one preliminary design meeting specific design conditions (volume II).

General Electric was assisted by two subcontractors: The Westinghouse Aerospace Electrical Division in Lima, Ohio, responsible for the alternator design, and Mechanical Technology Incorporated in Latham, New York, contributing bearing/rotor response, as well as bearing and seal analyses.

The following people were key contributors to the work: at WAED, alternator design: A. E. King, T. C. Allen, C. C. Kouba, J. L. McCabria, and T. G. Studt; at MTI, bearing/rotor response: W. D. Waldron; at GE, turbine fluid design and thermodynamics: Richard J. Rossbach and Gordon C. Wesling; mechanical design: Bluford L. Moor and Manfred O. Schnetzer; materials support: E. E. Hoffman, W. F. Zimmerman, W. R. Young, and H. A. Williams.





POTASSIUM TURBOALTERNATOR PRELIMINARY DESIGN STUDY  
FINAL REPORT, PHASE II

TABLE OF CONTENTS

	<u>Page</u>
1.0 <u>INTRODUCTION</u>	1
1.1 SPECIFICATIONS	1
1.2 SUMMARY OF RESULTS, Turbine; Alternator; Bearing - Rotor Response; Performance; Weights and Effectiveness.	6
2.0 <u>ALTERNATOR</u>	16
2.1 ELECTRICAL DESIGN AND PERFORMANCE STUDY, Introduction; Specification Change Review; Alternator Internal Design Variables; Final Alternator Design Configuration; Alternator Electrical Performance Data.	16
2.2 MECHANICAL DESIGN AND PERFORMANCE STUDY, Introduction; Thermal Analysis; Structural Weight Minimization; Rotor Stress Analysis; Bore Seal Assembly.	37
2.3 PRELIMINARY OVERALL DESIGN, Layouts of Alternator; Summary of Data.	83
2.4 MATERIALS SUMMARY	94
2.5 FAILURE MODE, EFFECT AND CRITICALITY STUDY	97
2.6 CONCLUSIONS AND RECOMMENDATIONS	100
2.7 REFERENCES	108
3.0 <u>TURBINE FLUID DESIGN</u>	109
3.1 TURBINE DESIGN STUDIES	109
3.2 SELECTED TURBINE DESIGN	119
3.3 SCROLLS AND DUCTS	132
3.4 INTERSTAGE CONDENSATE REMOVAL	137
3.5 INTERSPOOL CONDENSATE REMOVAL	139
3.6 SUMMARY OF KTA TURBINE FLUID DESIGN	149
4.0 <u>TURBINE MATERIALS</u>	151
4.1 MATERIALS SELECTION, Non-Rotating Parts; Rotating Parts; Bearings; Rubbing Materials; Bimetallic Joint.	151
4.2 DESIGN DATA RELIABILITY	160
4.3 FORGINGS, Shafts; Tie Bolt; Wheels.	165
4.4 MATERIALS SUMMARY	171
4.5 REFERENCES	173

## TABLE OF CONTENTS - Continued

	<u>Page</u>
5.0 <u>TURBINE MECHANICAL DESIGN</u>	174
5.1 INTRODUCTION	174
5.2 TURBINE MATERIALS	178
5.3 TURBINE WHEELS AND BUCKETS, Wheel Stresses; Airfoil Stresses, Turbine Torque and Power; Bucket Tip Clearances; Dovetail Stresses; Bucket Vibration.	182
5.4 TURBINE ROTOR CONSTRUCTION AND STRESSES, Curvic Coupling, Torque Tubes; Tie Bolt; Conical Stub Shafts.	207
5.5 CASING AND STATOR, Nozzle Diaphragms; Casing.	225
5.6 THERMAL CONSIDERATIONS, Differential Thermal Expansion; Insulation.	235
5.7 TURBINE ALTERNATOR COUPLING	241
5.8 INSTRUMENTATION	249
5.9 TURBINE SUMMARY	254
5.10 REFERENCES	258
6.0 <u>TURBINE FABRICATION</u>	259
6.1 FABRICATION AND JOINING, Joining Considerations.	259
6.2 FABRICATION AND ASSEMBLY, Final Assembly; Turbine Wheels; Turbine Casings; Nozzle Diaphragm Assembly; Seal Fabrication.	262
6.3 JOINING SUMMARY	271
7.0 <u>VISCO SEALS AND BEARINGS</u>	273
7.1 VISCO SEALS	273
7.2 BEARINGS - GENERAL	279
7.3 JOURNAL BEARINGS	280
7.4 THRUST BEARINGS	289
7.5 KTA START UP	297
7.6 HYDROSTATIC JACKING	303
7.7 BEARING AND SEAL JOURNAL STRESSES AND MATERIAL CONSIDERATIONS, General; Turbine Bearing/Seal Journals; Alternator Conical-End Journal.	311
7.8 SUMMARY AND CONCLUSIONS	322
7.9 REFERENCES	324
8.0 <u>BEARING ROTOR RESPONSE</u>	325
8.1 BEARING COEFFICIENTS AND EXCITING FORCES	326
8.2 ELEVEN STAGE TURBINE	328

TABLE OF CONTENTS - Continued

	<u>Page</u>
8.3 450 KW ALTERNATORS	335
8.4 HOUSING COMPLIANCE	341
8.5 COUPLED TURBINE AND ALTERNATOR	348
8.6 SUMMARY AND CONCLUSIONS	352
9.0 <u>CONCLUSIONS AND RECOMMENDATIONS</u>	354
9.1 REMAINING PROBLEM AREAS	356
9.2 RECOMMENDATIONS	358
10.0 <u>ALTERNATE DESIGN STUDIES</u>	360
10.1 MULTISTAGE MOISTURE REMOVAL	360
10.2 STATOR CONDENSATE REMOVAL	363
10.3 REHEAT	371

## I. INTRODUCTION

Of the various preliminary designs generated in Phase I of the KTA Preliminary Design Study, NASA selected a two-shaft, four-bearing arrangement with elastic coupling connecting the two shafts. Operating speed is 19,200 rpm. All four bearings are potassium lubricated. The turbine is subdivided into two spools and equipped with condensate removal devices in the cross-over ducting between spools and in the next to last rotor blade row of the low-pressure turbine. The rotor material selected is KDTZM molybdenum alloy. The rotor stages are connected by curvic coupling and pretensioned tie bolt. The turbine stator is to be constructed from weldable refractory materials such as tantalum alloy T-111 at the hottest portion of the casing and Cb-1Zr at temperatures below 1600°F. The alternator is of the homopolar induction type generating alternating current at 1600 Hz.

### 1.1 SPECIFICATIONS

The design specifications have been revised in Phase II resulting in a number of design changes as compared to the selected Phase I design. The layout power level for the alternator has been reduced from 550 to 450 kw<sub>e</sub>. Also reduced was the potassium coolant and lubricant temperature for the alternator from the range 800 to 1100°F to 700°F. The remaining alternator specifications of 10 poles, 480 volts line to neutral, 1600 Hz and 19,200 rpm were unchanged.

For the turbine, inlet as well as outlet conditions have been modified. The Phase II cycle state points are listed on Table 1.1-1. It should be noted that turbine performance is based on the fluid design conditions. The allowable stresses employed in the mechanical design, however, are based on the higher inlet conditions which reflect potential fluctuations in the system. The turbine outlet temperature has been reduced from 1280 to 1220<sup>o</sup>F, and turbine outlet pressure from 7.8 to 5.44 psia. The vapor flow rate has been reduced from 2.5 to 2.05 lb/sec based on systems considerations with a 2 MW<sub>th</sub> heat input limit from the reactor. The design power output, Table 1.1-2, has been limited to 450 kw<sub>e</sub> with a load power factor of .75 lagging. The alternator has to be capable of withstanding a 5 second overload of 900 KVA at .9 power factor. The turboalternator will be operating at 19,200 rpm speed continuously over an unattended 3 year period with growth potential to 5 years. A 120 percent overspeed to 23,400 rpm has to be accepted for a short time. The environmental specifications are based on P1224-1 and -2 of January 1967. The most crucial conditions are shock loads of 20 G during launch (KTA inoperative) and 3 G in orbital operation. A 3.5 G acceleration has to be tolerated for 5 minutes time in lift-off axis. Since the position of the KTA in the space vehicle is not established, all G-loadings have to be accepted in any direction.

As far as arrangement is concerned, the selection made and the design rules given are summarized on Table 1.1-3. It should be noted that additional stages are requested to improve turbine efficiency.

TABLE 1.1-1

CYCLE STATE POINTS

	<u>FLUID DESIGN</u>	<u>MECH. DESIGN</u>
TURBINE INLET TEMPERATURE, °F	2100	2150
TURBINE INLET TSAT.	2029	
TURBINE INLET PRESSURE, PSIA	165	190
TURBINE OUTLET TEMPERATURE, °F	1220	
TURBINE OUTLET PRESSURE, PSIA	5.44	
VAPOR FLOW RATE, LB/SEC	2.05	

TABLE 1.1-2

KTA SPECIFICATIONS - PHASE II

DESIGN POWER OUTPUT

ALTERNATOR MAXIMUM CONTINUOUS RATING

- 450 KW<sub>e</sub> AT LOAD P.F. = 0.75 LAGGING

5 SEC OVERLOAD - 900 KVA AT 0.90 P.F.

100% SPEED - 19,200 RPM, CONTINUOUS

120% OVERSPEED - 23,400 RPM, SHORT TIME

ENVIRONMENTAL SPECIFICATIONS                      P1224-1 and -2 of 1-31-67

SHOCK 20 G - DURING LAUNCH                      2.2.1.1  
(KTA Not Operating)

SHOCK 3 G - IN OPERATION IN                      2.3.1  
ANY DIRECTION

5 MIN. 3.5 G - IN LIFT-OFF AXIS                      2.3.3.1

DESIGN LIFE

3 YEARS - WITH GROWTH TO 5 YEARS



TABLE 1.1-3

ARRANGEMENT

KTA

2 SHAFTS, 4 BEARINGS, 1 COUPLING

TURBINE

6+4 STAGES, SPLIT SPOOL

INTERPOOL MOISTURE SEPARATION

ADDITIONAL STAGES TO IMPROVE EFFICIENCY

CONDENSATE REMOVAL FROM ROTOR NEXT TO LAST STAGE

ROTOR MATERIAL: TBM MOLYBDENUM

STAGE CONNECTION: CURVIC COUPLING

- TIE BOLT

LUBRICANT: POTASSIUM, TEMPERATURE UNDEFINED

ALTERNATOR

10 POLES

480 VOLTS

1600 HZ

700°F POTASSIUM LUBRICANT AND COOLANT

## 1.2 SUMMARY OF RESULTS

Based on the above set of specifications a new design has been generated which is illustrated in Figure 1.2-1. The outstanding design features of this design are listed on Table 1.2-1. It should be noted that the number of turbine stages has been increased to 7 overhung plus 4 cradled for a total of 11 stages. The two spools are in counterflow arrangement to reduce the net thrust. Four cross-over ducts connect the two spools and are equipped with centrifugal separators. Condensate extraction from the rotor is provided in Stage 10. With these condensate removal devices the lowest vapor quality within the turbine will be 0.907 entering stage 10. The vapor quality entering stage 7 will be 0.920. The split between 7 and 4 stages has been made to about equalize the lowest vapor qualities in both spools. Tip speed in the low pressure turbine is 850 ft/sec. The potassium lubricant for the turbine will be in the range from 800 to 900°F.

### Alternator

Significant improvements were realized in the Phase II alternator design. Relative to the basic conceptual design derived in Phase I, electrical efficiency was increased nearly two points to over 94 percent while the electrical weight decreased from 1.14 to 1.08 pounds per KVA. With these reduced electrical losses, the cooling configuration selected in Phase II was more than adequate to limit the stator hot spot temperature to only 902°F for the 700°F inlet coolant.

As part of the stator design studies, special efforts were concentrated upon reduction of weight of the inert structural hardware. As a result, over 200 pounds of weight was trimmed from the structure while still minimizing structural stresses to less than 30,000 psi.

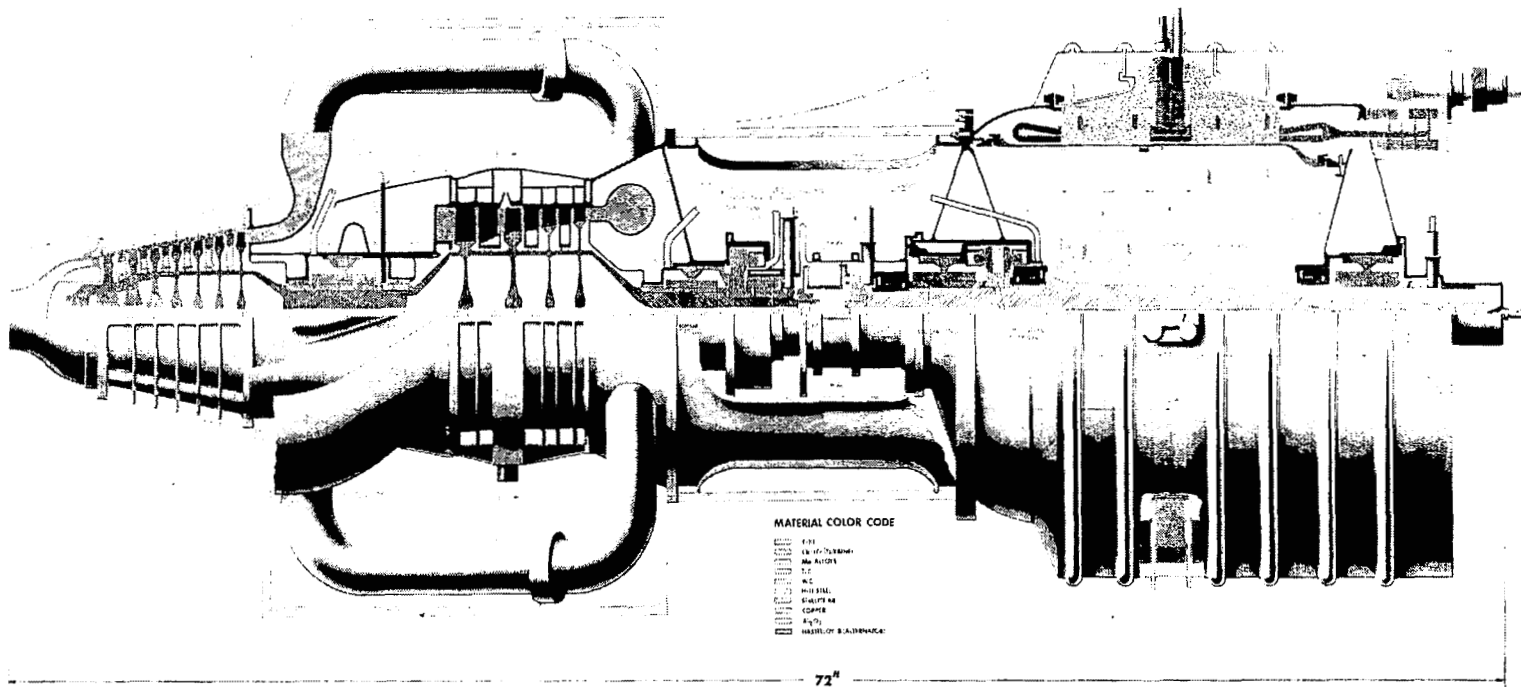


Figure 1.2-1. Potassium Turboalternator - 450 Kw<sub>e</sub>, 19,200 rpm, 1600 cps - Phase II Design.

TABLE 1.2-1

KTA PHASE II DESIGN FEATURES

KTA

2 SHAFTS, 4 BEARINGS, 1 COUPLING

TURBINE

7+4 STAGE, SPLIT SPOOL, COUNTER FLOW

4 CENTRIFUGAL SEPARATORS BETWEEN SPOOLS

CONDENSATE EXTRACTION NEXT TO LAST STAGE

LOWEST VAPOR QUALITY = 0.907, STAGE 10

LOWEST VAPOR QUALITY = 0.920, STAGE 7

TZM MOLY ROTOR

- CURVIC COUPLING, TIE BOLT

T-111 AND Cb-1Zr. STATOR, WELDED

LUBRICANT: POTASSIUM, 800 - 900<sup>0</sup>F

ALTERNATOR

700<sup>0</sup>F COOLANT - 900<sup>0</sup>F HOT SPOT

HIGHER EFFICIENCY - LESS WEIGHT

CREEP ELIMINATED AS A PROBLEM IN H-11 ROTOR

SLOTTED POLE FACES

BORE SEAL CONCEPT WITH BIMETAL TRANSITION JOINTS

TABLE 1.2-1 (Continued)

BEARINGS

RADIAL

- 4 PAD PIVOTED PAD BEARINGS
- $L/D = 1.0$
- $C/D = .0015$
- $D = 2.5 - 3.0$  INCH
- MATERIAL: TiC AND CARBOLOY 907

AXIAL

- 8 PAD PIVOTED PAD BEARINGS
- OUTER DIAMETER = 6.0 INCH

SEALS

INTERNAL

- HELICAL GROOVE
- $C/D = .0025$

EXTERNAL

- HELICAL GROOVE + LIQUID TRAP
- $C/D = .0025$

MATERIAL

- TiC AND STELLITE 6B

BEARING ROTOR RESPONSE

- 0.2 MIL MAX. AMPLITUDES AT 19,200 RPM

The impact of reducing the rotor coolant temperature to 700°F was found to be very significant in increasing the reliability of the design. Laminated pole tips were no longer needed and slotted pole faces became more than adequate to minimizing pole face losses that limited pole tip temperature to less than 900°F. The combined temperatures and stresses of the rotor were sufficiently low to eliminate rotor creep strain as a limiting design criteria.

Relative to the third major area of the alternator - - the bore seal - - a simpler, more reliable configuration was evolved for the end members and bimetallic transition joints. This was possible as a result of extensive analyses and consultations with experts in the area of bimetal joints. The resulting design integrates the requirements and desired features of the bimetallic joint with those previously defined for the ceramic to metal joint.

#### Bearings and Seals

The radial bearings on the turbine as well as the alternator are 4 pad pivoted pad bearings with length to diameter ratio = 1.0 and a clearance to diameter ratio - .0015. The turbine bearings are 3 inches and 2.5 inches in diameter, the alternator bearings are 3 inches. Each component, turbine as well as alternator, has its own thrust bearing, both of which measure 6 inches in outer diameter and employ 8 pad pivoted pad bearings. The bearing materials selected are titanium carbide for the turbine and tungsten carbide (carboloy 907) for the alternator. TiC has a columbium binder and carboloy 907 has a cobalt binder. The seals employed in the turbine and alternator are of the helical groove non-contact type with clearance to diameter ratio of .0025.

The design distinguishes between internal and external seals. "Internal" meaning sealing between potassium liquid and high pressure vapor, "external" sealing between liquid and low pressure vapor, the pressure of which is controlled by the temperature in the seal interface and molecular pumping. The so-called external seals are used on both sides of the alternator rotor cavity and on both sides of the coupling cavity. In both of these cavities it is important to maintain low vapor pressures to minimize windage losses and to avoid inleakage and accumulation of liquid potassium. For this purpose the seals are equipped with liquid traps based on an in-house GE development.

#### Bearing-Rotor Response

The turbine and alternator rotors were subjected to several critical speed and rotor response analyses which led to sufficient design improvements to rid the rotors of any perceptible resonance peaks. With reasonably large values of unbalance (100 micro-inches) the rotor maximum vibration amplitudes never exceed 0.4 mils at the 20 percent overspeed case.

The turbine and alternator when coupled together have dynamic characteristics almost identical to the components when operated independently. This is because the diaphragm coupling has a very low angular stiffness and cannot transfer any significant moment from one rotor to the other. This is an extremely desirable feature as each of the components can be analyzed and tested independently with the assurance, that when assembled together, they will be effectively dynamically decoupled.

The KTA has one torsional critical speed in the range between 0 and 30,000 rpm occurring near 7250 rpm. This first torsional critical, however, should be of little consequence since sufficient friction damping should be afforded by the stub shaft bearing sleeves to enable accelerating through the critical with a minimum of amplification.

The effect of housing flexibility on the alternator rotor vibrational characteristics was evaluated and found to be a significant factor. It was determined that the radial stiffness of the end bells should exceed 1.5 million lb/in in order to minimize the effect of housing flexibility and that stiffness values approaching  $10^7$  lb/in should not be difficult to obtain with proper reinforcement of the more compliant housing structural elements. Housing flexibility is not as critical a concern in the turbine because it operates above the second critical and additional system compliance further removes the operating speed from the area of the critical.

### Performance

The KTA performance summarized on Table 1.2-2 is based on turbine design specifications which in turn are based on a  $2 \text{ MW}_{\text{th}}$  heat input from the reactor. The actual power output of the KTA is  $386.5 \text{ kw}_e$ . The alternator electrical losses have been reduced to 24.6 kw as compared to the Phase I design ( $35.3 \text{ kw}_e$ ). The parasitic bearing and seal losses have been increased to 35.3 kw due to increased bearing diameters and a more complete assessment of secondary bearing losses, especially of thrust bearings. The resulting alternator efficiency is 86.6 percent. On the turbine, due to the weight flow reduction by limiting reactor power to  $2 \text{ MW}_{\text{th}}$ , the shaft power has been reduced from



TABLE 1.2-2

KTA PERFORMANCE SUMMARY

PHASE		<u>I</u>	<u>II</u>
POWER OUTPUT,	KWe	450	386.5
ALTERNATOR			
- INTERNAL LOSSES	KW	35.3	24.6
- PARASITIC LOSSES	KW	19.4	35.3
- OVERALL EFFICIENCY	%	89.2	86.6
TURBINE			
- SHAFT POWER	KW	504.7	446.4
- PARASITIC LOSSES	KW	23.2	36.6
- OVERALL EFFICIENCY	%	78.2	75.8
KTA			
- EFFICIENCY	%	69.6	65.6

504.7 to 446.4 kw while the parasitic bearing and seal losses increased from 23.3 to 36.6 kw for the same reasons as those for the alternator. With the addition of one turbine stage the overall turbine efficiency has been calculated to 75.8 percent. Combining alternator and turbine the resulting KTA efficiency was 65.6 percent.

#### Weights and Effectiveness

Table 1.2-3 summarizes the weights of alternator, turbine, coupling and frame. Compared to the Phase I design the weights have been substantially reduced to 1372 pounds or 3.5 pounds per kw<sub>e</sub>. The efficiency/weight effectiveness was defined in the Phase I report, Chapter 11.4 as

$$\begin{aligned}
 E &= \frac{W_t(1) + (\eta - \eta_l) 12000}{W_t} = \frac{1673 - .011 \times 12000}{1372} \\
 &= \frac{1673 - 131}{1372} \\
 &= \frac{1542}{1372} \\
 E &= 1.124
 \end{aligned}$$

This result represents an improvement over the selected Phase I design, which had an effectiveness number  $E = 1.087$ . The improvement expected was diminished by an increase in parasitic bearing and seal losses.

TABLE 1.2-3

WEIGHT SUMMARY

	<u>POUNDS</u>	
	<u>PHASE I</u>	<u>PHASE II</u>
ALTERNATOR	1273	894
TURBINE	520	450
FRAME	22	28
KTA	1815	1372

## 2. ALTERNATOR

### 2.1 ELECTRICAL DESIGN AND PERFORMANCE STUDY

#### Introduction

A review of the changes in specification, design points, and configuration that occurred as a result of the Phase I Conceptual Design Analysis Review was conducted and studies were performed to verify or adjust several of the alternator internal design variables established during the Phase I studies. Sufficient design computations were performed to establish the preliminary Phase II alternator electrical design configuration. Performance calculations were made to determine the electrical performance of the established alternator configuration to verify that the performance meets the specifications and electrical load requirements.

#### Specification Change Review

As a result of conclusions of the Phase I turboalternator design study, one alternator configuration was selected by the NASA for the Phase II preliminary design study. The design specifications of the selected configuration is as follows:

- (1) The alternator maximum continuous load rating shall be 450 kWe, 3 phase, at a 0.75 lagging load power factor.

Nominal alternator load rating shall be the same as the maximum continuous load rating unless otherwise specified.

- (2) The alternator design to the maximum extent feasible shall reduce to a minimum any adverse effects due to unbalanced magnetic forces.
- (3) The speed (frequency) control of the alternator is presently considered to be the parasitic load type, and frequency regulation is anticipated to be  $\pm$  one percent of design frequency for a change in external load from 10 percent to maximum load (450 kWe).
- (4) Specification MIL-G-6099A (ASG) per the latest revision in effect on date of this contract shall apply to the following:
  - (a) Wave form\* - Paragraph 4.5.16. In addition, the total RMS harmonic content of the line-to-neutral voltage wave, when the alternator is operating into a purely resistive load, shall be less than 5 percent from 10 percent to 100 percent maximum load (450 kWe).
  - (b) Phase balance - Paragraph 4.5.10, 4.5.10.1 and 4.5.10.2 except that paragraph 4.5.10.1 is amended to read "... the individual phase voltages shall not deviate from the average by more than 2.25, 4.5, and 9 percent, respectively.
  - (c) Output voltage modulation\*\* - Paragraph 4.5.13 except that modulation shall not exceed 0.5 percent.

---

\* To be retained as a design goal without analytical verification

\*\* A design goal; was not analytically verified.

(d) Overload - 900 kVA at 0.9 lagging load power factor for 5 seconds.

(e) Short circuit capacity - Paragraph 4.5.12 for a minimum of 5 seconds shall be included as a design goal.

(5) Frequency - 1600 Hz.

(6) Speed - 19,200 rpm  $\pm$  one percent.

(7) Voltage - 480 volts (L-N).

(8) Rotor coolant - liquid potassium at 700<sup>o</sup>F supply temperature.

(9) Stator coolant \* - liquid NaK at 800<sup>o</sup>F supply temperature.

The basic changes between the Phase I and Phase II requirements regarding the electrical design of the alternator are a reduction in maximum continuous rating from 733 kVA (550 kWe at 0.75 power factor, lagging) to 600 kVA (450 kWe at 0.75 power factor, lagging), a corresponding reduction in the overload requirement, and a reduction in rotor coolant temperature from 800<sup>o</sup>F to 700<sup>o</sup>F. Rotor material property data for the alternator design computer program was adjusted to reflect the decrease in rotor temperature. Several alternator internal design variable studies were performed to verify or adjust the values selected in the Phase I studies as a result of the changes listed above.

#### Alternator Internal Design Variable Review

Several alternator internal design variables were selected for study and verification because of changes occurring between the Phase I

---

\* Reduced to 700<sup>o</sup>F potassium during course of program.

and Phase II KTA tasks. An armature current density study was performed to verify the previously selected (Phase I) current density with the lower current of the 600 kVA rating. A field current density study was performed to determine the optimum field coil configuration with respect to field coil power, weight, limiting temperature, system weight, and exciter-voltage regulator requirements. A study of armature coil flux density was performed using new calculation procedures derived as a result of an experimental verification program, AEC Contract AT(04-3)-679, which indicated that armature iron losses with unwelded Hiperco-27 stacks were less than those previously calculated by a factor of  $2/3$  and that the amplitude of the ac circumferential flux in the armature core was also less than anticipated. These factors resulted in generally higher efficiencies and in conjunction with the lower Phase II kVA rating, in lower weights compared to Phase I results. The saturated vapor pressure of potassium at  $700^{\circ}\text{F}$  was assumed for the pressure of the rotor cavity for the design variable studies resulting in higher windage losses than those established for the final design. Study results are presented in Tables 2.1-1 through 2.1-3.

In all of the studies performed, alternator weight increased as efficiency increased necessitating the use of a tradeoff criteria in the form of a system weight penalty per kilowatt of loss. From discussions with the NASA, a preliminary weight penalty in the range of 59 to 79 pounds per kilowatt was determined to be suitable for use in the studies. A value of 70 pounds per kilowatt was chosen to determine the weight penalty associated with the alternator inefficiency.

TABLE 2.1-1  
ARMATURE CURRENT DENSITY STUDY

<u>Current Density (amps/in<sup>2</sup>)</u>	<u>Alternator Electrical Wt. (lbs)</u>	<u>Efficiency (%)</u>	<u>Armature Hot Spot Temp (°F)*</u>	<u>Alternator Weight + System Weight Penalty (lbs)</u>
8645	643	92.7	1283	3113
6310	662	93.4	1130	2882
4971	766	93.7	1060	2876
3864	842	93.7	1000	2952

\* Based on 800° F Stator Coolant Temperature



TABLE 2.1-2

ARMATURE CORE FLUX DENSITY STUDY

<u>Flux Density (kl/in<sup>2</sup>)</u>	<u>Alternator Electrical Wt. (lbs)</u>	<u>Efficiency (%)</u>	<u>Stator OD (inches)</u>	<u>Alternator Weight + System Weight Penalty (lbs)</u>
100	627	92.8	18.00	3057
80	640	93.1	18.30	2960
60	662	93.4	18.79	2882
40	729	93.9	19.72	2769
20	905	94.2	22.59	2835

TABLE 2.1-3

FIELD CURRENT DENSITY STUDY

<u>Current Density (amps/in<sup>2</sup>)</u>	<u>Alternator Electrical Wt. (lbs)</u>	<u>Efficiency %</u>	<u>Field Power (Watts)</u>	<u>Field Coil Wt. (lbs)</u>	<u>Field Coil Hot Spot Temp. (°F)**</u>	<u>Estimated* Exciter Wt. (lbs)</u>	<u>Field Coil Voltage</u>	<u>Alternator Wt. &amp; System Wt. Penalty (lbs)</u>
8285	630	92.7	9888	19.6	1480	119	59.7	3100
6540	644	93.1	7904	25.1	1230	95	47.5	2974
5174	661	93.3	6341	32.2	1120	76	37.9	2911
3257	706	93.7	4142	52.8	980	50	24.4	2816
1682	823	94.1	2183	104.7	880	26	12.4	2793

\* Based on 12 lbs/kw specific weight.

\*\* Based on 800°F stator coolant temperature.

Results of the armature current density study (Table 2.1-1) indicated an optimum current density of 5000 to 6000 amperes per square inch based on minimum system weight and a limiting armature hot spot temperature of 1100°F. This compares favorably with an armature current density of 6000 amperes/in<sup>2</sup> selected for the Phase I, 19,200 rpm, 800°F coolant temperature conceptual design.

Optimum armature core flux density (Table 2.1-2) occurs in the range of 20 to 60 kilolines per square inch based on minimum system weight. Accurate calculation of the penetration of the high frequency circumferential ac wave into the depth of the armature core is exceedingly difficult and very large core depths may not be fully utilized by the high frequency (1600 Hz) flux wave. The stator OD increased rapidly below 60 kilolines per square inch density due to an increasing armature core depth behind slot. A density of 60 kilolines/inch<sup>2</sup> was chosen because this value results in near minimum stator punching OD and near minimum system weight.

A field current density of 4000 amperes per square inch (Table 2.1-3) was selected based on results of the field current density study. The selected value results in near minimum system weight, minimum field coil plus estimated exciter weight, and a field coil hot spot temperature below 1100°F. A study of field coil conductor configurations performed in Phase I with regard to heat transfer characteristics has shown that a low voltage, wide strap field coil configuration with cooling manifolds located on each side of the field coil provides the lowest field coil operating temperatures. As shown later, more detailed analysis of the temperatures revealed hot spots well below 1100°F.

A field current density of 4000 amperes per square inch requires a full load field voltage of about 30 volts. A preliminary review of exciter-voltage regulator (VRE) characteristics indicates a VRE efficiency of about 80 percent for the 30 volt field coil configuration. Although a higher voltage, lower current field coil would provide a higher VRE efficiency, the selected configuration represents the optimum considering all of the factors previously discussed.

Re-analysis of the Phase I winding configuration with regard to the harmonic content of the armature MMF has shown that an increase in the pitch factor from 0.8 to 1.0 (full pitch) is desirable. Even harmonics can be present in the MMF distribution of 120 degree phase belt, 3-phase windings when the pitch factor is other than one (1.0). The value of pitch factor for a winding is selected on the basis of reducing or eliminating the amplitudes of an objectional harmonic or series of harmonics. In this case, all even harmonics are eliminated by the choice of a full pitch coil which is desirable from the standpoint of decreasing the load component of rotor pole face losses. Selection of a full pitch coil for the KTA alternator does not significantly increase the harmonic content of the terminal voltage because the harmonic distribution factors are low due to the relatively high number of slots per pole per phase.

The winding factors (product of pitch and distribution factors) for the 120 degree phase belt, full pitch winding of the KTA alternator are identical to those that would be produced if the armature were wound for 60 degree phase belts with  $\frac{2}{3}$  coil pitch. Calculated harmonic content of the no load voltage is 1.85 percent. A slight weight reduction (approximately 6 percent) was achieved by the increased pitch factor.

### Final Alternator Design Configuration

A final alternator electrical design configuration was established based on results of the Phase I studies and the internal design variable studies described in the preceding section of this report. Pertinent design information regarding the final alternator electrical configuration is listed below:

Rating:	600 kVA
Voltage:	480 volts (L-N)
Frequency:	1600 Hz
Speed:	19,200 rpm
Type:	Radial gap inductor
Coolant:	
Stator Inlet	700°F potassium
Rotor Inlet	700°F potassium
Armature Windings:	3-phase, wye connected 180 slots 5 parallel paths 2 parallel strands 12 series turns per phase Full pitch, 120°F phase belts 2 conductors per slot
Field Winding:	52 turns, strap wound
Machine Dimensions:*	
Stack length (each)	4.193 inches
Length between stacks	1.956 inches
Length over end extensions	15.010 inches
Rotor OD	15.109 inches
Stator OD	18.693 inches
Frame OD over field	22.610 inches
Rotor core OD	9.199 inches
Linear pole width	
(circumferential)	3.143 inches

\*Design dimensions are at operating temperature and maximum speed. Fabrication dimensions (R.T. at zero rpm) must be worked back from these by use of calculated temperatures and strains. These fabrication dimensions and associated tolerances must then be extended back upward to "off-design" conditions at near end of life (3 to 5 years) to assure fits, running clearances, etc. will remain satisfactory over the life of the machine.

#### Electrical Weight Breakdown:

Armature conductors	29.7 lbs
Field conductors	40.8 lbs
Armature stacks	149.0 lbs.
Frame	123.9 lbs.
Rotor	<u>303.5 lbs.</u>

646.9 lbs.

#### Resistance and Reactance:

Armature resistance per phase (hot)	0.0182 ohms
Armature leakage reactance	0.149 ohms
Field coil resistance (hot)	0.159 ohms
Direct axis synchronous reactance, $X_d$	0.553 per unit
Quadrature axis synchronous reactance, $X_q$	0.322 per unit
Transient reactance, $X'_d$	0.240 per unit
Subtransient reactance, $X''_d$	0.240 per unit
Quadrature subtransient Reactance, $X''_q$	0.322 per unit
Negative sequence reactance, $X_2$	0.281 per unit
Zero sequence reactance, $X_0$	0.013 per unit

#### Time Constants (hot):

Short circuit transient, $T'_{D1}$	0.067
Open circuit transient, $T'_{D0}$	10.110
Armature, $T_A$	0.0061

#### Materials:

Stator frame	Hiperco-27 forging
Armature laminations	Hiperco-27 .004 inch thick
Armature interlaminar insulation	Plasma-arc sprayed Alumina
Armature conductors	Anadur insulated nickel clad silver
Field coil conductors	Bare CUBE copper
Field coil insulation	Alumina and synthetic mica sheet
Rotor	Premium quality H-11 (AMS 6487)
Slot liners and wedges	Ceramic; 99.5% alumina
Pole face configuration	Grooved

The armature winding is a 120 degree phase belt, two conductor per slot winding. This configuration eliminates the need for conductor end extension joints with the nickel clad silver conductors. Coil ends are connected directly to the bus rings, there being a total of thirty joints required for the complete armature winding.

Joining of clad silver conductors to the bus rings is a much less complex procedure than making conductor to conductor joints in the winding end extensions. Access to the joint area is greater at the bus ring and the conductor ends can be embedded in the bus ring material. The latter can eliminate the need for elaborate pre-weld clamping procedures. Joints located at the bus ring do not require insulation and, because the bus rings are remote from the end extensions, the probability of damaging the armature insulation during the joining process is greatly reduced. Had 60 degree phase belts and/or 4 conductor per slot windings been used, the number of joints would have been increased by 50 percent or 100 percent with joints required in the end extensions as well as at the bus rings.

Armature windings are often referred to as integral slot windings or fractional slot windings. The basic difference between the two types is that the number of slots per pole per phase of an integral slot winding always equals an integer whereas the number of slots per pole per phase of a fractional winding is not an integer. The basic disadvantage of a fractional slot winding in this application is the greater number of harmonics present in the armature MMF as compared to an integral slot winding. Fractional slot windings can contain all odd harmonics, even harmonics, fractional harmonics (e.g., the order of 1.5) and in some cases sub-harmonics which rotate at very high speeds. The higher harmonic content of fractional slot windings can result in very high rotor pole face losses when the alternator is under load. Minimization of pole face losses is a prime goal in the design of high speed alternators for space applications. Integral slot, 60 degree phase belt windings contain only odd harmonics in the armature MMF and for this reason are well suited for high speed alternators. Integral

slot, 120 degree phase belt windings can contain all odd and even harmonics, but even harmonics are eliminated by selecting full pitch coils. This configuration was selected for the KTA application because end extension inter-connections are not required (as they are for 60 degree phase belts) and the selected coil distribution of the KTA armature configuration will result in low pole face losses.

For a given number of series turns per phase, the number of armature slots is directly proportional to the number of parallel paths and inversely proportional to the number of conductors per slot. A high number of slots is beneficial to machine performance with regard to lowering rotor pole face losses and providing better heat transfer of the armature winding loss from the slots. The tooth ripple (no load) component of pole face loss is reduced because of the lower slot pitch and amplitude of the tooth flux oscillation factor. Load harmonic losses and voltage harmonic content are reduced by means of lower harmonic distribution factors achievable for high slots per pole per phase designs.

Slot heat transfer is improved by reducing the heat flux density (watts per square inch) along the slot sides. The choice of 5 parallel paths and 2 conductors per slot for the armature winding attains the above listed design benefits by providing a high number of armature slots. The use of parallel paths in the armature has the further advantage of reducing unbalanced magnetic forces on the rotor under dynamic (rotating) conditions. The advantage of a 2 conductor per slot configuration has already been discussed.

Each slot conductor is comprised of two parallel strap wires to reduce localized eddy current losses in the conductors. The calculated



eddy current factor ( a multiplier for the D.C. armature resistance) is 1.26 at the alternator frequency of 1600 Hz and 700<sup>o</sup>F stator coolant temperature. The use of a higher number of parallel strands would further reduce the eddy current factor but would result in increased alternator weight caused by a corresponding decrease in slot space factor (i.e., ratio of wire area to slot area) with Anadur insulated wire.

The per unit direct axis synchronous reactance value for the Phase II KTA alternator (0.55) falls below the selected range specified in the Phase I studies (0.7 to 1.0). This results from the lower armature current of the Phase II kVA rating and maintenance of the same number of armature slots, conductors per slot, etc., as the Phase I design. Increasing the  $X_d$  of the Phase II alternator would require an increase in the number of armature slots or an increase in the number of conductors per slot from two to four. It is not desirable to increase the number of conductors per slot as previous discussions have made clear. The number of armature slots cannot be increased arbitrarily as there are inviolable rules governing slot, pole, phase, and parallel path relationships. The next highest number of slots for the KTA alternator is 210 (an increase of 30) if an integral slot winding is to be maintained. This configuration has an  $X_d$  of 0.91, an alternator weight of 608 pounds, and efficiency of 93.7 percent. This compares with an alternator weight of 647 pounds and efficiency of 94.4 percent for the selected 180 slot configuration. A system weight penalty of 70 pounds per kilowatt of loss results in a system weight savings of 461 pounds for the selected 180 slot alternator.

The per unit direct axis synchronous reactance " $X_d$ " for the KTA alternator is low (0.55) relative to values normally associated with aircraft alternators (e.g., 1.8). Although a low  $X_d$  machine suffers the disadvantage of higher weight, there are many over-riding advantages in this application. First, the load component of rotor pole face loss is minimized since this component is proportional, as a first approximation, to  $(X_d)^2$  for a given spectrum of armature harmonics. Also, there is less effect from distorted current wave forms that may be created by non-linear load characteristics. Unbalance of terminal voltage between the three phases for a given load unbalance is less with a low  $X_d$  machine. Field power requirements are lessened and the ability to meet three phase short circuit is enhanced as  $X_d$  is decreased. Finally, the low  $X_d$  in this application allows the use of a two conductor per slot winding configuration whose benefits have been previously described.

The armature stacks are built from 0.004 inch thick Hiperco-27 laminations with plasma sprayed alumina interlaminar insulation. The stacks are not welded in order to minimize core losses. Rigid ceramic slot liners are used in the slot channels of the armature stacks. In order to ensure that the slot liners can be inserted into the slot channels and the conductor can be inserted into the slot, a clearance between the slot liner and slot channel sides and the slot liner and conductor must be allowed. These clearances are detrimental to slot heat transfer, especially in a hard vacuum where slot heat conduction characteristics are almost entirely dependent on contact conductance and radiation. If the space gaps in the slot are not filled with a heat conducting material (e.g., a potting compound), then the slot heat flux density (watts per square inch) must be kept low. The best high

temperature non-organic potting compounds have high shrink rates during cure, high outgassing rates in hard vacuums, and their dielectric power factors and electric strength at high temperatures are poor. Because of the unavailability of a suitable high temperature inorganic potting compound for the KTA application, the armature will not be encapsulated. The low slot heat flux density of the KTA alternator design (approximately 5 watts/in<sup>2</sup>) provides for a reasonable temperature rise from conductor-to-tooth in a hard vacuum. Refer to Chapter 2.2 of this report for details on thermal performance.

A low voltage, high current strap wound field coil configuration was selected for the KTA alternator. Results of a study performed in the Phase I portion of the KTA program shows that this configuration provides better heat transfer characteristics than a high voltage, low current field coil. A high voltage design requires many turns of small diameter insulated wire which consequently results in a large number of insulation and contact gaps in the thermal path to the heat sink. The high current configuration requires a few turns of large cross sectional area strap conductors that are oriented so as to provide a minimum number of insulation and contact gaps in the thermal path. Coolant manifolds are located in the frame housing on each side of the field coil to minimize temperature rise. The field conductors are CUBE copper (BeO dispersion strengthened copper). Synthetic mica paper\* will be used for turn to turn insulation because of its low outgassing properties and adequate electrical properties at the operation temperatures and voltage of the KTA alternator field coil. Alumina

---

\* Plasma-arc sprayed alumina may be possible alternate.

insulation is provided for the field-coil to cooling-manifold insulation.

Because of the requirement for a ceramic bore seal separating the rotor and stator cavities, the radial gap between the stator and rotor must be large enough to accommodate the bore seal thickness plus provide adequate running clearance. The radial gap for the KTA alternator is 0.140 inches (with the machine hot and running) and was selected based on results of the Phase I parametric studies.

The selected gap was the larger of two alternate values (0.130 and 0.140) which provided nearly equal minimum system weight. The largest was chosen to minimize magnetic unbalance forces, provide increased radial clearance, and reduce pole face losses. The selection of a large radial gap tends to transfer losses from the rotor to the stator by reducing rotor pole face losses and increasing stator field losses. Removal of loss heat from the stator field coil instead of the rotor is a much simpler design task which provides many benefits regarding machine reliability and simplicity.

As mentioned in Chapter 2.1, Alternator Internal Design Variable Review, a new calculation procedure was derived as a result of an experimental verification program for determining the ac circumferential flux in the armature core. This new procedure was incorporated into the design program between Phase I and Phase II. It results in lower ac circumferential flux amplitudes than previously calculated and an approximate 10 percent corresponding weight reduction. Parametric trends for all studies performed in Phase I, except the armature core flux density studies, are not affected by the change. A rerun of the armature core flux density study (Reference to Chapter 2.1) using the new procedure

resulted in the same trends as in Phase I with the exception of lower alternator weights. Of course, the lower rating of the Phase II KTA alternator (600 kVA vs. 733 kVA for Phase I) also contributed to lower Phase II design weights.

#### Alternator Electrical Performance Data

Alternator electrical performance computations were made to verify that the performance meets the output and other requirements of the specification. Performance was determined at the alternator maximum continuous load rating (450 kWe, 0.75 lagging power factor) which was also specified as the nominal alternator rating for purposes of alternator performance calculations. Wave form and output voltage modulation requirements are retained as a final design goal without analytical verification.

Figure 2.1-1 presents the no load voltage saturation characteristic, the load saturation characteristic at 417 amperes, 0.75 power factor and at zero power factor lagging, and the three phase short circuit characteristic. It also presents saturation characteristics at the specified overload condition, that is 625A, 0.9 power factor, lagging. Required field current to obtain rated voltage at the no load, rated load, overload, and 3 per unit short circuit conditions are 109 amperes, 166 amperes, 187 amperes, and 189 amperes, respectively. Alternator electrical efficiency is presented in Figure 2.1-2 as a function of load at rated power factor.

Table 2.1-4 presents a breakdown of electrical losses, armature and field current densities, and flux density in the various alternator magnetic components at rated load conditions. Pole face losses were

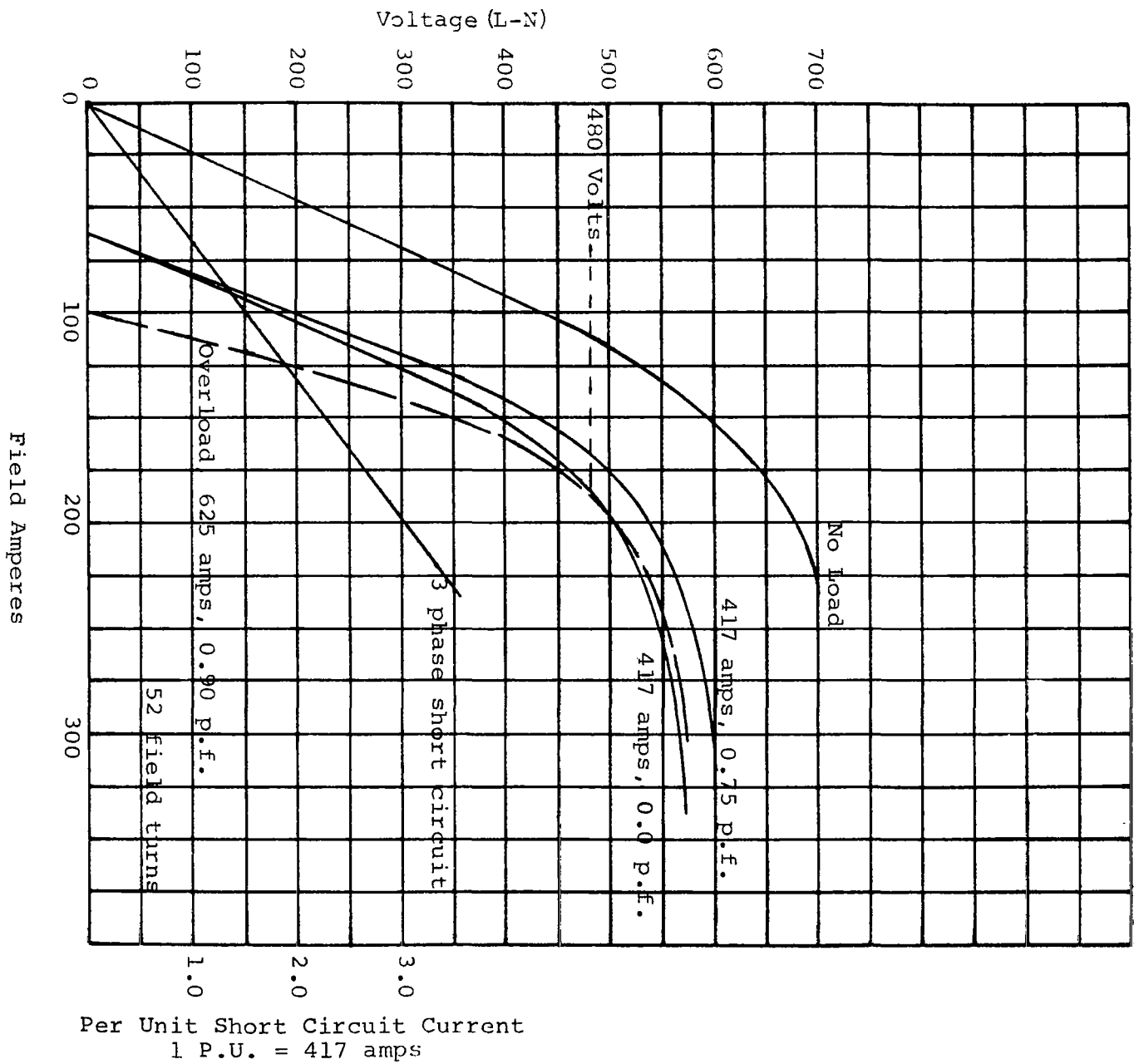


Figure 2.1-1. Saturation Curves.

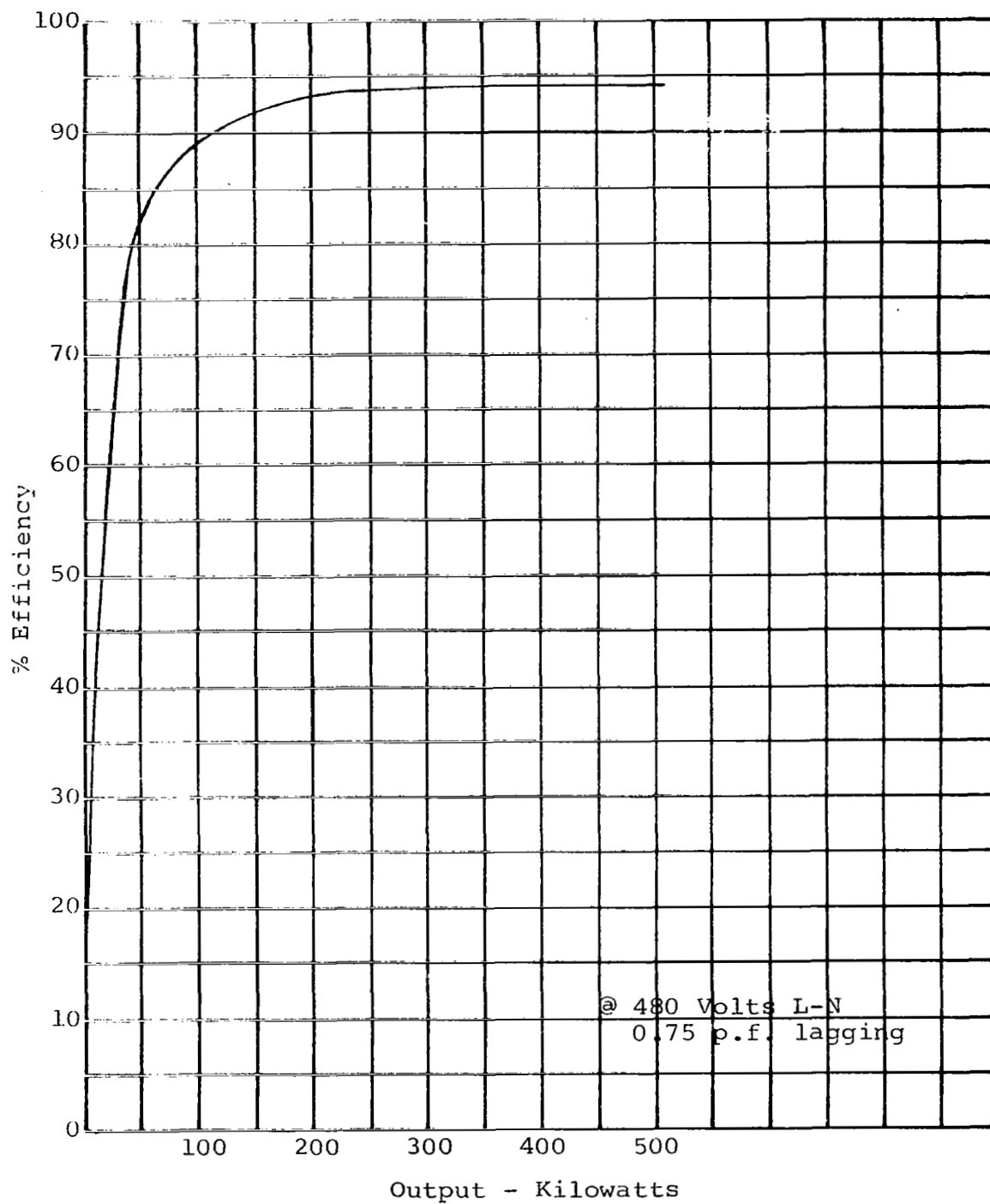


Figure 2.1-2. Alternator Efficiency (Excluding Terminal, Bus Ring, Bearing, and Seal Losses).

TABLE 2.1-4

ALTERNATOR PERFORMANCE DATA

Loss Breakdown	
Armature conductor	9.85 kW
Field conductor	4.37 kW
Armature stack loss	11.38 kW
Pole face loss	1.02 kW
Windage loss	<u>0.10 kW</u>
	26.72 kW
Electrical Efficiency:	94.4%
Current Density:	
Armature	5650 amps/in <sup>2</sup>
Field	4045 amps/in <sup>2</sup>
Flux Density Under Load:	
Depth behind slot	60 kl/in <sup>2</sup>
Teeth	124 kl/in <sup>2</sup>
Frame	114 kl/in <sup>2</sup>
Rotor core	80 kl/in <sup>2</sup>
Rotor Pole	69 kl/in <sup>2</sup>
Voltage Unbalance, 2/3 Rated Amps, 1 Phase:	5.7 % (L-N)



calculated for a grooved pole face configuration with 0.006 inch wide grooves, 0.100 inch deep, with a groove pitch of 0.034 inch. Calculated losses for this configuration are 1024 watts with 527 watts caused by the tooth ripple component of surface loss and 497 watts caused by the harmonics of the stator MMF when the alternator is under load. Windage losses were calculated as less than 100 watts; however, 100 watts are assumed for the efficiency calculation. The listed percent voltage unbalance corresponds to a single phase unbalance current of  $2/3$  rated current.

## 2.2 MECHANICAL DESIGN AND PERFORMANCE STUDY

### Introduction

The mechanical design studies included the final thermal analysis of the rotor and stator, the rotor stress analysis, the structural weight minimization and stress analysis and finally, the bore seal assembly design and analysis. The thermal analysis was based on the basic Phase I procedures as well as the cooling configuration selected from the Phase I studies. Because the Phase II electrical power loss density was lowered, the resulting temperature gradient between the hot spot and coolant was only about two hundred degrees fahrenheit instead of the three hundred degrees fahrenheit of Phase I. This, plus the reduction of the coolant temperature to  $700^{\circ}\text{F}$  kept all hot spots near or below  $900^{\circ}\text{F}$  even on slotted (unlaminated) pole faces.

The rotor stress analysis was completed with a recently developed computer program that, using finite element theory, determines a very accurate picture of the elastic/plastic stress pattern in the irregular

rotor body. Programs and calculation routines as complex and powerful as this one have previously been unavailable, awaiting the advent of bigger and faster computers.

Structural weight minimization studies were carried out in response to suggestions to Phase I design changes. By departing from aircraft alternator frame design techniques and using aerospace structural design techniques, significant weight reductions were achieved. The resulting light-weight frame did introduce some new problems associated with the rotor dynamics and vibrations, but they are solvable with design refinements at the next (hardware) stage of design.

The bore seal design effort concentrated upon the two tasks of becoming familiar with bimetallic joint technology and then doing basic stress analyses on the selected bore seal design. The study showed that the basics are well in hand for proceeding into a major development effort to bring the bore seal assembly up to the same developmental status as the rest of the alternator. A logical plan was derived that does not take a "shot-gun" approach to achieve, as quickly as possible, a high degree of developmental or operational success on the first bore seal assembly.

Once the needs of the bimetallic joint were realized, it was possible to configure a simpler but more reliable bore seal assembly design in Phase II (relative to that in Phase I). More importantly, however, was the realization that the design and fabrication of all the components of the bore seal assembly must be closely coordinated such that each of the seemingly separate areas of the design are in fact complimenting each other. In other words, the components of the

the assembly cannot be developed separately without a thorough knowledge of each of their requirements, functions or limitations.

### Thermal Analysis

The thermal design and analysis is based on the selected cooling configuration and calculation methods of the Phase I studies. Because of this, the complete details of the studies will not be repeated. Contained below is a basic description of the analytical model, the analytical methods and finally, a summary of the results.

Stator Cooling Configuration. The stator frame cooling configuration consists of four 360-degree circumferential cooling manifolds on the outside of the stator magnetic frame sections (Figure 2.3-1). These manifolds are ducted to the outside of the hermetic shroud around the alternator frame for access to the coolant supply lines. Cooling is achieved by conduction from the heat generating armature windings and stacks through the stator frame and manifold walls. The end turns of the stator (armature) windings are also cooled by radiation to the surrounding end bell and conduction to the stator frame. Between stacks, BeO spacers that double as heat sinks act to aid in transferring (by radiation and conduction) the armature losses there to the field coil cooling sink.

The thermal analysis of this configuration was calculated with the use of two computer programs. The first is a digital computer program for finding the transient and/or steady state ( $T_{\phi SS}$ ) temperature distributions of a three dimensional irregular body. This program, used in the Phase I studies, considers the heat transfer mechanisms

of conduction between internal points, conduction between internal and surface points, radiation between surface points, and radiation, free convection, and forced convection between surface and boundary points. It also considers internal heat generation which is a function of space and time. Boundary temperatures may vary as a function of time. The second program is a modified version of TØSS. This second program has eliminated the transient capabilities of TØSS and changed the solution of the general heat conduction equation from the explicit method used in TØSS to an implicit method, thereby allowing a larger time step and the use of less digital computer time. However, this second program (steady state), due to its method of solution, introduces an error to the results. For our calculations though, this error is quite tolerable. In general, most of the final results were obtained through use of the steady state program with occasional use of the TØSS program for result verification.

The calculation of a temperature distribution for the stator frame by use of these computer programs involves the setting up of a nodal grid work of the stator. For the sake of conserving computer storage space, a symmetrical axial section was taken as the analytical model. The three dimensional section comprised one-half a stator tooth pitch plus one-half a slot pitch for a section comprising 1.0 degree of arc circumferential volume. An axial length of one-half the total stator length was chosen for the symmetrical model. These models correspond to the basic configurations reported in Phase I as do the property data and configuration constants such as the critical  $0.2 \text{ watts/in}^2/^{\circ}\text{C}$  equivalent slot conductance.

Field Coil Cooling Configuration. In the KTA Phase I study, it was shown that it is desirable that direct cooling of the field coil be included in the stator cooling configuration. The Phase II design has two separate circular cooling ducts the full height of the field coil, one on either axial side of the coil (see Figure 2.3-1). They are electrically isolated from the coil by ceramic insulation. The cooling ducts on the coil sides provide a short, direct thermal path to the coolant for each electrical turn as well as additional cooling for the stack and ac windings between the stacks. These coolant ducts are ducted to the outside of the alternator hermetic frame-shroud for access to the coolant supply. The field coil cooling ducts and the stator frame cooling ducts should be in parallel flow but may be in series if volumetric flow requirements penalize the system cooling configuration (See Figure 2.3-1).

Initially, an analytical model representing a simulation of the stator frame with assumed rotor pole tip surface temperatures as fixed boundary values was run on the computer programs. These results were found to be inconclusive due to the assumed rotor conditions. It was concluded that a new model that included the collected stator and rotor geometries should be analyzed. This analytical model better simulated the actual physical situation in one sense but because of computer storage limitations, prevented analyzing the rotor temperatures in the circumferential direction. Thus, the rotor temperatures calculated were based on an analytical model of 1.0 degree of arc off an axial plane through the center of the pole.

Rotor Cooling Configuration. The rotor cooling configuration consists of a central coolant hole with the 700<sup>o</sup>F coolant passing

through the hole in series with the anti drive end bearing lubricant. For calculation of the complete rotor-stator temperature distribution, heat transfer mechanisms of both conduction to the coolant passage and radiation to the end bell housing were considered. The effects of windage losses and losses for both slotted and solid rotor pole face configurations were included in the analysis.

Summary of Results. The temperature distributions shown in Figures 2.2-1 and 2.2-2 represent the computer outputs for a 700<sup>o</sup>F stator coolant and slotted rotor pole faces. An analysis for an 800<sup>o</sup>F stator coolant for slotted rotor pole face configurations is given in Figures 2.2-3 and 2.2-4. The 800<sup>o</sup>F stator coolant models do not contain temperature distributions for the end bell extensions above the stator end turns due to the late addition of this section to the main thermal analytical model. It should be noted that this addition raised the end turn temperatures approximately 10<sup>o</sup>F over the original 700<sup>o</sup>F stator without end bells (not shown). The relative difference in this addition is negligible to the total thermal map. The coolant and boundary temperatures shown are necessary approximations (of expected results) for computer input requirements. The coolant approximations are based on the average of inlet and outlet temperatures. The void temperatures, used as radiation heat sinks, are based on approximations through experience with preliminary calculations.

A significant feature should also be noted in the figures in comparison of the 700<sup>o</sup>F and 800<sup>o</sup>F stator coolant models. The heat flux across the air gap and bore seal between rotor and stator reverses itself with the reduction of coolant temperature. This is also illustrated in a comparative summary of the significant temperatures, Table 2.2-1.

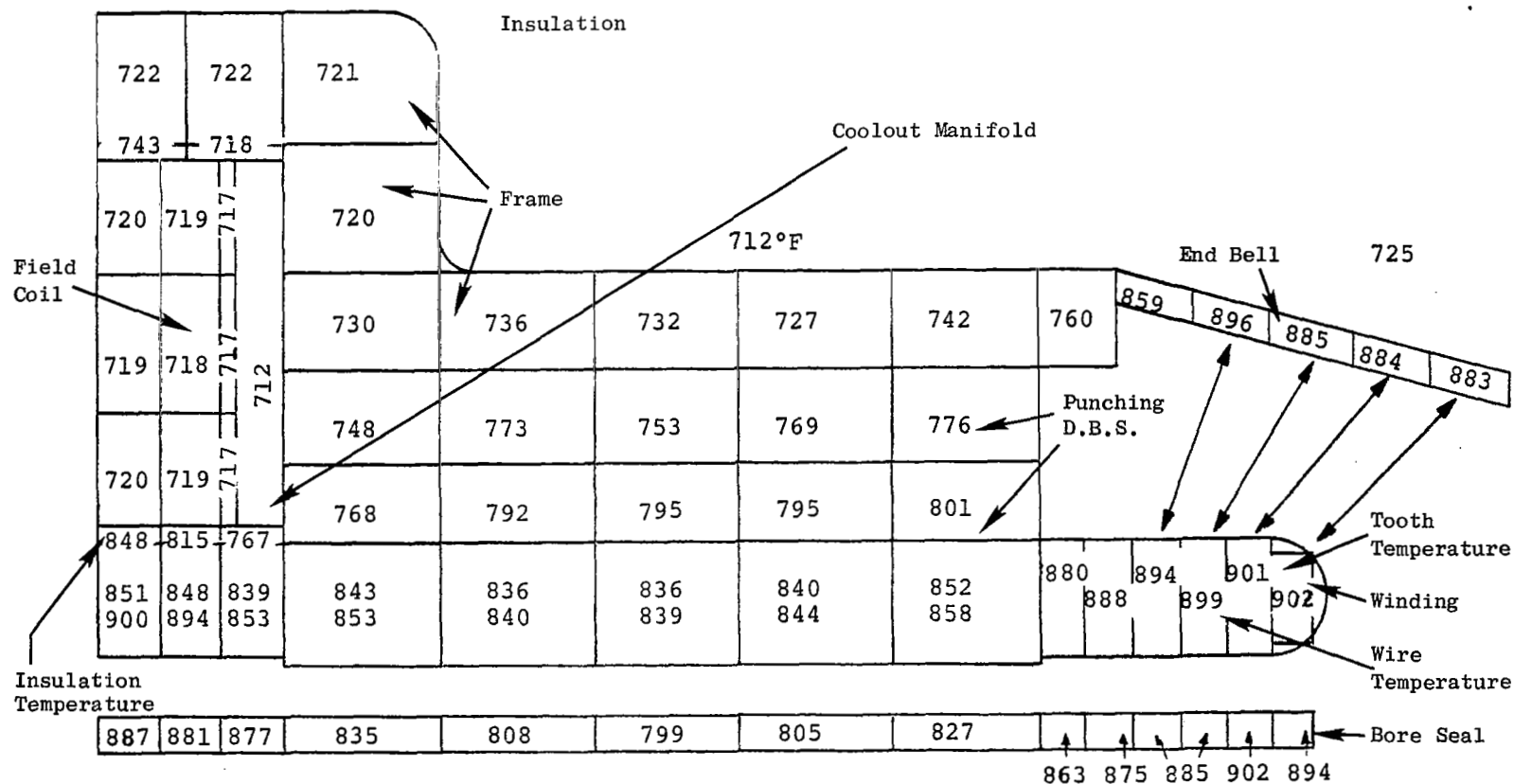


Figure 2.2-1. Stator Configuration 700°F Stator Coolant Slotted Rotor Pole Faces.

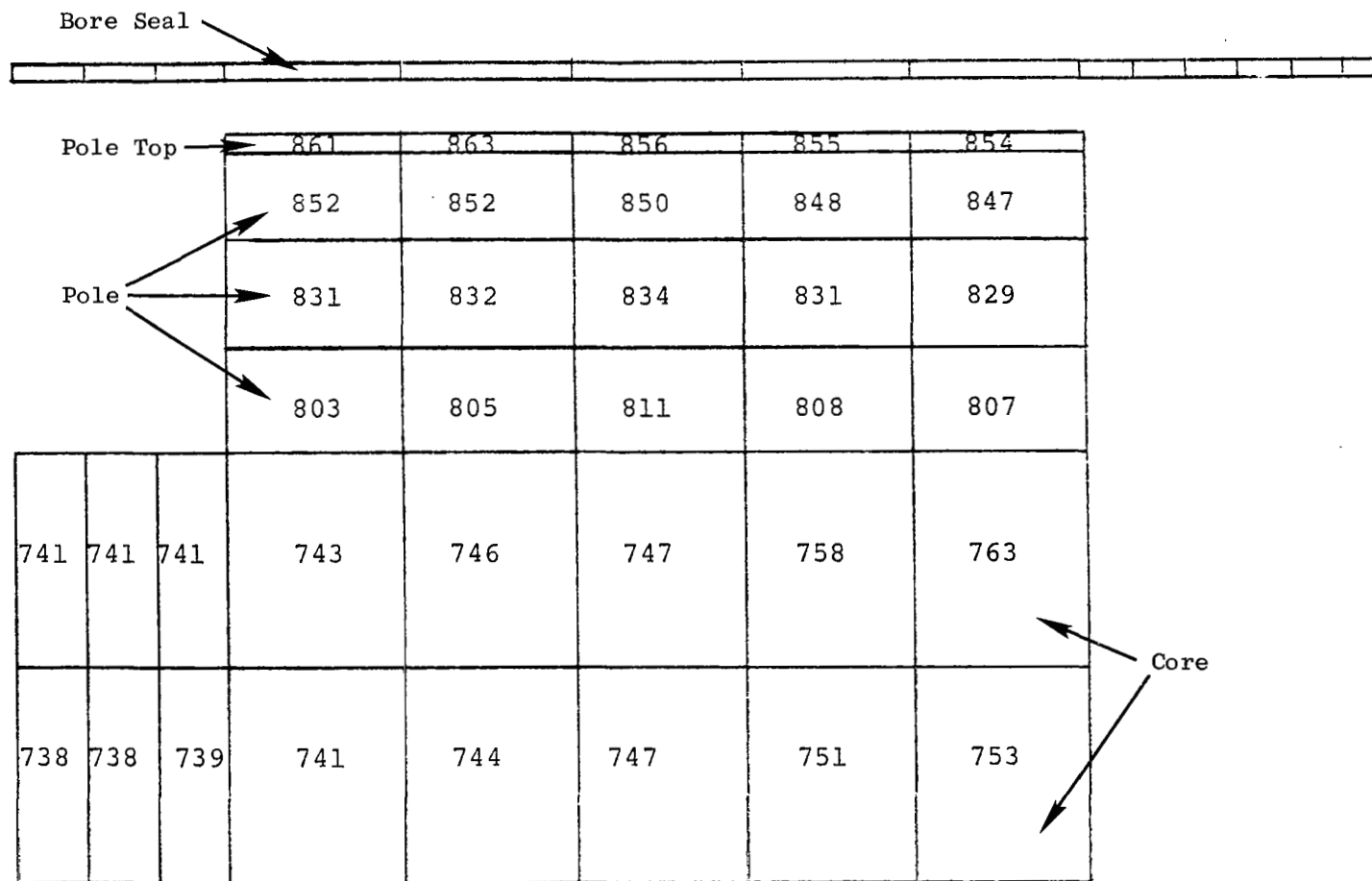


Figure 2.2-2. Rotor C Configuration 700°F Stator Coolant Slotted Pole Face.



Figure 2.2-3. Stator Configuration, 800°F Stator Coolant, Slotted Rotor Pole Faces.

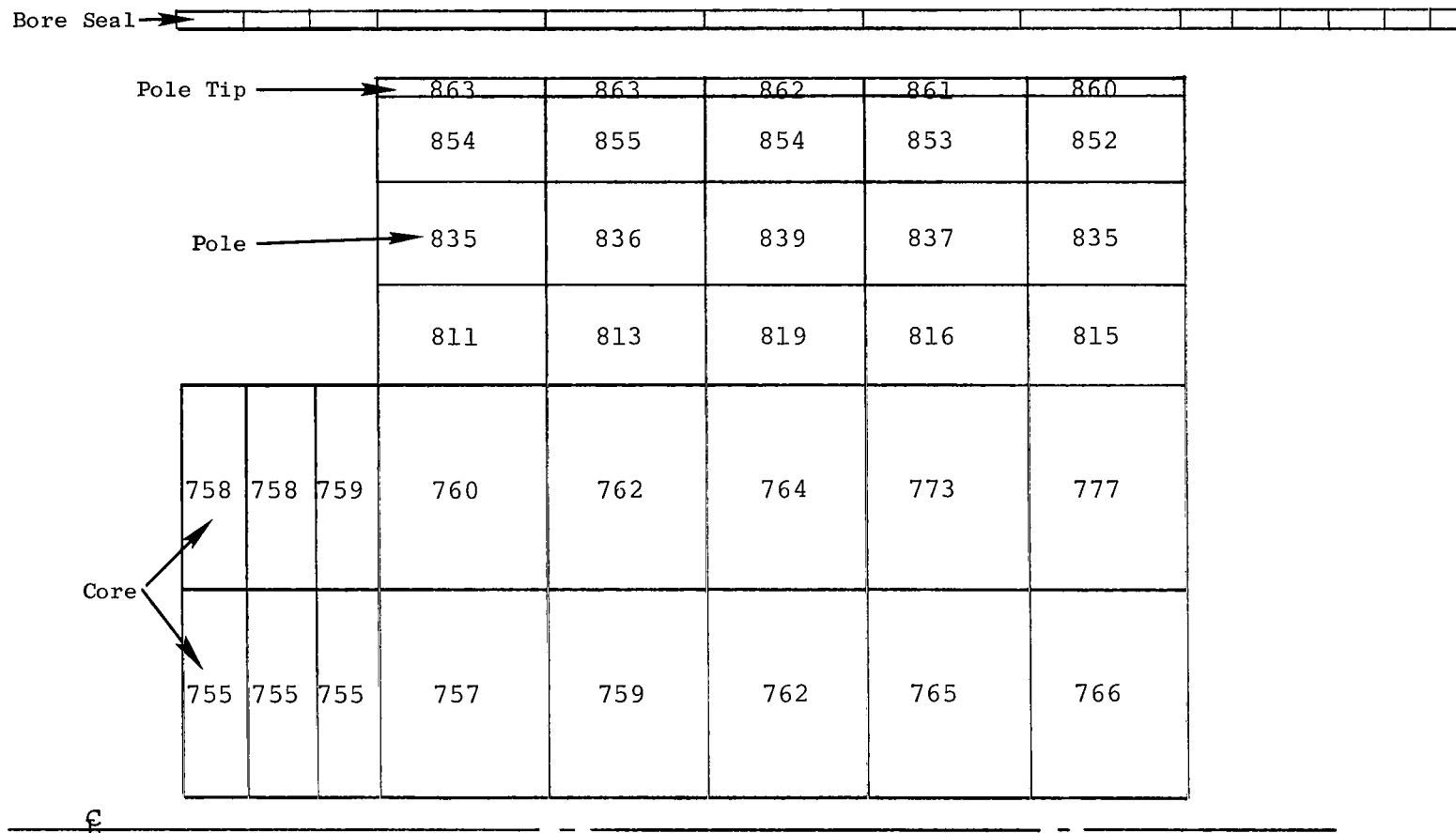


Figure 2.2-4. Rotor C Configuration, 800°F Stator Coolant, Slotted Rotor Pole Faces.

TABLE 2.2-1

PRELIMINARY COMPARATIVE ALTERNATOR TEMPERATURES\*

	700°F Stator Coolant		800°F Stator Coolant	
	Slotted Rotor Pole Face	Solid Rotor Pole Face	Slotted Rotor Pole Face	Solid Rotor Pole Face
Hot Spot	900°F	900°F	929°F	929°F
Location	Arm. Wind. Below F.C.	Arm. Wind. Below F.C.	End Turns	End Turns
End Turn Avg. Temp.	875°F	875°F	927°F	927°F
Armature Wind. Avg. Temperature	867°F	867°F	912°F	912°F
47 Stator Tooth Avg. Temperature	835°F	835°F	897°F	897°F
Field Coil Avg. Temperature	720°F	720°F	820°F	820°F
Rotor Pole Face Avg. Temperature	862°F	874°F	862°F	873°F
Heat Flux Direction Between Stator/Rotor	Rotor to Stator	Rotor to Stator	Stator to Rotor	Stator to Rotor
Calculated Pole Face Losses	1024 watts	1410 watts	1024 watts	1410 watts

\* Excludes the effects of the end bell between the armature end turns and the 725°F void ambient. Was done prior to including the simulated end bell into the analytical model.

One of the major conclusions coming from the thermal analyses was that the reduction in rotor coolant temperature to 700<sup>o</sup>F obviated the need for laminated pole faces. The pole tip temperatures will be less than 900<sup>o</sup>F with slotted pole faces; hence, reliability should be enhanced with the solid pole bodies. In fact, based on the calculated results shown on Table 2.2-1 solid pole faces should suffice. In the interests of reliability and design conservation, however, it is proposed the slotted pole face construction be used.

Scavenge System Performance. Part of the alternator rotor coolant flow circuit consists of a scavenge system which can be used to scavenge liquid potassium from various compartments within the assembly. The compartments from which liquid potassium can be scavenged are (1) the enclosure around the drive shaft coupling, (2) the rotor cavity, and (3) the low pressure chamber between the liquid and vapor shaft seals. Liquid potassium will leak into the enclosure around the drive shaft before start-up and during the initial acceleration of the rotor since the liquid within the bearing compartments is confined by dynamic seals. These seals will not effectively confine the liquid until the rotor has been accelerated to a minimum "sealing" speed. The point at which the seals will become effective depends upon the pressure within the bearing compartment. For example, if the unit were started with approximately 5 psia pressure in the bearing compartments, the liquid might be effectively confined at speeds as low as 4000 rpm. For the worst design case, it is reasonable to assume that the coupling enclosure will be filled with liquid before the seals become effective. This liquid must be removed before the rotor is accelerated to design speed in order to prevent damage of the coupling from hydrodynamic forces.

Liquid will flow into the rotor cavity if the shaft seals between the bearings and rotor cavity are less than perfect. These shaft seals can only be designed to prevent a large volume of liquid potassium from leaking into the rotor cavity. The rotor cannot be accelerated without damage of the bore seal if a large volume of liquid were present within the rotor cavity. Any liquid which passes through the shaft seals must be removed as liquid or vapor through the molecular pumps or the auxiliary scavenge system. Since the pumping speed of the molecular pumps are very low, they will be unable to remove the vapor associated with a significant amount of liquid. Thus, the liquid which flows into the rotor cavity must be removed, for the most part, by the auxiliary scavenge system.

The scavenge scheme for the various compartments consists of a dynamic slinger in the anti drive end of the rotor as illustrated in Figure 2.2-5. The slinger contains equally-spaced chambers which are vented into the bearing cavity. These chambers produce solid body rotation of the liquid which produces large centrifugal forces upon the dense liquid. The centrifugal head generated in the slinger is sufficient to overcome the pressure within the bearing even for the liquid vapor pressure at the central portion of the slinger as illustrated in Figure 2.2-6. The low pressure in the central portion of the slinger provides a sink for the liquid within the rotor cavity, coupling enclosure, and the low pressure chamber between the shaft seals.

A pressure head is necessary to circulate the liquid from the drain port on the coupling enclosure and/or the rotor cavity to the scavenge ports on the anti drive end of the alternator. This can be accomplished by operating the assembly in a vertical position with the anti drive

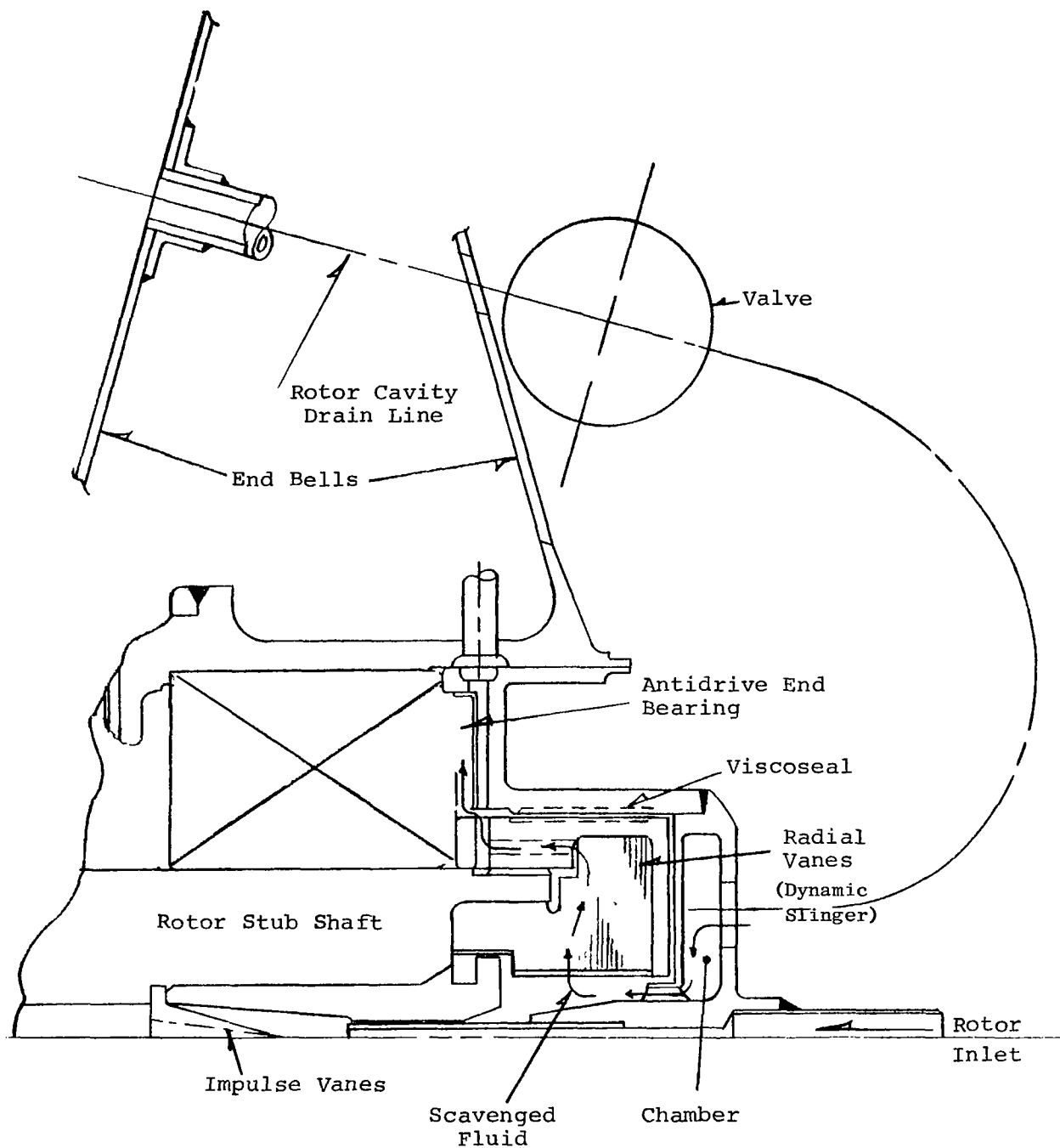


Figure 2.2-5. Rotor Cavity Scavenge System Details.

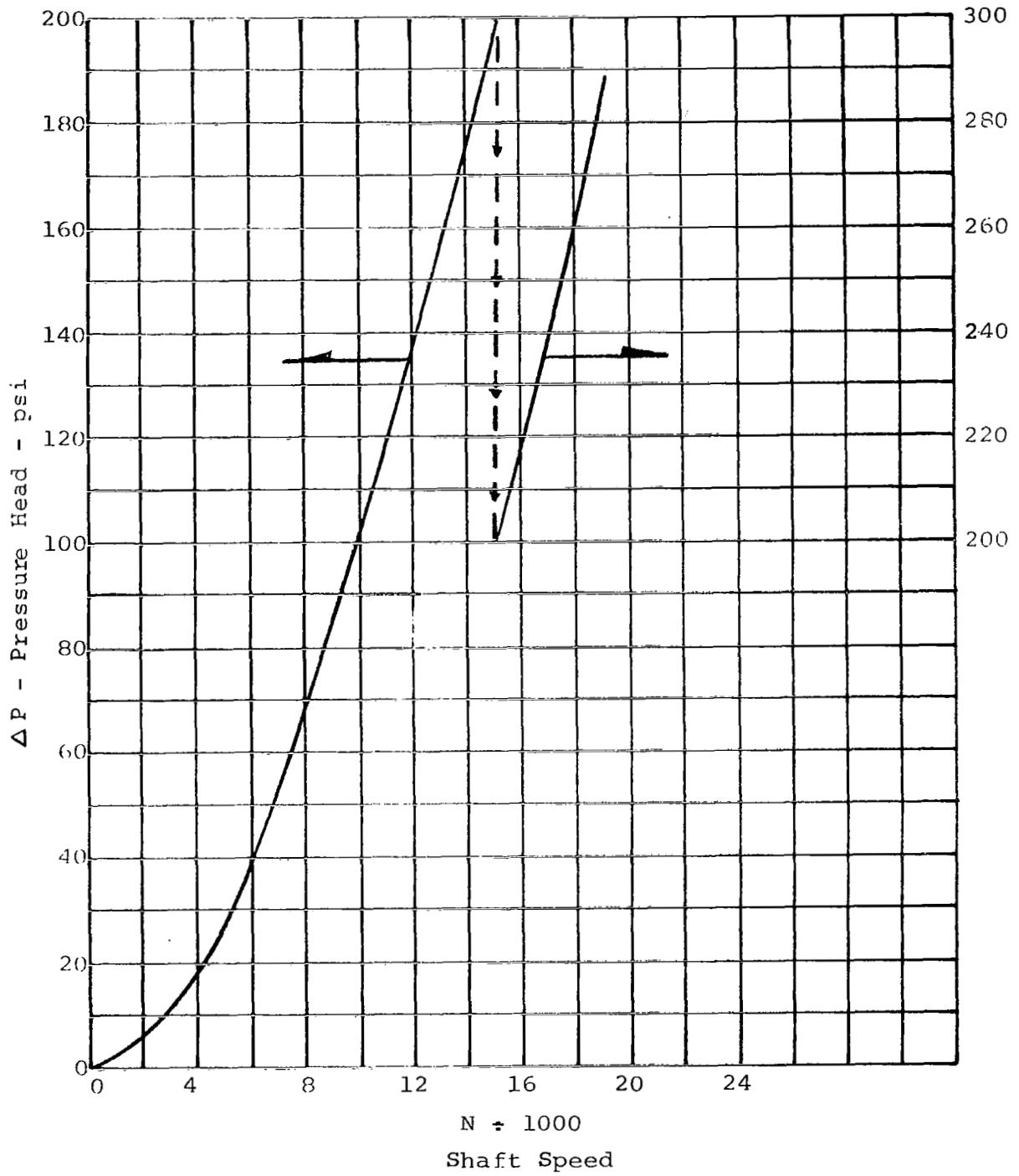


Figure 2.2-6. Slinger Centrifugal Head.

end down, using gravitational forces to circulate the liquid. Such an arrangement would not work unless gravitational forces exist. For the KTA, however, dynamic slingers can be incorporated on the rotating parts to provide sufficient velocity head to circulate the liquid from the various drain ports to the scavenge ports in the anti drive end of the alternator.

The rotor cavity cannot be vented into the scavenge system before the central portion of the slinger is empty; if it were, liquid could flow into the rotor cavity. Thus, the drain line from the rotor cavity must contain a valve which can be opened and closed at the proper time during the start-up cycle. The valve would be closed after the rotor cavity is drained so the molecular pumps can reduce the pressure within the rotor cavity.

#### Structural Weight Minimization

Introduction. The total rotor and stator weight required in this 600 kVA machine for proper electrical efficiency plus unavoidable bearing, housing and stub shafts is approximately eight hundred forty (840) pounds. The Phase I alternator scaled to this 600 kVA size had an additional end structure or end bell weight of about two hundred (200) pounds. Initial attempts in Phase II to minimize this end bell weight resulted in a reduction of the two hundred (200) pounds to about one hundred (100) pounds. At that point in the Phase II design, structural experts from the Westinghouse Astronuclear Laboratories were brought into the design team to evolve a lighter weight configuration without sacrificing strength. As a result of the study at Astronuclear Laboratories, a preliminary end bell configuration was



evolved which meets the structural requirements and has a weight of about half of the one hundred (100) pounds, i.e., forty-six (46) pounds. The study to evolve this design did not allow for refinements on this "first" minimum weight design. Therefore, the present design must be considered preliminary at this stage.

It is believed that this end bell concept is for all practical purposes a minimum weight design. The concept shown is stability limited rather than deflection or size limited with one exception. Analysis by the General Electric Company and Mechanical Technology Inc. revealed that the radial and axial deflections or spring rates were such that they affected the rotor dynamics characteristics. Therefore, in the next phase (hardware type phase), it will be necessary to add stiffening to the design in the conical end bell areas to increase the spring rates. It also appears that it could be possible to obtain another weight reduction of about twenty (20) pounds by stiffening the weaker sections with some sort of sandwich structure at the expense of increasing the cost and complexity of the components by perhaps a factor of five to ten. This additional twenty (20) pound reduction in a nine hundred (900) pound machine does not appear practical.

Design Summary. Certain ground rules were followed for the preliminary structural design. No attempt will be made to list every constraint but the more significant ones are tabulated below.

- (1) The end bell material must be non-magnetic and compatible for mounting to the Hiperco-27 stator material.
- (2) The end bells must be sufficiently rigid to prevent bearing housing deflections from exceeding 0.010 inches translation

and 0.012 degrees rotation while withstanding environmental shock and vibration loadings as well as design pressure and temperature as specified.

- (3) The bearing housing configuration must be maintained so that the interfaces with the bearing and seal housings are not altered.
- (4) Provision must be made for penetration of the anti-drive-end end bell by thirty electrical leads with approximately one-half inch clearance around each lead.
- (5) The design must also provide for suitable sealing of the rotor cavity and lend itself to reasonable assembly procedures that are restricted somewhat by the requirements of the bore seal and the design of the integrated stator and rotor.

All of the above requirements were considered in arriving at the structural design. In some areas, the resulting design is over-designed; i.e., the stresses were low compared to the material allowable stress. In some areas, another limit has been reached - - the stress in the sheet metal components is limited by buckling. No attempt was made to optimize the situation on a cost basis, that is, choose a cheaper, weaker material.

The choice of end bell material is limited by certain requirements dictated by the electrical design. Basically, these are (1) the material must be non-magnetic, (2) it must be compatible with the operating temperature of approximately 900°F, and (3) the coefficient of thermal expansion must be between  $4.1$  and  $6.4 \times 10^{-6}$  inches per inch per °F.

The coefficient of a thermal expansion requirement is one of the more critical limitations because it is necessary to match as closely as possible the expansion of the Hiperco-27, the H-11 and the bore seal end member assembly structure. Coefficients of expansion which exceed the range or are much lower than the range complicate the design problem, especially in the bore seal end member design, and can affect the reliability of the design as a result. The primary candidate materials considered for the end bell are listed in Table 2.2-2. Of the five materials shown, only two have coefficients of expansion which fall into the desired range. One of them, the Titanium alloy, looks quite attractive except for the oxidation resistance at temperature. The second one, the Carpenter-42, is magnetic up to about 700<sup>o</sup>F which would preclude the capability of testing the alternator at room temperature; thus, it cannot be seriously considered. The Hastelloy B material has properties which look attractive except the coefficient of thermal expansion is slightly higher than the range specified and the yield strength is only 39,000 psi at temperature.

For purposes of the analytical study to determine stress, the Inconel 718 alloy was arbitrarily selected\* for the representative end bell material because of its high strength at temperature, its reasonably close match to the required thermal expansion, its magnetic properties and its excellent fabricability. As shown later, the stresses calculated for the design using the Inconel 718 were

---

\*It was selected prior to the survey of Table 2.2-2 being completed. As seen in the Table, Inconel 718 cannot be considered one of the better choices due to its high coefficient of expansion. Nevertheless, the stress data given for Inconel 718 end bells are given because (1) it was the only case calculated and (2) it should be representative of the stresses in the Hastelloy B end bell material finally selected.

TABLE 2.2-2

END BELL MATERIAL COMPARISON

	Required Property	Hastelloy B Ni, 2.5Co, 28Mo, 1Cr, 6Fe	Inconel -18 53Ni, 26Cr, 5Cb, 3Mo	B120CVA Ti, 13V, 11Cr, 3Al	Carpenter-42 Fe, 41.5Ni	Mar-M-302 Co, 21.5Cr, 13W, 9Ta
1. Coeff. Therm. Exp. (in/in-°F)	4.1-6.4x10 <sup>-6</sup>	6.66x10 <sup>-6</sup> (rt-1000°F)	8.0x10 <sup>-6</sup> (rt-1000°F)	5.5x10 <sup>-6</sup> (rt-1000°F)	4.95x10 <sup>-6</sup> (rt-1000°F)	7.6x10 <sup>-6</sup> (rt-1000°F)
2. Temp. Range (°F)	rt-890°F					
3. Stress (psi)	30,000 psi					
4. Non-Magnetic (μ)	1.0 - 2.0	Paramagnetic, 1.000 &lt; 1.001	1.001	1.00005	Curie 715°F	Non-Magnetic
5. Properties:						
E		27.8x10 <sup>6</sup> @ 800°F	26x10 <sup>6</sup> @ 890°F	10.7x10 <sup>6</sup> @ 890°F	21x10 <sup>6</sup> @ rt	36x10 <sup>6</sup> @ rt
ρ		0.334 lb/in <sup>3</sup> @ rt	0.296 lb/in <sup>3</sup> @ rt	0.175 lb/in <sup>3</sup> @ rt	0.293 lb/in <sup>3</sup> @ rt	0.333 lb/in <sup>3</sup> @ rt
K		102 Btu-in/ft <sup>2</sup> -hr-°F @ 890°F	97 Btu-in/ft <sup>2</sup> -hr-°F @ 890°F	105 Btu-in/ft <sup>2</sup> -hr-°F @ 890°F	74 Btu-in/ft <sup>2</sup> -hr-°F @ rt	155 Btu-in/ft <sup>2</sup> -hr-°F @ rt
σ <sub>y</sub>		39,000 psi @ 890°F	127,000 psi @ 890°F	100,000 psi @ 890°F	40,000 psi @ rt	72,000 psi @ 890°F
σ <sub>t</sub>		104,000 psi @ 890°F	159,000 psi @ 890°F	160,000 psi @ 890°F	82,000 psi @ rt	110,000 psi @ rt
Elongation		68% - 890°F	18% - 890°F	20% - 890°F	30% - rt	2% - rt
6. Weldability		All common methods except oxygen/ acetylene	Very good	Excellent	Good	Good
7. Fabricability		Mach. Index 12	Good mach.	Good	Good	Difficult
8. Available Forms		Sheet, Cast, Forge	Sheet, Cast, Bar	Sheet, Bar, Forge	Strip, Bar	Cast
9. K Resistance		< 1100°F	< 1700°F	< 1100°F	< 1100°F	< 1600°F
10. Oxidation Resistance		< 1400°F	Good	< 800°F	Good	Good

sufficiently low as to allow eventual use of a weaker structural material such as the Hastelloy B in the final design. As a result of the stress analysis and the review of the material properties of Table 2.2-2 it is recommended that Hastelloy B be used as the end bell material for the final design. Stress analyses were not repeated for the Hastelloy B end bell material.

Double cones were used in order to provide bearing housing longitudinal and angular rigidity while maintaining the bearing housing location and the electrical envelope of the stator (see Figure 2.3-1). Elliptical wire penetrations were provided near the outer edge of the reinforced cones on the anti-drive end. The bore seal is welded to the inner cone of this perforated end bell from the input end of the alternator. Because of the arrangement of the leads through the perforations, this anti-drive-end end bell becomes a permanent part of the stator assembly and would not ordinarily be removed on a normal teardown dis-assembly.

The end bell on the drive end frame is ordinarily removed on dis-assembly and provision is allowed for such by seal welding the bore seal to an axial (tubular) housing extending from the Hiperco-27 frame. Separate bolt circles are provided in the area of the joint between the axial housing and drive end bell to allow for (1) the attachment of the end bell and the seal welding of the joint to seal the rotor cavity, and (2) the mounting location for the cold frame truss to the turbine. Separate schemes were devised where these two bolt circles could be combined as one with the requirement that the hermetic sealing of the rotor cavity be combined with the cold frame mounts. This saves weight but complicates the design in that the cold frame truss must become a

permanent part of the alternator end bell. An alternate scheme was devised whereby the bolt circle for hermetically sealing the rotor cavity was lowered to a diameter near the bearing housing OD. However, this design complicates the bore seal end member configuration and the design functions it must fulfill. Also, because of the very rigid nature shown by the double cone configuration, it may be possible to use only one cone and still build the alternator to meet the requirements.

Summary of Analysis. The environmental specification supplied by NASA for launch loads indicates that the alternator must withstand very severe sinusoidal vibration with excitation from 5 to 2000 cps at G levels up to 15 G's peak. The shock requirement specified is a 20 G half-sine-pulse of 10 millisecond duration. The acceleration requirement is less severe than either of these. Orbital operating requirements are also less severe than these launch requirements.

Since it is not practical to design the unit with natural frequencies high enough to avoid resonance, it is recommended that a vibration isolating mount be incorporated into the vehicle interface with the turbine-alternator assembly. These two units should be rigidly joined to provide proper shaft alignment. The mount will tend to amplify loadings at its natural frequency and attenuate loadings at higher frequency. The natural frequency of the mount should be selected to be below all component resonances so that the full input G level does not excite such resonances.

It is further suggested that a mount be considered to suspend the system at a natural frequency of about 20 cps with at least 10 percent of critical damping. This mount would amplify the excitation to about

15 G's at 20 cps where resonances can probably be avoided but would attenuate the loadings above 30 cps where resonances are likely to be encountered. At 100 cps for example, the applied loading could be attenuated by about a factor of 10 and at 200 cps by a factor of 30. This mount system would also attenuate the shock loading below the input pulse level.

The analysis for the stresses in the end bell structure was performed assuming a G level of 20 G's, internal pressure difference between the rotor cavity and the environment of 30 psi, and a uniform operating temperature of 850<sup>o</sup>F. The G load could, of course, act in any direction. Under the isothermal condition, the bearing center spacing increases 0.103 inch. It was assumed that this thermally expanded bearing spacing is the reference point from which the deflections are limited. It should be mentioned that the effect of thermal transients and gradients have not been included at this time since these considerations are beyond the scope of the present conceptual design effort. Now that the thermal analysis has been completed, the gradients in the cones can be included (next design phase). If the gradients cause severe stress increases over those shown, it may be necessary to later use single cones rather than double cones.

The stress analysis was done using a computer program similar to that used for the bore seal stress analysis as discussed below. The computation technique uses finite element theories requiring large and fast computers.

The results of the analysis are tabulated below:

- (1) Isothermal Heating to 850<sup>O</sup>F - There are stresses resulting due to differential expansion between the Hiperco-27 and the end bell. The maximum effective stress in the Hiperco-27 is 19,700 psi. Since the yield stress is about 55,000 psi and the stress for one percent creep in 10,000 hours is about 45,000 psi, this stress level is acceptable. The maximum effective stress in the end bell is 23,200 psi. Because of the low stresses in the end bell, it can be concluded the structural material can be one having low strength. The review of materials listed in Table 2.2-2 indicates that the logical choice would be the Hastelloy B material. The analysis was not rerun using the Hastelloy B material since, for all practical purposes, the analysis used\* verified the integrity of the preliminary design. At such time that final design refinements are included into the configuration, the analysis should be re-done using Hastelloy B material.
- (2) Rotor Cavity Pressure - The assumed 30 psi rotor cavity pressure produces maximum effective stresses in the Hiperco-27 of 840 psi and in the end bell of 5500 psi. Both values are negligible. The translation of the bearings (relative to each other) is 0.0013 inch. The 30 psi was assumed to act in the direction causing the maximum deflection to the end bells, i.e., internal pressurization.

---

\*In the discussion given, Inconel 718 is the end bell material. It will be Hastelloy B in the eventual design but stress calculation data was not prepared for use of this material at this time.



- (3) 20 G Axial Load - The loading produces a maximum stress of 1050 psi in the Hiperco-27 and 8400 psi in the end bell. Again, the stress levels are low. The relative bearing housing translation is 0.0038 inch.
- (4) 20 G Lateral Load - This loading produces 920 psi in the Hiperco-27 and 10,000 psi in the end bell. The angular rotation of the bearing housing is about 0.011 degree. These values are acceptable.

The above deflections can be superimposed directly. The maximum relative translation of the bearings is 0.0051 inch while the maximum rotation is 0.001 degree. These values are well within the desired limits specified at the start of the study. One effect that has not been included is the gyroscopic effort that would exist due to turning of the unit. The specification does not include pitch or yaw velocity requirements which would be needed to determine these effects. Also, as mentioned previously, the end bell stiffness needs to be increased to improve upon the rotor dynamics.

The above stresses do not superimpose directly. In addition, discontinuities complicate the analysis. The maximum stress (approximate) in the Hiperco-27 is an acceptable 20,000 psi. The stress (again approximate) in the end bell is less than 30,000 psi. The limiting condition in the end bell is the 10,000 psi compressive stress in the conical members during G loading. The critical stress is difficult to determine, but has been estimated at about 20,000 to 30,000 psi which should provide sufficient margin against buckling.

## Rotor Stress Analysis

Analytical efforts were continued toward better determining the stresses in the rotor. Although these analyses on the Phase II design were basically a continuation of those in Phase I, the computation methods were changed as the result of the acquisition of two newer, more powerful computer programs during the Phase I to Phase II interim.

The programs consist of a routine to generate element and nodal point data for input to a comprehensive stress program and the stress program itself. The stress program is a finite element computer program for plane elastic-plastic problems based on the theory of plasticity and the finite element displacement method. Five different types of stress-strain curves have been incorporated into the program. It can determine displacements and stresses in arbitrary plane shapes with a variety of boundary conditions and loadings. They include boundary tractions, body forces, and temperature variations.

Rotor Stress. The rotor stress was determined for a symmetrical section normal to the centerline through a section consisting of one-half pole pitch (just as in Phase I). The radial temperature profile according to Figure 2.2-2 was included to take into account the thermal stresses. As part of the computer program output, several stress maps are machine plotted. A portion of these are presented in Figures 2.2-7 through 2.2-10 to illustrate the conditions of rotor stress. The first two figures present the equivalent (Von Mises) stress for normal speed and 20 percent overspeed. The latter two present the maximum principal stresses and their direction (flow lines). The jaggedness of the plotted lines is due to machine plotter routines (interpolations) rather than actual operating stresses. Note that the majority of the rotor core is below 55 kpsi at design speed.

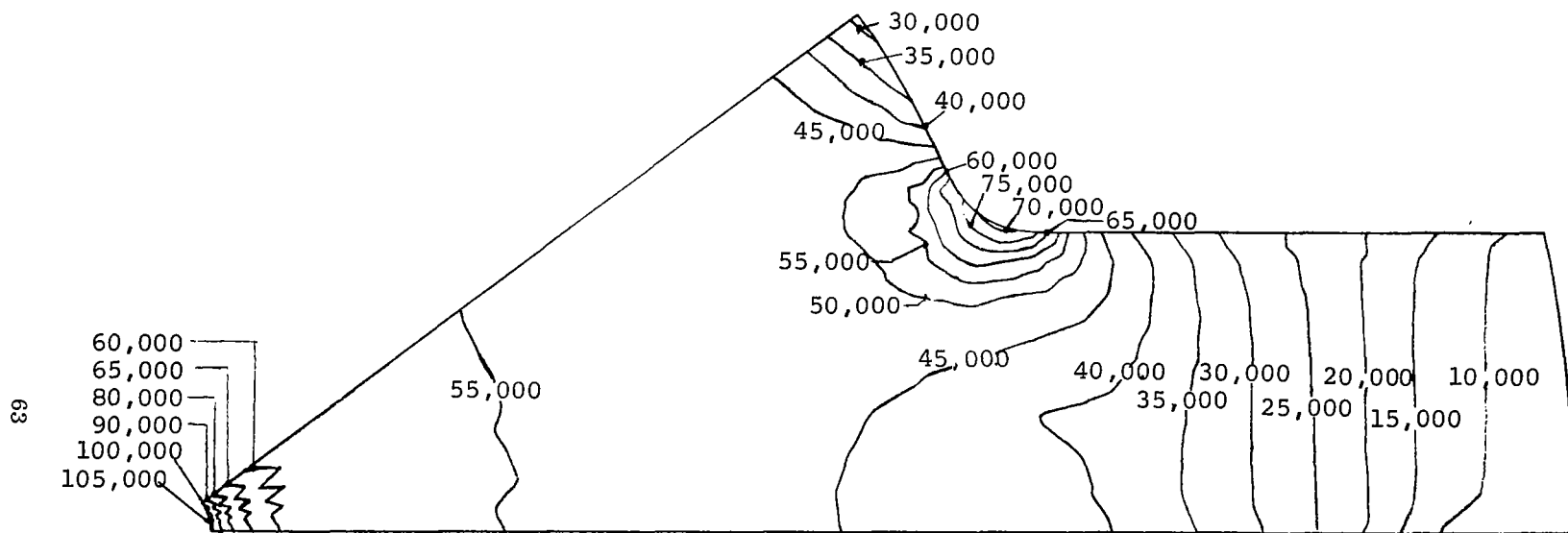


Figure 2.2-7. Equivalent Stress, Design Speed.

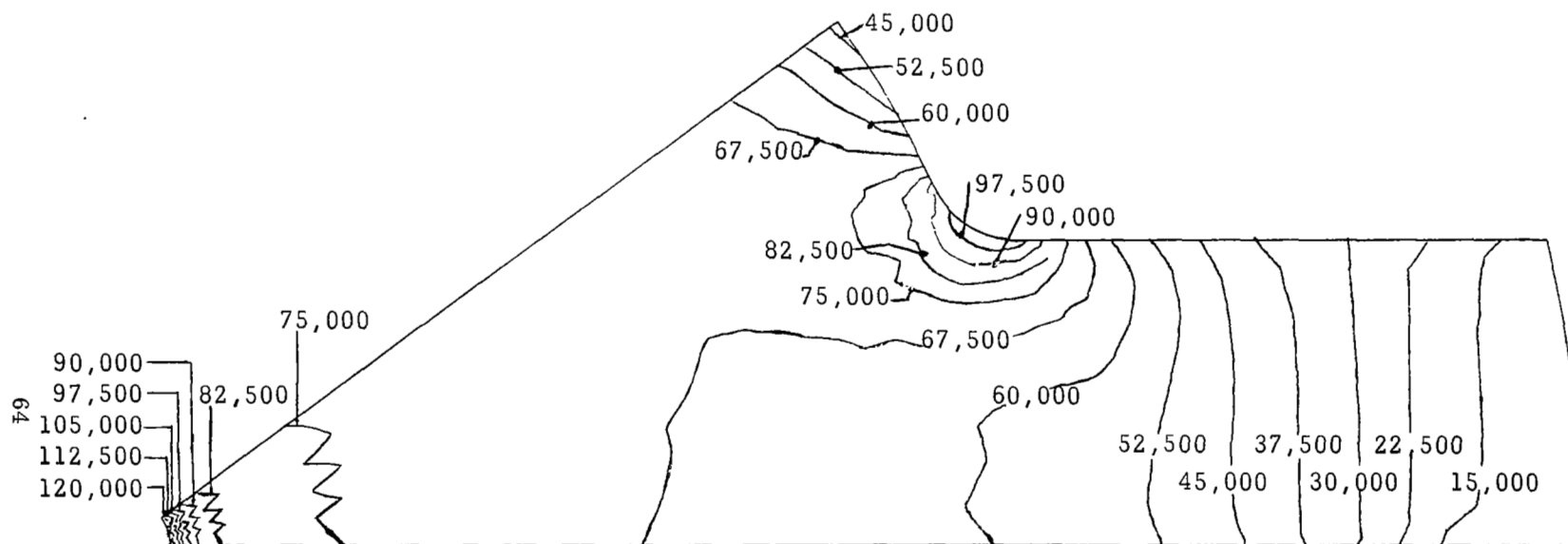


Figure 2.2-8. Equivalent Stress, 20% Overspeed.

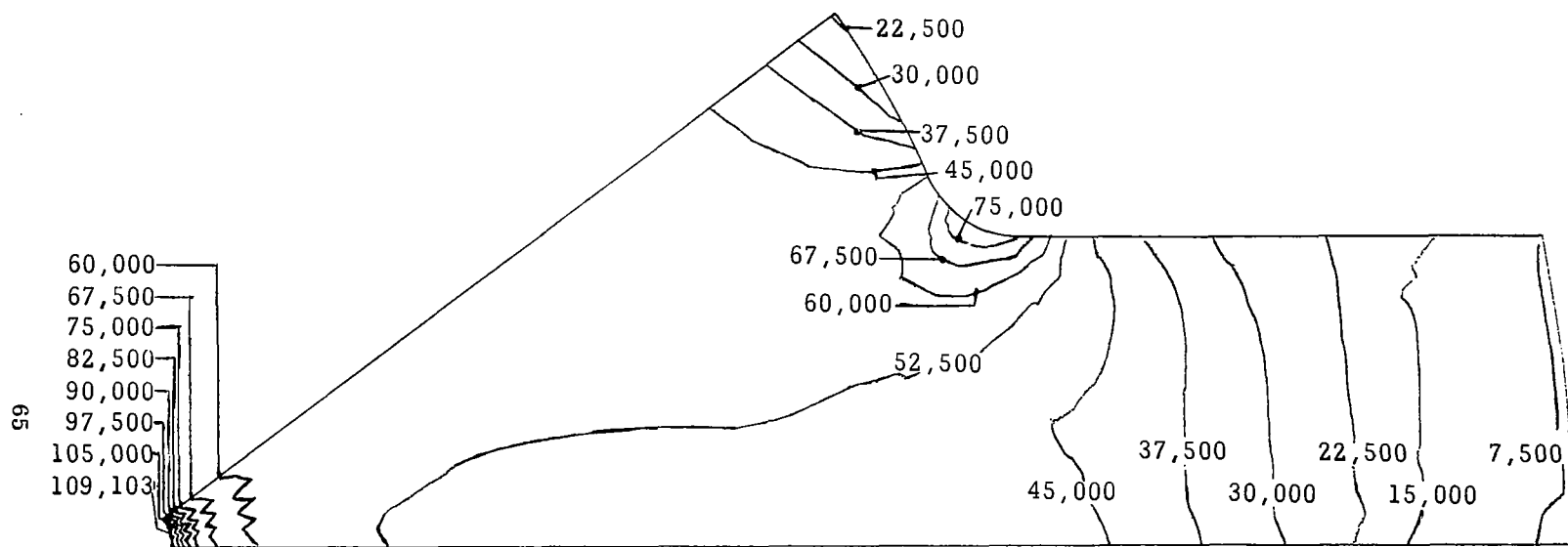


Figure 2.2-9. Maximum Principal Stress, Design Speed.

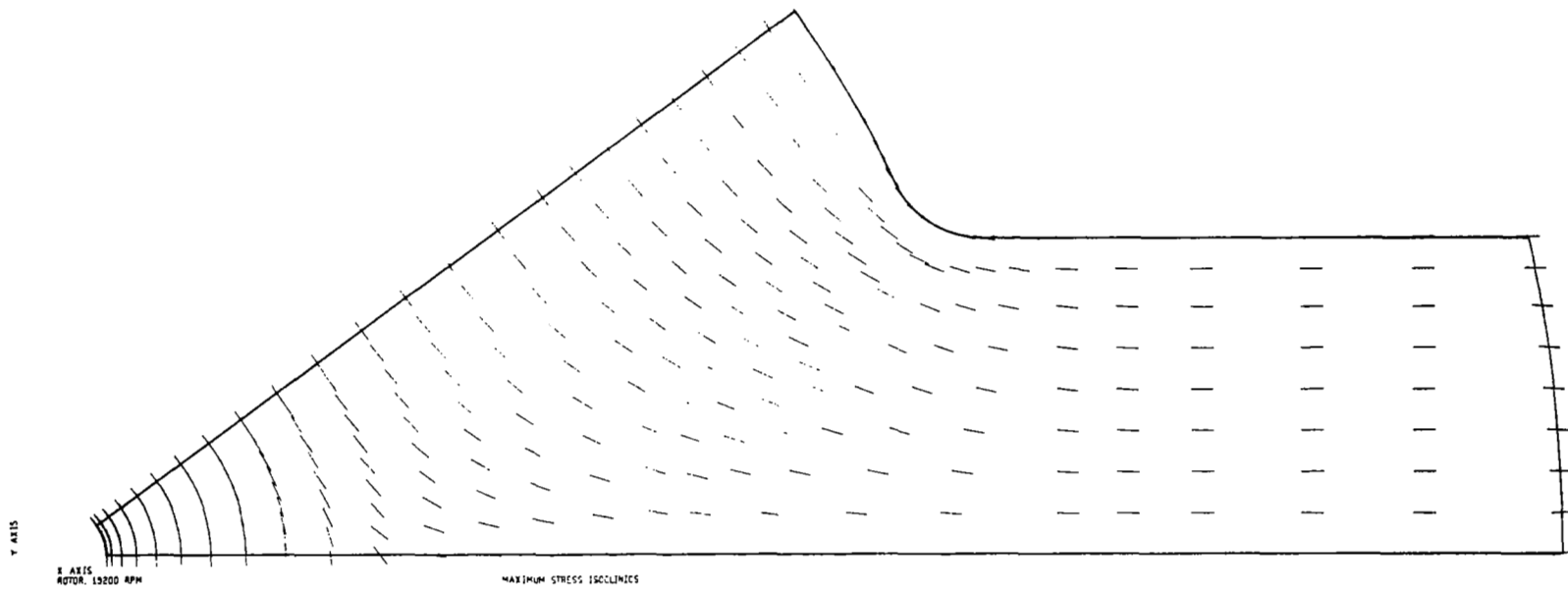


Figure 2.2-10. Maximum Principal Stress Isoclinics, Design Speed.

At 20 percent overspeed, the stress at the center bore is beyond the proportional limit of the H-11 steel indicating the material around the bore will undergo a permanent deformation. However, the integrated creep rate over the rotor radius at design speed and overspeed is below 0.1 percent which essentially eliminates creep growth as a critical design criteria. However, to be conservative, the radial gap is sized to absorb at least 0.1 percent creep strain without rubbing. Only at very small radii around the bore are the creep rates in excess of 0.1 percent. These are shown on Figure 2.2-11.

The combined dynamic and thermal growth of the pole tips and one-half inch rotor bore are 0.1006 and 0.0046 inch for 19,200 rpm operation at full load. The combined growths at 20 percent overspeed are 0.1084 and 0.0054 inch.

Because of the low stresses and correspondingly low creep strains, it should not be necessary to pre-spin the rotor to either pre-strain it or to check for internal flaws or integrity. Recall that, in Phase I, analytical studies indicated critical size flaws could be detected by non-destructive methods.

Although the design is based on a one-half inch diameter rotor bore, the final design could be made with any size bore desired. The one-half inch hole was sized as an approximation of the minimum that might be needed for bore heat transfer surface area (0.419 inches diameter). Increasing the diameter to say one inch would only slightly increase the rotor OD (a few mils) but would double the bore surface area and provide more room for the coolant-flow ducting to be placed in the center.

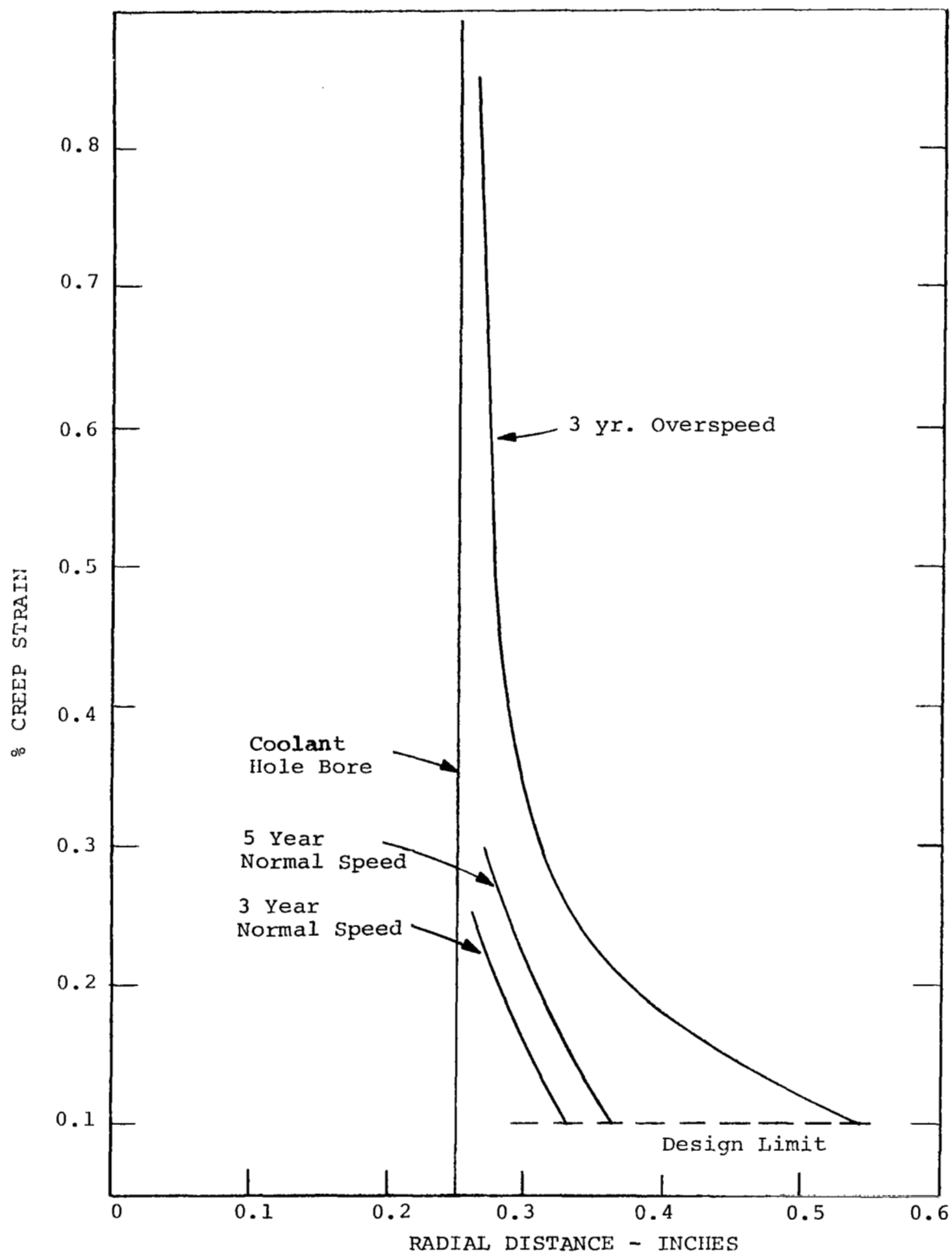


Figure 2.2-11. KTA Rotor Creep.



## Bore Seal Assembly

Chapter 2.4 of Part I of this report presents the background on the bore seal assembly and the summary of the Phase I studies. As indicated in that section, a basic concept was derived near the end of Phase I whereby the two contradictory design requirements -- rigidity and flexibility -- could both be satisfied. However, a review of that section will also reveal a promise for design refinements and detail stress analyses in Phase II. These were promised in recognition of the complexities introduced by the curvic-type couplings plus the then lack of recognition of the bimetallic joint technology requirements and limitations.

The plan for Phase II consisted of first familiarizing the bore seal assembly designer with Cb-1Zr to steel bimetallic joint technology and secondly, feeding this into an improved design. As a result of defining the bimetallic joint technology, a much simpler end member assembly was configured which should give greater reliability over that proposed in Phase I. Once the basic design was derived, stress analyses were run to determine the basic stresses and stress problem areas remaining as well as to identify the solutions.

The above point of only analyzing the "basic stresses" warrants explanation before proceeding further. As part of the studies for designing the KTA alternator bore seal, a rather clear-cut definition of the task to develop the bore seal began to emerge. Also, it became very apparent that the "bore seal" must include all the assembly components from the radial "air" gap to the stator end bell and that the design must be compatible with all the separate component requirements. This puts a special requirement on the

assembly in that its development must be closely coordinated from a central point, preferably at the alternator designer. The desirability for placing this responsibility with the alternator designer is best illustrated by one of the points in this emerging definition, namely, there is a definite need for very thorough analytical treatment (well beyond the scope of Phase II) of all possible conditions the bore seal assembly may see from the time it is in fabrication to the end of its life in the alternator. This is because the defined operating conditions are the easiest to design to and the undefinable, off-design conditions are the most difficult to design to but are the most likely to cause failures.

If off-design conditions causing failures can be defined and automatic controls to prevent their catastrophic effects can be included in the system, then the probability of survival should be enhanced. Since it is possible to identify off-design or abnormal conditions numbering in the hundreds, the scope of such an analytical study is necessarily extensive. Compound this with a complex irregular cross section requiring the latest, most powerful computer programs and you have a very comprehensive task. The "basic stresses" of the Phase II are just one set of stresses for a "more than likely" off-design condition -- design temperature with 20 psi (external) pressure difference across the seal. In addition, the light-weight end bell structure designed in Phase II has the effect of further compounding the task by readily transmitting the rotor vibratory effects into the stator housing near the bore seal ends. While one might balk at the initial cost of such an extensive analytical task, one must note it is easy to prove that it will pay for itself many times over if such an

analysis leads to preventing just one off-design bore seal failure in the first test alternator.

The overall development plan that emerged from the studies is depicted on Figure 2.2-12 along with the present status. The next step in the development plan, prior to initiating the analysis discussed above, is to reach agreement among the various technologies concerned -- alumina body, ceramic to metal joint, bimetallic joint, high temperature preload spring, assembly welds -- to verify that the Phase II configuration is indeed compatible with each individual component requirement. After the analysis and process development, this mutual agreement stage must be repeated because beyond that point, the test samples, test programs, and any set-backs or failures can become relatively costly. The remainder of the steps on Figure 2.2-12 are self explanatory with an emphasis noted on the thorough test of the first full size bore seals.

As indicated above, one of the principal steps in the Phase II bore seal design study involved familiarization with bimetallic joint technologies. The technology required for bimetallic joints on the bore seal assembly was reviewed extensively with Westinghouse Astronuclear Laboratories personnel experienced in the fabrication of bimetallic bonds for adverse environments. It was concluded that large diameter joints could be made if proper configurations and fabrication techniques were used. Both explosive and gas pressure bonding techniques could be used to make a metallurgical bond between a columbium alloy (Cb-1Zr) and a steel which has low nickel content. A joint consisting of concentric rings appears to be the best configuration from the standpoint of minimum space requirements. However, an explosive

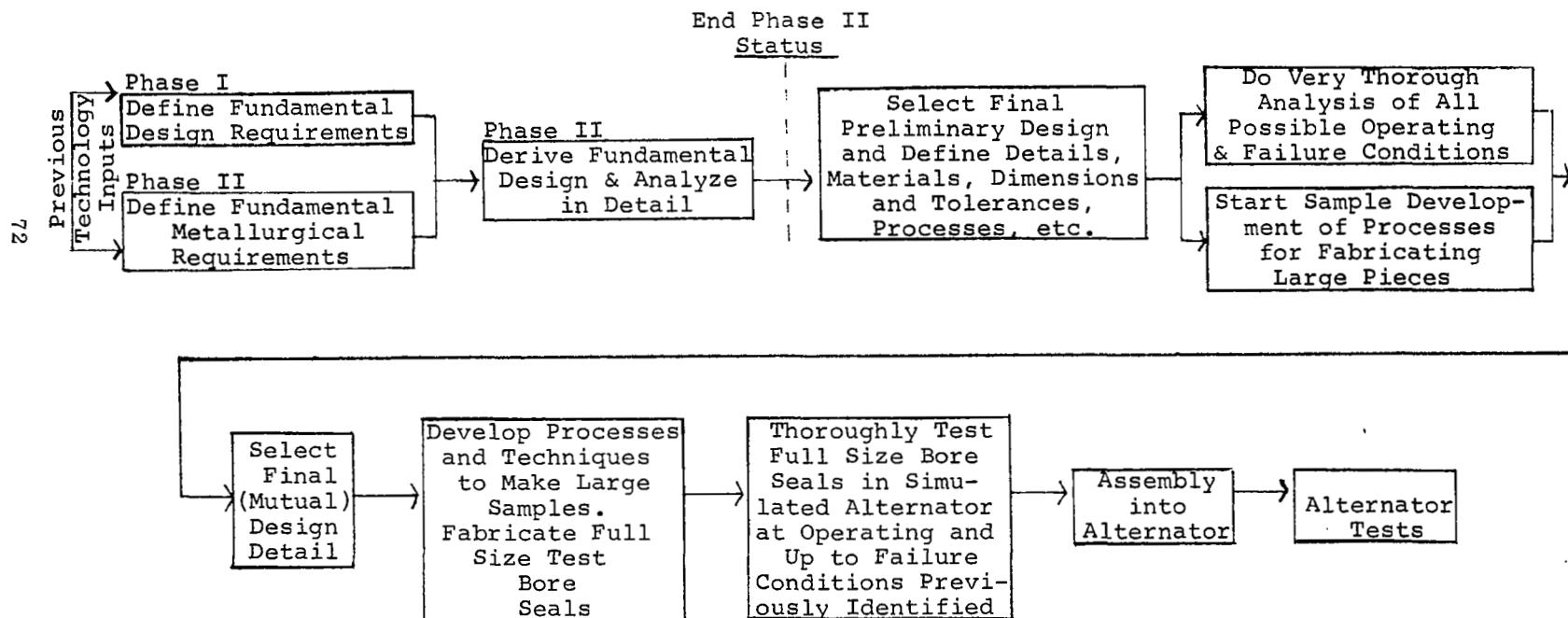


Figure 2.2-12. Bore Seal Design and Fabrication.

bond of two concentric rings is difficult to fabricate because the bond must be made on two sheets which are later formed into concentric rings. Gas pressure bonding appears to be a better approach since a bond between concentric rings can be made easily. In this process, the joint is formed at operating temperature (or slightly higher) so that the joint is stressed at room temperature and has a low locked-in stress intensity at operating temperature. Autoclaves capable of forming such a joint on rings 18 inches in diameter are presently available through Battelle Memorial Institute. This diameter is sufficient for the KTA design.

Once the joint is formed, however, it must survive the several hundred thermal cycles it will have to undergo over its lifetime. Proper design and materials choice can eliminate this problem rather easily. Tests on a quantity of samples at Westinghouse Astronuclear Laboratories show that the joint will not become brittle if the inter-diffusion zone of the bimetal joint is less than one-half mil (0.0005 inch) thick. These same samples show this zone will not grow that thick over the life of the alternator at the less than 1000<sup>o</sup>F alternator temperatures. These conclusions are based on Inconel 600 to Cb-1Zr samples at 1250<sup>o</sup>F for 20,000 hours.

A low nickel content (e.g., twenty percent) steel must be used to minimize the rate of inter-diffusion. If a steel with low nickel content and a coefficient of thermal expansion near the Cb-1Zr could be found, then the strains the joint must undergo each thermal cycle are minimized. Eighteen percent nickel has an expansion coefficient such that strains will be less than 0.2 percent. The desirability of having elastic strains only on each thermal cycle is obvious to enhancing reliability.

This latter point is one of the key elements in designing the end member assembly to survive a relatively large number of thermal cycles over its lifetime. In going from the Cb-1Zr end members to the Hastelloy B end bells, the end member assembly must absorb a total of 0.25 percent relative strain. If this can be broken up into smaller strains and distributed throughout the materials in the end member assembly, elastic strains are all that will be prevalent. As indicated in Table 2.2-3, materials can be selected to accomplish this. The reader is referred to the footnotes of Table 2.2-3 for the reasons for not recommending the "desired configuration" shown.

With the selection of the basic design materials and concepts, the proposed design of Figure 2.2-13 was developed. The design contains the same features of the Phase I design except the concentric piloting of the cylinder is maintained by snug-fitting concentric diametral fits and square shoulders rather than the curvic type couplings. The various functions and operating characteristics of the assembly are summarized briefly below.

- (1) Alumina Body - 99.8 percent pure material, approximately 15 inches diameter; 0.090 inches minimum thick, maximum thickness decided by that allowed when all assembly tolerances, growths, etc. are figured into detail design drawings; sandwich construction for ceramic to metal joint; necked down configuration details to be defined by ceramic body developer prior to finalizing design, necked down section is to provide for allowing mirror image (rather than inverted image) of end member configuration on each end and for one-half inch clearance around armature coils.

TABLE 2.2-3

RELATIVE STRAINS

Material	@875 <sup>o</sup> F in/in/ <sup>o</sup> F	Relative Strain at 875 <sup>o</sup> F	
		Con Desired Configuration*	Recommended Configuration
Al <sub>2</sub> O <sub>3</sub> (body)	4.6x10 <sup>-6</sup>	0.043%	0.093%
Cb-1Zr	3.54x10 <sup>-6</sup>		
B-33	4.06x10 <sup>-6</sup>	0.124%	0.180%
18% Ni Maraging** (steel part of bimetallic)	5.6x10 <sup>-6</sup>		
Hastelloy B (end bell)	6.6x10 <sup>-6</sup>	0.088%	0.088%

\* The B-33 alloy is more compatible from the standpoint of relative strains but introduces new unknowns in the ceramic to metal joint and the bimetal joint. Besides that, there may be a bigger question of its availability and potassium resistance. The latter could possibly be improved with the addition of 0.5 to 1.0 percent zirconium or hafnium.

\*\* The choice of 18% Ni Maraging steel was made based upon low nickel content, desirable coefficient of thermal expansion and high strength. The material choice must be approved yet by the bimetal joint developer since the 18% Ni Maraging steel undergoes a phase transformation at about the operating temperature, thereby introducing a new unknown into the joint design. There is strength data to indicate the transformed steel still has sufficient strength.

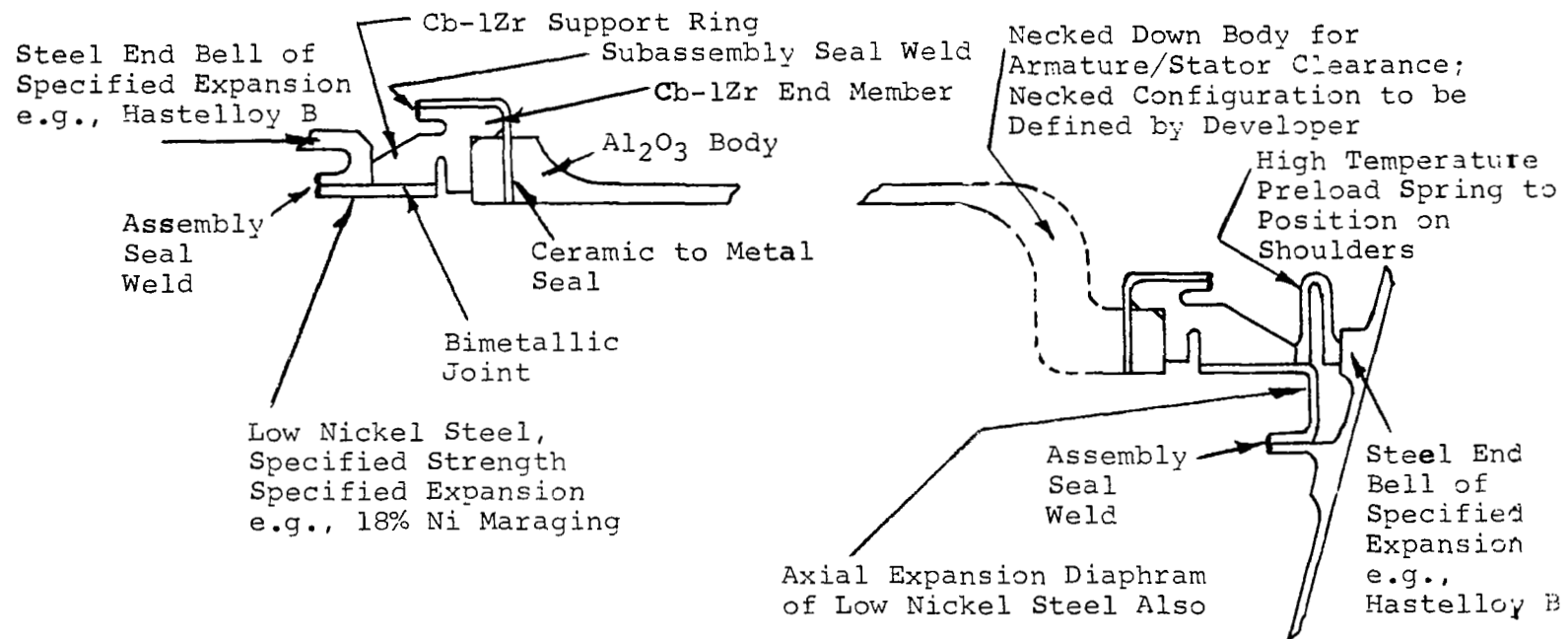


Figure 2.2-13. Phase II Bore Seal Assembly.



- (2) Ceramic to Metal Joint - Same as Phase I (and prior) except now have mirror image of each end; 0.017 inch thick Cb-1Zr; Cb-1Zr material selected as result of successful previous developments; has short radial height of metal end member after leaving joint to minimize stresses and liberal braze alloy fillet to minimize stress concentration; uses active metal braze; is a major development item.
- (3) Cb-1Zr Support Ring - Provides alignment function, not as precise as curvic couplings but should be adequate (e.g., as much as 0.010 TIR) even though it is a weld joint, back up pilot fit not fused with weld is included; weld has undercut to limit depth of penetration; ring shoulders squarely against alumina body and supports 0.017 inch metal end member; seal welds to Cb-1Zr subassembly anneal process development required; has relatively large undercut to isolate stresses between Cb-1Zr end member side and bimetallic joint side; one of two basic parts for fabrication of the bimetallic joint.
- (4) Bimetallic Joint - Gas diffusion bonded; starts as two plain concentric rings less than 18 inches in diameter and machined to configuration shown after bonding; steel material is on ID of Cb-1Zr ring to keep joint in compression at temperature; joint is minimum of one-half inch long; steel must be low nickel with specific thermal expansion values to keep joint strains in elastic region and to prevent inter-diffusion zone from exceeding 0.0005 inches and becoming brittle; should survive hundreds of thermal cycles; is a major development item.

- (5) Low Nickel Steel - Should be of order of 20 percent nickel; must have reasonably high strength, e.g., 100,000 psi yield; coefficient of expansion must provide "step" to absorb relative thermal strain between Cb-1Zr support ring and steel end bell; must be readily weldable alloy; weld to end bell, has undercut to limit depth of penetration; piece on right end must also absorb axial expansion of at least 0.0131 inches (operating expansion); final selection subject to metallurgists approval because of its influence on the bimetallic joint.
- (6) High Temperature Preload Spring - Must maintain compressive force for life of machine to isolate radial and axial relative thermal expansions and to shoulder the alumina cylinder squarely between end bells (aids concentricity). Gives bonus of also keeping ceramic to metal joint in compression.

The assembly welds are made with the bore seal compressing the high temperature inverted "U" preload spring (Figure 2.2-13). Compression is to a specific amount required to maintain axial compression when relative axial thermal expansion takes place. The compression load at 0.0131 inches relative expansion (operating condition) must be greater than 308 pounds. With the assembly in compression from one Cb-1Zr supporting shoulder and bimetallic to the opposite supporting shoulder and bimetallic, the bore seal body and Cb-1Zr end member do not "see" any of the relative axial movement between the bore seal and stator frame. Thus, these members need only be designed to absorb radial differential expansion and pressure differential forces. The only axial relative expansion each end member sees is that which occurs within its own assembly boundaries.

The majority of the differential radial expansion is absorbed in the low nickel steel pieces; the rest is absorbed in the various materials and interfaces. As previously discussed, design materials are selected so that the extent of the strain in each of these locations is kept as low as possible in a step-wise fashion.

Random radial motion between the stator punching bore and bore seal OD is minimized by the Cb-1Zr support shoulders on each end (piloting off the end of the alumina body) and by snug fits between the members at the seal weld assembly joints. The loosest link in this fit-up occurs when the latter fit loosens upon heating to temperature. Locked-in weld stresses may cause some radial movement but should not cause "cocking" due to the bore seal (square) shouldering concept above. The design should absorb at least 0.010 TIR radial movement (if not twice as much) without jeopardizing the radial running clearances. Conical shaped support shoulders (like on journal bearing sleeves, Figure 2.3-1) might be possible to minimize the amount of radial motion to less than the 0.010 TIR.

The design should not be temperature sensitive except when extreme gradients occur to shift differential expansion in opposite directions relative to those which occur at operating or uniform temperatures. This could upset the shouldering concept or over-stress joints due to the fact that relative movements are not always free to occur unlimited in the opposite direction; e.g., if the low nickel piece were considerably hotter than the end bell on the drive end (an unlikely situation).

The stress analysis of the bore seal end members was made with the use of two computer programs. The stationary end member of the bore

seal used a recently developed digital computer program called "A Finite Element Computer Program for Axisymmetric Elasticity Problems". It is based on the displacement method (finite element theory) and can determine the displacements and stresses in arbitrary solids of revolution subject to axisymmetrical tractions, body forces, temperature variations and prescribed displacements. The materials of the solids are assumed to obey Hooke's Law. A theoretical model of the end member was calculated with the respective loadings and geometries. This was then broken down into a grid type mesh for computer program input. The computer program output consists of machine plotted contour stress maps of the end member along with the standard digital stress results. The equivalent or Von Mises stress contour map with its respective isostress lines is shown in Figure 2.2-14.

A summary of the stresses on the map are given in Table 2.2-4. The maximum values are usually associated with stress concentrations that, with later design refinements, can be minimized. For example, the 27,645 psi stress associated with the bimetallic joint occurs there because the analytical model placed the corner and the joint line coincident, a situation that should be avoided in actual hardware.

The stress analysis for the bore seal positioning end member (right end) was calculated with the use of an in-house digital computer program that, while similar to the above program, is easier to use but less versatile. A model similar to the stationary end member was developed with its respective loadings and geometries. The principle loading of this end member was the tensile force associated with the differences in thermal expansion between the stator and bore seal. The relative axial expansion of the stator as compared with the bore

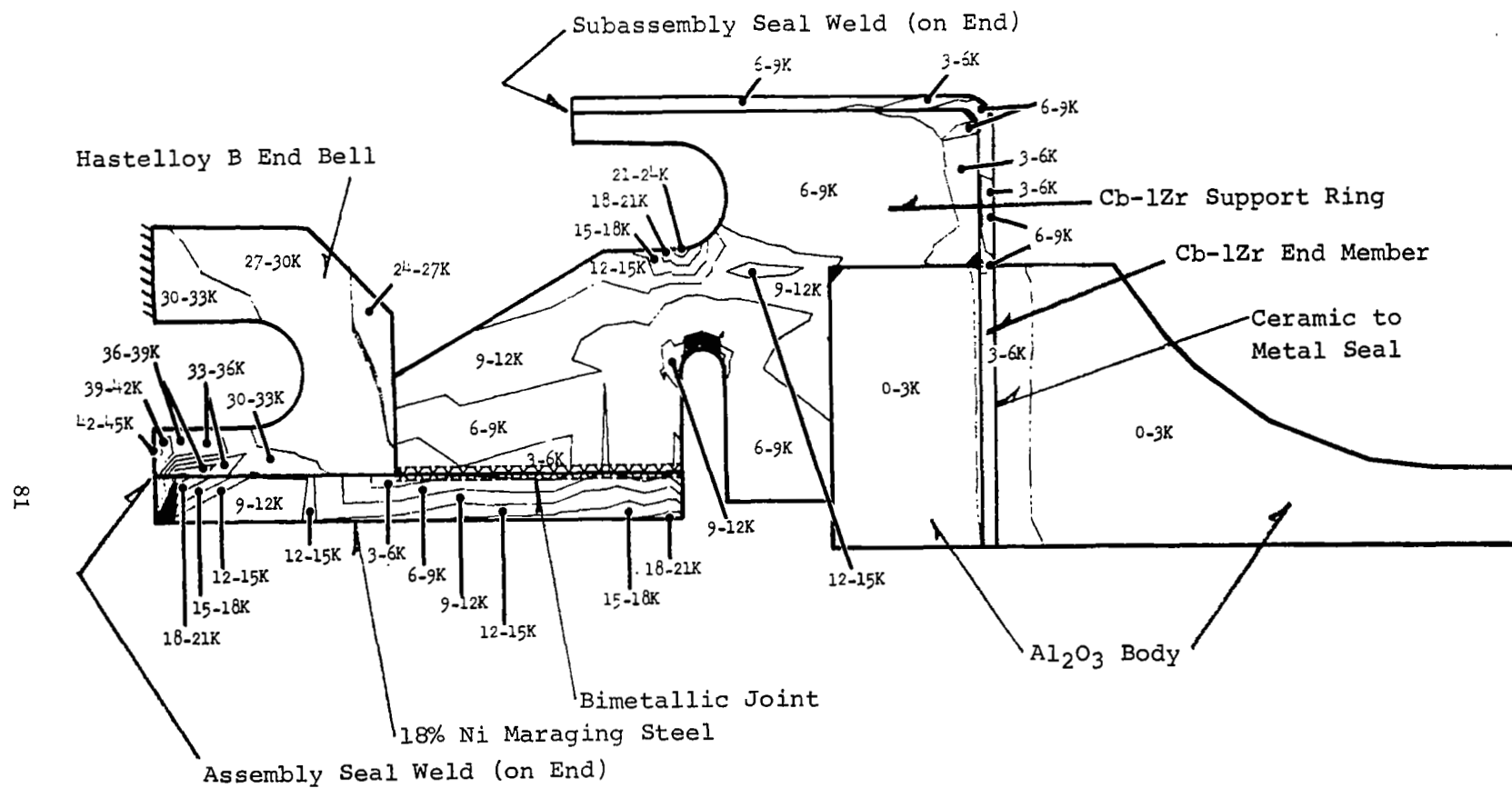


Figure 2.2-14. Bore Seal End Member Assembly, Equivalent Stresses.

TABLE 2.2-4

PHASE II BORE SEAL DESIGN DATA

EQUIVALENT STRESSES

<u>Component Location</u>	<u>psi</u>		<u>Maximum Stress Location</u>
	<u>Minimum</u>	<u>Maximum</u>	
Ceramic Bore Seal:	582	6946	Top, Cb-1Zr End Member Interface
Cb-1Zr End Member:	3032	7209	End Member Shoulder Piece Weld Joint
Cb-1Zr Shoulder Piece:	3433	30647	□ Undercut
Bimetallic Joint:	4095	27645	Hastelloy B, 18% Nickel/Cb-1Zr Shoulder Interface
18% Nickel Piece:	4095	19595	Bottom Edge, Undercut Face
Weld Joint:	10033	44311	□ Hastelloy B Piece
Hastelloy B:	3433	30879	Frame Interface

seal was found to be 0.0131 inches at operating temperatures. A uniform seal temperature of 550<sup>o</sup>F was found to give the same relative axial expansion. A pressure differential of 20 psi on the external (stator) side of the end member was also assumed for input to account for any differentials between the rotor and stator cavities. Initial input of a 60 mil wall thickness on the end member proved to be too stiff and the stresses calculated exceeded the material properties. A thinner and hence more flexible wall was then input. With a wall thickness of 30 mils the maximum bending stresses calculated were approximately 71,000 psi which is within the property limits.

The 550<sup>o</sup>F soak temperature limit introduces a new problem. Since it is reasonable to assume the minimum allowable thermal soak temperature might be 700<sup>o</sup>F, the design must be refined to handle it. For the 0.030 inch thick member above, the relative expansion at 700<sup>o</sup>F uniform is 0.0167 inches requiring a 2830 pound thrust force from the preload spring. This results in a maximum 90,000 psi bending stress in the end member.

## 2.3 PRELIMINARY DESIGNS

### Layouts

The significant features of the alternator electrical and structural design are found in the rotor, stator and bore seal configurations of Figures 2.3-1 and 2.3-2. The bearing, shaft seal and stub shaft configurations are discussed in Chapters 7 and 8 of this report. The vapor seals and scavenge system previously discussed in Part 2.2 of this section of the report act to reduce the rotor cavity

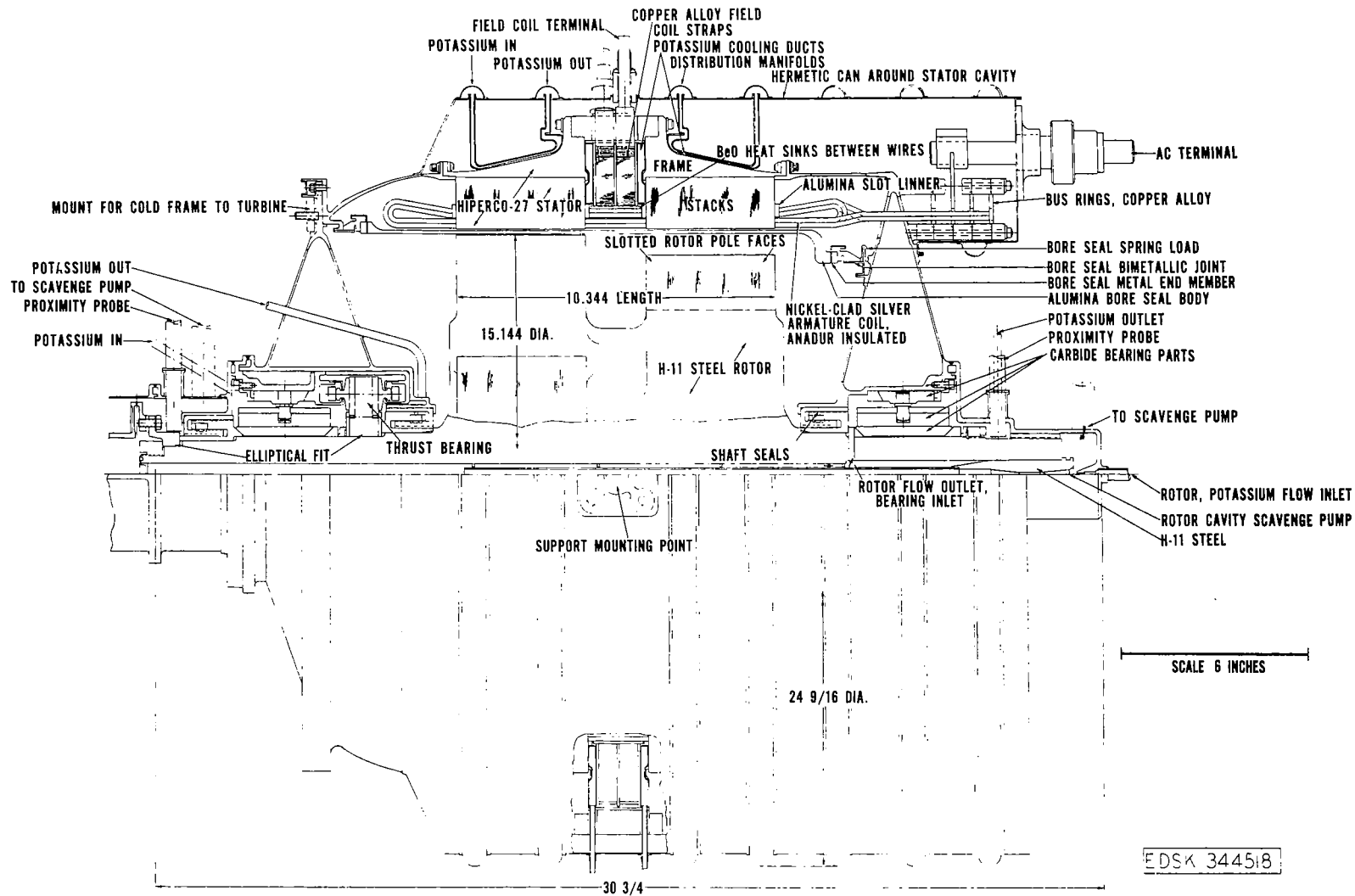
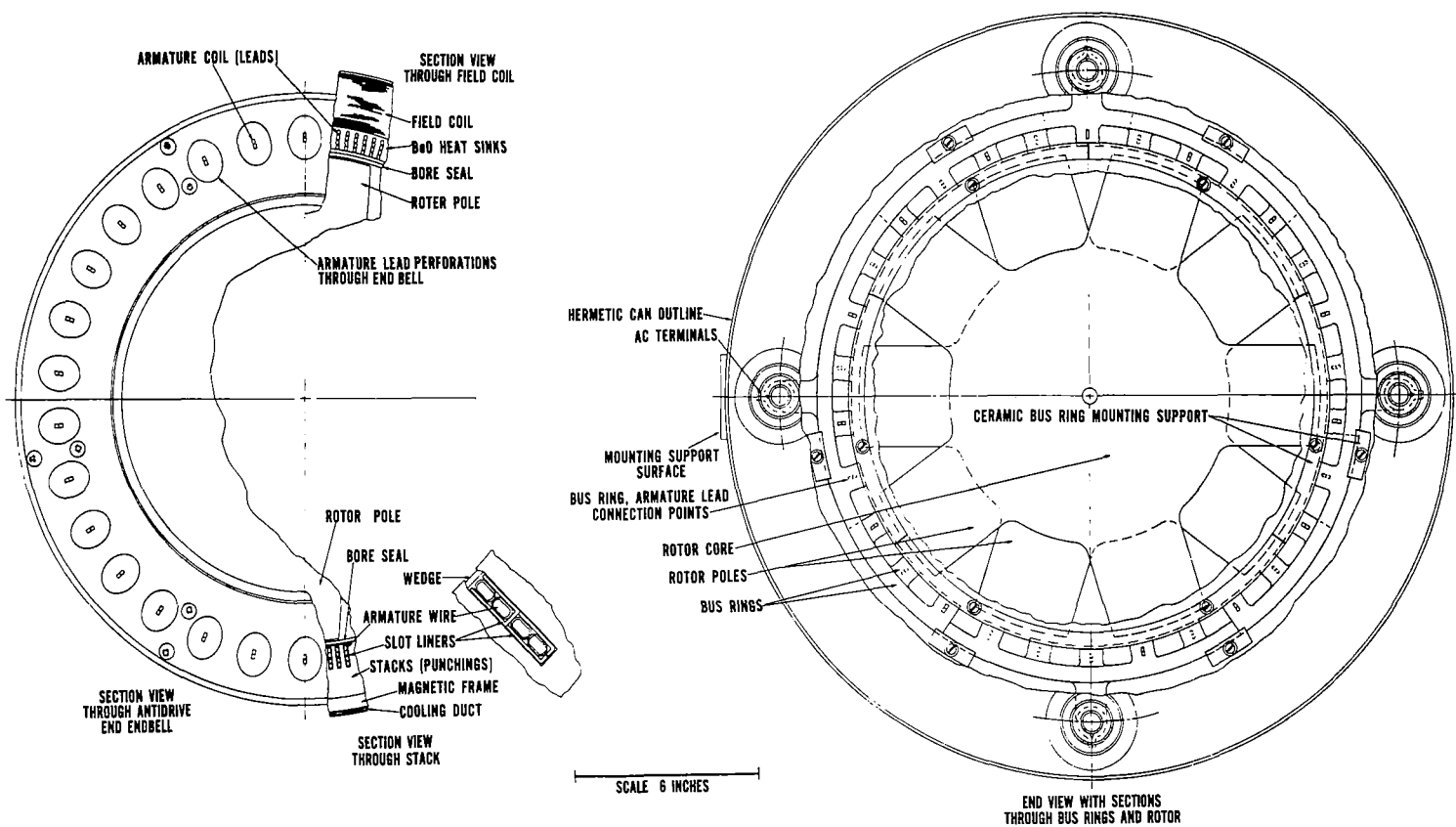


Figure 2.3-1. Generator, AC 600 KVA 0.75 PF 19,200 RPM 1600 HZ  
480 Volts L-N 700°F, Potassium Cooled.





EDSK 344516

Figure 2.3-2. Generator, AC 600 KVA 0.75 PF 19,200 RPM 1600 HZ  
480 Volts L-N 700°F, Potassium Cooled.

pressure to 0.004 psia to minimize windage losses. The details of the rotor cavity scavenge system plus those of the bore seal configuration were discussed in the previous section. Likewise, because the electrical design and materials selection have been discussed elsewhere, they are not repeated in this section.

As seen on Figure 2.3-1, the basic alternator is made up of the rotor, the magnetic frame, the Hiperco-27 stacks, the armature coils and the field coils. The rest of the configurations around these fundamental components are to transfer the coolant in and out, transfer the power out and support the stator and rotor as an integrated unit. The end bells mounting the bearing housings to the stator frame are mechanically fastened directly to the magnetic frame to utilize the structural rigidity associated with the relatively large magnetic frame. Because of the armature coil leads passing through the anti-drive end bell to the bus rings, the anti-drive end bell becomes a permanent part of the electrical assembly upon completion of the electrical winding. In passing through this end bell, one-half inch spacing is allowed around each lead. This is to minimize eddy current heating due to the high frequency alternating flux surrounding the lead. This half-inch spacing is adhered to as a general rule for all the electrical leads of the AC armature coil.

The stators are hermetically sealed to permit operation without subjecting the stator components to corrosion damage by either air or moisture external to the generator or potassium vapor internal to the rotor cavity. The ambient of this hermetically sealed cavity is a hard vacuum or in flight, space vacuum. The hermetic shroud is a thin wall reinforced can whose thickness is 30 to 40 mils. There are reinforcing

rings around the can that also double as coolant distribution manifolds for the stator coolant. The stator coolant enters and leaves through these toroidal shaped manifolds. These distribution manifolds feed the toroidal shaped coolant ducts that are bonded directly to the Hiperco-27 frame. It should be pointed out that the stator coolant ducts bonded to the frame shown are only meant to be schematic. Thermal cooling analyses indicate there are at least a half-dozen different ways these cooling ducts can be configured to the frame; the actual details are therefore left to the final hardware stage and the manufacturing engineer's selection. The field coil cooling ducts must be according to the configuration shown, i.e., basically on the side of the two bundles of coil straps and bonded to the frame sides. The various cooling ducts are in parallel flow with each other to minimize the temperature rise through the stator and therefore minimize the temperature gradients.

The stator punchings are 0.004 inch thick Hiperco-27 magnetic alloy, have a semi-closed slot to reduce pole face losses, and are assembled into an unwelded stack to reduce iron losses. A 0.0004 inch thick layer of plasma-arc sprayed alumina constitutes the interlaminar insulation. The small block of material shown on the ends of the stacks are small tabs on the ends of the slot liners. Those hold and align the unwelded stacks preventing the thin teeth from flaring excessively. As seen on Figure 2.3-2 in the section view through the stack, the bottom slot liner must be slit into an "L" shape in order for the slot liner to be assembled into the semi-closed slot. The upper slot liners are "U" shaped and can be assembled from the ends of the stack at the time of winding. The segmented BeO heat sink between the stacks acts as a spacer to serve the same function of preventing excessive flair between

the stacks. As the name implies, the BeO heat sinks act to carry the armature coil heat from between the stacks into the cooling sink of the copper field coil above it. The size of the segment will be determined by manufacturing economies. The field coil is wound into two (series connected) toroids of flat straps. They are electrically insulated from each other and the cooling ducts. There is a flat-to-round transition section between each coil bundle and terminal.

There are four bus rings on the anti-drive end of the generator. The parallel phase groups of the armature are connected to each bus ring in such a manner that the bus ring  $I^2R$  losses are held to a minimum which in turn permits the rings to be cooled by radiation to the stator cavity walls. The maximum bus ring temperature can be expected to be less and  $900^{\circ}\text{F}$  with a  $700^{\circ}\text{F}$  sink temperature. The bus rings are supported by ceramic insulation and a mechanical mount as illustrated in the end view of Figure 2.3-2. The rings are not continuous rings, but are partial arcs allowing for thermal expansion without diametral growth. The insulation pieces are spaced quite widely on the O.D. of the rings to permit a good field of view for radiation cooling. The tabs on the rings are held by the continuous (segmented) inner ceramic mounting rings. Bonded to these tabs are the leads of the armature coils. These leads come straight off the armature coil into bus rings as seen in Figure 2.3-1. This is important to the design of the alternator since it will be necessary to bake out the Anadur and fire it prior to assembly of the windings. This pre-bake is to obtain a better slot fit-up at assembly by accounting for the 35 percent Anadur shrinkage prior to winding. As mentioned previously, there are only 30 wire ends that are to be attached to the bus rings and as seen by the

figures, these are in readily accessible areas. This minimizes bonding problems.

The Anadur pre-bake and shrinkage problem could be alleviated somewhat by using segmented slot liners that would not be completely inserted until after winding and baking processes. These would be similar to the configuration of the segmented PBN insulation pieces being tested on Contract NAS3-10941 at Westinghouse. The PBN material being evaluated on that contract was not selected for the KTA slot insulation because of the lack of need for the specialized higher temperature capabilities of the PBN material and the economies that result with the more readily available alumina. Nevertheless, these PBN evaluations are being followed closely because of the impact any adversely low slot conductance (measured conductance) would have on the assumptions used in the stator cooling design.

There is one terminal per bus ring, centrally located about the armature connections. Because of the temperatures brought on by the high current density and because of the limited space, special terminal studs are required. They are sized rather large to have sufficient cross sectional area to permit them to be self-cooled by radiation. Nickel plating is used to obtain an emissivity of 0.4 on the outer surfaces. They can be cooled by radiation alone to less than  $900^{\circ}\text{F}$  for a  $700^{\circ}\text{F}$  ambient.

The features of the rotor design are found in the slotted pole faces and in the central cooling hole and scavenge system. The material is solid H-11 steel, heat treated to  $45 \pm 1R_c$ . The slotted pole faces have 0.006 wide by 0.100 inch deep slots, approximately 30 per inch, that are cut with gangs of carbide cut-off wheels. The process for doing this has previously been developed by Westinghouse.

The central hole in the rotor core serves a number of functions, the first of which is for heat treatment to obtain the 45 R<sub>C</sub> hardness and the second of which is for rotor cooling. Also, with the center of the forging drilled out, reliability should be enhanced by eliminating any center line inclusions. The coolant flow coming into the rotor is jetted through impulse turning vanes, passes along an inner tube down to the drive end stub shaft, is dumped onto the rotor bore there and subsequently returns to the anti drive end bearing cavity. Because of the rotational speed of this inner tube and the bore, the coolant will only form as a thin film on the inside of rotating surfaces. The thickness (or thinness) of this film can be controlled by the over-flow edge on the anti drive end stub shaft near where it is labeled "Rotor Flow Outlet, Bearing Inlet" on Figure 2.3-1. The pumping head created by any fluid in the bearing inlet tube will overcome the back pressure of the bearing cavity.

With proper control of the coolant film thickness in the rotor bore, the minimum temperature rise across the rotor as well as the maximum heat transfer coefficient may be obtained. A very slight change in the thickness of the coolant film along the axial length of the bore(s) is all that is necessary to provide a self pumping action to move the coolant along the bore(s) in the axial direction. These concepts have previously been demonstrated and reported in the references 2.3-1 and 2.3-2. The center tube is maintained concentric to the concentric rotor bore by four spacers shown on Figure 2.3-1. Concentricity between the central bores and the rotational center is very important to the cooling flow as well as the rotor unbalance. This is because the thin film in the central bore is sensitive to any runout due to poor

manufacturing or control of concentricities. The details of the rotor cavity scavenge system on Figure 2.3-1 are a rough schematic only; see Figure 2.3-3 for expanded details.

The basic assembly sequence of the alternator is as follows:

First, wind the field coil and assemble the frame (with bonded coolant duct assemblies) around the field coil. Then assemble the frame cap to form the magnetic frame structure. The frame cap is split into two half-moon sections and forms a mechanical connection between the two frames over the stacks. This has the undesirable feature that, once the field coil is assembled, it is difficult to disassemble the stator to repair the field coil without losing concentricity between stacks. However, this may be overcome with proper tooling to hold the assembled alternator stacks concentric, but the high reliability expected of the rather simple field coil configuration should eliminate need for replacement.

With the frame assembled, the stacks are mounted into the frame and the armature coils are wound into the slots along with the rigid ceramic insulation. Once this is completed, the anti-drive end bell and the drive-end frame extensions are mounted to mechanically lock the unwelded punchings into the frame. At this point, the various mounting diameters\* may be ground concentrically as an assembly. These would consist of the mounting diameter for the drive-end end bell and the bearing housing ID's on the anti-

---

\*Excludes the stack ID. That diameter would be used as a reference diameter to be set up concentrically into the grinder. This is to avoid contaminating the stator with foreign particles.

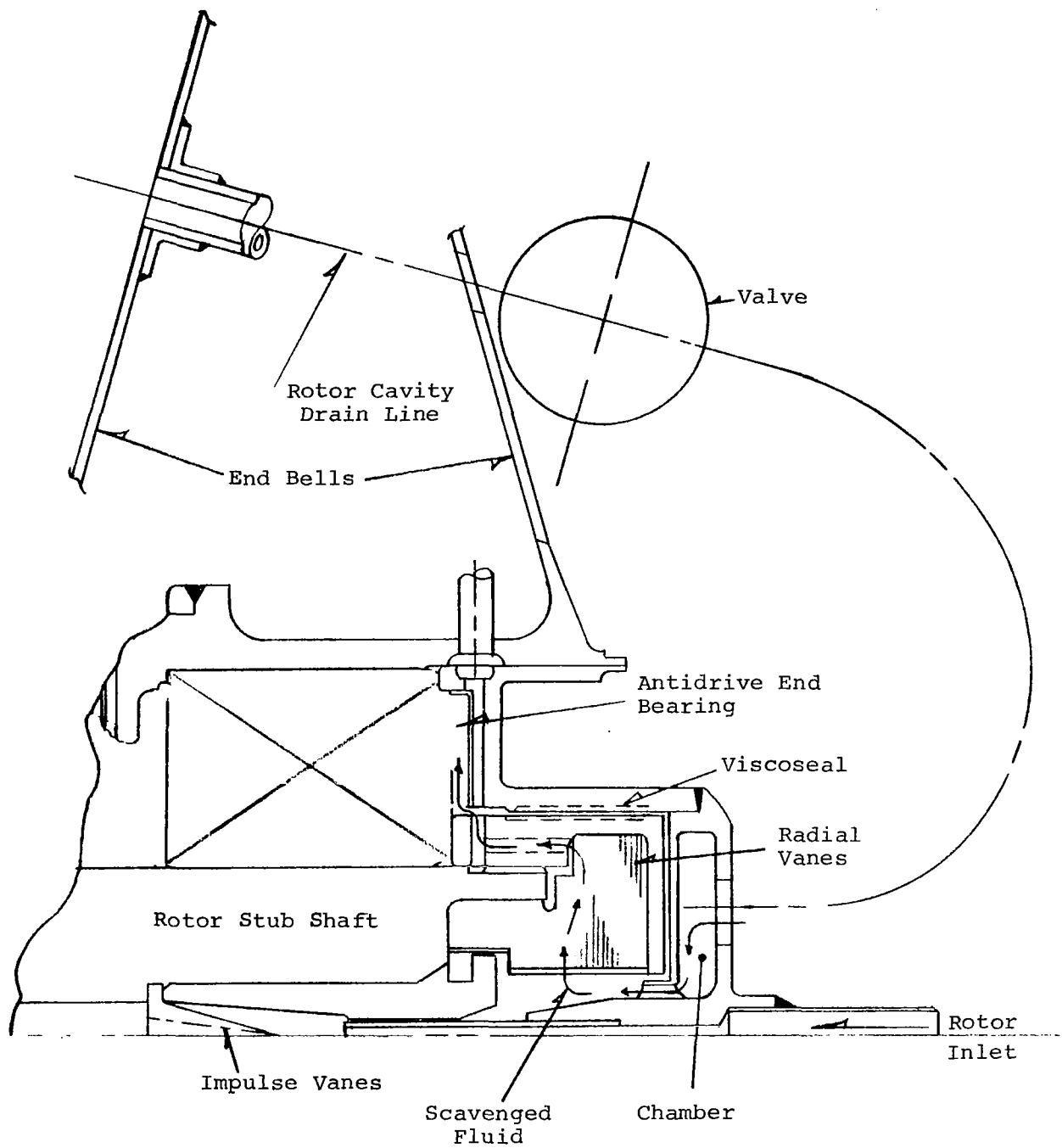


Figure 2.3-3. Rotor Cavity Scavenge System Details



drive end. After that, the bus rings and terminals may be assembled onto the ends of the assembly of the hermetic shroud around the stator cavity with its field coil terminals and reinforcing/coolant manifold rings.

As seen by the discussion so far, the stator can be assembled as a unit separate from the rotor and bearing stub shaft assemblies.. This is an important feature for disassembly capability after tests with potassium or for general maintenance.

The last step to the stator assembly is to insert the bore seal, placing the bore seal preload spring in proper compression and making the seal welds between the bore seal end member assemblies and the steel frame or end bells.

The final phases of the assembly consist of assembling the bearing components at the same time inserting these plus the rotor into the stator assembly. The sequence for this will be to insert the rotor and assemble the anti-drive end bearing at the same time. This will be followed by attaching the drive-end end bell and inserting that bearing at the same time. The two ends of the bearing housings are then capped off to complete the total alternator assembly. Disassembly is in the reverse direction.

The alternator is attached to the turbine through the "Mount for Cold Frame". A pilot fit and studs are provided to mechanically attach the frame. Just above that fit is the drive-end end bell connection. Because this joint must be hermetically sealed, it appears to require a second pilot fit and bolt circle over that already used for the cold frame to turbine. Since combination of these two fits would save weight,

TABLE 2.3-2

WEIGHT SUMMARY

Electrical Weight (1.08 lbs/kVA)

Stator	343.4
Rotor (without stub shafts)	<u>303.5</u>
Sub-total, Electrical	646.9 lbs

Inert Hardware Weight

Stub Shafts, Bearings & Housings - DE	71
ADE	<u>39</u>
	110 lbs.
End Bells DE	25
ADE	<u>21</u>
	46 lbs
Hermetic Shroud	20 lbs
Bus Rings, Terminals, Misc.	<u>62 lbs</u>
Sub-total, Inert	238 lbs

$$\text{Total Specific Weight} = \frac{894 \text{ lbs}}{450 \text{ kw}} = 1.99 \text{ lbs/kw} \quad 884.9 \text{ lbs.}$$

$$\text{Specific Weight, } \frac{884.9}{450} , 1.96 \frac{\text{lb}}{\text{kw}}$$

magnetic component materials selections were based on an investigation of individual material properties relative to application requirements. Table 2.4-1 lists the generator electromagnetic materials and the general basis for their selection.

## 2.5 FAILURE MODE, EFFECT AND CRITICALITY STUDY

The Failure Mode, Effect and Criticality Study (FME&CS) was carried out for purposes of identifying and cataloging the various modes and effects of component failures down to and including sub-assembly levels wherever possible. The components and subassemblies were categorized by a reliability model that consisted of:

- (1) Rotor and rotor coolant,
- (2) Stator and stator coolant,
- (3) Bore seal assembly,
- (4) Field winding and insulation, and
- (5) Armature winding and insulation combined, and the inert hardware.

The bearings and seals were not considered as part of the reliability model. These are not part of the specific alternator electromagnetic design task.

The FME&CS was undertaken at a joint meeting of the materials, design, and reliability engineers most experienced in the KTA design philosophies. At this meeting, all known possible failure modes were identified, discussed, and tabulated. The failure modes identified were correlated according to immediate or long term effects on the system.

TABLE 2.4-1

ALTERNATOR MATERIALS

<u>Component</u>	<u>Material</u>	<u>Selection</u>
Stator Frame	Hiperco-27	Based on results of work presented in Reference 2.4-5. Has high magnetic induction at elevated temperatures, high thermal conductivity, good magnetic stability, adequate mechanical strength.
Armature Laminations	Hiperco-27	Based on results of work presented in Reference 2.4-5. Thermal expansion characteristics same as for mating frame.
Lamination Insulation	Plasma-Arc Sprayed Alumina	Based on results of work presented in Reference 2.4-3. Good stability and minimum outgassing at high temperature levels.
Armature Conductor	Nickel Clad Silver	Based on results of work presented in Reference 2.4-3.
Armature Conductor Insulation	Anadur-Refractory Oxide and Glass Frit Over S-Glass Fiber Serving with Silicone Resin Bonding	Based on results of work presented in Reference 2.4-3.
Field Conductor	CUBE Copper- BeO Dispersion Strengthened Copper	Based on results of work presented in Reference 2.4-3. Good high temperature stability, high electrical conductivity, joints do not require cladding protection. Poor coil forming characteristics judged adequate for simple field coil configuration.

TABLE 2.4-1 (Continued)

ALTERNATOR MATERIALS

<u>Component</u>	<u>Material</u>	<u>Selection</u>
Field Conductor Insulation	Synthetic Mica Paper	Based on results of work presented in Reference 2.4-3. Low outgassing at field coil temperature, good abrasion resistance.
Armature Slot Liners and Wedges	Alumina, 99.5% Purity	Based on results of work presented in Reference 2.4-4. Good stability at high temperature, high thermal conductivity, minimum outgassing.
Bus Rings	CUBE Copper	Same as "Field Conductor" above.
Bore Seal	Alumina, 99.8% Purity	Based on results of work presented in Reference 2.4-4. Alkali metal compatibility with high electrical resistance.
Bore Seal End Member	Cb-1Zr	Based on results of work presented in References 2.4-4 and 2.4-8. Alkali metal and braze joint compatibility.
Bimetallic Joint Steel	18% Ni Maraging Steel	Coefficient of expansion, low Ni content, weldability, strength, potassium resistance.
Rotor Forging	H-11 (AMS 6487)	Based on results of Phase I studies and work presented in References 2.4-6 and 2.4-7.
End Bells	Hastelloy B	Coefficient of expansion, non-magnetic, oxidation, and potassium resistant, adequate strength, readily available; can be readily fabricated in complex end bell shapes.
Hermetic Shroud and Cooling Ducts	L-605	Coefficient of expansion, non-magnetic, oxidation and potassium resistant, adequate strength, readily available and fabricable.

For the study, it was assumed the alternator was in an operating condition and successful operation constituted the ability to produce useful power. The "power system" was defined as the KTA and its ability to produce power. The effect of the failure on the power system was evaluated from the standpoint of life, power output, overload, shorts, vibration, unbalance, overspeed capability, etc. The guiding philosophy in cataloging the failure modes was "How does the power system respond to the various failure modes". The probable causes of the failure are listed to explain how a particular failure might occur.

The tabulation of the FME&CS is presented in Table 2.5-1. In all, thirty-six failure modes are catalogued in the table.

## 2.6 CONCLUSIONS AND RECOMMENDATIONS

The stator electrical design can be assumed to be relatively fixed at this stage of the design. Further analyses to seek electrical design refinements will probably not yield sufficient return to warrant the effort required. The only change that might be anticipated is if sample tests ever show that the slot conductance is much less than  $0.2 \text{ watts/in}^2$  C used in the design. There is at least a 5:1 safety margin in the design not to obviate as best as practical the need for any later redesign. The slot conductance must be measured in a simulated stator to determine if the 5:1 margin is adequate.

The stator structural design concepts are basically fixed but are subject to final design refinements in the hardware design stage for (1) the selected structural material, and (2) stiffening the end bell spring constants.

TABLE 2.5-1

NASA/KTA ALTERNATOR  
FAILURE MODE, EFFECT & CRITICALITY ANALYSIS

<u>Mode of Failure</u>	<u>Probable Causes Of Failure</u>	<u>Immediate Effect On Operation</u>	<u>Long Range Effect on Operation</u>	<u>Effect On Power System</u>
<u>ROTOR</u>				
Non-Uniform creep rate or yield	Due to non-uniform properties	Increased vibration	---	---
Stub shaft rub seals	Due to loss of concentricity	Increased vibration	Wear or seizure	Loss of system
Stub shaft fatigue	Abnormal bearing whirl	Breaks off	---	Loss of system
Crack propagation in rotor core	Due to embrittling and high stress	Increased strain	Rotor disintegrates	Loss of system
Mass transfer, stress corrosion & galvanic corrosion	All due to mass transfer	Added solids into coolant	Increased stress, strain & possible loss of rotor	Shorten life, loss of system
MHD & plasma erosion on bore seal	Due to Corona & $\bar{U} \times \bar{B}$ in plasma	Reduce output	Loss of bore seal	Loss of output
Major loss of concentricity	Due to loss of bearing	Rub and/or loss of rotation	---	Loss of system

TABLE 2.5-1 (Continued)

<u>Mode of Failure</u>	<u>Probable Causes Of Failure</u>	<u>Immediate Effect On Operation</u>	<u>Long Range Effect On Operation</u>	<u>Effect on Power System</u>
Material Property change	Embrittlement, creep, resistivity, permeability	Minor change in power output	Excessive creep or yield	Shorten life
<u>ROTOR COOLANT</u>				
Excessive coolant temperature	Due to system malfunction	Possible plastic yield or rupture	Excessive creep or yield	Loss of system or shorten life
Loss of cavity vacuum control	Due to seal failure or vent plugging	Increased cavity pressure & windage	Excessive rotor creep rate, failure of bore seal members	Loss of system
<u>BORE SEAL ASSEMBLY</u>				
Loss of Hermetic Seal	Due to fatigue in joint, tube, bellows or end member; stress corrosion, mass transfer or plasma erosion, instability of brazing alloy	---	Stator shorts	Loss of output
Loss of assembly structural integrity	---	Allows rub	---	Loss of system
Seal ID shorts with conductive film	Due to excessive potassium	Increased losses	Increased thermal stress on bore seal	Loss of system
Fretting wear	Contact with stator or rotor	---	Loss of hermetic seal	Shorten life or loss of system



TABLE 2.5-1 (Continued)

<u>Mode of Failure</u>	<u>Probable Causes Of Failure</u>	<u>Immediate Effect On Operation</u>	<u>Long Range Effect On Operation</u>	<u>Effect On Power System</u>
Abnormal temperature excursion	System malfunction	Excessive thermal stress	Loss of Hermetic seal or assembly	Loss of output or system
<u>STATOR &amp; STATOR COOLANT</u>				
Leak in cooling duct	Due to fatigue stress corrosion mass transfer	Stator shorts, increased stator cavity pressure to induce corona	---	Loss of output or system
Flow blockage decreased or stopped	Due to solids accumulation or system malfunction	Excessive temperatures and losses	Accelerate insulation deterioration	Shorten life
Duct separating from frame	Due to bond or contact pressure loss	excessive temperatures and losses	Accelerate insulation deterioration	Shorten life
Stack clamps fatigue	Due to mechanical or electrical fatigue	Separation of stack, loss of power	Fretting wear on bore seal	Noise, loss of system
Excessive coolant temperature	Due to system malfunction	Excessive losses, loosen stack fits	Accelerated deterioration of increased vibration	Shorten life
Fatigue of teeth	Due to mechanical or electrical vibration	Breaks off, flux unbalance	Decrease output, wears through bore seal	Shorten life or loss of system

TABLE 2.5-1 (Continued)

<u>Mode of Failure</u>	<u>Probable Causes Of Failure</u>	<u>Immediate Effect On Operation</u>	<u>Long Range Effect On Operation</u>	<u>Effect On Power System</u>
<u>WINDINGS &amp; INSULATION</u>				
Extended Short Circuit operation	System Malfunction	Armature Conductors open	---	Loss of Output
Slot cell insulation	Due to mechanical and electrical vibration	Loss of slot liner or wedges, increased temperatures	Stator shorts	Reduces output
Anadur frets away	Due to mechanical and electrical vibration	Loosening of windings, Accelerated increased temperatures	insulation deterioration	Shorten life
Cladding breaks	Due to handling abuse, electrical stress, poor manufacturing	Silver core is exposed	Wire strength reduced. May break vibration	Reduced Output
Joint cladding instability	Due to plating or cladding breaks or chemical reaction	Loss of solid bond	Silver evaporation	Reduced output or loss of output
Armature conductor opens	Due to mechanical or electrical failure	Reduction in output, phase unbalance	---	Reduced or loss of output
Field Conductor opens	Due to mechanical or electrical failure	Loss of output over speeds	---	No output
Excessive coolant temperatures	Due to system malfunction	Increased losses, bus rings and wires sag	Accelerated deterioration, possible short	Shorten life losses output

TABLE 2.5-1 (Continued)

<u>Mode of Failure</u>	<u>Probable Causes Of Failure</u>	<u>Immediate Effect On Operation</u>	<u>Long Range Effect On Operation</u>	<u>Effect On Power System</u>
Bus rings & leads fatigue	Due to mechanical and electrical vibration	Open circuits	---	Reduces output or losses output
Electrical shorts	Due to vibration	Excessive temperatures and losses, reduced output	Accelerates insulation deterioration	Shorten life, reduced output
<u>INERT HARDWARE</u>				
Loss of rotor cavity hermetic seal	Due to joint failure or fatigue crack	Lower cavity pressure, less windage	Loss of potassium	Shorten life
Excessive coolant temperature	Due to system malfunction	Thermal stress & distortions	Creep rate loosens fits, lose concentricity	Shorten life or loss of system
Fatigue of housings, end bells, etc.	Due to excessive vibration	---	Loss of potassium	Shorten life
Reduction of emissivity on stator ID	Due to evaporation of coating	Armature temperatures increase loss	Accelerate insulation deterioration	Shorten life
Mounting flange loosens	Due to vibration	Increased vibration, loss of concentricity, loss of stack compression	Accelerated fatigue and breaking up	Shorten life, loss of system

There are several minor developments to be resolved in the stator design but they are amendable to resolution during fabrication of first stator. They include:

- (1) development of the bonding of the L-605 cooling manifolds to the Hiperco-27 magnetic frame,
- (2) development of the detail process techniques for even  $(0.0004 \pm .0000 \text{ inches thick})$  application of the inter-laminar plasma-sprayed insulation,
- (3) development of the fabrication techniques for electrical coil winding with pre-baked Anadur insulation, and
- (4) development of the bonding of the electrical winding joints at the bus rings and terminals.

The rotor electrical and mechanical design can also be assumed to be relatively fixed at this stage. The only change that might be anticipated is if H-11 stability tests indicate long term decay of magnetic properties leading to a reduced rating or a required increase in the rotor (and alternator) size.

The bore seal assembly is the most under-developed of the three major electrical subassembly components. As indicated in the report, the bore seal assembly or "bore seal" must be a coordinated design of all the critical components. These include the alumina body, the ceramic to metal joint, the bimetallic transition joint assembly and the refractory-to-refractory- and steel-to-steel seal welds at assembly. The most development is required on the ceramic to metal joint and on the bimetallic joint. Such a development program must be geared around the specific KTA alternator requirements and be based

on the actual KTA dimensions, stresses, strains, coefficients of expansion, material properties, etc. It will require close coordination of the KTA design with the materials and process development programs to arrive at a successful configuration the first time it is assembled and tested. The bore seal assembly must be put through a very comprehensive analysis and test program simulating the variety of conditions the alternator will see prior to risking the assembly in an actual test alternator.

## 2.7 REFERENCES

- 2.3-1 SNAP 50/SPUR 467 kVA Experimental Generator Design Summary, USAF Systems Command Report AFAPL-TR-67-7, May, 1967.  
Prepared by Westinghouse Electrical Corporation, Aerospace Electrical Division, Lima, Ohio.
- 2.3-2 Topical Report, Experimental Verification, U.S. Atomic Energy Commission Research & Development Report SAN 679-7, February, 1968. Prepared by Westinghouse Electric Corporation, Aerospace Electric Division, Lima, Ohio.
- 2.4-3 Electrical Conductor and Electrical Insulation Materials Topical Report, NASA Lewis Research Center Report, NASA-CR-54092, October, 1964. Prepared by Westinghouse Electric Corporation, Aerospace Electrical Division, Lima, Ohio.
- 2.4-4 Bore Seal Technology Topical Report, NASA Lewis Research Center Report, NASA-CR-54093, December, 1964. Prepared by Westinghouse Electric Corporation, Aerospace Electrical Division, Lima, Ohio.
- 2.4-5 Magnetic Materials Topical Report, NASA Lewis Research Center Report, NASA-CR-54091, September, 1964. Prepared by Westinghouse Electric Corporation, Aerospace Electrical Division, Lima, Ohio.
- 2.4-6 High Temperature Magnetic Materials, Westinghouse Electric Corporation, Aerospace Electrical Division, Lima, Ohio. Report No. WAED 67.34E, October, 1967, Prepared on "Contract for Development and Evaluating Magnetic and Electrical Materials Capable of Operating in the Temperature Range from 800° to 1600°F". Contract No. NAS3-6465.
- 2.4-7 AC Generator Rotor Materials Topical Report, USAF Systems Command Report AFAPL-TR-66-127, January, 1967. Prepared by Westinghouse Electric Corporation, Aerospace Electrical Division, Lima, Ohio.
- 2.4-8 SPUR Generator Stator Seal Development, Topical Report, USAF Systems Command Report ASD-TDR-63-677; Part I, August, 1963; Part II, February, 1967. Prepared by Westinghouse Electric Corporation, Aerospace Electrical Division, Lima, Ohio.

### 3. TURBINE FLUID DESIGN

#### 3.1 TURBINE DESIGN STUDIES

According to the Work Statement, the Phase II turbine design was to consist of a six stage high-pressure turbine and a multi-stage low pressure turbine with a vortex separator between the two turbines. In addition, interstage moisture extraction was to be provided in the next to the last stage of the low pressure turbine. Shown in Table 3.1-1 are the design conditions for the Phase II turbine. The flow rate has been reduced from 2.51 lb/sec in Phase I to 2.05 lb/sec in Phase II. In addition, the exit pressure has been lowered from 7.8 psia to 5.44 psia.

In arriving at the final design for the Phase II turbine, a number of fluid dynamic designs of turbines were considered from which the final design was chosen. Initially, two six stage high pressure turbines were designed with high and with moderate loadings. The non-dimensional loadings for the highly loaded turbines varied from 1.75 to 1.95 for each stage. In the moderately loaded turbine, the stage non-dimensional loading varied from 1.5 to 1.53.

In the design study, each of these high-pressure turbines was combined with a four, five and a six stage low pressure turbine.

The variation in turbine efficiency with the number of stages for the two turbine families is shown in Figure 3.1-1. The moderately

TABLE 3.1-1  
DESIGN CONDITIONS

SIX STAGE HIGH PRESSURE TURBINE

ROTATIVE SPEED 19200 RPM

FLOW RATE 2.05 LB/SEC

INLET CONDITIONS 2100°F & 165 PSIA

EXIT CONDITIONS 1220°F & 5.44 PSIA

CONDENSATE REMOVAL

BETWEEN HIGH PRESSURE AND LOW PRESSURE TURBINES

NEXT TO LAST STAGE IN LOW PRESSURE TURBINE



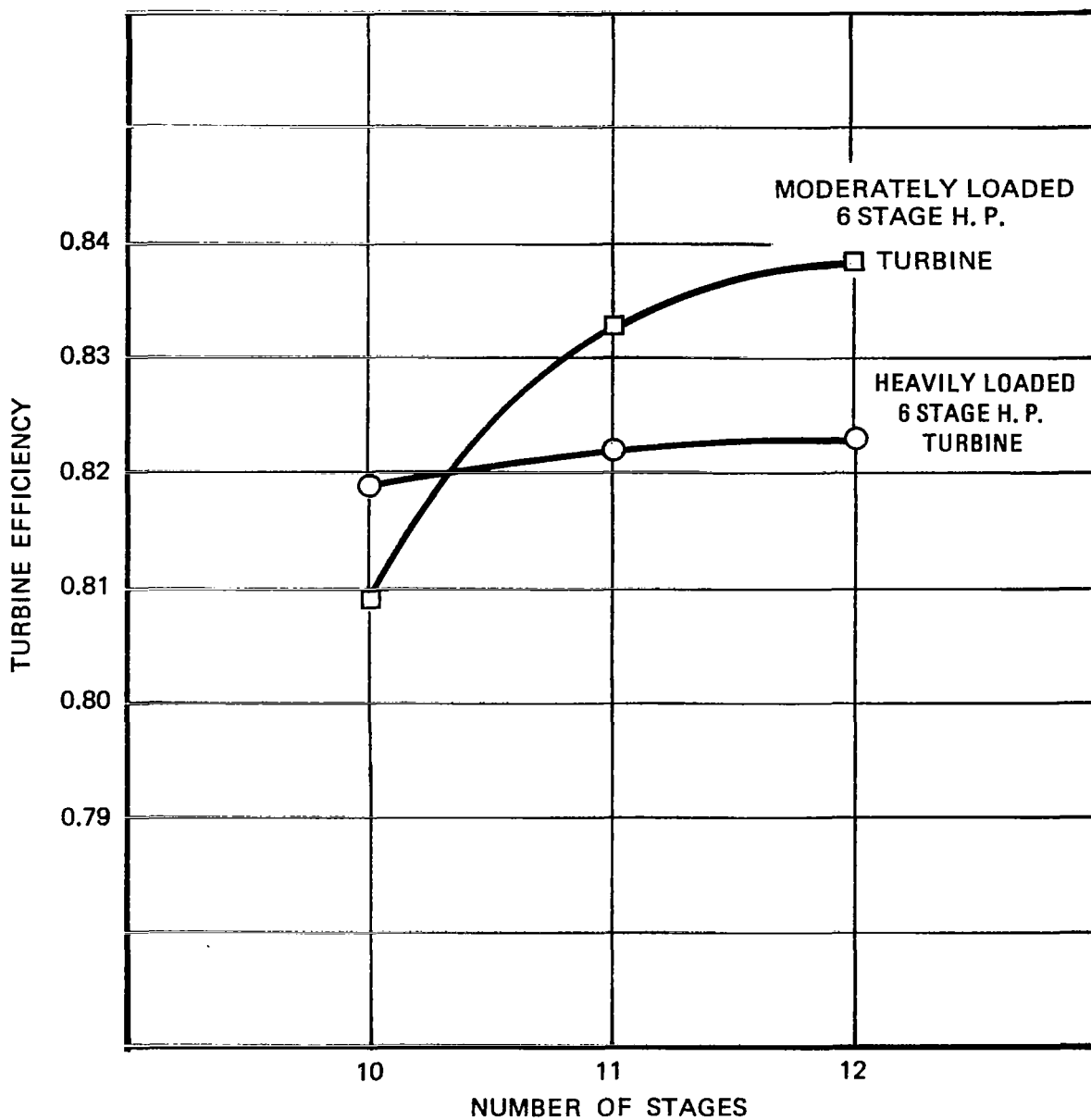


Figure 3.1-1. Effect of Number of Stages and Stage Loading on Efficiency.

loaded six stage high pressure turbine design family has an efficiency above 83 percent with 11 stages and almost 84 percent for 12 stages. Except for the ten-stage design, the heavily loaded six stage high-pressure families are about 1 percentage point lower in turbine efficiency. At the present time, there are no data which would guarantee that a given design of a turbine would withstand erosion by potassium droplets. An attempt to obtain this information is being made on the three-stage potassium test turbine program under Contract NAS3-10606. It was therefore felt that if turbine designs could be made such that the maximum tip speed and the maximum amount of moisture entering any stage were equal to or less than the values projected for the three-stage potassium test turbine, then when test data was obtained on the endurance of this turbine in potassium vapor the data would be directly applicable to the KTA turbine. The maximum tip speed and moisture quantity at stage inlet for the three-stage potassium test turbine are about 850 ft/sec and 9.5% moisture, respectively. Thus, all the turbine designs executed in order to select the final KTA design were limited in tip speed to 850 ft/sec. It is instructive now to see what the moisture content was in the stages of the turbines in the two families, one having a highly loaded high-pressure turbine and the other having the moderately loaded six stage high-pressure turbine. In the turbine designs, it was conservatively estimated that the vortex separator between spools would have an effectiveness of 80 percent and the interstage extraction device an effectiveness of 25 percent.

Shown in Figure 3.1-2 is a variation of stage inlet moisture fraction with stage number for turbines with moderately loaded high pressure turbine. For reference, the three-stage turbine condensate

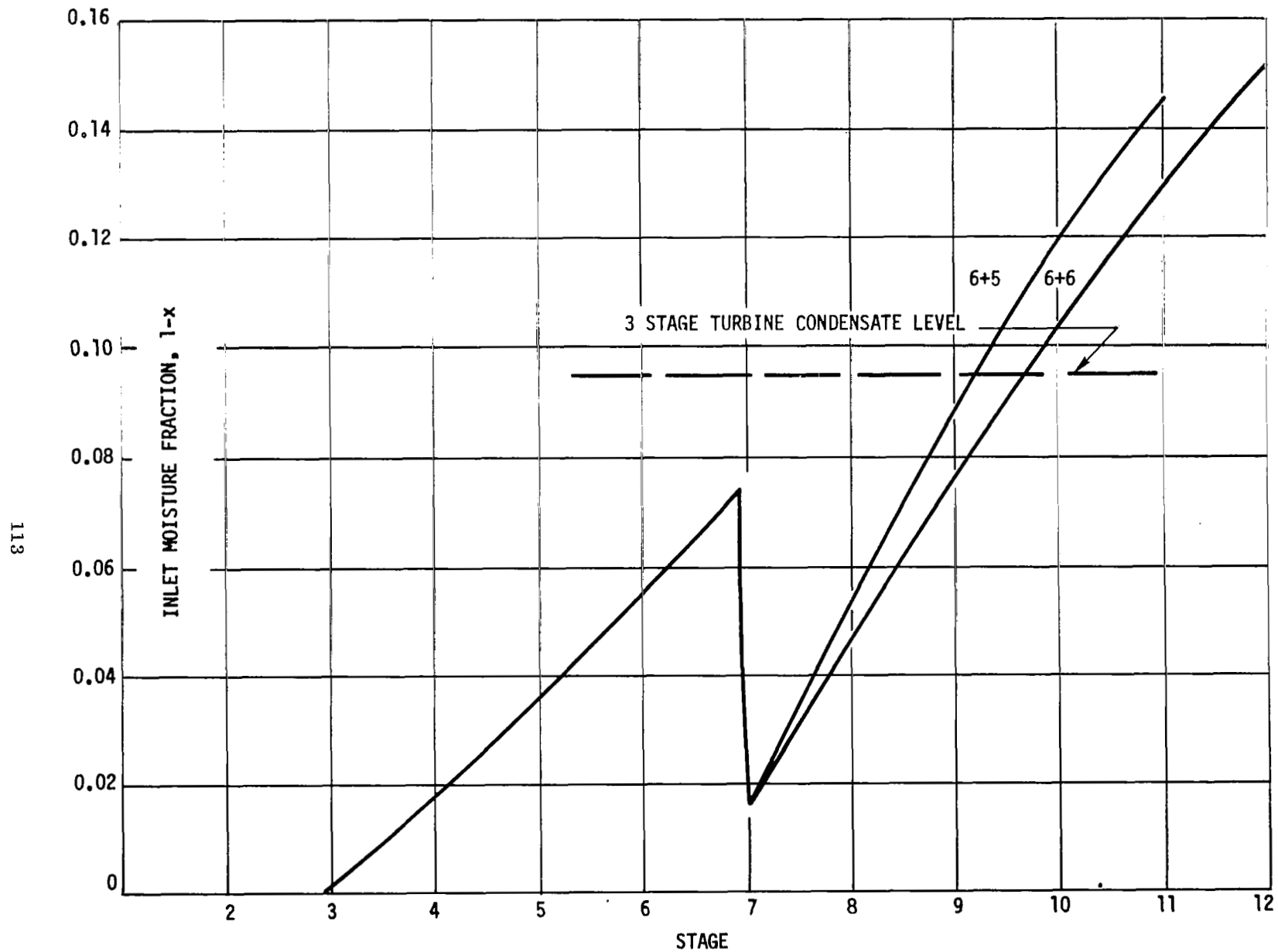


Figure 3.1-2. Turbine Moisture Distribution. Moderately Loaded H.P. Turbine.

level is shown by dashed line. It is seen that for both the 5- and 6-stage low-pressure turbines, the moisture into stage ten would exceed the 9.5 percent. On the other hand, the moisture generated before the vortex separator is only about 7.5 percent. Shown on Figure 3.1-3 is the same variation for the turbine family in which the high-pressure turbine was heavily loaded. On this design family also, the moisture entering stage ten exceeds the value of the three-stage turbine condensate level. This occurs in spite of the fact that the moisture at the exit of the six-stage turbine is about 10 percent. Shown in Figure 3.1-4 is the effect of putting two interstage extraction devices in the turbine with the moderately loaded, high-pressure turbine and five-stage low-pressure turbine. It is seen that with two extraction stages the condensate level can be kept below the three-stage condensate level. Shown in Figure 3.1-5 is a variation of inlet moisture fraction with the stage number of a heavily loaded, high-pressure turbine with six stages. In this turbine, a single interstage extraction device keeps the condensate level below the three-stage condensate level value. However, the efficiency of this turbine is only 81.9 percent compared with 83.2 percent for the turbine with the moderately loaded, high-pressure turbine. Shown in Figure 3.1-6 is the variation in turbine efficiency with the number of stages for turbines with only one low-pressure turbine extraction stage. The turbines represented in this figure all have a four-stage low-pressure turbine and have high-pressure turbines which result in a need for only one low-pressure turbine extraction stage. It is seen that each additional stage adds approximately 1 percentage point to the turbine efficiency. For the final design of the KTA turbine, the

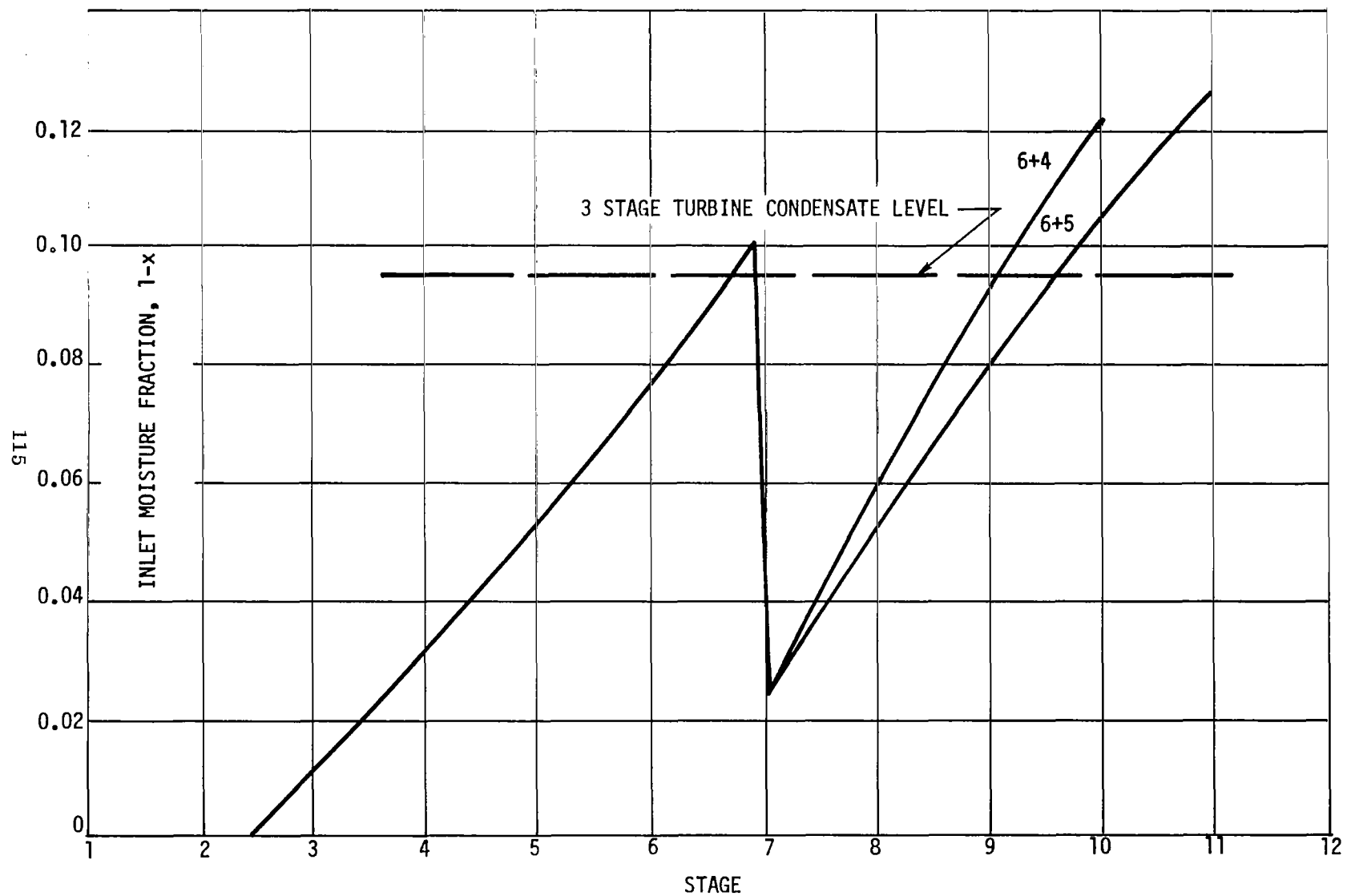


Figure 3.1-3. Moisture Distribution. Heavily Loaded H.P. Turbine.

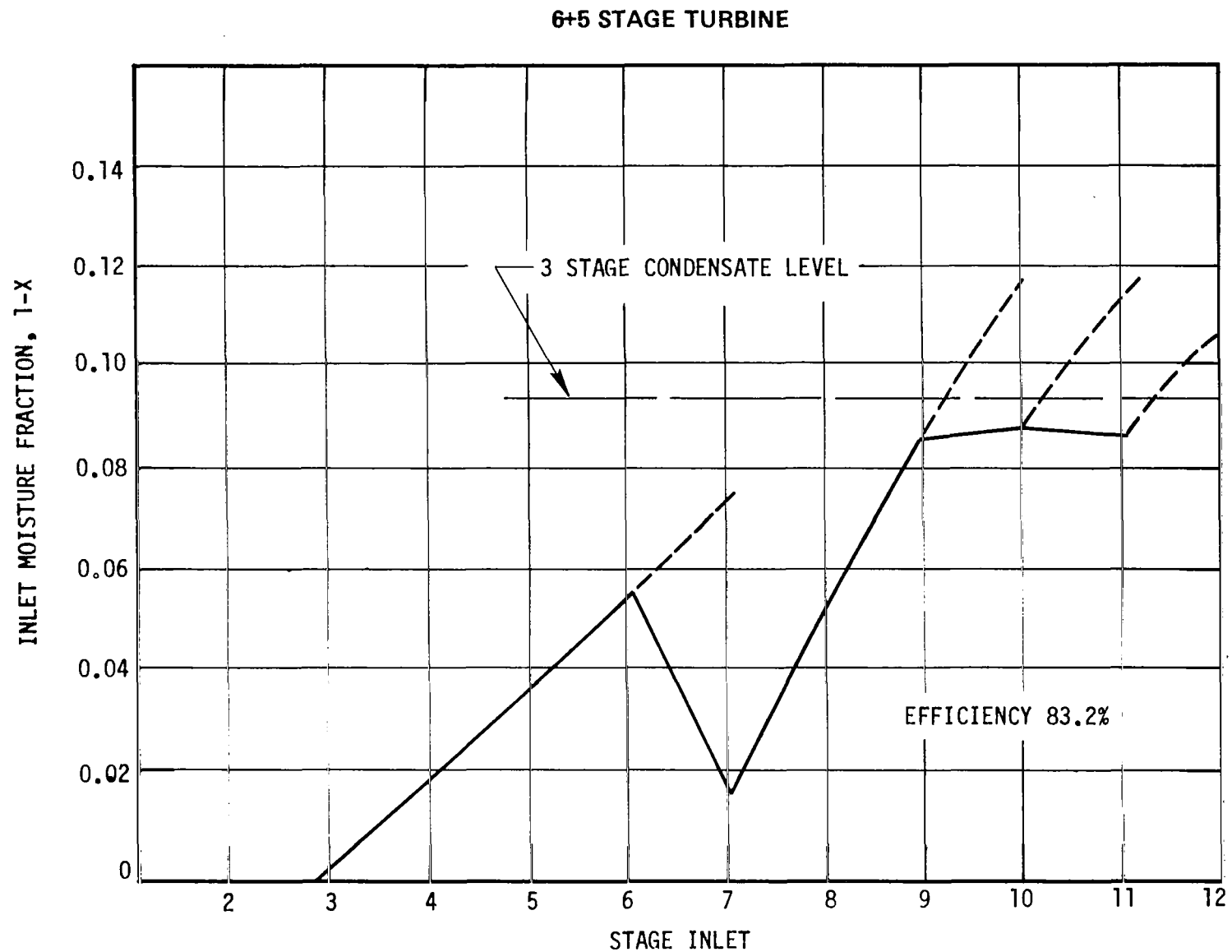


Figure 3.1-4. Turbine Condensate Buildup Moderately Loaded H.P. Turbine.

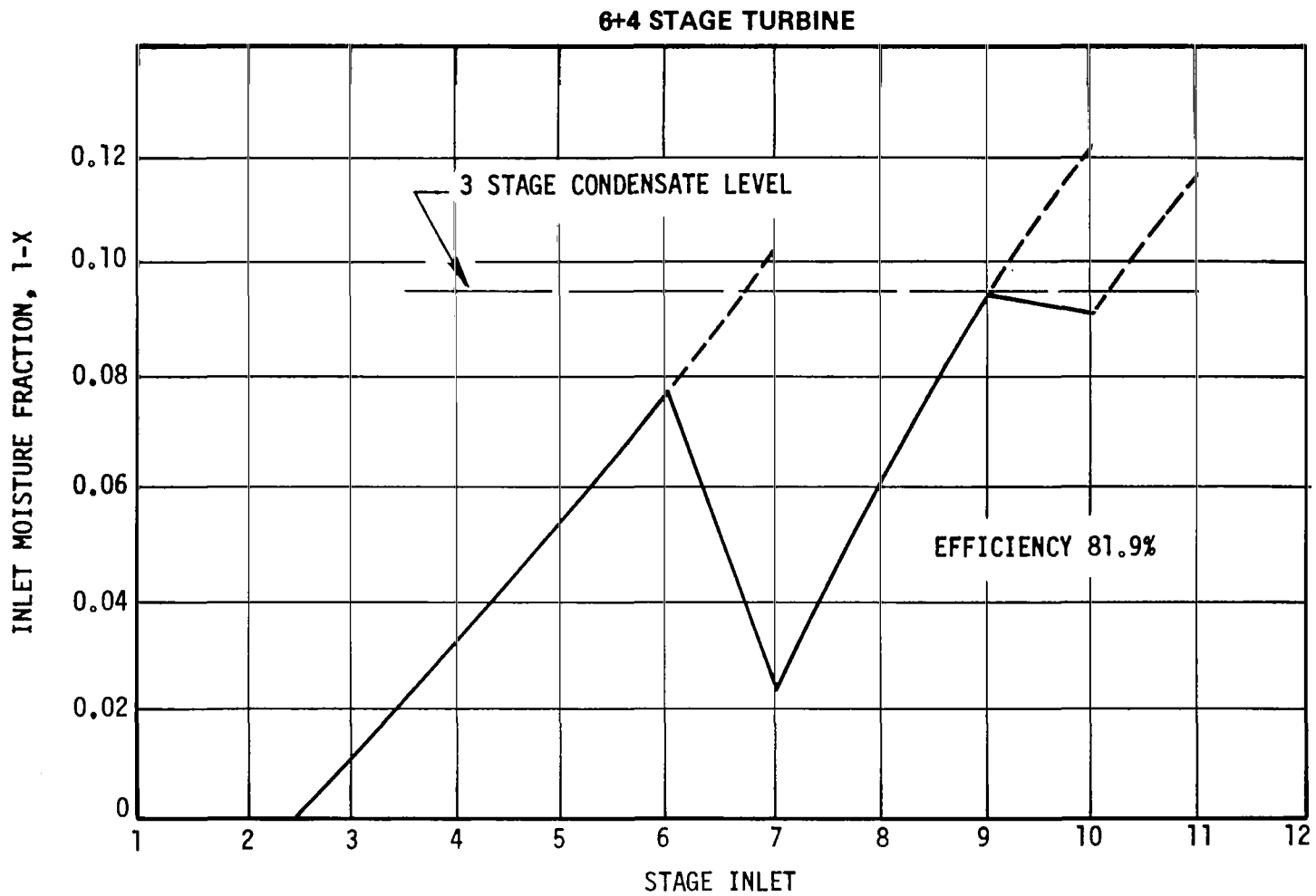


Figure 3.1-5. Turbine Condensate Buildup Heavily Loaded H.P. Turbine.

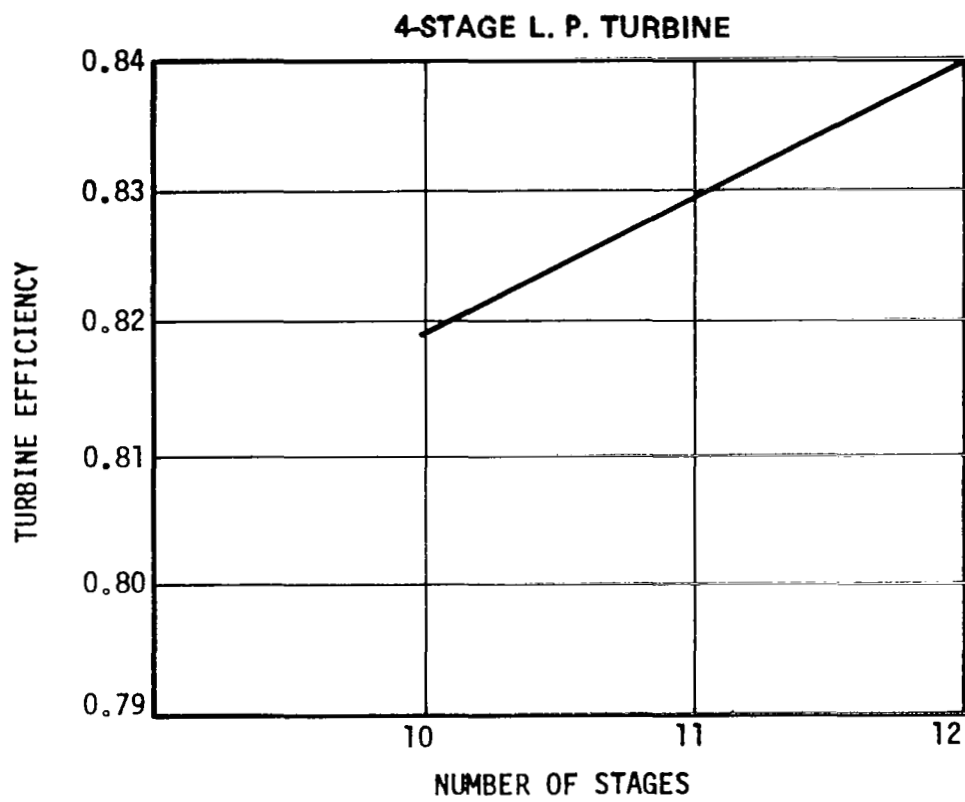


Figure 3.1-6. Efficiency Variation With One L.P. Extraction Stage.



eleven stage turbine was selected. The reason for not selecting the twelve-stage turbine is that it would mean overhanging eight stages in the high-pressure turbine. The overhanging of seven stages in the high pressure turbine, resulting in an eleven-stage turbine, gave an overhung mass moment approximately equal to the overhung mass moment of the three-stage turbine which operates without vibrational difficulties.

Shown in Figure 3.1-7 is the variation of inlet moisture fraction with the stage number for the selected Phase II potassium turbine. This turbine has seven overhung stages in the high-pressure turbine and four stages in the low-pressure turbine with a single interstage extraction device on the low-pressure turbine. As can be seen on the figure, the moisture entering the seventh stage is slightly over eight percent and the moisture entering the tenth stage is approximately  $9\frac{1}{2}$  percent. This turbine, then, combines a high efficiency of 82.9 percent with the requirement for a single interstage extraction device giving an acceptable solution for the KTA turbine.

### 3.2 SELECTED TURBINE DESIGN

The selected KTA turbine design for the Phase II is comprised of a seven-stage moderately loaded, high-pressure turbine and a four-stage moderately loaded low-pressure turbine. Interspool condensate removal with an effectiveness of 80 percent is provided between the high- and low-pressure turbine. In addition, interstage moisture extraction on the tenth stage is provided to keep the moisture content entering any stage below 9.5 percent.

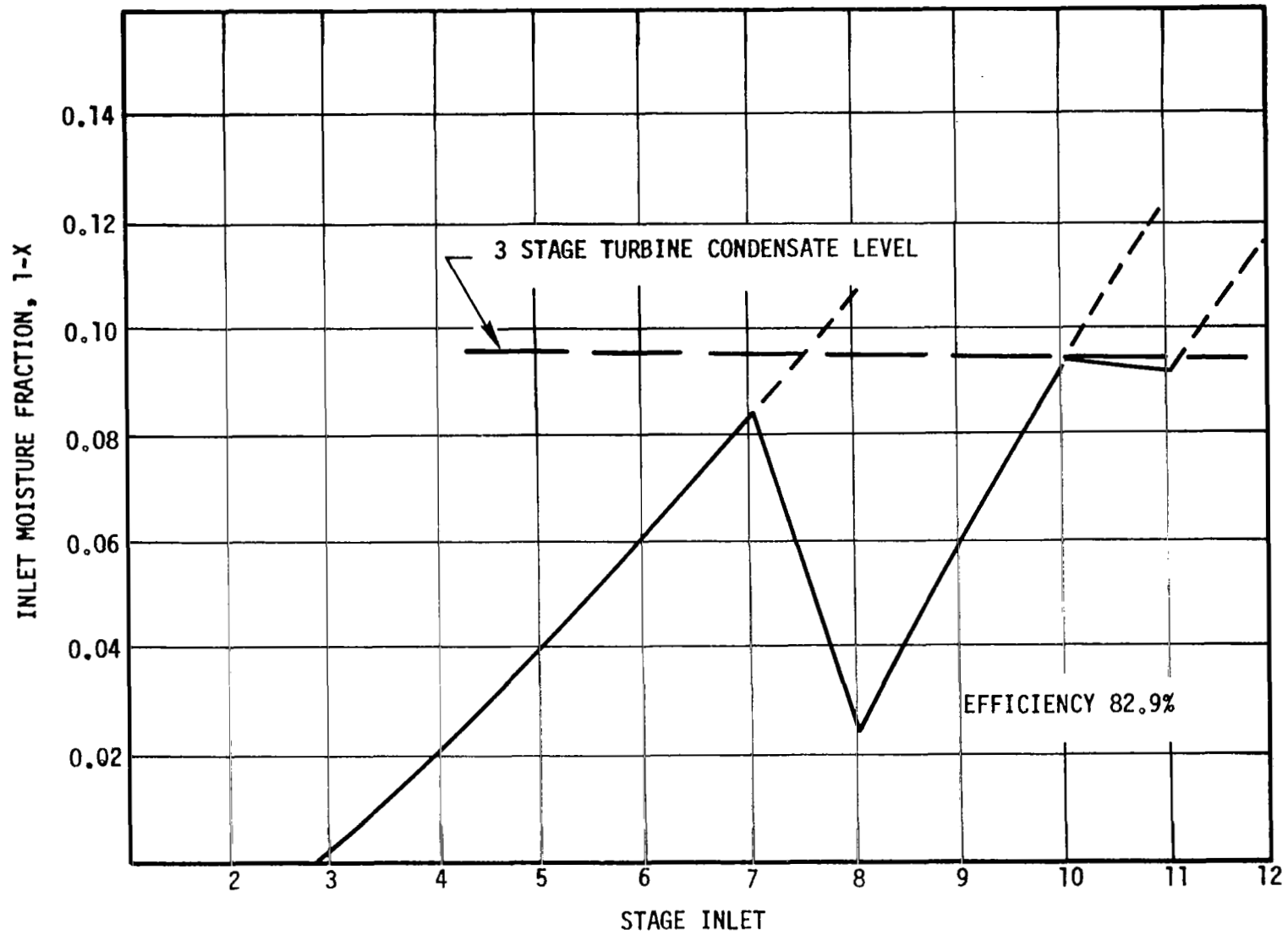


Figure 3.1-7. Turbine Condensate Buildup - 7 Stage H.P. Turbine + 4 Stage L.P. Turbine.

Shown in Figure 3.2-1 is the Mollier diagram for potassium with the state line for the potassium turboalternator turbine superimposed. Shown in Figure 3.2-2 are drawings of the high- and low-pressure turbines. The potassium vapor enters the high-pressure turbine at 2100°F and at a pressure of 165 psia. The potassium leaves the high-pressure turbine at a temperature of 1570°F and a pressure of 33.7 psia. The absolute velocity at the exit to the high-pressure turbine is 278 ft/sec. The high-pressure turbine has a velocity-diagram efficiency of 85.3 percent, which excludes any losses due to the presence of moisture and bearings or seals. The axial thrust of the high-pressure turbine aft is 1969 lbs.

The vapor flows from the high-pressure turbine through a vortex separator, not shown, into the aft end of the low-pressure turbine. It then flows in the opposite direction and discharges between the high- and low-pressure turbines. The vapor enters the low pressure turbine at a temperature of 1560°F and a pressure of 32.2 psia. This pressure drop of 1.5 psi is used up in ducts and scrolls and in the vortex separator. The vapor leaves the low-pressure turbine at a temperature of 1220°F and a pressure of 5.44 psia. The velocity at this point is 412 ft/sec. The velocity diagram efficiency of the low-pressure turbine is 89.1 percent and the thrust load forward is 752 lbs. These two turbines combine in giving a blading efficiency of the entire turbine of 82 percent, which includes all losses except parasitic losses, including bearings and seals.

Shown in Figure 3.2-3 are the turbine design parameters on a stage-to-stage basis which define the selected KTA turbine design.

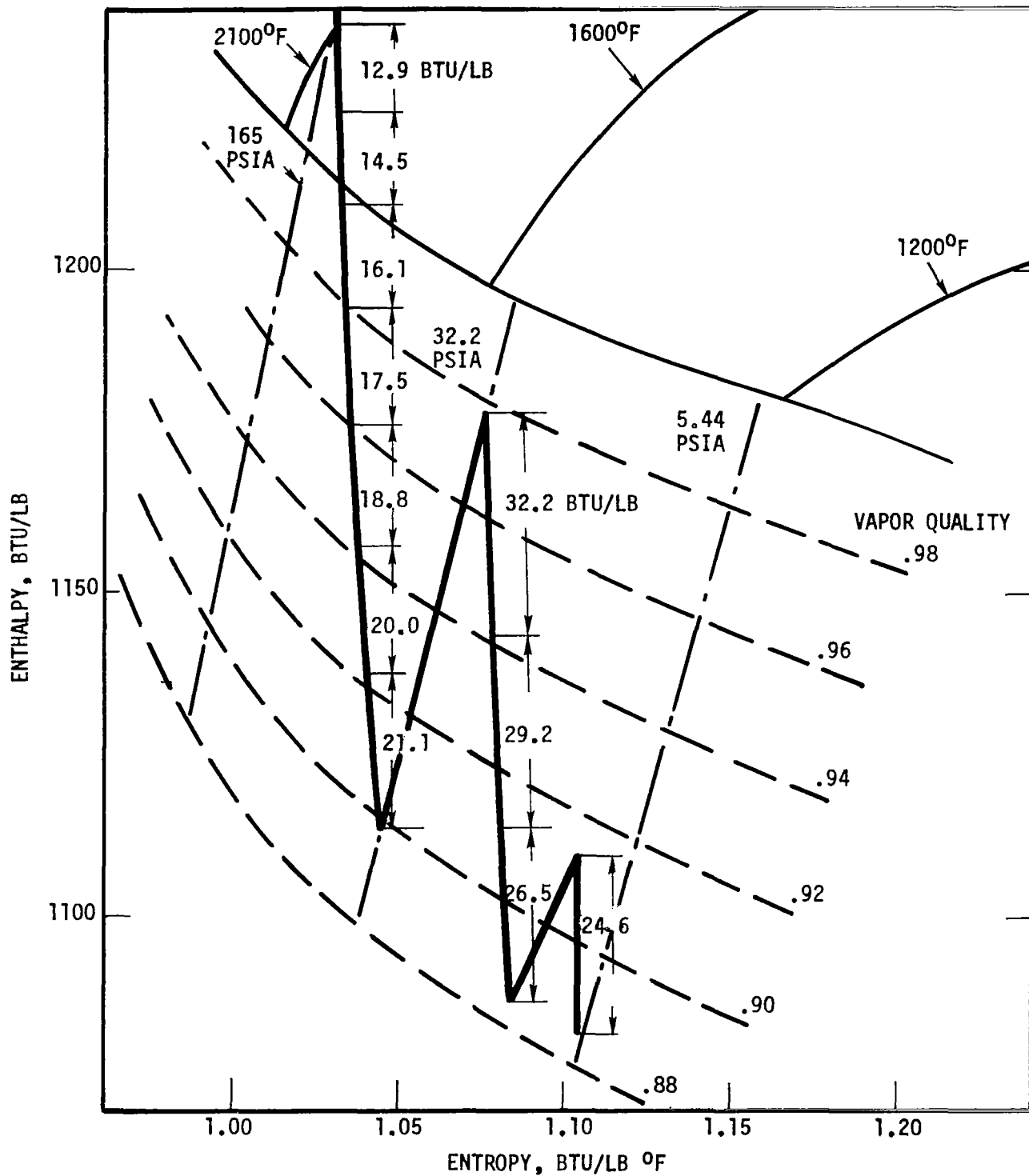
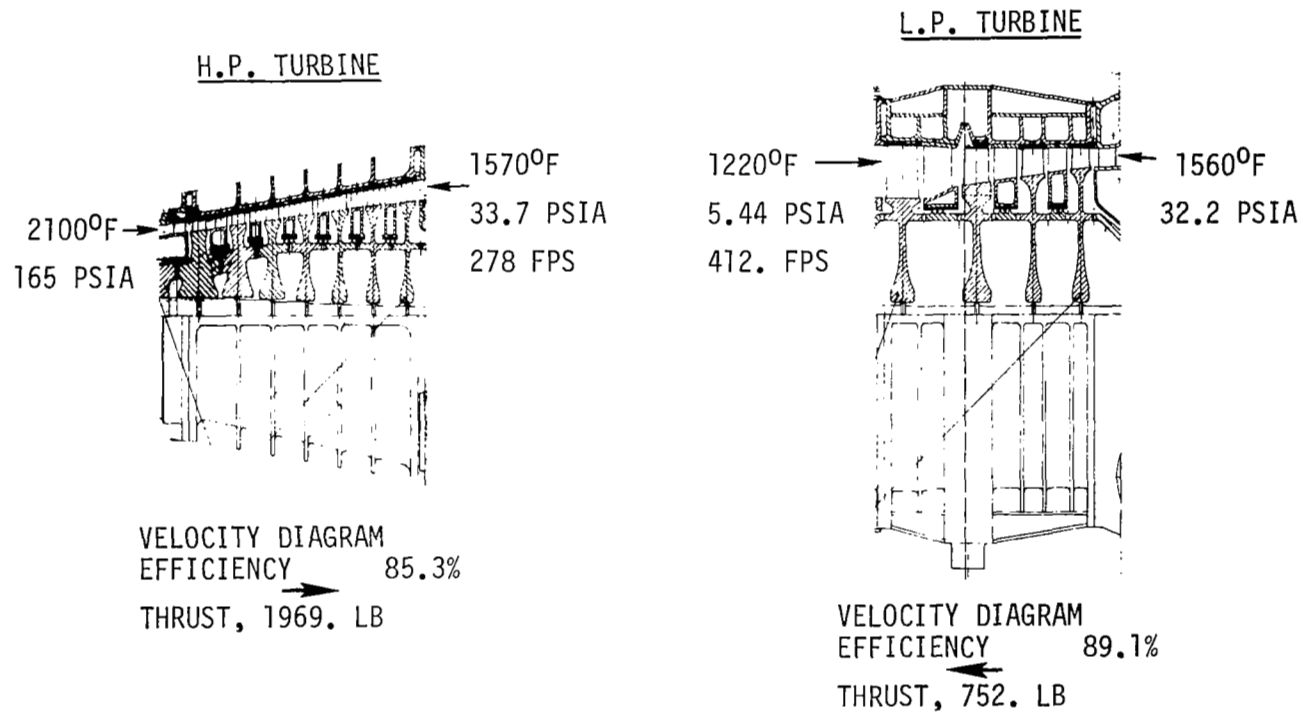


Figure 3.2-1. KTA Turbine State Line.



BLADING EFFICIENCY, 82%

Figure 3.2-2. KTA Split Spool Turbine.

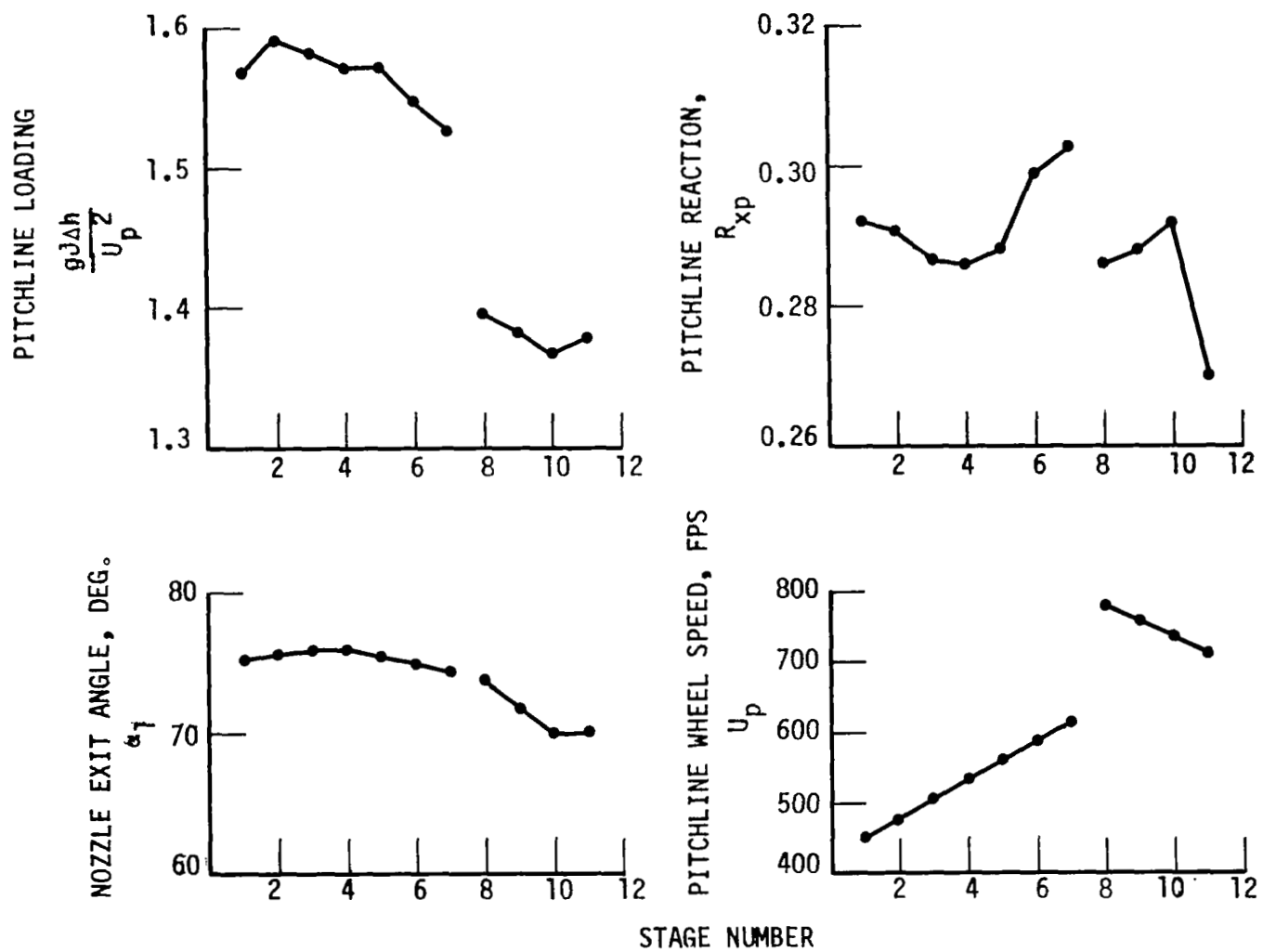


Figure 3.2-3. Turbine Design Parameters.

For the design of this turbine, supersaturated expansions were assumed for the first two stages with reversion to equilibrium conditions after the second rotor. Equilibrium expansions were assumed for all the other stages, which were in the wet region, and the condensed moisture loss was calculated as a function of the vapor quality at each stage. This design calculation model which was used for the final design is different from the one used for Phase I and reflects improvements made from the evaluation of the three stage potassium vapor turbine under Contract NAS3-10606. Shown in Figure 3.2-4 are the variations of the turbine design characteristics which result from the input values shown on the previous chart. Starting in the upper left hand corner and reading across, there is the rotor hub turning angle. As in Phase I this angle was limited to  $130^{\circ}$  because experience has shown that the expressions for loss values used in turbine design tend to break down when this rule is exceeded. The hub reaction is shown next, and is limited by zero reaction at the hub since at negative values of the reaction, efficiency of a stage devreases rapidly. It is seen that only in the last stage was the limiting value required. This is because of the high volume flow requiring that the hub speed be very much lower than the tip speed. The inlet vapor quality is shown in the next graph, followed by the tip speed. Here again it is seen that only on the last stage was the maximum tip speed of 850 ft/sec required. The rotor exit swirl angle is shown next and it is seen that it never exceeded 10 degrees in the plus or minus direction. The blade height was considerably below 0.5 inch. This was brought about by the reduction in mass flow, from 2.51 lbs/sec in Phase I to 2.05 lbs/sec in Phase II. As can be inferred from the hub reaction at the top of the figure, all the stages have a large amount

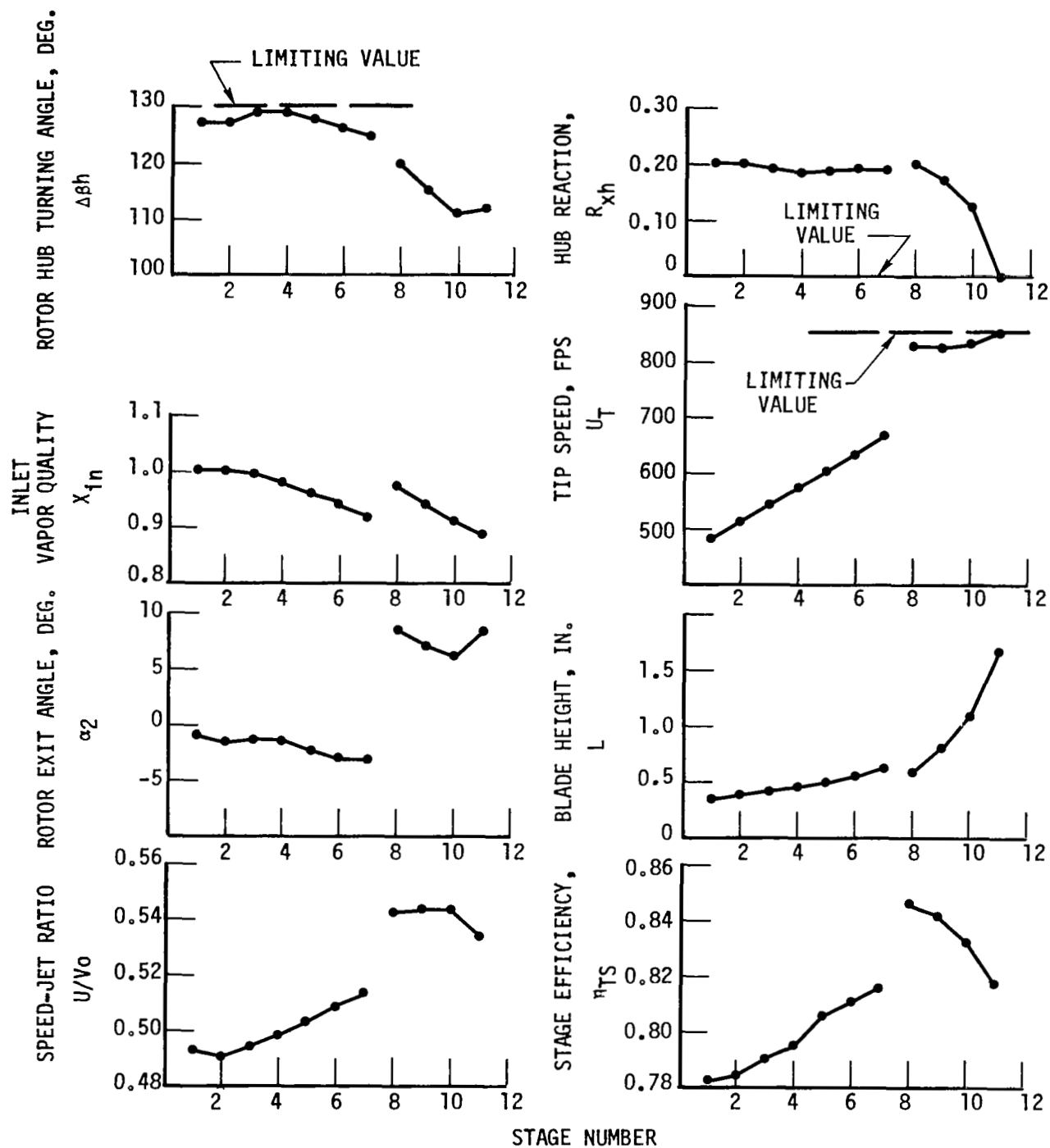


Figure 3.2-4. Turbine Design Characteristics.



of reaction at the pitch line. Thus, in the plot of speed - jet ratio it is seen that the values exceed 0.5 for most stages. Stage efficiency is shown in the final graph as a function of the stage number.

In the evaluation of the various designs, the blading losses were in three categories, namely, profile loss, secondary flow loss, and tip clearance loss. The distribution of these losses in the selected design is shown in Figure 3.2-5 as a function of stage number. It is seen that in the early stages, the tip clearance loss is significant because of the small blade height and also the secondary flow loss is sizeable due to the adverse aspect ratio effects. Shown in Table 3.2-1 are additional fluid dynamic losses which were considered. They include the loss in the cross-over duct interstage removal device and the exit. Turbine parasitic losses are shown in Table 3.2-2. Significant losses which were not evaluated in Phase I have been added to the list for Phase II, and they are the reason that the parasitic losses in Phase II are larger than those in Phase I. The most significant of these is the liquid drag loss which amounts to 13 kilowatts. This drag loss is primarily due to the exposed surfaces of the thrust bearing in the turbine, but also includes losses from other exposed portions of the shaft where the shaft is immersed in liquid metal.

Shown in Table 3.2-3 are several efficiency values associated with the turbine. The velocity diagram efficiency is 91.7 percent. This efficiency was calculated only taking into account the profile loss, secondary flow loss, and the tip clearance loss. When the condensate losses and the condensate removal losses are subtracted, the blading efficiency becomes 82 percent. Finally, when the parasitic

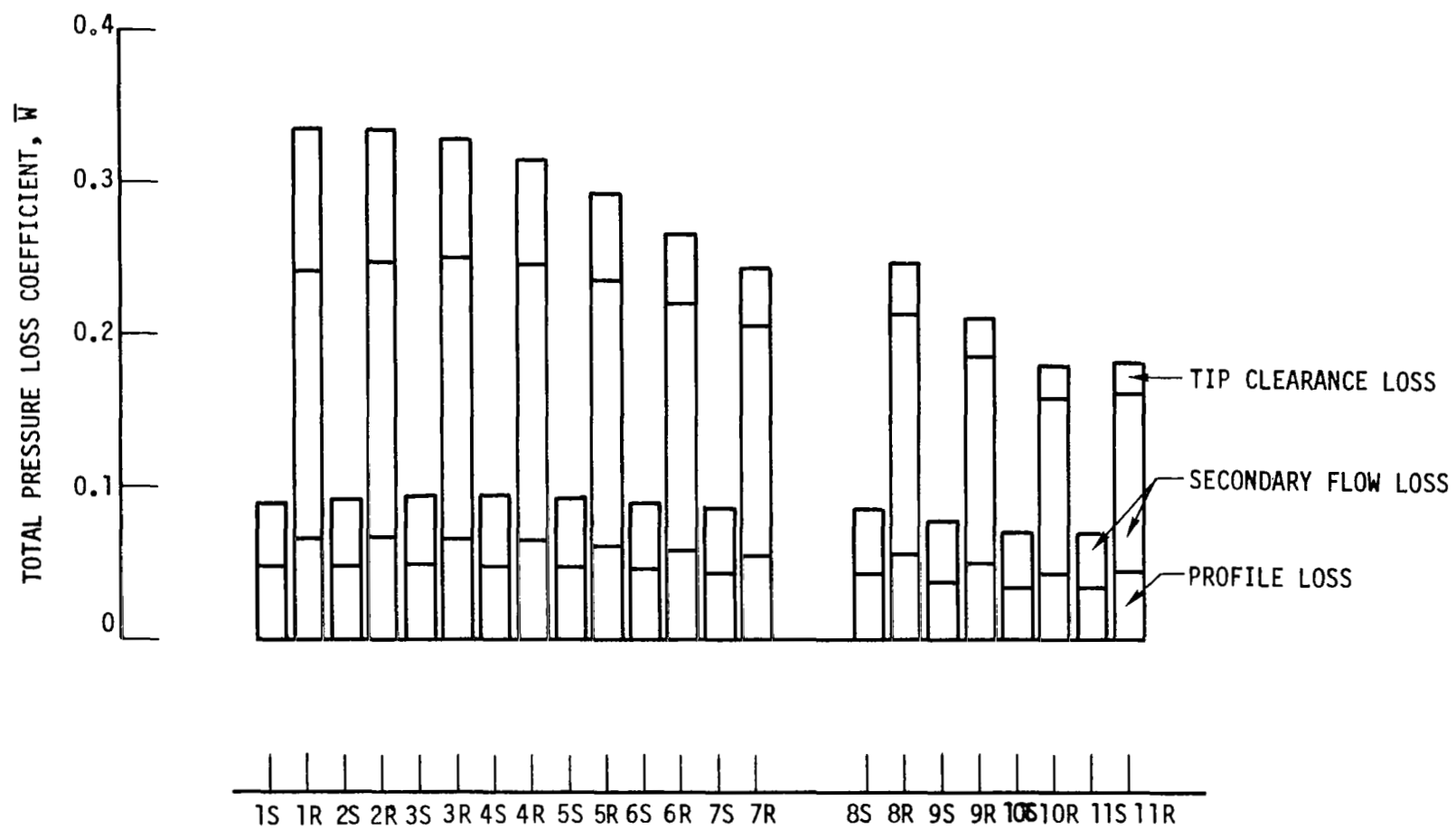


Figure 3.2-5. Blading Loss Breakdown.

TABLE 3.2-1  
ADDITIONAL FLUID DYNAMIC LOSSES

CROSS OVER DUCT

PRESSURE DROP, PSI	1.5
--------------------	-----

VORTEX SEPARATOR

EFFECTIVENESS, %	80
------------------	----

VAPOR BLEED, %	0.5
----------------	-----

INTERSTAGE REMOVAL (TENTH STAGE)

EFFECTIVENESS, %	25
------------------	----

VAPOR BLEED <sup>*</sup> , %	1.0
------------------------------	-----

EXIT

<u>TOTAL PRESSURE LOSS, %</u>	50
-------------------------------	----

EXIT DYNAMIC HEAD

<sup>\*</sup> LISTED WITH PARASITIC LOSSES

TABLE 3.2-2  
TURBINE PARASITIC LOSSES

<u>PHASE</u>	<u>I</u>	<u>II</u>
LABYRINTH SEAL LEAKAGE, KW	8.9	6.5
JOURNAL BEARING, KW	5.2	5.6
THRUST BEARING, KW	8.1	10.3
SCREW SEAL, KW	1.0	0.5
INTERSTAGE MOISTURE EXTRACTION, KW		0.5
CASING HEAT LOSS, KW		0.2
LIQUID DRAG LOSS, KW	<u>      </u>	<u>13.0</u>
TOTAL PARASITIC LOSS, KW	23.2	36.6

TABLE 3.2-3  
TURBINE EFFICIENCY

VELOCITY DIAGRAM EFFICIENCY		<u>91.7</u>
CONDENSATE LOSSES, KW	<u>35.</u>	
CONDENSATE REMOVAL LOSSES, KW	<u>22.</u>	
BLADING EFFICIENCY		<u>82.0</u>
PARASITIC LOSSES, KW	<u>36.6</u>	
SHAFT EFFICIENCY		<u>75.8</u>

losses are subtracted, which include the bearing and seal losses and the heat loss from the casing, shaft efficiency becomes 75.8 percent.

Shown in Figure 3.2-6 is the variation in turbine efficiency with tip clearance. In the mechanical design of the Phase II KTA turbine the tip radial clearances were sized such that at the end of three years they would all be ten mils. Because of the high creep rate on the first two stages, the tip clearance is significantly bigger than ten mils when the turbine is first started. However, as shown in the figure, this initial efficiency is insignificantly below the efficiency after two years.

### 3.3 SCROLLS AND DUCTS

It was established in Phase I that a reasonable velocity in the ducts and scrolls was approximately 250 ft/sec. Therefore, that velocity was used in all duct and scroll sizing. Shown in Figure 3.3-1 is a model which was made in order to demonstrate what scrolling and ducting would be necessary for the Phase II KTA turbine. The inlet where the flow enters the high-pressure turbine from the right is hidden by the duct in the foreground. At the exit to the high-pressure turbine, the flow annulus is divided into four quadrants. Each one of these quadrants gradually changes its shape until it becomes a circle. Since the absolute velocity leaving the high-pressure turbine is 278 ft/sec, very little diffusion is required to bring it to the velocity of 250 ft/sec which was used for the duct velocity. After the exit flow reaches the circular cross-section, an elbow is provided. The flow then enters the vortex separator where 80 percent of the moisture is removed. After leaving the separator, the flow enters the low-

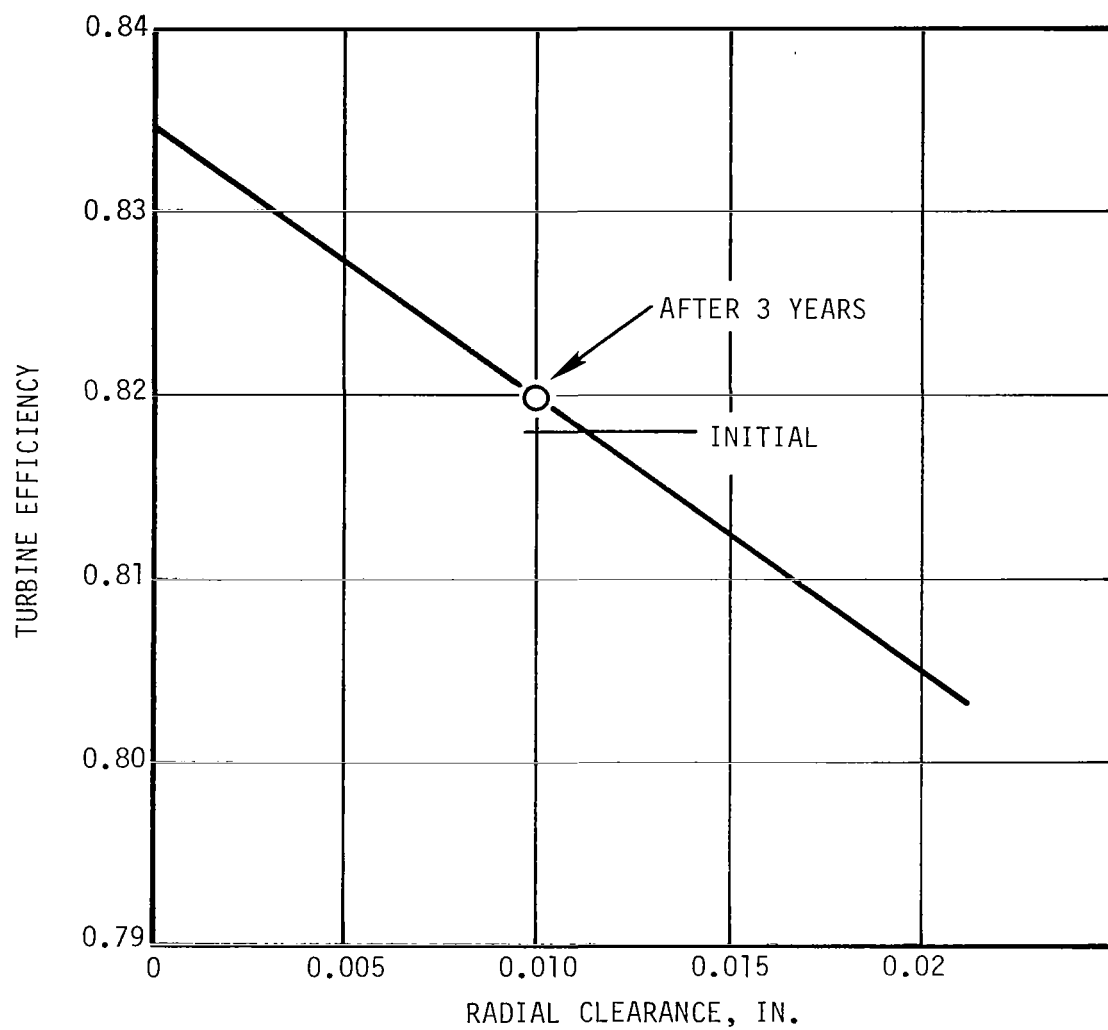


Figure 3.2-6. Effect of Tip Clearance on Efficiency.

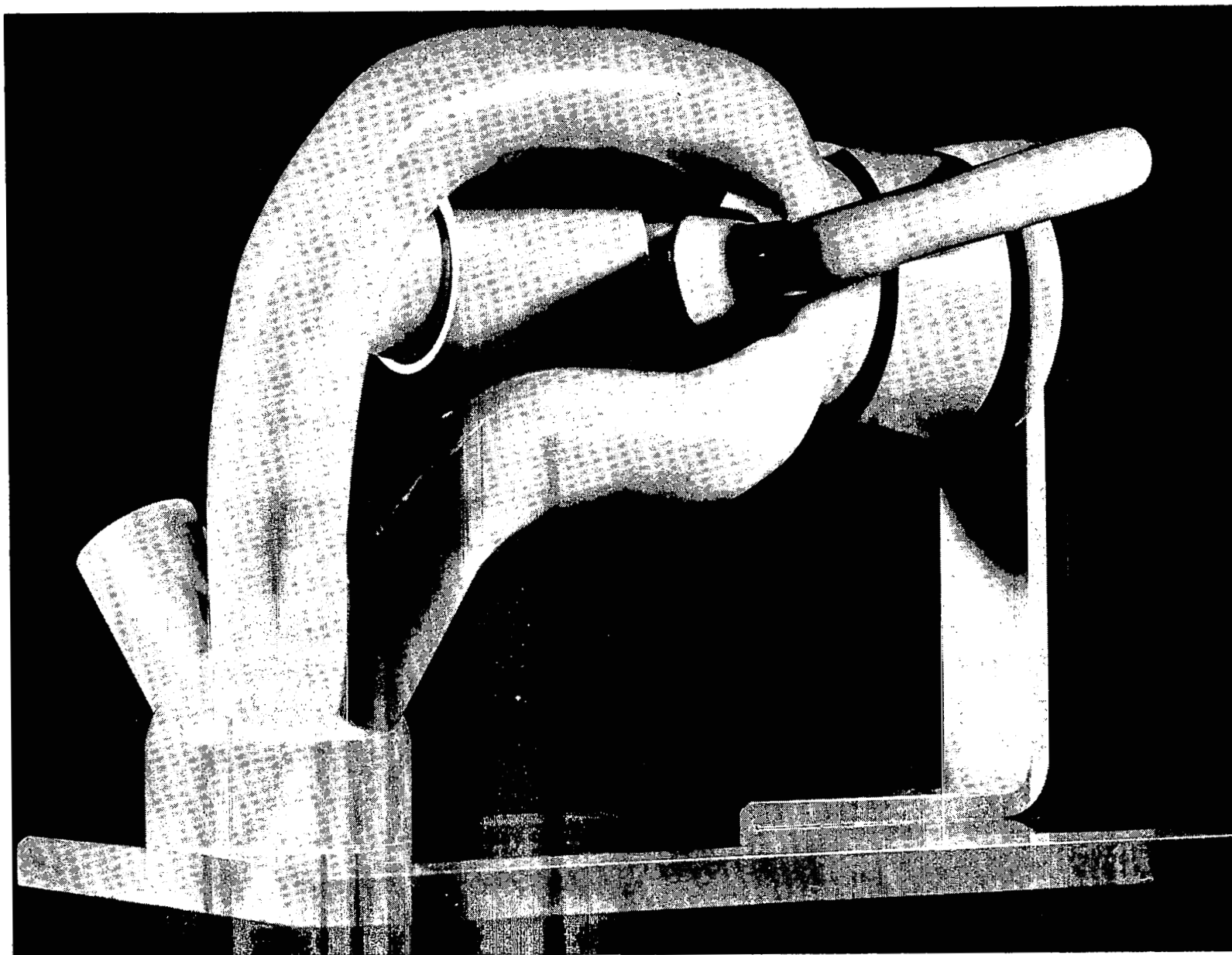


Figure 3.3-1. KTA Turbine Ducts and Scrolls with Single Inlet and Exit.



pressure turbine in a tangential manner, by means of a scroll. The flow through the low-pressure turbine is in the opposite direction to that in the high-pressure turbine. At the exit of the low-pressure turbine the flow again enters four quadrants. The flow at this location has a velocity of 472 ft/sec and therefore has to be diffused down to a value of 250 ft/sec. The flow takes a first bend at full velocity and then is decelerated in a conical diffuser. Finally, it takes a second bend bringing it to the horizontal direction. Four pipes, 4.8 inches in inside diameter, then conduct the flow to a single outlet pipe which is connected to the condenser.

The main reason for dividing the flow into four parts as it leaves the low-pressure turbine is the high volume flow and the fact that the flow through the low-pressure turbine is in the opposite direction to that in the high pressure turbine so that the thrust of the two turbines tend to balance each other. With the counter flow arrangement, it is very difficult to provide enough room for the large scroll which would be required to remove the flow from the low-pressure turbine in one duct. Not only does the counterflow arrangement result in the reduction in net thrust on the turbine shaft, but it also makes possible placing the bearings next to turbine stages of moderate temperature.

An alternate way to divide the flow into four parts to remove it from the turbine is to duct the flow streams into four condensers parallel with the shaft axis. This arrangement is shown in Figure 3.3-2 and indicates that the length of the ducts and the number of turns are decreased by this arrangement compared to the arrangement shown in the previous photograph.

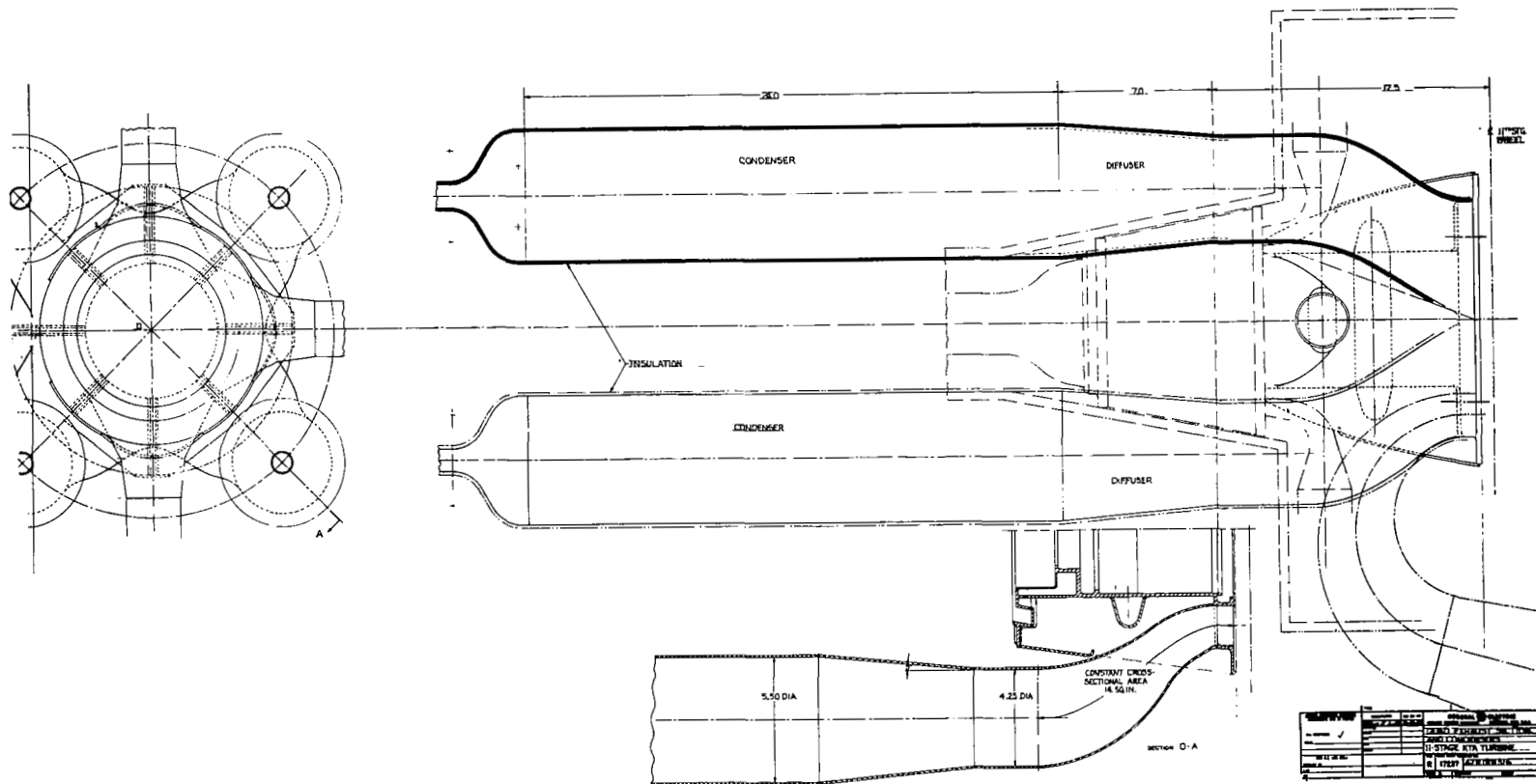
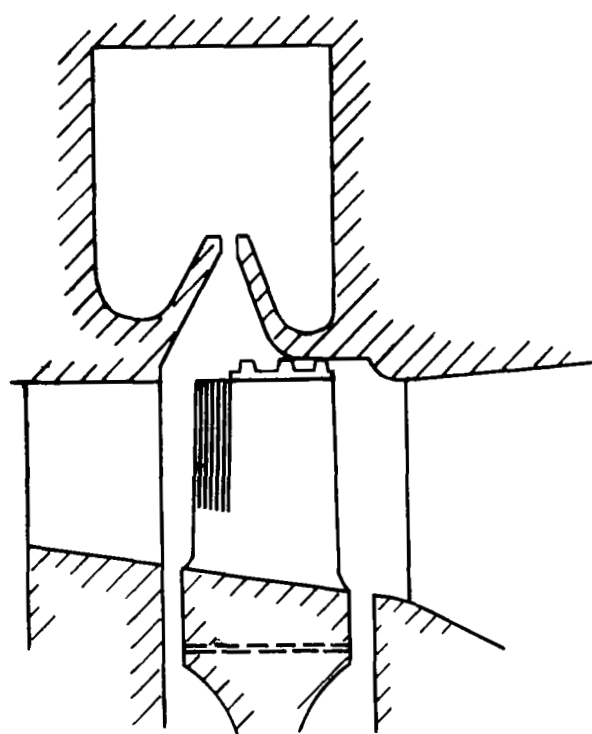


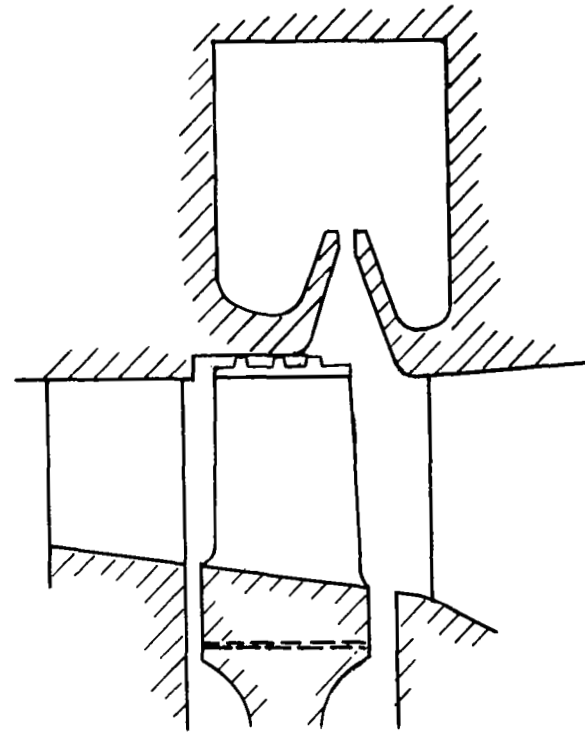
Figure 3.3-2. KTA Turbine with 4 Condensers Attached.

### 3.4 INTERSTAGE CONDENSATE REMOVAL

Based on steam turbine practice in the low pressure stages of central-station power plants and in all stages of central station nuclear power plants, two types of rotor moisture extraction can be considered for the KTA turbine. Shown in Figure 3.4-1 are the two concepts applied to the tenth stage of the KTA turbine. On the left-hand side of the figure is shown a leading edge extraction device. In this device, although the rotor blades have a rotating tip shroud, the tip shroud is cut back some fraction of the chordal distance to permit moisture collecting on the blade surface to be centrifuged into the removal device radially adjacent to the turbine blade. In order to improve the effectiveness of the device, radial flutes are placed in the surface of the blade near the leading edge so that by capillary attraction the droplets will be captured and centrifuged to the tip along the flutes. The cutting back of the tip shroud results in increased tip losses. For this reason it was decided to use the trailing edge rotor moisture extraction device in the three-stage potassium test turbine (Contract NAS3-8520). Accordingly, the same type of device was selected for the KTA turbine. This is shown in the right-hand side of the figure. With this type of device, the liquid which is stripped from the trailing edges of the stator vanes impinges upon the leading edge of the rotor blades on the suction surface (convex side) and here is quickly centrifuged to the region of the rotating tip shroud. Vapor drag forces are counted on to transport the liquid from the leading edge to the trailing edge of the rotating tip shroud where the centrifugal acceleration is about 52,000 G's and the liquid is thrown into the removal device and then withdrawn



A. LEADING EDGE



B. TRAILING EDGE

Figure 3.4-1. Rotor-Blade Condensate Removal.

to the condenser. The design of the interstage condensate removal device for the tenth stage of the KTA Phase II turbine is summarized in Table 3.4-1.

### 3.5 INTERSPOOL CONDENSATE REMOVAL

The means for removal of the condensate in the vapor flow leaving the high-pressure turbine chosen is the General Electric developed vortex separator, as indicated when discussing the ducts and scrolls for the separators required for each turbine. The required separator is shown in Figure 3.5-1. The flow enters from the left and leaves from the right. The swirl vanes which surround the inlet centerbody cause the liquid to be slung against the inner wall of the separator. To assure that no liquid will enter the core, or be taken closer to the center of the separator, a sharp lip is provided on the aft end of the forward centerbody to make certain that separation of the liquid occurs. The vapor flows through the separator at substantially pipe velocity, namely 250 ft/sec, and after traversing a certain length of pipe reaches a moisture extraction slot. This specially contoured slot effectively removes the moisture from the flow path, where it can be discharged to the condenser. Downstream of the extraction slot is a second centerbody which is provided with two sets of deswirl vanes to remove the swirl in the flow with as small as possible pressure drop.

Shown in Figure 3.5-2 is typical separator design data in which the required separator length is plotted against the minimum droplet diameter that can be completely separated. This plot was made for a mean line swirl angle of approximately  $25^\circ$  and assumes that the drop starts its radial motion from a radius ratio of 0.1. Shown on the

TABLE 3.4-1  
INTERSTAGE CONDENSATE REMOVAL  
DESIGN, STAGE 10

STAGE INLET VAPOR QUALITY	0.910
STAGE EXIT PRESSURE, PSIA	8.49
STAGE EXIT TEMPERATURE, °F	1293
TIP SPEED, FPS	830
CENTRIFUGAL ACCELERATION, G'S	52,000
STAGE EXIT VAPOR QUALITY	.906
BLEED, %	1.0

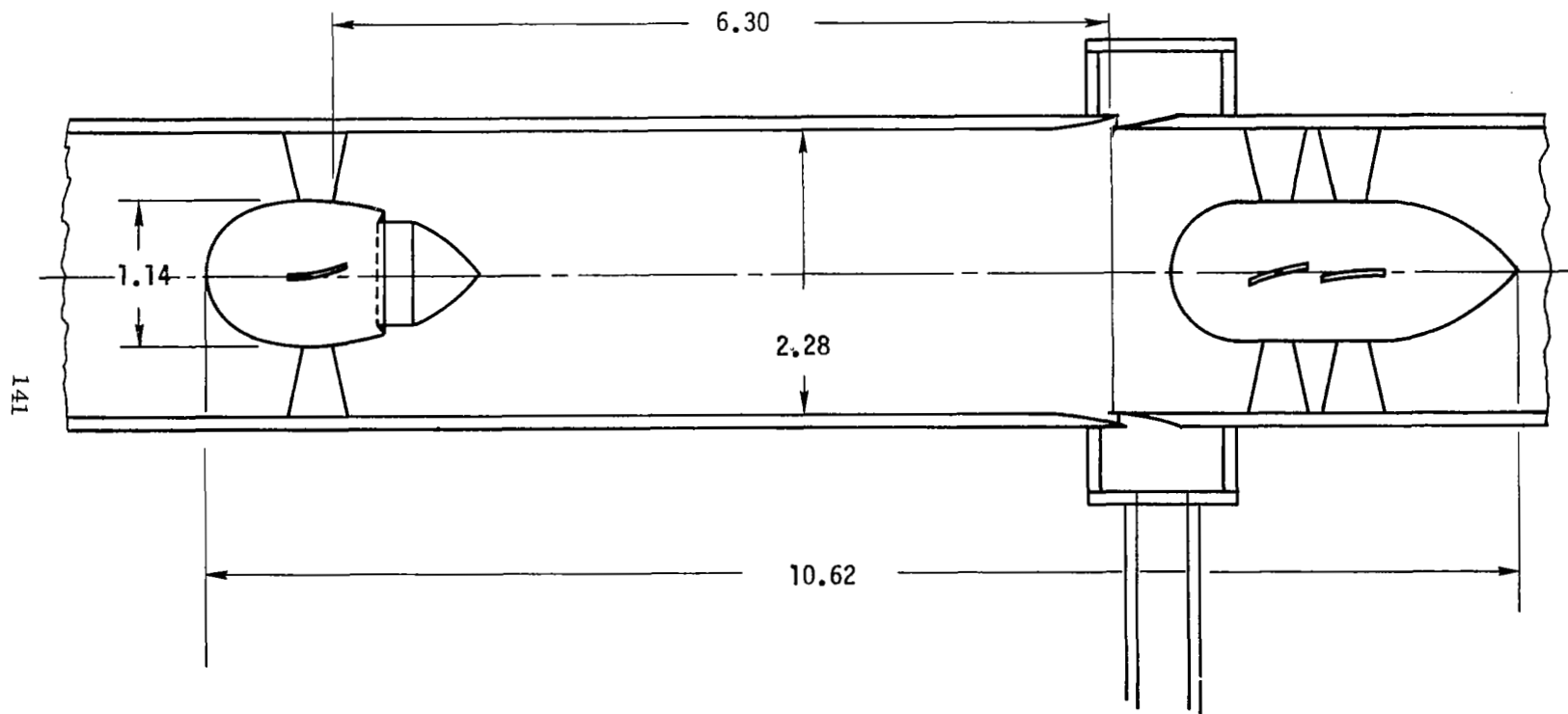


Figure 3.5-1. KTA Vortex Separator 4 Required.

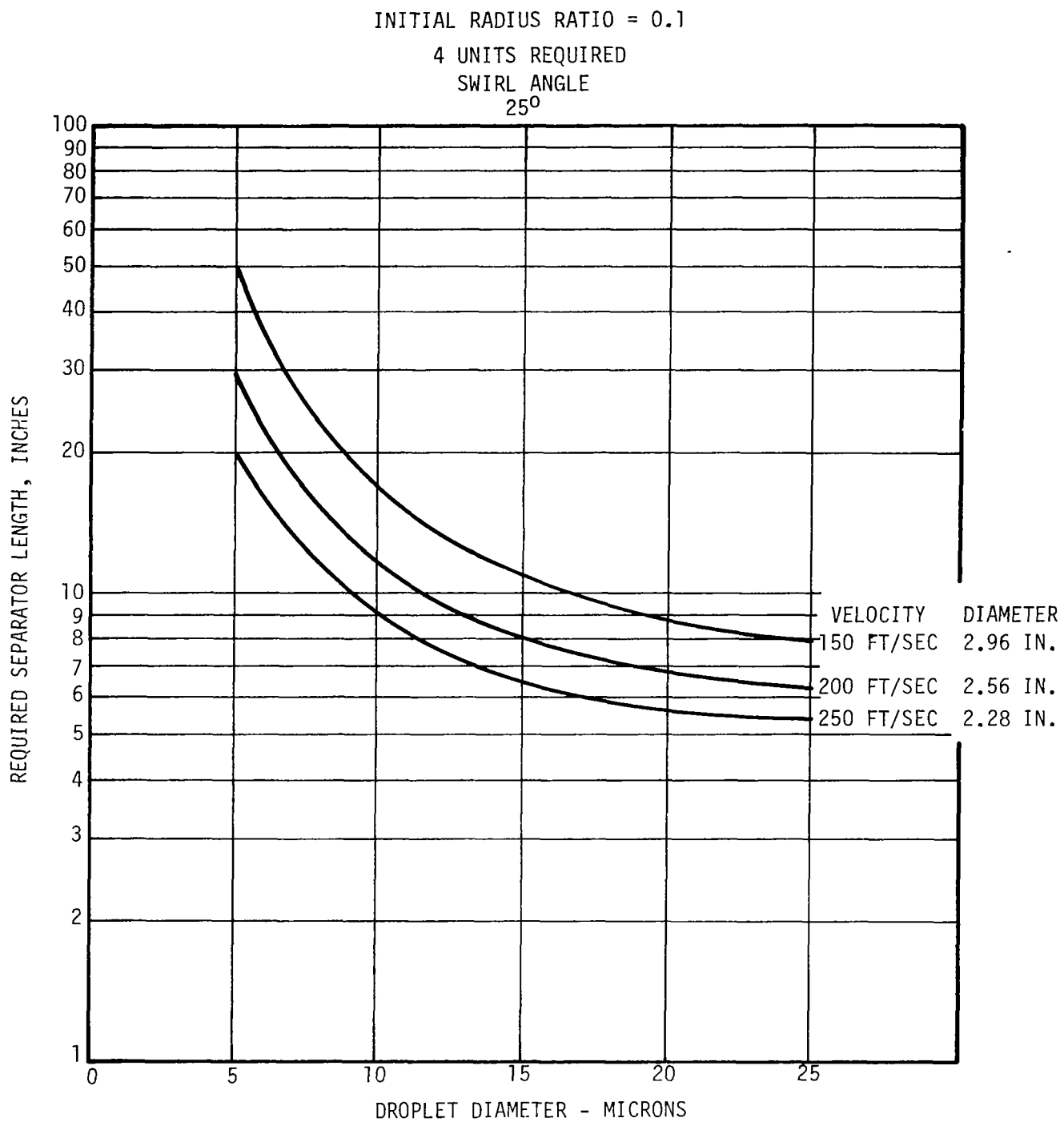


Figure 3.5-2. Vortex Separator Length Versus Droplet Diameter.



figure are through flow velocities of 150, 200, and 250 ft/sec. The corresponding diameters of the separators are shown beside the values of velocity. As is well known, when the droplet size becomes small, the length to cause separation increases rapidly, and this is what the plot shows. In order to establish a design for the separator, it is necessary to establish the drop size for which the separator must be designed. Because of the surface areas present at the exit of the high-pressure turbine, it is very difficult to calculate the minimum drop size or the drop size distribution that can be expected. It is known from steam practice, however, that the droplet size must be quite large, otherwise the high extraction effectiveness that is obtained from such separators and for that matter, from interstage extraction devices, would not be possible. One thing that can be considered, however, is that the liquid present in the vapor flow leaving the high-pressure turbine may impinge upon the swirl vanes as it does on the stator vanes in the turbine, and there form large droplets. The maximum stable drop size coming off the swirl vanes can be estimated by assuming a Weber number of 15. This gives a maximum stable drop size of 47.2 microns. In reference 3.5-1 it has been found possible to correlate the drop size distribution by plotting the fraction of volume of drops smaller than a certain diameter against the drop diameter. Such a curve for the present separator is shown in Figure 3.5-3. It can be seen from this figure that approximately 1.5 percent of the volume of liquid has a drop size smaller than ten microns. Therefore, in the design of the vortex separator for the KTA turbine, a drop size of ten microns was used. Data then from figures like Figure 3.5-2 but for different values of swirl angle were utilized

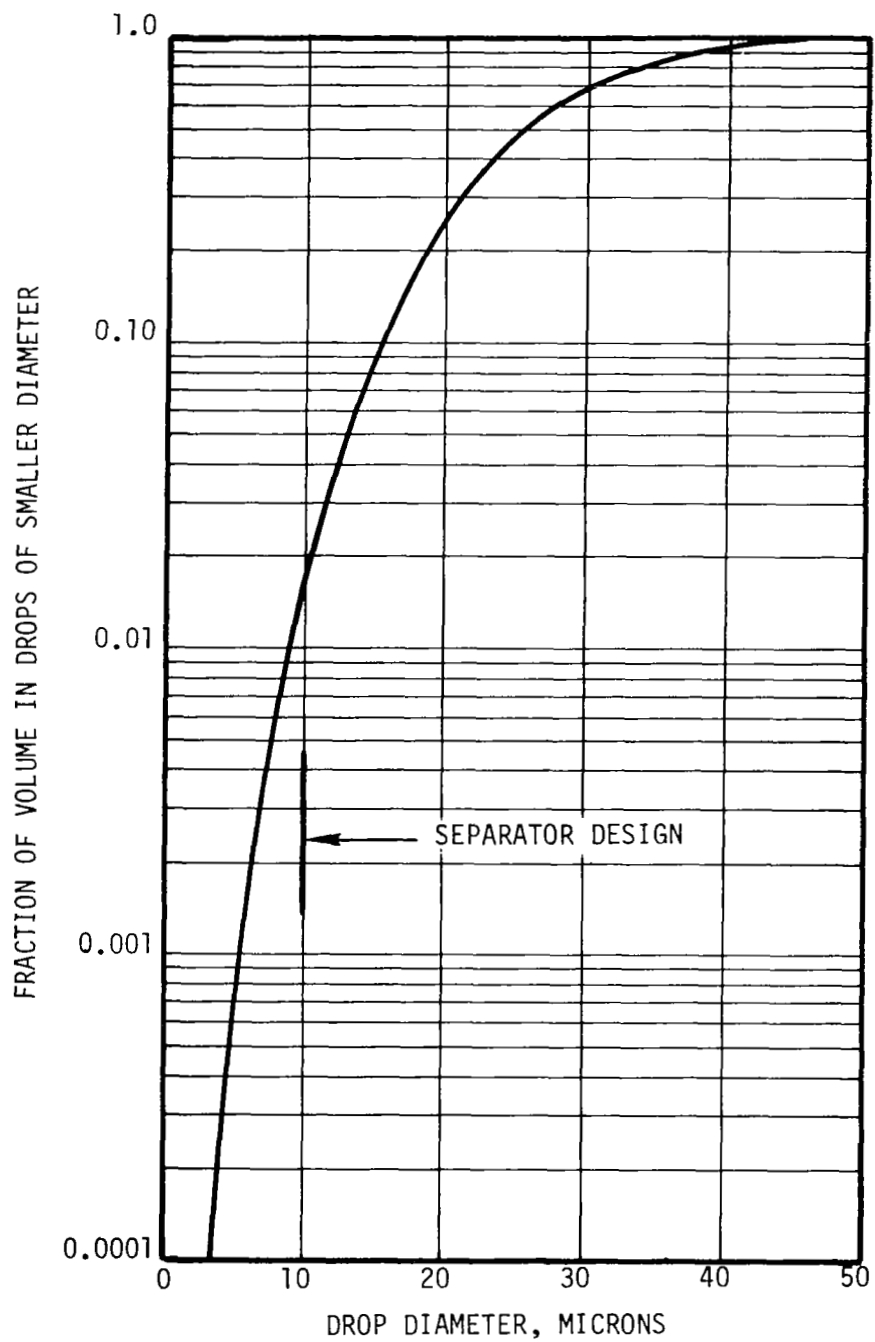


Figure 3.5-3. Vortex Separator Drop Size Distribution.

to obtain the variation of separator lengths with swirl angle and through flow velocity. Since the absolute velocity at the exit of the high pressure turbine is 278 ft/sec, conical diffusers with an included angle of  $10^\circ$  were assumed between the exit of the turbine and the inlet to the separator. The pressure drop of these conical diffusers was estimated from reference 3.5-2 and then in Figure 3.5-4 the overall pressure drop of the separator was plotted against the length of the diffuser plus the separator. It can be seen from the figure that the increase in the axial velocity through the separator reduces the length of the separator plus diffuser markedly. Also, it can be seen that the decrease in the swirl angle markedly decreases the pressure drop of the separator and diffuser. The most desirable designs of diffusers plus separators are found in the lower left hand corner of the figure. No velocities over 250 ft/sec were considered, however, because at some velocity, as yet unknown, the vapor tends to re-entrain the liquid flowing along the wall. To date, the General Electric Company has tested separators only to a velocity of 260 ft/sec. Therefore, it was not possible to use higher velocities in the choice of the KTA separator. The actual separator selected had a through flow velocity of 250 ft/sec and a mean swirl angle of  $25^\circ$ , respectively. The design of the vortex separator for the KTA turbine is summarized in Table 3.5-1. The perusal of test data indicates that an effectiveness of at least 80 percent can be obtained with a bleed flow of no more than 0.5 percent.

Shown in Figure 3.5-5 is the variation of separator collection efficiency against the through flow velocity in the separator. These data were obtained in steam tests of separators at General Electric

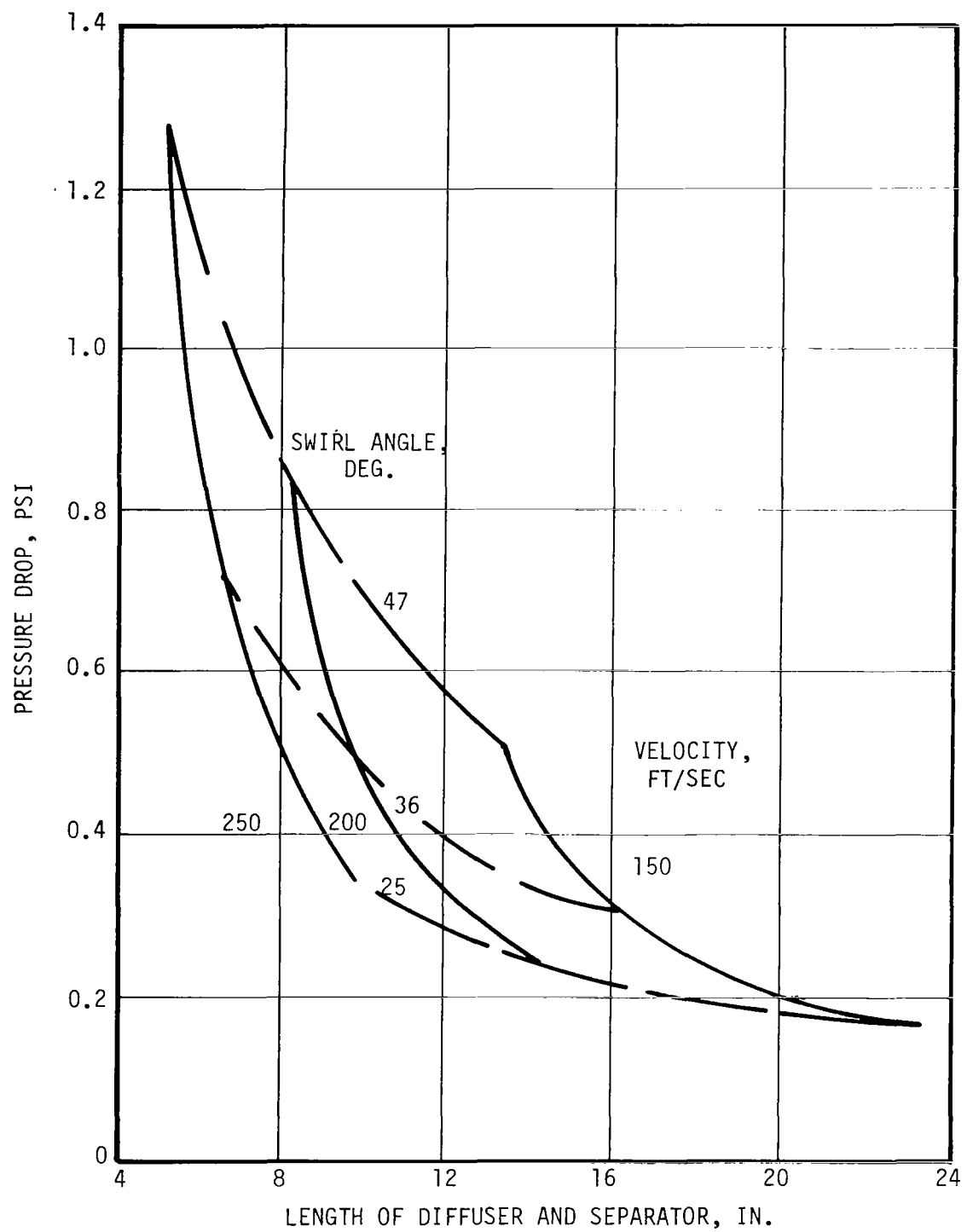


Figure 3.5-4. Selection of KTA Separator - Smallest Drop Separated, 10 Microns.

TABLE 3.5-1  
VORTEX SEPARATOR DESIGN  
 (4 Units Required)

INLET PRESSURE, PSIA	33.7
INLET TEMPERATURE, °F	1570
INLET FLOW, PPS	2.05
INLET VAPOR QUALITY	0.897
THROUGH FLOW VELOCITY, FPS	250
MEAN SWIRL ANGLE, DEG.	25
PRESSURE DROP, PSI	0.34
EFFECTIVENESS	0.8
EXIT VAPOR QUALITY	0.979
BLEED, %	0.5

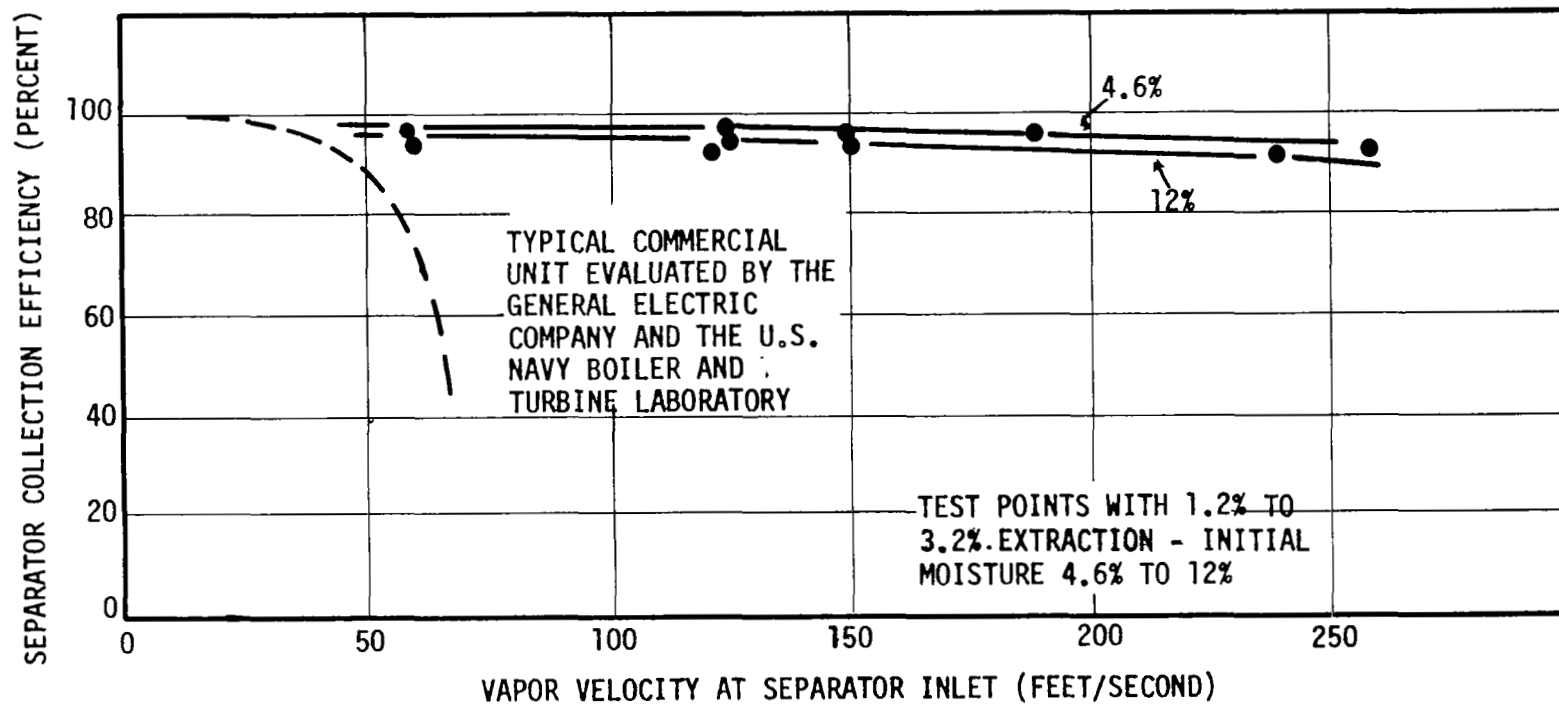


Figure 3.5-5. Measured Steam Performance of Eight-Inch Diameter Vortex Separator.

Company. As can be seen, the results indicate that effectivenesses higher than 90 percent, but also the bleed rates are somewhat higher than the 0.5 percent shown on the design summary.

### 3.6 SUMMARY OF KTA TURBINE FLUID DESIGN

The summary of the KTA turbine fluid design can be found in Table 3.6-1. The turbine has a blading efficiency of 82 percent and produces a blading power of 483 kilowatts. The maximum tip speed is 850 ft/sec and a maximum moisture content at stage inlet is 9.3 percent. The turbine has seven high pressure stages and four low pressure stages. It has a condensate removal device between the high pressure and low pressure turbine with an effectiveness of 80 percent, and it has an interstage condensate removal device in the tenth stage with an effectiveness of 25 percent.

TABLE 3.6-1

KTA TURBINE FLUID DESIGN SUMMARY

7 - STAGE H.P. TURBINE

POWER TO SHAFT 262. KW

VELOCITY DIAGRAM EFFICIENCY 85.3 %

STAGE INLET MAXIMUM CONDENSATE 8.2 %

INTERPOOL VORTEX SEPARATOR (4 Req'd)

(10.62 IN. x 2.28 IN. I.D.)

EFFECTIVENESS 80 %

PRESSURE DROP 0.34 PSI

BLEED VAPOR 0.5 %

4 - STAGE L.P. TURBINE

POWER TO SHAFT 221. KW

VELOCITY DIAGRAM EFFICIENCY 89.1 %

STAGE INLET MAXIMUM CONDENSATE 9.3 %

MAXIMUM TIP SPEED 850. FPS

INTERSTAGE CONDENSATE REMOVAL (TENTH STAGE)

EFFECTIVENESS 25. %

BLEED VAPOR 1 %

TURBINE

BLADING EFFICIENCY 82. %

BLADING POWER 483. KW



## 4.0 TURBINE MATERIALS

### 4.1 MATERIALS SELECTION

The selection of materials for the turbine has been based upon information from many sources. These include mechanical property data (principally from the NASA sponsored creep program on refractory alloys, Reference 4.1-1) bearing materials properties and behavior under vacuum and liquid potassium conditions (from the NASA sponsored bearing materials program, Reference 4.1-2, and from General Electric Company liquid metal bearing tests) and (from direct General Electric experience) general technology on (1) the fabrication, brazing, and welding of refractory alloys, (2) the alkali metal corrosion resistance of materials, (3) the preparation and evaluation of bimetallic joints, and (4) the manufacture and assembly to superalloy and refractory alloy turbine components.

As the result of Phase I effort, KDTZM was selected for all wheel alloys and, where possible, for all torque tubes and shaft sections. As will be discussed below, TZC has been included for the tie bolt. The weldable alloys, T-111 and Cb-1Zr, which were selected for structural parts in Phase I, were confirmed in Phase II. The compositions of these principal materials are shown in Table 4.1-1.

#### Nonrotating Parts

The weldable alloys, T-111 and Cb-1Zr, were selected for all

TABLE 4.1-1

ALLOY COMPOSITIONS OF PRINCIPAL TURBINE MATERIALS

Alloy	Density- lb/in <sup>3</sup>	Thermal Expansion (70-2000°F $\alpha \times 10^{-6}/^{\circ}\text{F}$	Composition - Wt %								
			Mo	Ta	Cb	W	Re	Hf	Zr	Ti	C
Wheel Alloys:											
TZC	0.363	3.3	Bal	-	-	-	-	-	0.15	1.25	0.15
KDTZM 1175	0.367	3.3	Bal	-	-	-	-	-	0.12	0.61	0.035
Containment/ Structural Alloys:											
T-111	0.604	3.9	-	Bal	-	8.0	0	2.0	-	-	-
Cb-1Zr	0.31	4.51	-	-	Bal	-	-	-	1.0	-	-

structural nonrotating parts. An attempt was made to use Cb-1Zr whenever stress, time, and temperature considerations would permit; all static components including ducts, nozzle diaphragms, and tip seals are to be made of T-111 from the turbine inlet duct through the outlet of the high-pressure stage. Although a portion of the first-stage casing might have been made from Cb-1Zr, this would have required a special bimetallic weld joint between T-111 and Cb-1Zr at the end of the second stage. Making this weld in a heavy section of the in-process case and then annealing and finish machining to size was an undesirable approach; accordingly, T-111 was selected for the entire casing for the high-pressure stage. Because of high vapor loads on the nozzles in the high-pressure stage, the hot strength of T-111 was needed. The nozzles in the high-pressure stage and the subseal surfaces were to be fabricated from T-111. All other structural nozzle, bearing housing, ducting, and casing components were to be made of Cb-1Zr. It was intended that many of these nonrotating parts be machined from bar stock or plate, or fabricated from smaller section bar stock, plate, or sheet by roll and weld techniques to produce the many different required shapes. Stress relief annealing of these welded components was intended immediately prior to finish machining; for example, the bearing housing would be fabricated in this manner from small and large diameter bar stock and plate into a welded and machined assembly.

The design data curves for the T-111 and Cb-1Zr alloys were given in the Phase I portion of the report.

#### Rotating Parts

While weldable alloys were considered as possible rotating components in Phase I, that study eliminated them from consideration because of their

lower strength-to-weight ratio as compared to the nonweldable molybdenum alloys. At the conclusion of Phase I, extrapolated creep life data on KDTZM-1175 indicated that this alloy should have a 0.5 percent three-year creep stress capability superior to TZC at temperatures up to 2090°F; accordingly, TZC was dropped from further consideration as a wheel material and all wheels in both the high- and low-pressure stages were to be made from KDTZM-1175 type of material. This same alloy composition would be used for shafts and torque tubes in an attempt to achieve similarity of materials and properties throughout the turbine; the turbine tie bolt would be made of TZC since reliable strengths have been developed in this material as properly processed round bar stock. The reliability of design data and the forging of these components will be discussed further below.

The materials design curves for the KDTZM-1175 type of material as revised at the beginning of Phase II are shown in Figure 4.1-1; the design curves for TZC were given in the Phase I section of this report.

### Bearings

In the turbine, which has an all refractory alloy liquid metal lubricant system and which operates at 900°F, a bearing and seals materials system is necessary which is sufficiently stable so as not to permit the transfer of carbon from the bearing material to colder portions of the system where adverse containment materials effects might be produced. In the bearing materials program, Reference 4.1-2, TiC + 10% columbium has demonstrated such carbon stability at 1100°F well above the intended bearing operating temperature; it has also evidenced very satisfactory sliding friction characteristics both in dry vacuum and under liquid

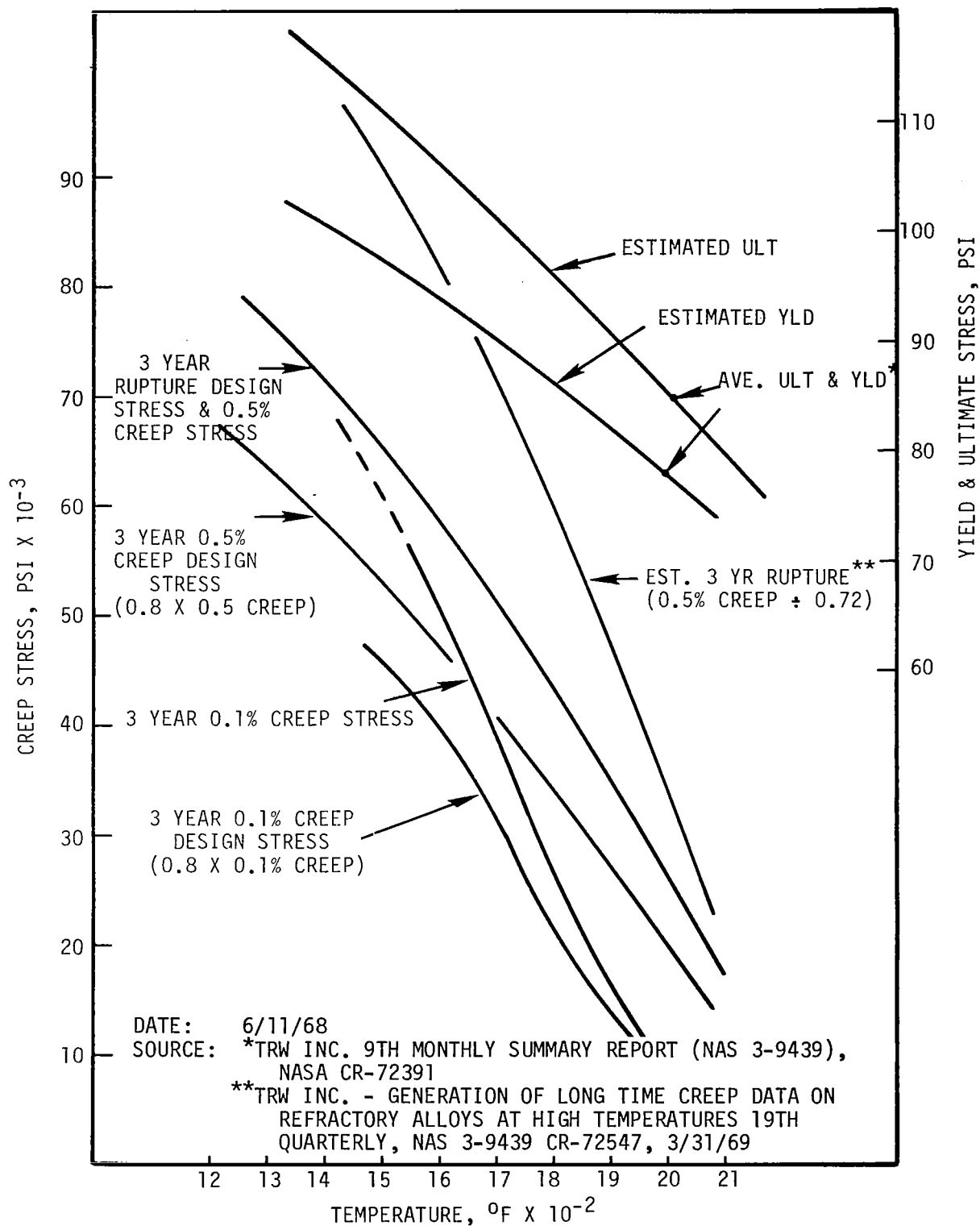


Figure 4.1-1. KDTZM Materials Design Curves.

potassium. Its principal disadvantage may be a short-range one which can be overcome by manufacturing experience: the material has not yet been produced in sufficient quantities and sizes to offer convincing proof of its reproducibility without various forms of distortion, cracking, and/or uniformity of composition and properties. Nevertheless, it has a very good potential and must be considered as the first choice for turbine bearings and for liquid metal seals.

Carboloy 907 should also be considered as a potential alternate to the above selection. Both materials are commercially available, and the processing and reproducibility have been well established. The composition of Carboloy 907 has been evaluated in a NASA sponsored bearing materials program where its resistance to carbon transfer was good at 800°F, but showed some instability at 1100°F.

Excellent full-scale liquid metal bearing tests have been performed at temperatures to 800°F using the Carboloy 907 composition, Reference 4.1-3. Additional tests are contemplated; as a means of determining the highest utility temperature for this proven bearing material, such tests should be run at 900°F for evaluating the possibility of carbon transfer to refractory metal specimens in the cold zone. For comparative purposes, the compositions and the extent of evaluation of these materials under contract NAS3-2534 are shown in Table 4.1-2.

TABLE 4.1-2

TYPICAL BEARING MATERIALS EVALUATIONS

<u>Designation</u>	<u>Composition</u>	<u>Extent of Work*</u>		
		<u>Individual Tests**</u>	<u>Dry Sliding Friction</u>	<u>Liquid Potassium Friction</u>
TiC+10Cb	83.6TiC-9.54Cb- 5.85WC-0.73Co- 0.33Fe	x	Vs Mo-TZM & TiC+10Cb	Vs TiC+10Cb
Carboloy 907	74WC-20TaC-6Co	x	Vs Mo-TZM & 907	No

---

\* Based on NAS 3-2534

\*\* Such as Hardness, Stability, Corrosion, Thermal Expansion, Compressive Strength, Elastic Modulus, etc.

In the stainless steel containment system for the generator liquid metal bearings, where the maximum temperature is only 700°F, Carboloy 907 bearings have demonstrated, in full-scale bearing tests, that they should be very sufficient.

Because of the relatively high centrifugal stresses in the larger diameter thrust bearings, the lower density of the TiC type materials for thrust bearings (as contrasted to the higher density of the WC type bearings) would tend to favor the use of TiC type materials for thrust bearings. Meager information on TiC + 10% Cb indicates its strength, as determined in a transverse rupture test, is only  $65 - 75 \times 10^3$  psi at room temperature; this contrasts with transverse rupture values of  $250 - 325 \times 10^3$  psi for WC-6Co materials and  $150 - 175 \times 10^3$  psi transverse rupture strength for the nickel-molybdenum bonded TiC cermets on which data is available. In order to finalize detailed designs, some additional testing of the thrust bearing materials at room and elevated temperatures will be necessary in order to determine the available strengths of these lower density TiC bearing materials.

#### Rubbing Materials

In the high-pressure turbine stage, T-111 honeycomb structures have been selected for the vapor phase seals at the turbine tips and interstage areas. In a similar fashion, Cb-1Zr would be used in the low-pressure turbine stage. The ability of this type of honeycomb structure to deform readily in the event of a rub is unquestioned. However, little is known regarding the possibility of galling and metal transfer in the rubbing contact of



tantalum and columbium alloys in vacuum or in potassium at turbine temperatures. Because of the ductility and relatively low hardness of the tantalum and columbium alloys, it must be presumed that some gross metal transfer might occur; rubbing tests would be of value if they were to simulate the type of rub conditions and the types of geometric conditions which may exist in an actual turbine.

The relatively small diameters and absence of any significant creep at the liquid metal bearings make the occurrence of gross rubbing much less likely than at the turbine tips. In these areas, hard, bearing type materials with little galling tendency will be used. TiC + 10%Cb will be used in the turbine liquid metal seals and Stellite 6B (1.1C-55Co-33Cr-6W-3.5Fe-3Ni) will be used in the generator.

#### Bimetallic Joint

In the transition of structural materials between the turbine and the generator, a nonrotating bimetallic joint about 3 1/2 inches in diameter will be required. A joint of this diameter between Cb-1Zr and Hastelloy C (for example) is well within the range of present technology for both brazed and coextruded joints. A brazed joint has been selected based upon the demonstrated excellent thermal shock and thermal cycling resistance of tantalum-stainless steel joints when quenched in mercury from 1300°F, Reference 4.1-4. Currently, improvements are being made in ultrasonic inspection techniques to validate the quality of the joints after brazing, Reference 4.1-5.

## 4.2 DESIGN DATA RELIABILITY

In Phase I the importance of reliable design data was stressed and the nature and risk of the extrapolations made at that time were cited. The decisions made at the end of Phase I corrected some of these extrapolations and original estimates. In some cases, the need for additional data was eliminated, but, in general, Phase II also confirmed the need for more mechanical property documentation in order to assure either data reliability or component performance. The following instances illustrate this.

The absence of stress relaxation data on interstage bolting materials such as TZC and TZM prevented the development of ultimate designs of bolted turbine wheels. Such design data would have been essential had a bolted wheel design been selected. The use of a single tie bolt in the current design eliminates the pressing need for stress relaxation design data since only the hottest portion of the bolt is subject to stress relaxation. Inasmuch as the major portion of the tie bolt is elastically loaded and acts as a spring, the hottest portion of the tie bolt near its head is loaded under practically constant load rather than constant strain. Consequently, the creep and rupture characteristics of the TZC tie bolt are now more important; while stress relaxation information would be desirable, it no longer rates first-order consideration.

The reliability of mechanical property data on the KDTZM-1175 type molybdenum alloy wheel material is of most concern. The available 0.5 percent creep data represents one heat and one forging configuration which are shown in Figure 4.2-1. This creep data represent tests performed at 1600°F and higher; however, none of the specimens were stressed

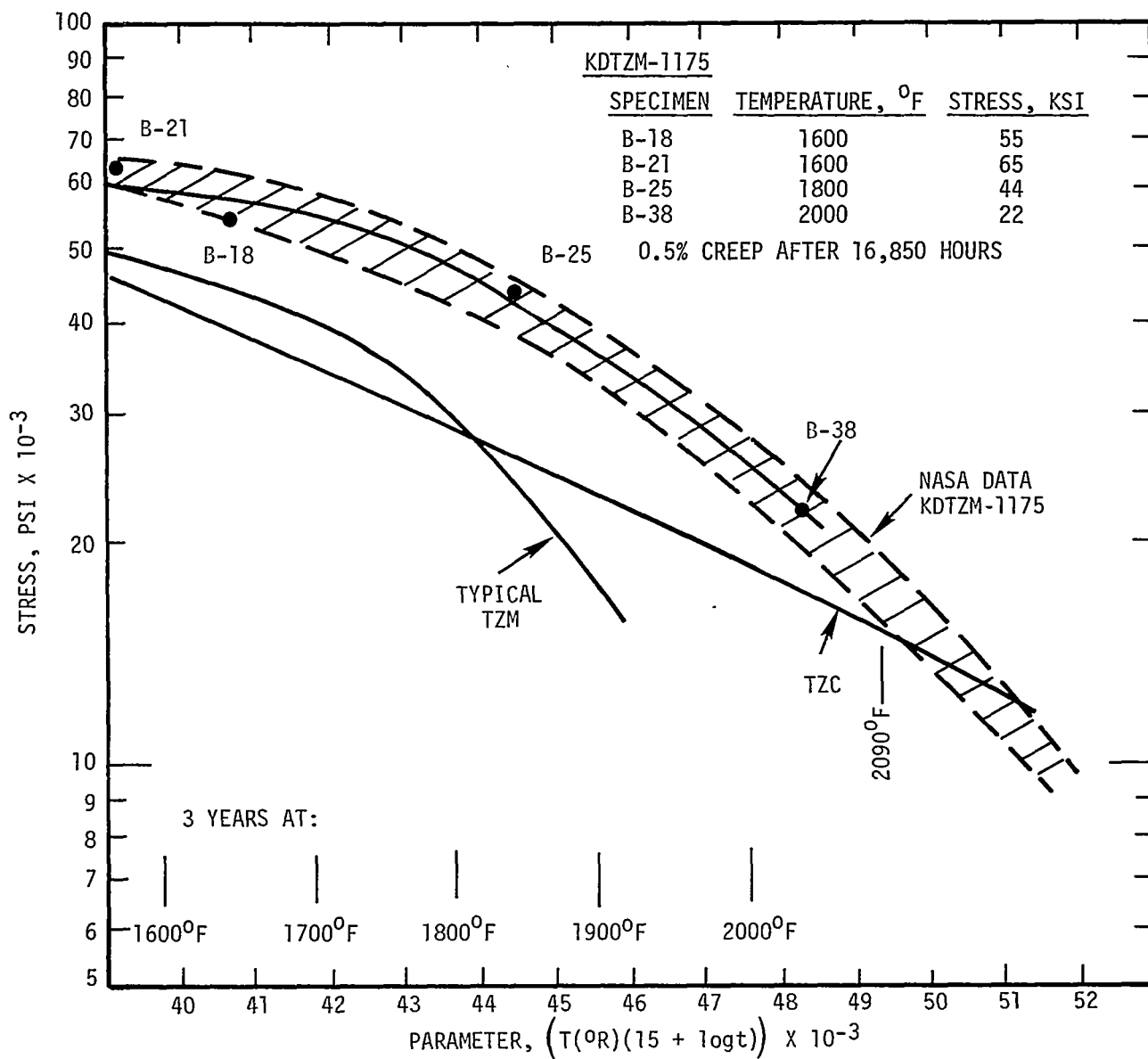


Figure 4.2-1. 0.5% Creep Strength of TZM, KDTZM-1175 and TZC.

to produce rupture. The scatter band shown in the Figure indicates the anticipated scatter in the 0.5 percent creep data and formed the basis for the Phase II design effort. While existing and extrapolated data of the above type do present a reasonable basis of preliminary designs, additional confirming data is required for reliability purposes prior to designing component parts for manufacture. More data are being obtained under existing NASA contracts.

A limited amount of testing is required of actual KDTZM-1175 type forged wheel components prepared for eventual turbine construction.

This testing should include:

1. Limited tensile tests at various temperatures to develop 0.2 percent yield strength, ultimate tensile strength, and ductility plots as a function of temperature.
2. Limited notched tensile and impact tests in the radial and axial direction of the wheel forging at various temperatures to determine ductile-to-brittle transition temperatures.
3. Limited short-time creep and rupture tests at various temperatures to establish parameter curves showing the stress-parameter relationships for various levels of creep and for complete rupture and to define that parameter which best fits data determined at all temperatures.
4. One or two long-time creep tests to verify the reliability of extrapolated short-time parameter plot data to the long-time conditions.

As can be seen from Figure 4.2-1, the 0.5 percent creep data at the beginning of Phase II indicate a superiority of the KDTZM-1175 type alloy over TZC at temperatures to 2090°F based on extrapolation of tests then in progress. Extrapolated data assumes a constant second stage creep rate which in itself makes the reliability of the data questionable. An example of this is the superiority of KDTZM-1175 type alloy was reduced below 1980°F by an increased second-stage creep rate in this specimen.

Another example of the uncertainties introduced into data because of necessary assumptions in data extrapolation is shown in Figure 4.2-2. The original 0.1 percent creep data was derived from an observed 65 percent (approximate) relationship between the 0.1 percent and 0.5 percent creep data for KDTZM. The original 0.1 percent creep design curve was then based upon 65 percent of the 0.5 percent creep curve. It was appreciated that the data was probably too conservative at the lower temperatures, but the magnitude of the error in estimation was not known. Data later supplied by NASA indicated this curve for 0.1 percent three-year creep stress versus temperature was much steeper; as the result of this data revision, additional 0.1 percent creep strength was available below 1790°F, but the available strength was significantly reduced above this temperature, and the first-stage wheels became necessarily heavier than when the earlier data was used.

Although there is sufficient material property data available in this developmental alloy (KDTZM-1175) to complete an acceptable design, the above comments indicate the necessity for a larger quantity of test data of a diverse nature from which to increase the reliability of

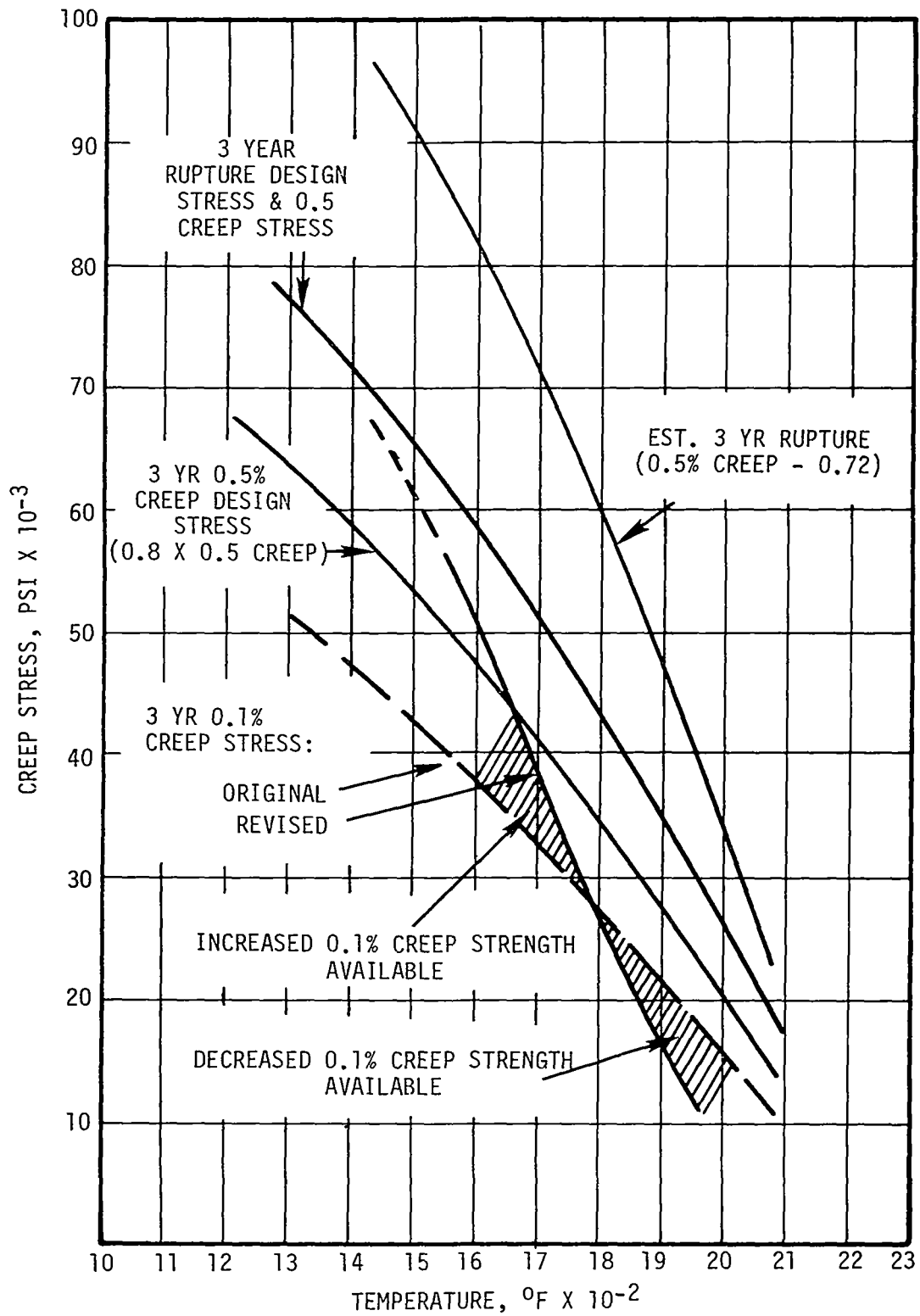


Figure 4.2-2. KDTZM - 1175 Design Data.

the design curves.

#### 4.3 FORGINGS

The development of the superior high-temperature strength properties found in KDTZM-1175 was undoubtedly associated with the special processing which this material received, as will be described below. Since the original processing was applied to thin pancake wheel forgings, it is doubtful if similar processes can readily be developed for alternate forms such as shafts or tie bolts.

##### Shafts

Since the shafts are large in diameter, they must be made from extruded and partially rolled or forged round billet. Additional forging work can be imparted to the upset ends of the sections of the shafts which require flaring. However, it is doubtful if the type of processing required to achieve the shaft shape will provide the amount of hot work in the appropriate temperature range to result in KDTZM-1175 type properties. Since these components do not require high creep strength, inability to reproduce the KDTZM-1175 type strength will be of no serious consequence.

##### Tie Bolt

It is essential to the success of the tie bolt that it develop the highest possible creep strength at the highest turbine temperatures. Processes have been reliably developed, Reference 4.3-1, for forming

1 1/2-inch-diameter TZC bar stock with good room temperature ductility and rupture strength typical for TZC. An upset forging operation will be required in order to gather enough material for the bolt head; this operation can be performed by resistance heated, upset forging operations similar to those used to form a tie bolt for the three-stage potassium vapor turbine, Reference 4.3-2. The reliability of this approach as contrasted to the uncertainties of reproducing the strain age processing in KDTZM recommend the use of TZC for tie bolts rather than KDTZM.

### Wheels

The forging process by which the original KDTZM-1175 disc was prepared is shown in Figure 4.3-1 along with two additional suggested processes. The original process involved: first, ingot breakdown to 6 1/2-inch diameter and subsequent recrystallization at 2800°F; second, hot forging to 4 1/8-inch diameter at 3400-2800°F and aging at 2950°F (the forging operation was performed in the In Fab room at Universal Cyclops); and third, upset forging a 4-inch-diameter x 4-inch-high billet through 81.2 percent reduction in height from 2800°F to 2160°F to produce the worked structure and final strain age precipitation which is believed to be responsible for the good creep strength, hot hardness, and resistance to recrystallization which has been observed in this material.

It has recently been determined, Reference 4.3-3, that seven additional, much thicker wheel forgings, 1 5/8-inch to 1 3/4-inch thick by ten inches diameter, were processed in a similar fashion for use in the SNAP-50 - SPUR program. Difficulty was encountered in forging from 2780°-2850°F because of the necessary height-to-diameter ratio of the forge billet. (The forge billets were four inches in diameter x 8 1/4



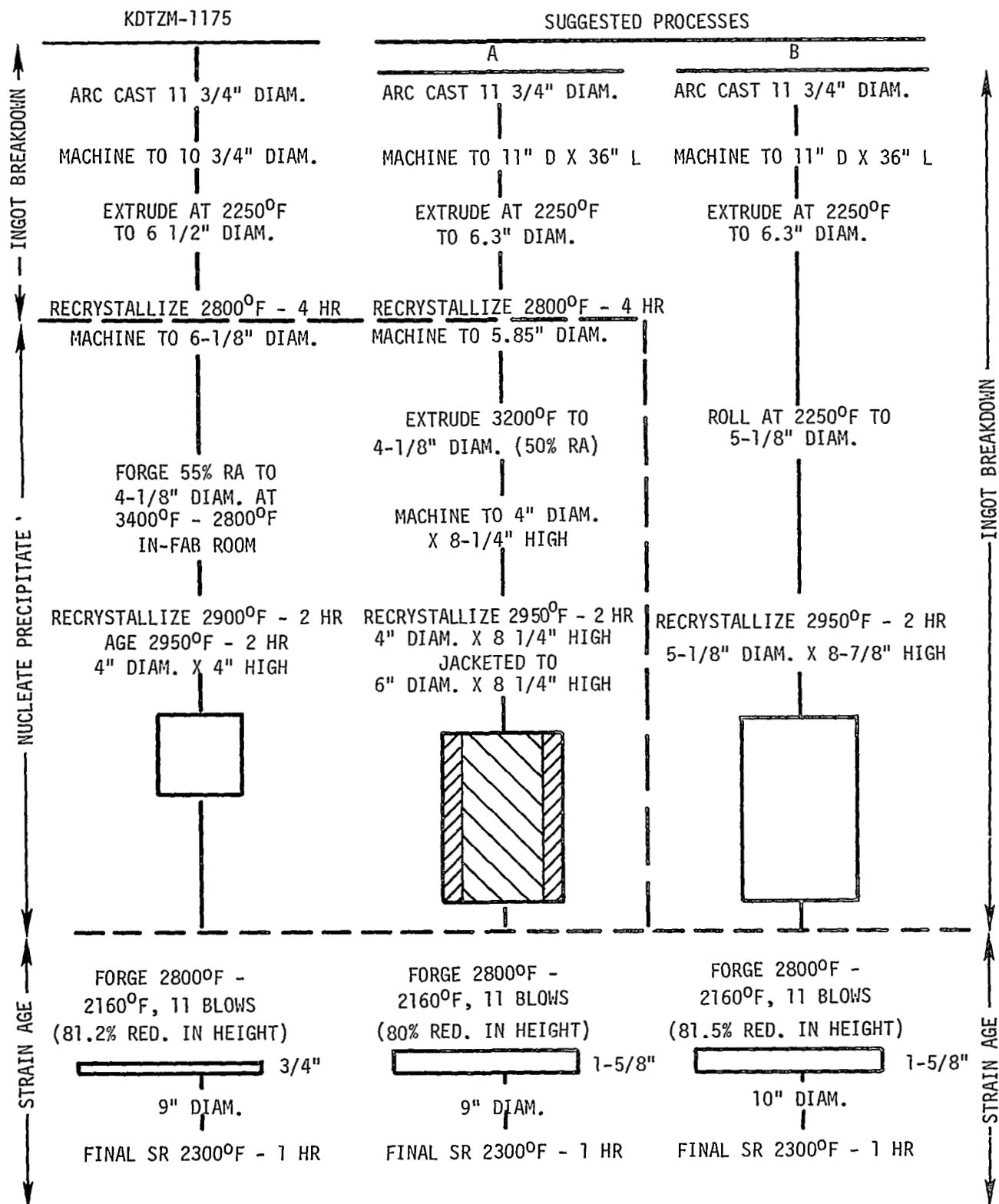


Figure 4.3-1. Wheel Forging Processes

inches high.) The high upset ratio was necessary to achieve a thicker pancake forging and, also, to achieve similar percentage reductions in height as in the original KDTZM-1175 pancake. As many as 31 and as few as 17 blows were required to forge the billets; blows were light at first until the forging was reduced to five inches in height and then heavier blowers were used to reduce the pancake to final thickness. Finish forging temperatures varied generally from 1870°F to 2100°F; naturally, the forging process was not exactly the same as that for the original high-strength forging from heat KDTZM-1175, and attests to the difficulty of exactly reproducing the original process. The possibility should be investigated of procuring and of metallurgically and mechanically evaluating these SNAP-50 - SPUR forgings prior to initiating a component forging program.

The advantages of 3400°F hot forge processing as contrasted to conventional 2400°F forging were stressed by C. R. Mueller of Universal Cyclops; he contended that the 3400°F forging resulted in the formation of fine carbide dispersions, some or all of which, even after subsequent recrystallization at 2950°F for two hours, remained as dispersed nucleating sources for further precipitation during final pancake forging at 2800°F-2160°F. Mr. Mueller cited Universal-Cyclops work on the Molybdenum Sheet Rolling Program, Reference 4.3-4, in which recrystallization resistance and hot hardness were favorably affected by the 3400°F forging treatments as compared to the 2400°F forging treatment. It was not directly evident from the report, however, that the same recrystallization resistance and hot hardness improvements could not be achieved by forging directly from much lower temperatures, such as 2800°F and avoiding, completely, the 3400°F forging step.

A simple set of swaging experiments on KDTZM-1175 type molybdenum alloy composition could be performed to determine if the hot hardness in the final product or if the in-process microstructures were affected by the insertion or deletion of this 3400°F forging step in the process.

The necessity for determining the essential nature of the 3400°F forging step is evident when the high costs are considered of opening up the In-Fab room for limited KDTZM-1175 type forging operations.

It has been suggested, Reference 4.3-5, that a plastic type shelter, erected over a commercial source forging hammer and equipped with induction heating facilities, argon atmosphere, and argon breathing apparatus, could be used for the forging facility in lieu of the In-Fab room.

Other alternative forging processes which bear consideration are indicated as processes A and B; their process outlines are located adjacent to the original process outline in Figure 4.3-1.

In Process A, an extrusion process is suggested to replace the In-Fab room forging operation. Of necessity, a large reduction occurs in the forging billet diameter during the 3200°F nucleate precipitation process. This reduction would occur in the In-Fab room of the original process or in the extrusion step shown in process A. Even starting with a large ( 8 1/4 inch) initial billet height for reduction purposes, the molybdenum forging billet after the 3200°F process step has a large height-to-diameter ratio and is very susceptible to buckling during pancake forging. This is one of the factors which caused problems in the forging of 4-inch-diameter x 8 1/4-inch-high KDTZM-1175 billets which were intended to make 1 3/4-inch-thick pancake forgings for the SPUR - SNAP-50 program.

To eliminate the buckling problem, it is suggested that the slender forge billets from Process A be jacketed in stainless steel as indicated in Figure 4.3-1 to permit rapid strain age forging.

A final process for preparing thick pancake forgings (shown as Process B in Figure 4.3-1) would eliminate the reduction in billet diameter required by the nucleate precipitation process at 3400°F. Instead Process B would upset forge an unjacketed but larger diameter molybdenum alloy billet to avoid buckling and would rely upon strain aging during the pancake forging operation to develop material strength.

A final factor which must be considered in forging pancake forgings of greater final thickness is the larger mass of material which must be forged and the effect of this mass on the cooling rate during forging. (It is assumed that rapid cooling and rapid working are necessary to reproduce the strain-aged precipitate as it occurred in the original forging.) If a significant metallurgical effect is evident here, forging trials may indicate that the original strengths are simply not attainable because of the kinetics of the strain aging process.

It is evident that the factors affecting the forging process must be better understood in terms of their influence upon final mechanical properties of the forging.

In summarizing the prospects for duplicating the original high-strength KDTZM-1175 forging, the following observations are offered:

1. Large forging reductions appear necessary for strain age precipitation.
2. Thicker forgings will result in:
  - (a) greater upset distances,
  - (b) possible forge billet buckling,

- (c) the need for larger diameter billets or jacketing of billets,
  - (d) massive forgings and slower cooling of the billet during forging precipitation.
3. The need for 3400°F nucleate precipitation requires confirmation or rejection.
- (a) Are fine precipitates nucleated in the process and can they be observed metallographically?
  - (b) Are alternative processes, which eliminate this step, equivalent in terms of final mechanical properties, hot hardness, and microstructures?
  - (c) What are the process variation limits?
4. Simple, small-scale processing studies should be undertaken to explore metallurgical structures and hot hardness as a function of process history.
5. Unless the process control limits are understood, variations in properties can be expected in large-size forgings.

#### 4.4 MATERIALS SUMMARY

1. The materials property data upon which the selection of materials and the preliminary design configurations have been made are generally adequate, but the extrapolations of limited data and the uncertainty of the reproducibility of some data require that further design strength data and other necessary property data be acquired on actual hardware component materials.

2. The bearing materials for the generator are relatively well proven by full-scale liquid metal bearing tests; the same confirming test experience must be gained on the TiC + 10%Cb bearing material after its reproducibility and tensile strength properties have been more adequately determined and integrated into the bearing design.
3. The preparation of the bimetallic joint required in the turbine itself, represents no significant change from the present state of the art and should be readily achieved.
4. The processes for the preparation of raw stock and the forging of shafts and tie bolts are sufficiently well developed as to be capable of producing materials with the required strength levels; however, the wheel forging process and its ability to produce the required properties in the forging sizes necessary are still unproven. Simple process studies in this area and the associated material properties are necessary before final design curves can be prepared.

#### 4.5 REFERENCES

- 4.1-1 J. C. Sawyer and E. A. Steigerwald, "Generation of Long-Time Creep Data on Refractory Alloys at Elevated Temperatures," Contract NAS 3-2545, TRW Equipment Laboratories, Cleveland, Ohio.
- 4.1-2 R. G. Frank, "Materials for Potassium and Lubricated Journal Bearings, Final Report Volume I - Summary," General Electric Report No. GESP-100, NASA Contract NAS 3-2534, Cincinnati, Ohio.
- 4.1-3 M. O. Schnetzer, R. J. Rossbach, W. D. Richards, "Development of Liquid Metal Lubricated Bearings and Seals for Space Power Turboalternator, General Electric Report No. GESP-52, July, 1968.
- 4.1-4 S. R. Thompson and J. Holowach, "SNAP-8 Mercury Thermal Shock Test of Bimetallic Joints," General Electric Report No. GESP-45, NASA Contract NAS 3-10610, Cincinnati, Ohio.
- 4.1-5 "A Proposal for Development of Optimum Brazing Techniques for Tantalum/Type 316 Stainless Steel Tubular Transition Joints," General Electric Response to Proposal GENSP-E-69-050, NASA RFP C-406914Q, Cincinnati, Ohio.
- 4.3-1 H. E. Nichols, R. W. Fink, and W. F. Zimmerman, "Three-Stage Potassium Vapor Turbine - Fabrication and Assembly," NASA Contract NASA CR-72051, Cincinnati, Ohio.
- 4.3-2 Ibid
- 4.3-3 W. McCue, Steel Improvement and Forge Company, Personal Communication, May 3, 1968.
- 4.3-4 L. M. Bianchi, W. A. McNeish, R. G. McLaughlin, "Molybdenum Sheet Rolling Program," BuAer Contract NOas 59-6142-C, October 22, 1964, p. 122, 159, 160.
- 4.3-5 R. Davies, NASA, LRC, Personal Communication, August 8, 1968.

190 psia (total) to 39 psia across the high pressure turbine  
26 psia to 5 psia across the low pressure turbine  
2085°F to 1585°F across the high pressure turbine  
1485°F to 1245°F across the low pressure turbine

- The turbine wheels are joined by means of curvic couplings in the torque tubes and cone shafts, retained by the axial force of a central tie bolt. While interstage leakage can occur, the aft end of the tie bolt is sealed to stop leakage.
- Labyrinth seals opposing honeycomb are used to seal against leakage beneath nozzle diaphragms.
- Honeycomb opposes the blade tips to minimize leakage with relatively low possibility of blade fracture if a rub occurs.
- The rotor blades are integral with the wheels for all stages except stage ten.
- Stage ten has shrouded buckets to facilitate moisture removal from that stage. Because of manufacturing complexity, dovetailed non-integral blades are required.
- Conical stub shafts are utilized to reduce the rotor diameter from that of the torque tubes to that of the bearing journals.
- In both the forward and aft bearing areas, TiC + 10% Cb is the bearing and seal material (static and rotating components). The bearings are tilted-pad type, with four pads. Screw seals at each end of the bearings control leakage of the potassium lubricant, which is supplied at 900°F. Proximity probes are included to monitor bearing position.
- A thrust bearing capable of absorbing either forward or aft loading is present in the aft bearing area.
- A flexible diaphragm coupling joins the turbine and the alternator. This type of coupling does not require lubrication.



- Some typical geometrical dimensions of the turbine are:
  - 36.7 inch total rotor length
  - 5.710 - 7.808 inch diameter across blade tips in the high pressure turbine
  - 9.846 - 10.053 inch diameter across blade tips in the low pressure turbine
  - 4.5 inch diameter of high pressure turbine interstage labyrinth seal tips
  - 3.0 inch diameter forward bearing
  - 2.5 inch diameter aft bearing
- An axial inlet duct is used.
- The casing components around the turbine wheels are horizontally split and welded to forward and aft flanges and at the split lines.
- The high pressure casing is externally waffled with rings and stringers. It is of T-111 Ta alloy in order to have sufficient strength as well as weldability. Internal cavities are avoided. The casing locates the nozzle diaphragms and seal rings and is their attachment body.
- The low pressure turbine casing is an assembly of plates and cones, split by the moisture extraction nozzle. Its material is Cb-1Zr, which provides adequate strength and weldability.
- The inlet and outlet nozzles are integral with the ducts and scrolls.
- The fluid path between the high pressure and low pressure turbines is split into four crossover ducts which contain moisture extraction devices. These ducts deliver the higher quality vapor to the low pressure turbine inlet scroll.
- The turbine forward bearing/seal housing and a pierced-cone support structure join the high and low pressure turbines.

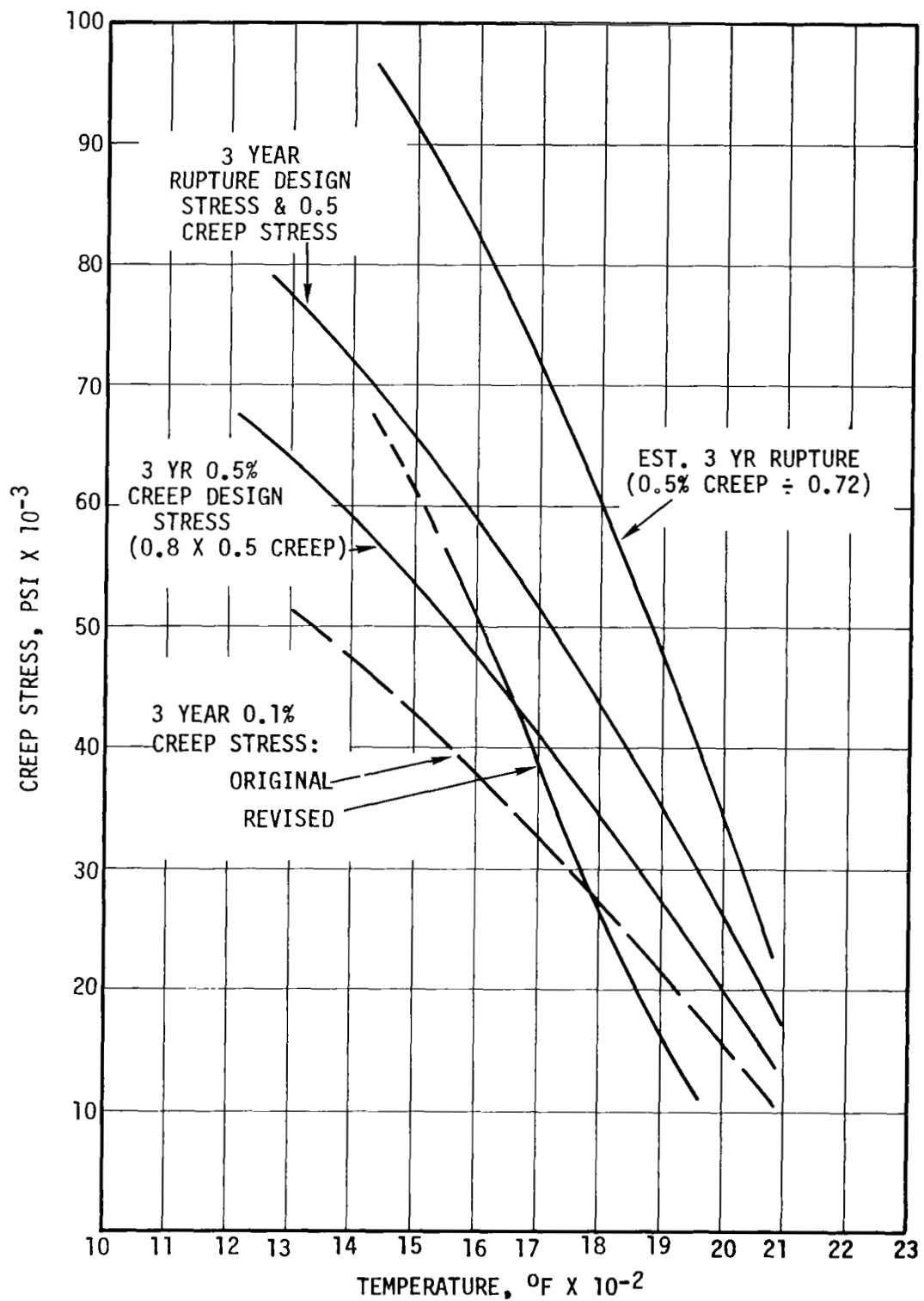


Figure 5.2-1. KDTZM-1175 Design Data.

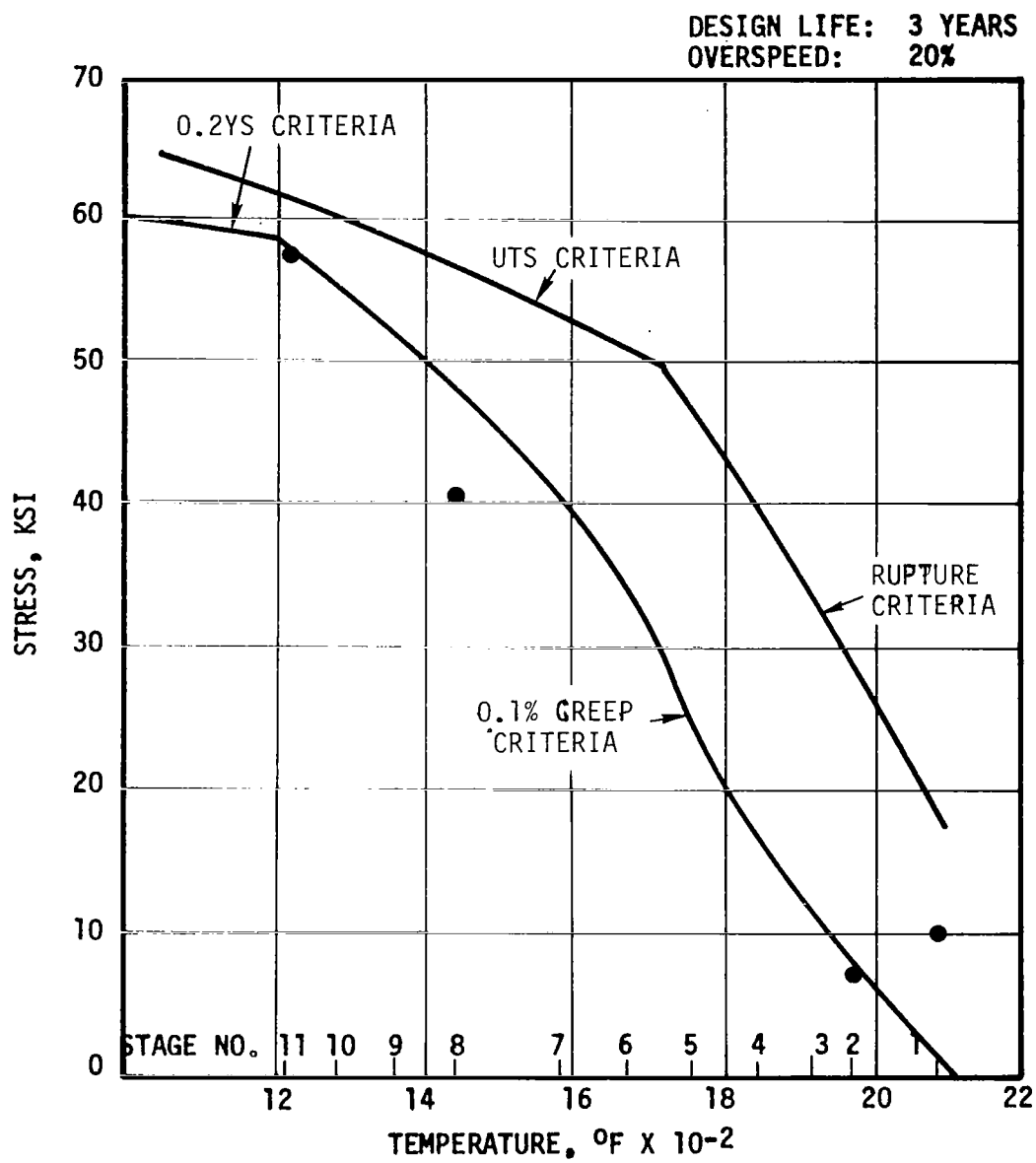


Figure 5.2-2. Allowable Stress Design Curves for KDTZM-1175 Rotors.

### 5.3 TURBINE WHEELS AND BUCKETS

#### Wheel Stresses

The basic design criteria for wheel and bucket design are stress and deflection. Where more than one principal stress occur at the same point, the stresses are combined according to the Hencky-von Mises "minimum energy of distortion" criterion into an effective stress as reported in the Phase I discussion on this subject.

The wheel deflections due to loads and stresses calculated by the ELASTIC DISK or ROTOR computer programs are short-term effects. Their magnitude is much less than the thermal and long-term creep deformations, which will be of primary interest.

The general mechanical design computational approach to turbine wheel analysis is to treat them as constant-stress disks with corrections made for central holes, thickened rims, torque tubes, etc. After screening possible turbine designs with the general method, the well-developed ELASTIC DISK computer program is used to determine wheel radial, tangential, and effective stresses with high accuracy.

The material design curves show that all stages are creep-limited rather than limited by short-term overspeed effects or by onset of rupture. Despite the lower centrifugal loading of small radii and blade heights, the earlier stages are the harder ones to fit into the desired limitations. Stage one of the chosen design, for instance, would be about 100 inches thick at the hub if the average stress level is to be two ksi in a wheel with hole. Therefore, the desirability of holding wheel stresses below the level of three-year 0.1 percent creep stress was subjugated to the desires for a more compact

and light weight design with lower flow losses. The penalty of a larger initial tip clearance requirement is accepted.

The first estimate of the required wheel neck thickness is the thickness calculated by the general mechanical design computer program previously described for ideal disks without central holes. An empirical correction factor based upon experience with prior ELASTIC DISK wheel analyses is utilized. The radius of the neck section of the wheel is calculated by forcing a cubical wheel thickness function to pass through the wheel rim corners which exist at the thickness of axial chord +0.1 inch.

The contour of the wheel below the neck section is established by assuming a 2.5 power corrector to be applied to the thickness at each radius which was calculated for the ideal disk case. The thickness calculated at 0.7 inch radius is used as the constant hub thickness from 0.5 - 0.7 inch radius.

The Data Net computer program IDEALW was written to make the above calculations at steps of 0.05 inch, and to calculate the wheel weight, inertia properties, and shear area.

This procedure is required because the advanced wheel stress analysis program can only analyze the geometry which is input, and cannot design the wheel directly. When the estimated contour does not produce a completely satisfactory stress pattern, the process must be repeated with a new empirical correction factor based upon the latest stress analysis.

The effective stresses in one typical wheel, stage two, are shown by Figure 5.3-1. The goal of 0.1 percent creep in three years

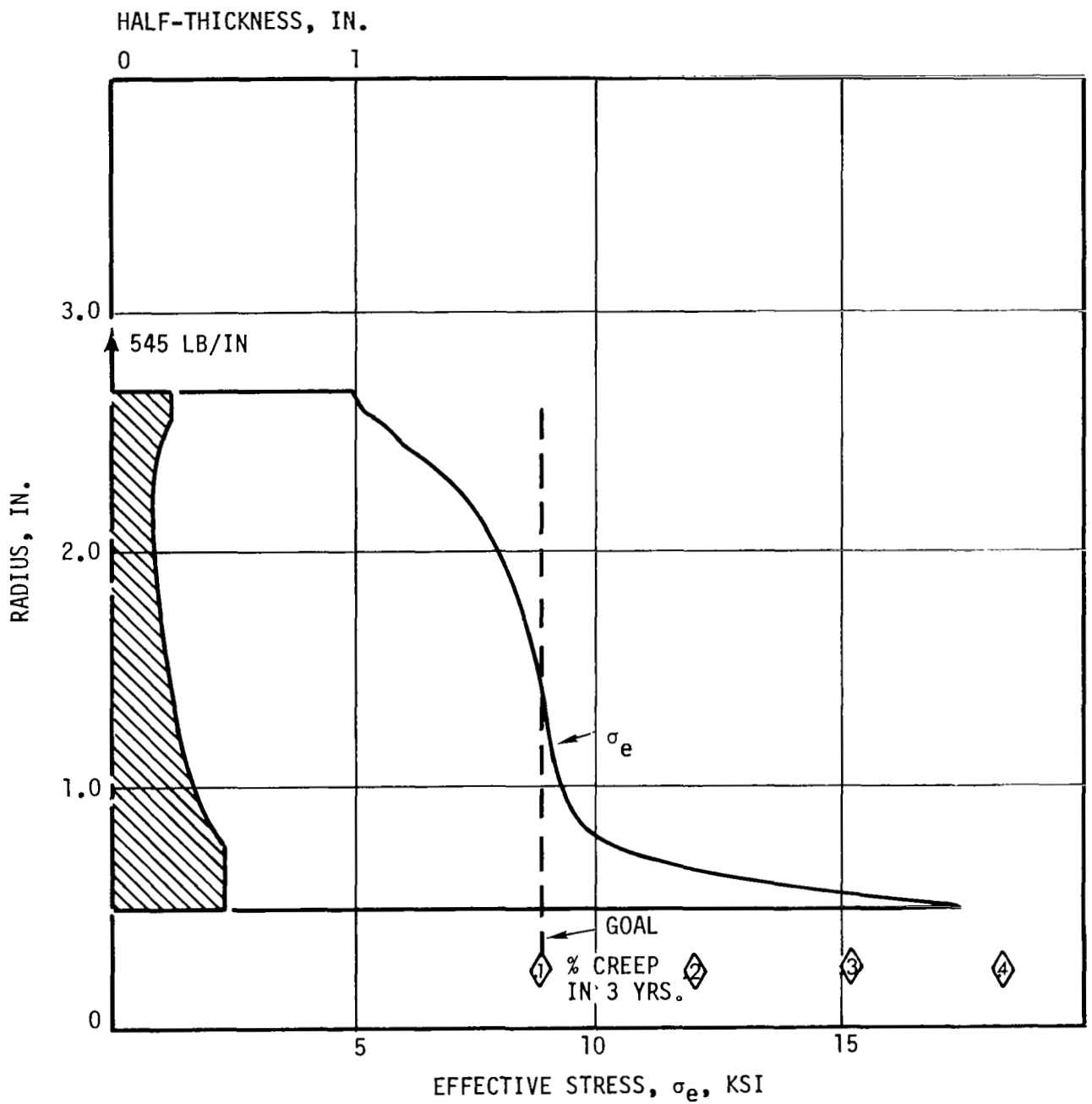


Figure 5.3-1. Effective Stresses in Stage 2 of 7+4 Turbine at 19,200 rpm.

is indicated, and basically is met over the majority of the radial extent of the wheel. The shape of the effective stress curve for this wheel is characteristic: low stress at the wheel rim because the radial stress is zero, and high stress at the hub bore because the tangential stress tends toward infinity, even though the radial stress is zero. The most efficient design would have a constant effective stress equal to the allowable stress, but the previous considerations will always prevent its achievement. The peak bore stress approaches the three-year 0.4 percent creep stress but is not a matter of concern. As creep develops in the bore, the fibers radially outboard are stressed, until an equilibrium condition exists at which the bore stresses are decreased while others are increased. This design is considered acceptable, but could be improved by adding minor amounts of material to decrease the bore stresses.

The designations of three-year creep rates on the above figure and others following are linear interpolations between the previously established three-year 0.1 percent and 0.5 percent design creep rates.

The effective stresses in another typical wheel, stage eight, are shown by Figure 5.3-2. The characteristic pattern is present, with the stress level of almost the entire wheel well below the three-year 0.1 percent creep stress. The reason this occurs is that a lower limit of 0.100 inch was placed on the wheel neck thickness, so that undiscovered small material or fabrication discrepancies do not cause major increases in stress. Although the peak bore stress is only slightly greater than the 0.1 percent creep stress, it is a matter of some concern because the allowable rupture stress (overspeed criterion) is very little higher than the bore stress. This design is considered acceptable, but

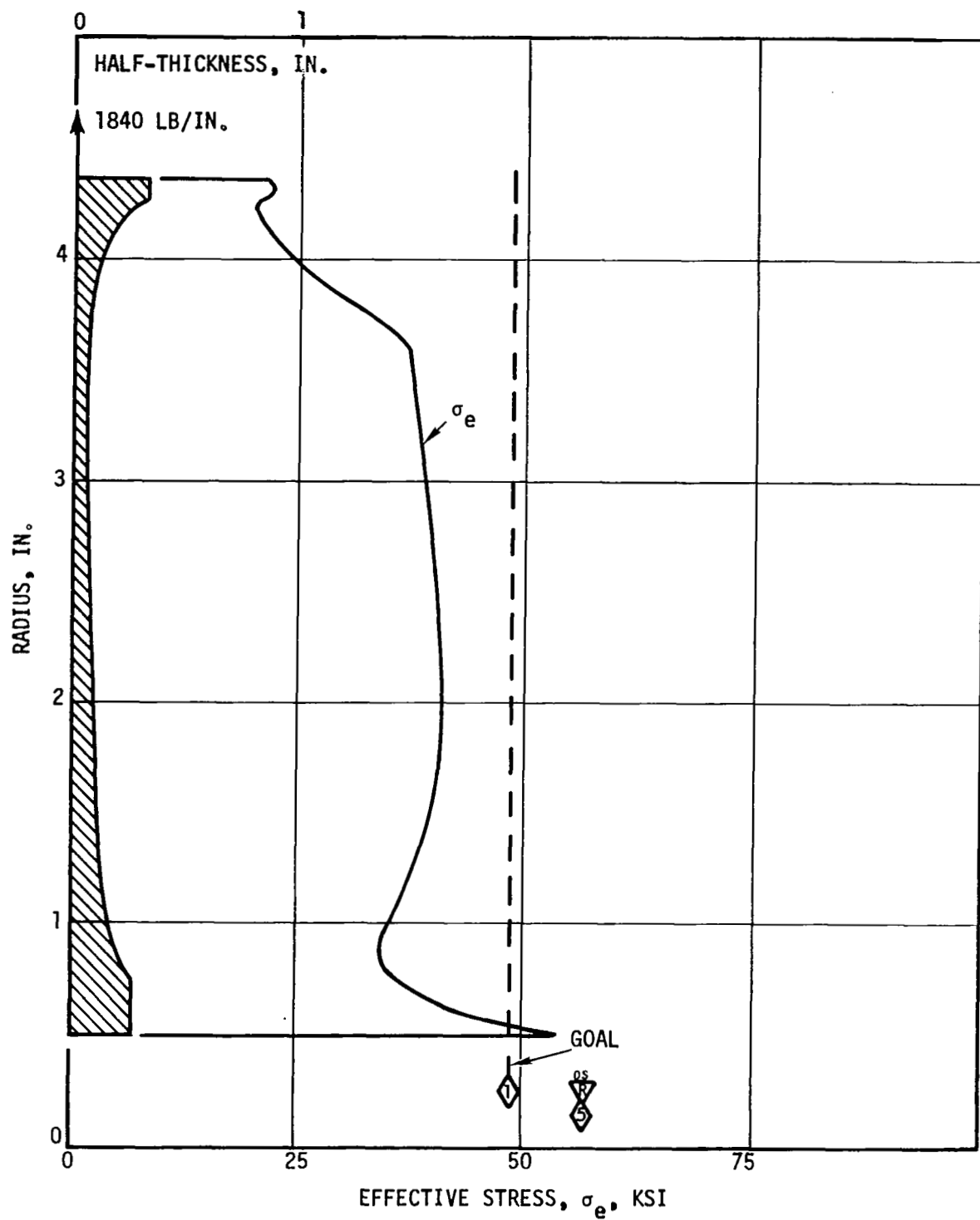


Figure 5.3-2. Effective Stresses in Stage 8 of 7+4 Turbine at 19,200 rpm.



the next iteration could decrease the bore stresses and lower the average tangential stress level to a smaller fraction of the available rupture stress.

The effective stresses in the only wheel with dovetailed blades, stage ten, are shown by Figure 5.3-3. This design is not considered acceptable without further iteration because the effective stresses exceed the desired three-year 0.1 percent creep stress and overspeed rupture criterion over significant areas. However, the weight and inertia properties of this design will be changed only slightly by redesign, and are, therefore, useable as calculated. It is necessary to conclude the turbine wheel studies when an acceptable solution is closely approached, because of the complexity of the calculations involved. This wheel design, for instance, was analyzed by the approximate methods of the general mechanical design computer program. A special time-sharing computer program was written to estimate the shape of the wheel which is required. An ELASTIC DISK analysis was made, with unacceptable results, and several more refined estimates of geometry were made, followed by further detailed ELASTIC DISK analyses. The further refinement of wheel analyses to their ultimate conclusion delays to an unacceptable degree the analyses of other components.

A synopsis of critical wheel mechanical design parameters for these and other stages is listed in Table 5.3-1. It shows similarity in the stress pattern of stages one (plot to be shown) and two, with no distinct peak in the effective stresses except at the bore. Stages 3 - 11 have stress patterns similar to those shown for stages eight and 11, with a stress peak between the wheel neck and the bore and a stress

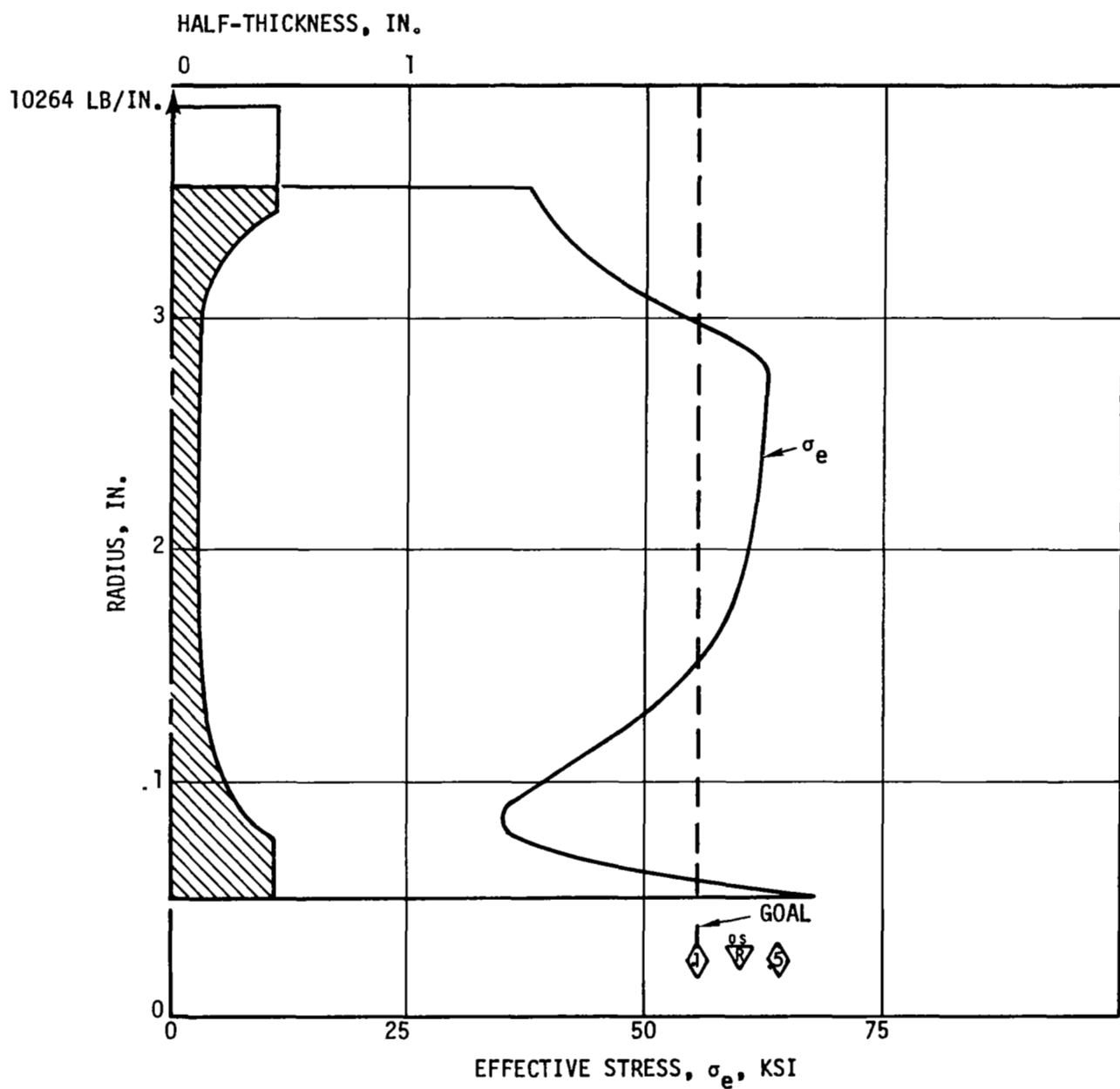


Figure 5.3-3. Effective Stresses in Stage 10 of 7+4 Turbine at 19,200 rpm.

TABLE 5.3-1

TURBINE WHEEL MECHANICAL DESIGN PARAMETERS  
FOR 7+4 TURBINE (KDTZM-1175 MATERIAL)

<u>Stage Number</u>		<u>1</u>	<u>2</u>	<u>3</u>	<u>4</u>	<u>5</u>	<u>6</u>	<u>7</u>	<u>8</u>	<u>9</u>	<u>10</u>	<u>11</u>
Dovetails		No	No	No	No	No	No	No	No	No	Yes	No
Tip Radius	in.	2.855	3.025	3.208	3.386	3.565	3.758	3.904	4.923	4.906	4.933	5.027
Rim Radius	in.	2.516	2.669	2.820	2.964	3.108	3.249	3.375	4.388	4.167	3.901	3.449
Axial Chord	in.	0.400	0.400	0.400	0.400	0.400	0.400	0.400	0.550	0.650	0.850	1.000
Temperature	°F	2085	1977	1920	1846	1756	1672	1586	1442	1363	1283	1207
Deformation Stress	ksi	2.3	8.9	12.3	17.8	25.9	33.8	40.6	48.6	52.2	55.7	58.8
Fracture Stress	ksi	18.4	28.2	33.2	39.6	46.9	51.3	53.5	56.9	58.7	60.5	61.9
Peak Stress	ksi	7.9	9.3	12.2	17.0	22.3	25.9	28.0	40.5	50.5	62.7	63.3
At Radius	in.	1.0	1.0	2.0	2.1	2.1	2.2	1.9	2.0	2.8	2.8	2.6
Bore Stress	ksi	15.3	17.6	19.0	23.5	28.8	31.5	34.0	53.6	62.0	68.3	68.5
Rim Deflection <sup>(1)</sup>	mils	0.4	0.5	0.6	0.8	1.0	1.4	1.5	2.7	3.8	3.7	3.2
Wheel Weight <sup>(2)</sup>	lb	4.5	4.1	3.3	2.9	2.7	2.8	2.9	5.9	5.8	10.8	8.7
Axial M.I.	lb-in. <sup>2</sup>	11.7	12.5	11.5	11.8	12.5	14.2	16.3	54.4	47.0	38.6	36.0
Bursting Force	klb	24.7	24.6	22.7	22.1	22.7	25.0	28.1	56.7	78.5	139.1	110.0
Profile Area	in. <sup>2</sup>	1.4	1.2	0.9	0.7	0.6	0.6	0.6	0.9	0.8	1.2	1.1
Avg.Tang.Stress	ksi	8.8	10.3	12.8	16.1	19.9	22.7	24.8	30.3	47.6	57.1	51.0
Avg.Tang.Stress	--	0.48	0.36	0.38	0.41	0.42	0.44	0.46	0.53	0.81	0.94	0.82
Fracture Stress												

NOTES: (1) Due to short-term centrifugal loading only - thermal expansion and creep not included

(2) Buckets included

minimum just above the hub. The primary difference in these stages is the proximity of the mid-radius peak stress to the allowable three-year 0.1 percent creep stresses. Further iterations would be desirable in stages 9 - 11, primarily because the allowable deformation stresses are so nearly the same as the allowable fracture stresses. In later iterations, a desirable goal would be to obtain a ratio of average tangential stress/allowable fracture stress of 0.50 to hold the peak stresses well below the fracture level.

The most critical stage, stage one, is analyzed in more detail than the less critical ones. After reaching a solution using the approaches previously outlined, the wheel with tie bolt head plate and torque tube is analyzed by the ROTOR finite-element computer program. With rotation, a pressure differential across the wheel, a 12540 pound tie bolt force, but no thermal gradients, the effective stresses of Figure 5.3-4 are obtained. The presence of the stage two wheel is simulated by deformation restraints on the aft end of the torque tube. Acceptable stresses are found in the wheel and torque tube, since the peak stress is at the bore and only slightly exceeds the three-year 0.5 percent creep stress. Further iteration could bring improvements, but the peak stress cannot be greatly improved because of practical limitations on wheel thickness. A crossplot of the stresses through the axial centerline of the wheel would show the characteristic stress distribution of the previous figures.

The peak effective stress of 15 ksi in the tie bolt head plate occurs beneath the curvic coupling. This stress may be reduced by further iteration of the head plate geometry.

KDTZM-1175 AT 2085°F

3-YR ALLOWABLE RUPTURE STRESS = 18,370 PSI  
 0.5% CREEP STRESS = 13,700 PSI  
 0.1% CREEP STRESS = 2,300 PSI

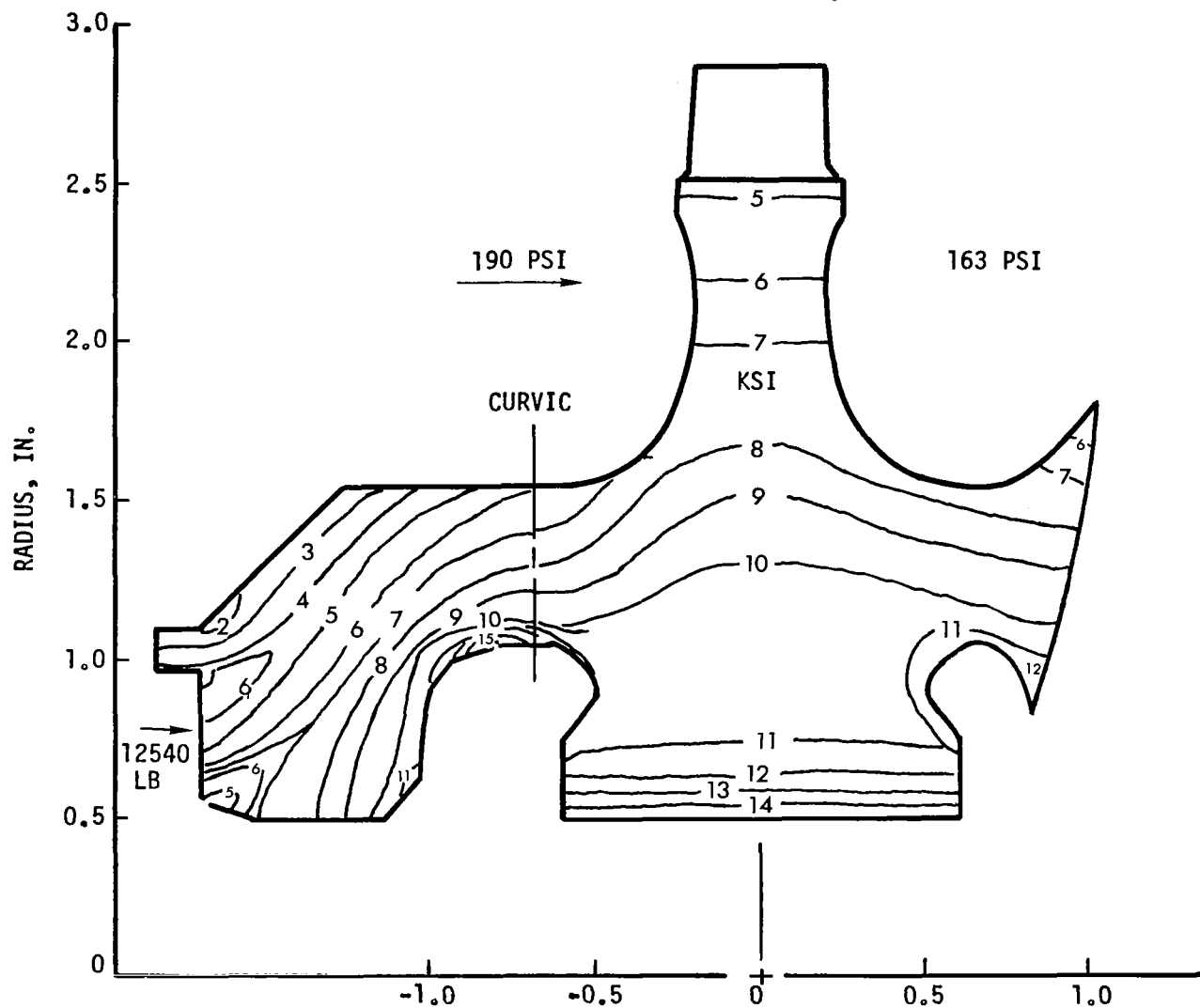


Figure 5.3-4. Effective Stresses in Stage 1 of 7+4 Turbine at 19,200 rpm. With Torque Tube, Thrust, and Tiebolt Loads.

An attempt was made to eliminate the tie bolt head plate by matching the tie bolt head geometry to the bore of the wheel. The effective stresses of Figure 5.3-5 resulted. Since a peak bore stress of 26 ksi resulted, this design is unsuccessful and would require more investigation before the approach could be made workable.

#### Airfoil Stresses, Turbine Torque and Power

A summary of representative airfoil stresses, torque, and power produced by the turbine is shown in Table 5.3-2. The airfoil root stresses are the most basic stresses in the rotor because little can be done to vary them once the flow path geometry and rotative speed is fixed. For this study, the assumptions were made that the airfoils have a root area of  $A_R = 0.2363 c^2$ , where  $c$  is the axial chord of the stage. The factor 0.2363 is derived from preliminary design criteria of Kamadoli (Reference 5.3-1) for approximately one-inch wide symmetrical airfoils with a turning angle of  $60^\circ$  and a pitch/chord ratio of 0.667.

It is further assumed that the ratio  $b = \frac{\text{tip section area}}{\text{root section area}} = 0.7$  for linearly tapered airfoils, and a stress concentration factor of 1.05 is applied at the airfoil roots. These criteria cannot be greatly improved until the final airfoil contour is fixed in detail. For all stages except stage one, the root stresses are well below the allowable three-year 0.1 percent creep stresses. For stage one, the root stress is well below the allowable three-year 0.5 percent creep stress - an estimated creep rate of 0.13 percent occurs in three years. This will have a minor effect upon allowable initial tip clearances.

The bending stresses which result from the aerodynamic loads on the airfoils are insignificantly low, based upon the analysis of the

KDTZM-1175 AT 2085°F

3-YR ALLOWABLE RUPTURE STRESS = 18,370 PSI  
 0.5% CREEP STRESS = 13,700 PSI  
 0.1% CREEP STRESS = 2,300 PSI

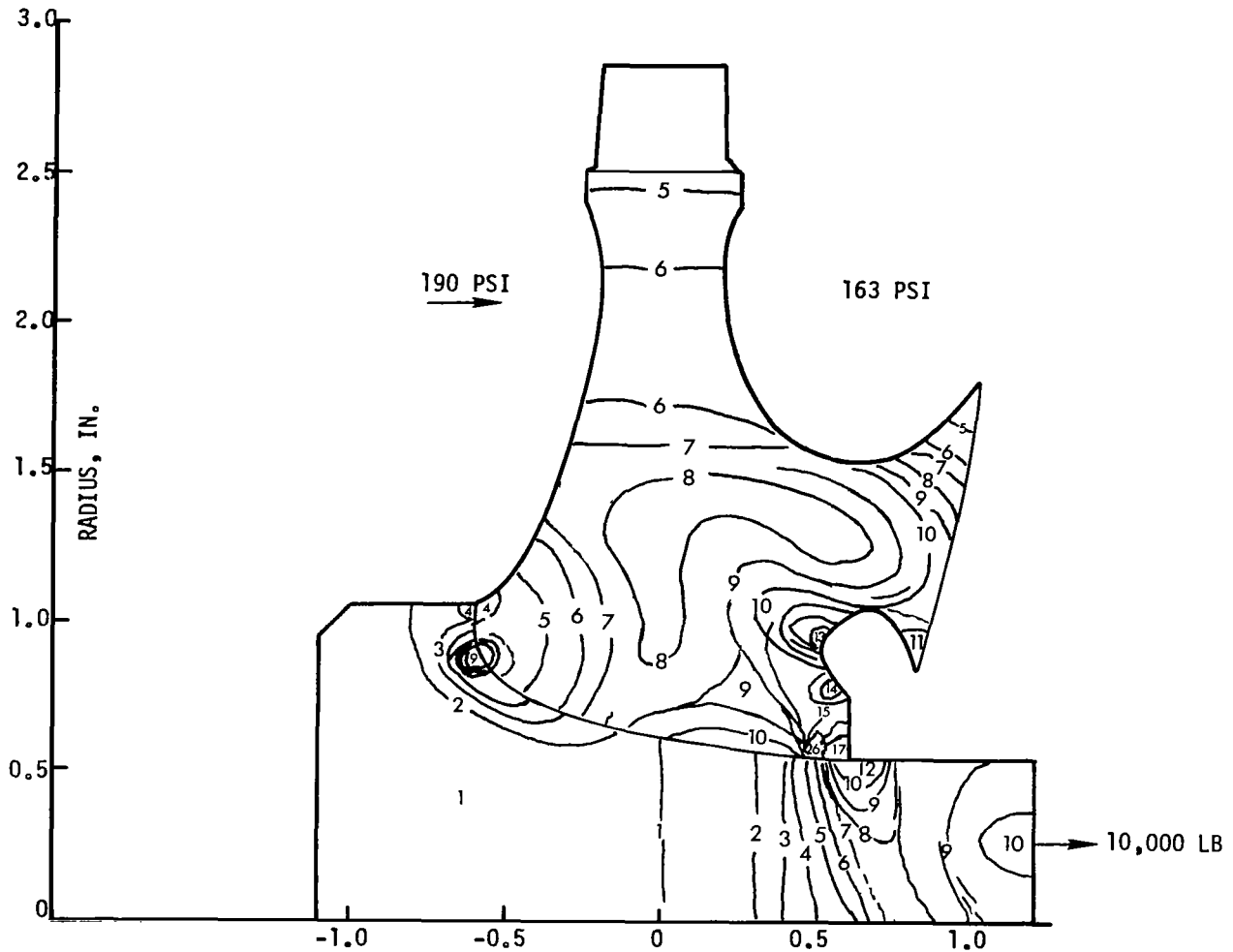


Figure 5.3-5. Effective Stresses in Stage 1 of 7+4 Turbine at 19,200 rpm With Torque Tube, Thrust, and Tiebolt Loads (No Head Plate).

**TABLE 5.3-2**  
**REPRESENTATIVE BLADE STRESSES, TORQUE, AND POWER IN 7+4 TURBINE**

Stage No.	Root Stress $\sigma_r$ , psi	Bending Stress $\sigma_b$ , psi	Torque Per Stage $T_q$ , in.-lb	Total Torque $\Sigma T_q$ , in.-lb	Horsepower Per Stage HP hp
1	3290	120	125	125	38
2	3660	110	143	267	43
3	4220	130	156	424	48
4	4840	150	170	593	52
5	5500	170	182	775	55
6	6430	200	193	969	59
7	6950	210	204	1172	62
8	9000	100	286	2165	87
9	12110	130	259	1879	79
10	22020	170	235	1619	71
11	24150	360	212	1385	65

659 = total horsepower

492 = total kilowatts



airfoils as cantilevered beams with minimum moments of inertia similar to those of the three-stage potassium turbine buckets.

The torque per stage, total torque through each stage, and horsepower produced per stage are listed in order to provide familiarization with the magnitude of these quantities. The most useful of these for further mechanical analysis is the total torque transmitted through each stage, which must be carried by the torque tubes.

#### Bucket Tip Clearances

The rotor bucket tip clearances which are required initially in order to obtain 0.010-inch radial clearances at the end of three years of running at design speed and temperatures are shown by Figure 5.3-6. Stage one, with the allowable 0.1 percent creep stress exceeded both in the wheel and in the buckets, requires an initial clearance of 0.019 inch. All other stages require less clearance, and stages six, seven, eight, and nine have particularly low creep rates which produce less than one mil of radial creep during the operation period. The slopes of the curves between 0 - 3 years are merely estimates of the general trend, since detailed knowledge of the creep curves over this period of time is not known.

#### Dovetail Stresses

In order to establish that stage ten of the KTA turbine is sufficiently similar to stages two and three of the three-stage turbine that their dovetail stress and bucket vibration parameters can be confidently applied, Figure 5.3-7 was made. The very close geometrical similarity lends confidence to the use of the developed analysis methods.

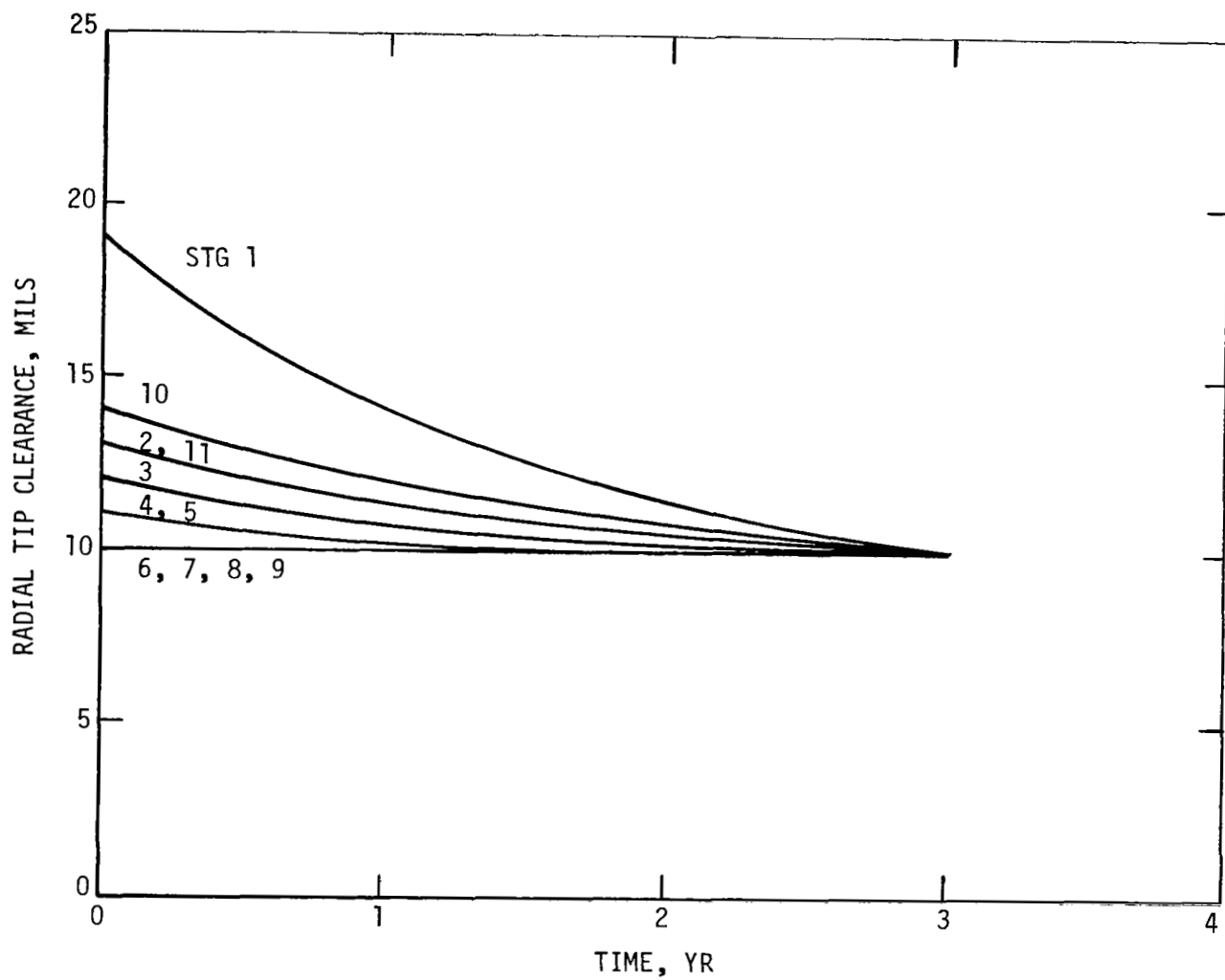


Figure 5.3-6. Rotor Bucket Tin Clearances for 7+4 Turbine.  
(Slope of Curves Arbitrary)

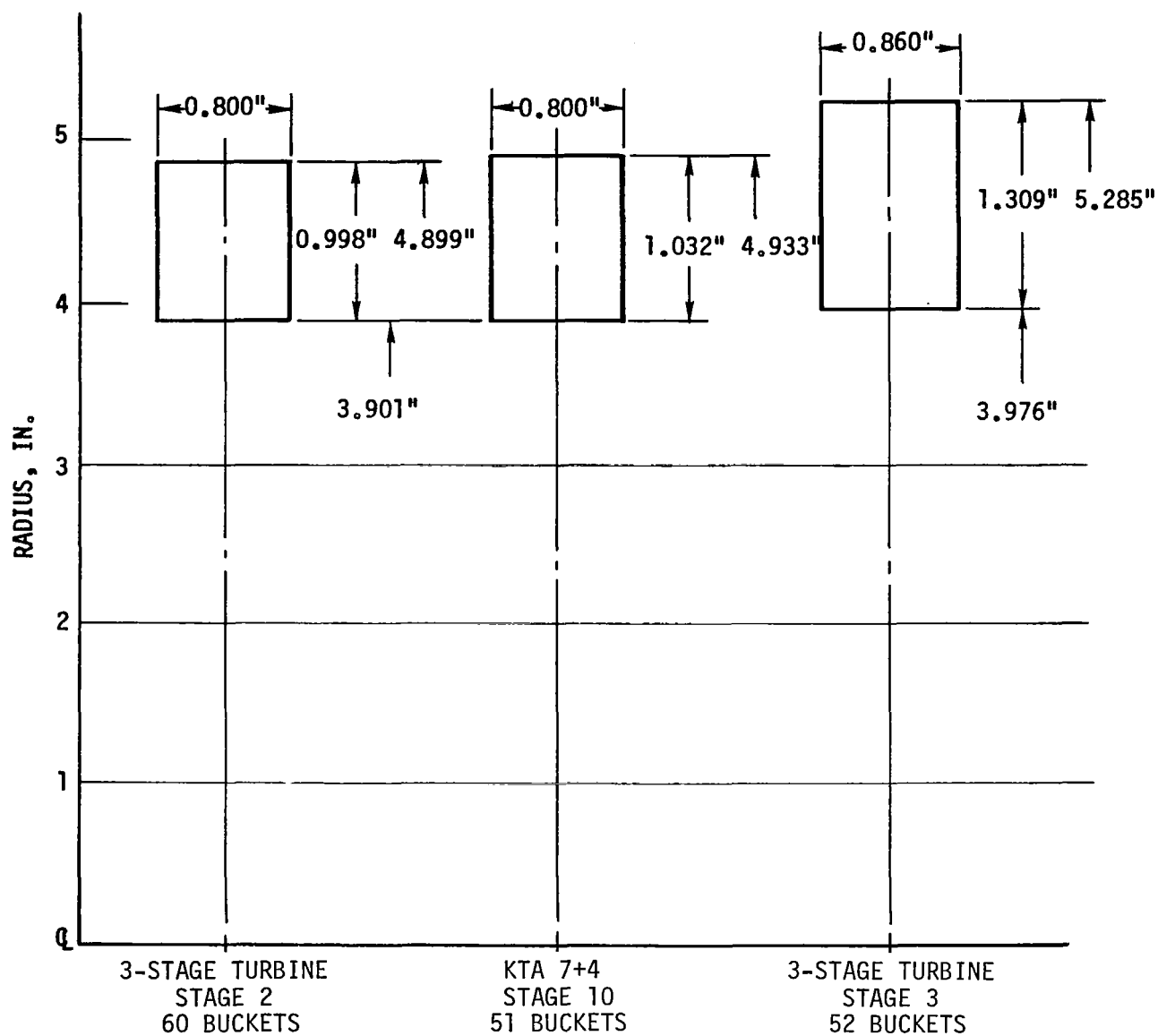


Figure 5.3-7. Geometrical Comparison of Rotor Buckets - Stage 10 of 7+4 Turbine Versus Three-Stage Potassium Turbine Stages 2 and 3.

The bucket and wheel dovetail stresses are analyzed approximately as a part of the basic mechanical design analysis program by calculating a dovetail neck section stress equal to the centrifugal forces of the airfoil plus bucket dovetail section above the upper dovetail neck, divided by the area available for the bucket dovetail neck. The gross section stress is multiplied by factors derived from the three-stage turbine analyses, which relate the gross section stress to the maximum combined stresses in the bucket dovetail and the wheel dovetail. A further criterion is that dovetails would not be desirable in wheels of small radius if the required number of buckets is large, because the available circumferential space for each blade would lead to dovetail neck sections so small that undected minor fabrication or material discrepancies would cause catastrophic failure.

Table 5.3-3 shows the results of the preliminary screening analysis of dovetail design parameters as made by the basic mechanical design program. It shows that dovetails would not be desirable in stages 1 - 8 of the turbine because of the small space available for dovetails. It would be very difficult to make dovetails work safely in the last two stages of the turbine because the high centrifugal loads exceed the allowable fracture stresses, even though these are high. Only in stage nine does the screening analysis indicate that an acceptable dovetail solution might be found. The screening analysis predicts conservatively high stresses.

The dovetails for stage ten are analyzed in greater detail by using the tang geometry and analytical approach which were successfully used in the three-stage turbine, with the values of bucket centrifugal force and circumferential spacing which are peculiar to the KTA stage

TABLE 5.3-3

DOVETAIL MECHANICAL DESIGN PARAMETERS  
FOR 7+4 TURBINE (KDTZM-1175 MATERIAL)

<u>Stage Number</u>		<u>1</u>	<u>2</u>	<u>3</u>	<u>4</u>	<u>5</u>	<u>6</u>	<u>7</u>	<u>8</u>	<u>9</u>	<u>10</u>	<u>11</u>
Deformation Stress	ksi	2.3	8.9	12.3	17.8	25.9	33.8	40.6	48.6	52.2	55.7	58.8
Fracture Stress	ksi	18.4	28.2	33.2	39.6	46.9	51.3	53.5	53.5	58.7	60.5	61.9
Dovetail Stress	ksi	12.8	14.2	16.4	18.8	21.2	24.8	26.8	34.4	46.3	63.0	92.3
Neck Width	in.	0.06	0.06	0.06	0.06	0.06	0.06	0.06	0.08	0.11	0.13	0.15

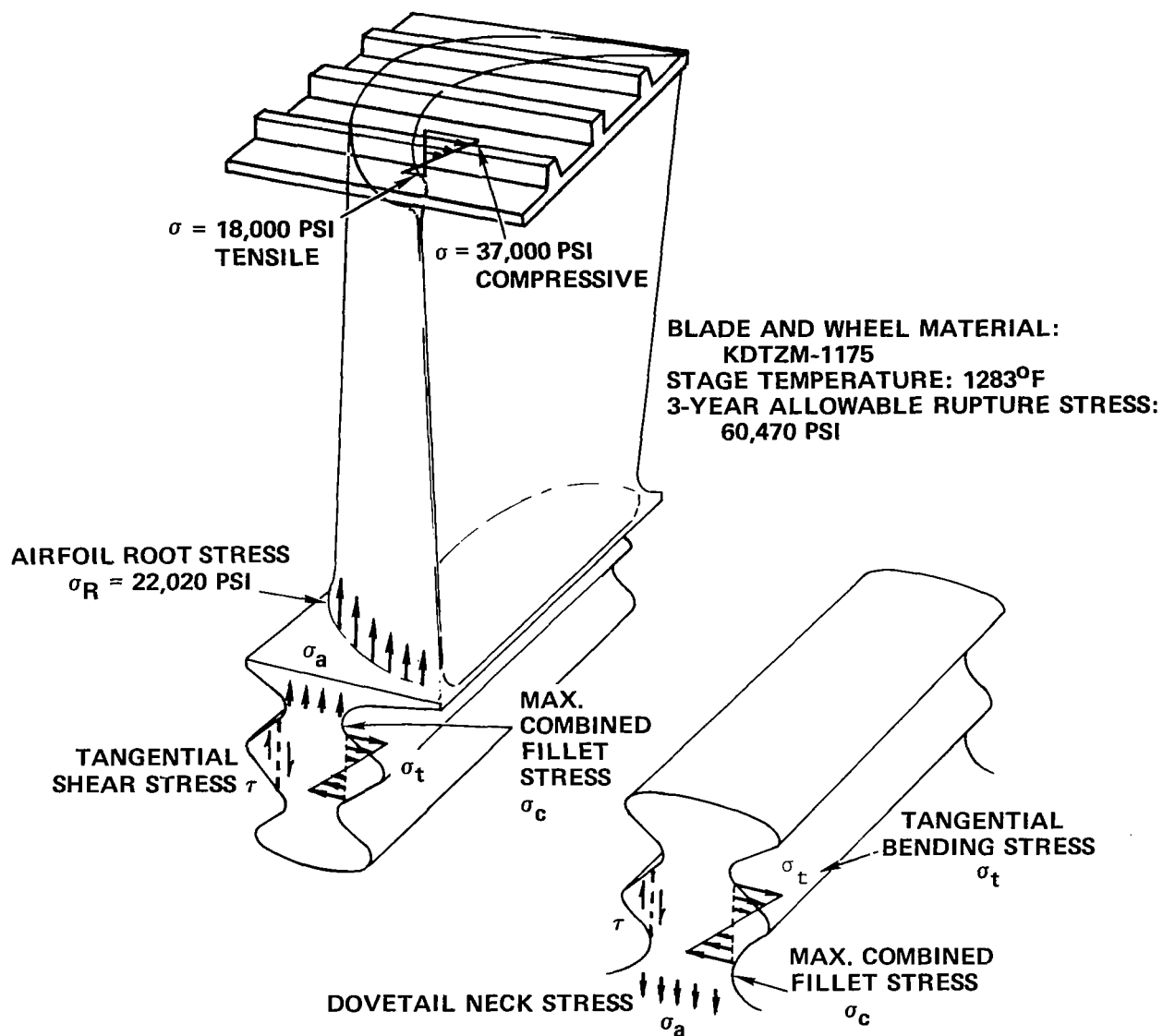
ten. The analytical results are shown by Figure 5.3-8. The tip shroud, airfoil root, bucket bottom tang, and wheel top tang stresses are satisfactorily lower than the allowable three-year rupture stress of 60,500 psi and 0.1 percent creep stress of 55,700 psi. However, the bucket top tang and wheel bottom tang combined stresses are sufficiently close to the allowables that a clear warning is sounded. A factor of safety with respect to fracture of more than  $\frac{60500}{54910} = 1.10$  is desirable, because a favorable stress redistribution cannot be relied upon to prevent yielding from proceeding to catastrophic fracture. Therefore, the existence of an acceptable solution to the stage ten dovetail stress problem is indicated, but several more iterations would be desired to raise the factor of safety.

#### Bucket Vibration

The bucket vibration analysis technique is also based upon the use of the analytical techniques developed for the three-stage potassium turbine, with cross-sectional and stiffness properties of those airfoils used. The bucket critical frequency is expressed as a function of a correlation factor  $C_n$ , airfoil radius of gyration  $r$ , airfoil height  $H_B$ , and material constant  $K_m$ :

$$f_n = C_n \frac{r}{H_B^2} K_m \times 10^4 \quad \text{Hz}$$

Correlation factors were developed which allowed the above formula to predict the bucket critical frequencies which were calculated by an advanced computer program and observed on bench tests of sample buckets. Corrections were made for the absence of tip shrouds in all stages except stage ten. The basic geometrical parameter of the buckets





BLADE DOVETAIL			WHEEL DOVETAIL		
STRESS (PSI)	TOP TANG.	BOTTOM TANG.	STRESS (PSI)	TOP TANG.	BOTTOM TANG.
$\sigma_a$	22720	12890	$\sigma_a$	17830	19370
$\sigma_t$	34610	25610	$\sigma_t$	27980	45090
$\tau$	20800	15480	$\tau$	12030	12750
$\sigma_c$	48490	33170	$\sigma_c$	38720	54910
					

Figure 5.3-8. Dovetail Stress in Stage 10 of 7+4 Turbine.

is the ratio of radius of gyration divided by (airfoil height)<sup>2</sup>. While airfoil height is known, the radius of gyration cannot be accurately calculated until the detailed airfoil contours are fixed. Therefore, two estimates of radius of gyration were made for the buckets which are significantly smaller than those of the three-stage turbine, but a radius of gyration (0.2 inch) similar to that of the three-stage turbine buckets was assumed for KTA buckets of similar size. The predicted bucket critical frequencies are shown on Figure 5.3-9. The lower natural frequencies of the shrouded stage ten stand out clearly from those of the unshrouded buckets, whose second and third criticals are off-scale. The lower first critical frequencies of stages 1 - 7 when  $r = 0.1$  inch is assumed are shown.

Excitation frequencies of rotating speed  $N_d$  times number of nozzle vanes  $n_n$  are assumed to excite the rotor buckets:

$$f_e = \frac{N_d n_n}{60} \quad \text{Hz}$$

Figure 5.3-10 shows the calculated excitation frequencies, with circles indicating the condition of excitation frequency within  $\pm 10$  percent of the critical frequency of a stage. One method of increasing the margin between excitation and natural frequencies is indicated - that of changing the excitation frequency by varying the number of nozzle vanes by an amount which does not decrease efficiency unacceptably. A better method of avoiding resonant conditions or decreasing the chances of catastrophic excitation is that of staggering the spacing of the nozzle vanes (Reference 5.3-2). This produces a larger number of excitation frequencies, but each has decreased pulse energy. Resonant conditions within the operating speed range were avoided in the three-stage turbine when this approach was used.



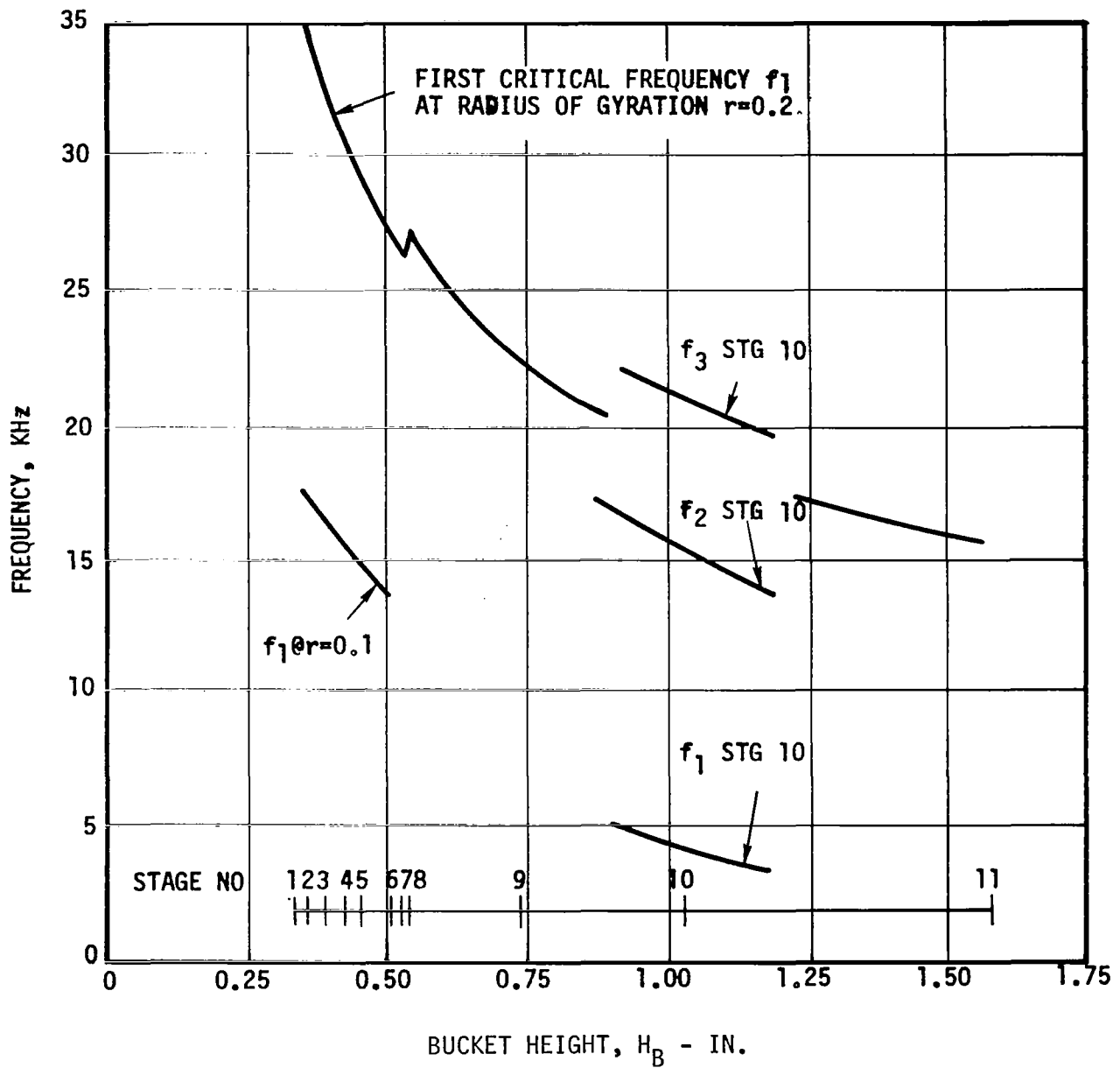


Figure 5.3-9. Rotor Bucket Critical Frequencies for 7+4 Turbine.

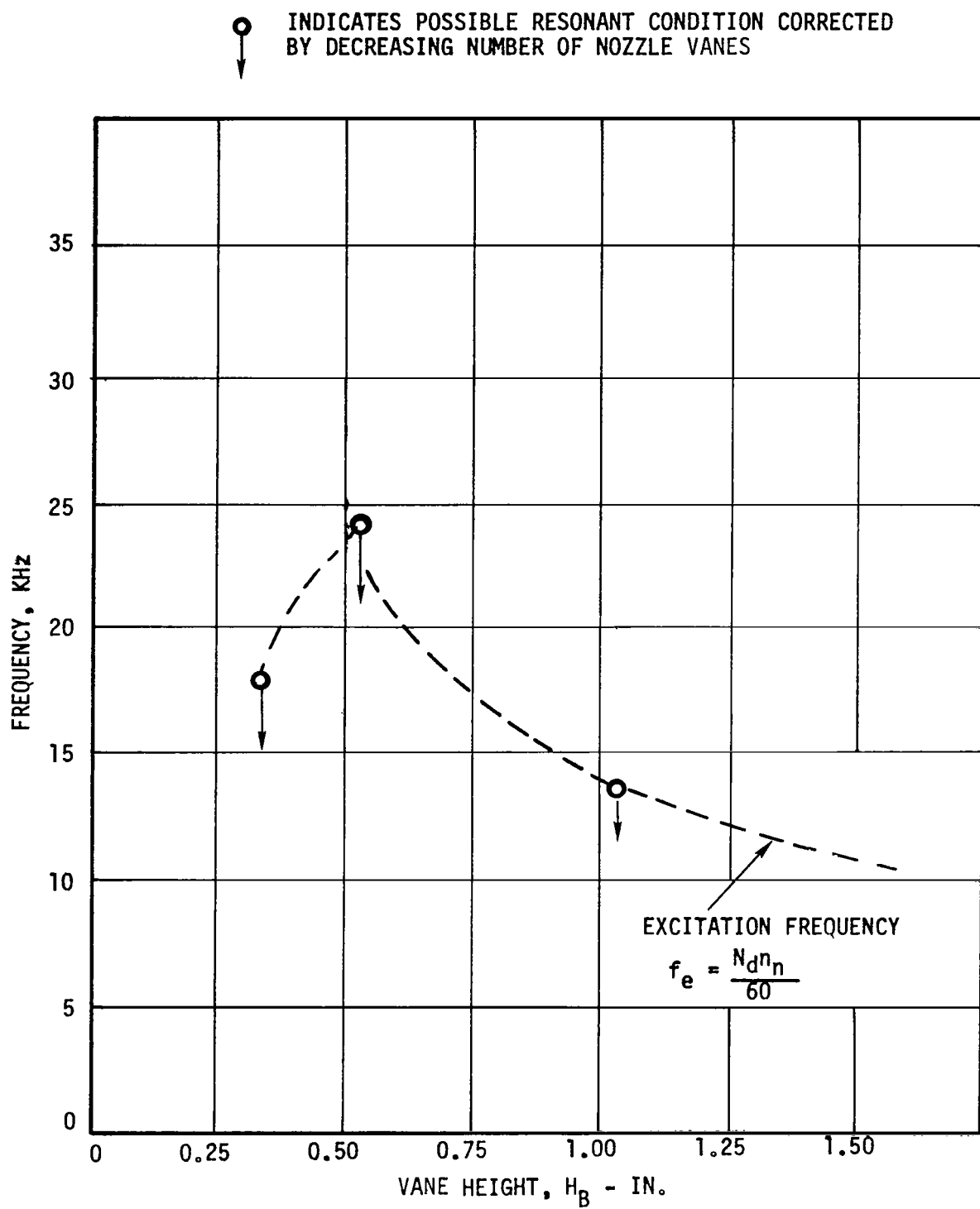


Figure 5.3-10. Excitation Frequencies for 7+4 Turbine.

The calculated numbers of rotor buckets and nozzle vanes upon which the vibratory response calculations are based are shown in Table 5.3-4, with nozzle vane calculations listed above and rotor bucket calculations below. The stator axial chords are those seen on the turbine drawings, being projected lengths on a plane through the centerline of rotation, and differ from the true stator chord lengths from leading edge to trailing edge. These values are assumed to be the same, for computational purposes, for the rotor buckets. The pitch diameters  $D_p$  and solidity parameters  $\sigma_N$  and  $\sigma_R$  are listed, with number of nozzle vanes and rotor buckets computed by the formulas below. They compute the pitchline circumference  $\pi D_p$  and divide it into equal increments of  $c/\sigma_N$  or  $c/\sigma_R$  pitch spacing available per airfoil, where the solidity parameters are the ratio of chord length to pitch:

$$\text{No. of nozzle vanes} \quad n_n = \frac{\pi \sigma_N D_p}{c}$$

$$\text{No. of rotor buckets} \quad n_B = \frac{\pi \sigma_R D_p}{c}$$

TABLE 5.3-4

NUMBER OF NOZZLE VANES AND ROTOR BUCKETS  
FOR 7+4 TURBINE

<u>Stage</u>	<u>Stator Axial Chord, in.</u>	<u>Stator Chord, c, in.</u>	<u>Pitch Diameter D<sub>p</sub>, in.</u>	<u>Solidity, <math>\sigma_N</math></u>	<u>No. of Vanes</u>
1	0.348	0.435	5.37	1.52	59.
2	0.348	0.435	5.69	1.53	63.
3	0.348	0.435	6.03	1.54	67.
4	0.348	0.435	6.35	1.54	71.
5	0.348	0.435	6.67	1.53	74.
6	0.348	0.435	7.01	1.52	77.
7	0.348	0.435	7.33	1.51	80.
8	0.480	0.600	9.31	1.50	73.
9	0.565	0.706	9.07	1.45	59.
10	0.700	0.875	8.83	1.41	45.
11	0.870	1.087	8.48	1.41	35.

<u>Stage</u>	<u>Rotor Axial Chord, in.</u>	<u>Rotor Chord, c, in.</u>	<u>Pitch Diameter D<sub>p</sub>, in.</u>	<u>Solidity, <math>\sigma_R</math></u>	<u>No. of Buckets</u>
1	0.40	0.40	5.465	1.70	73.
2	0.40	0.40	5.765	1.71	77.
3	0.40	0.40	6.105	1.72	82.
4	0.40	0.40	6.430	1.72	87.
5	0.40	0.40	6.720	1.71	90.
6	0.40	0.40	7.060	1.70	94.
7	0.40	0.40	7.385	1.65	97.
8	0.55	0.55	9.265	1.68	89.
9	0.65	0.65	9.025	1.54	67.
10	0.80	0.80	8.785	1.46	51.
11	1.0	1.0	8.450	1.43	38.

## 5.4 TURBINE ROTOR CONSTRUCTION AND STRESSES

### Curvic Coupling

The method of joining the turbine wheels to each other by utilizing curvic couplings machined into the torque tubes is illustrated in Figure 5.4-1. In the three-stage turbine, the TZM first stage wheel (with most dovetail slots) was joined to the TZM second stage wheel with full-barrel teeth. The TZM second stage wheel was joined to the U-700 third stage wheel with half-barrel teeth to accommodate differential thermal expansion. The stage three wheel is joined to the rotor shaft (both of U-700 material), with a full-barrel curvic tooth. The successful use of this joining method in many rotating machines, including the two-stage and three-stage potassium turbines, attests to its reliability and its efficiency as an axial and radial locating device. After 1500 hours of testing of the three-stage turbine, no deterioration of the curvic teeth by deformation, galling, spalling, fretting, or cracking could be detected.

In order to have a satisfactory curvic coupling assembly, the tie bolt must supply sufficient force to overcome all separating forces under all conditions to be encountered. As indicated by Figure 5.4-2, the main separating forces are components of the torque transmitted through the teeth, the moment which bends the shaft, and the axial thrust. The factors of safety of the teeth are determined by the following criteria:

- The allowable shear stress, estimated very conservatively as ten percent of the three-year allowable rupture stress, divided by the shear stress due to the torque force acting on the roots of the curvic teeth.

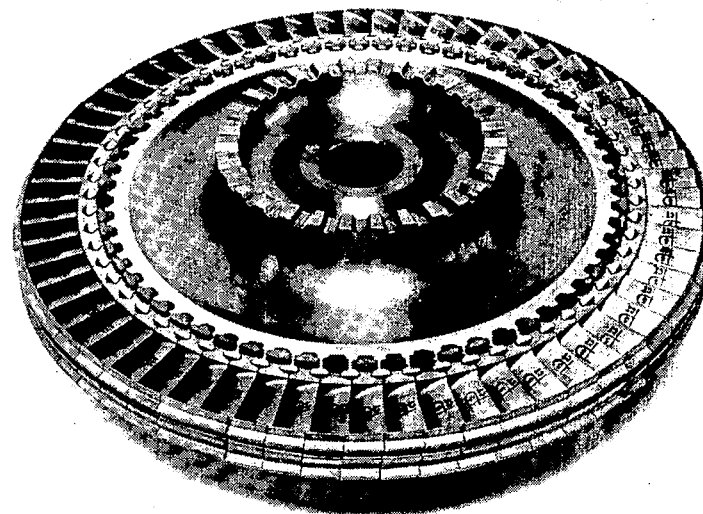
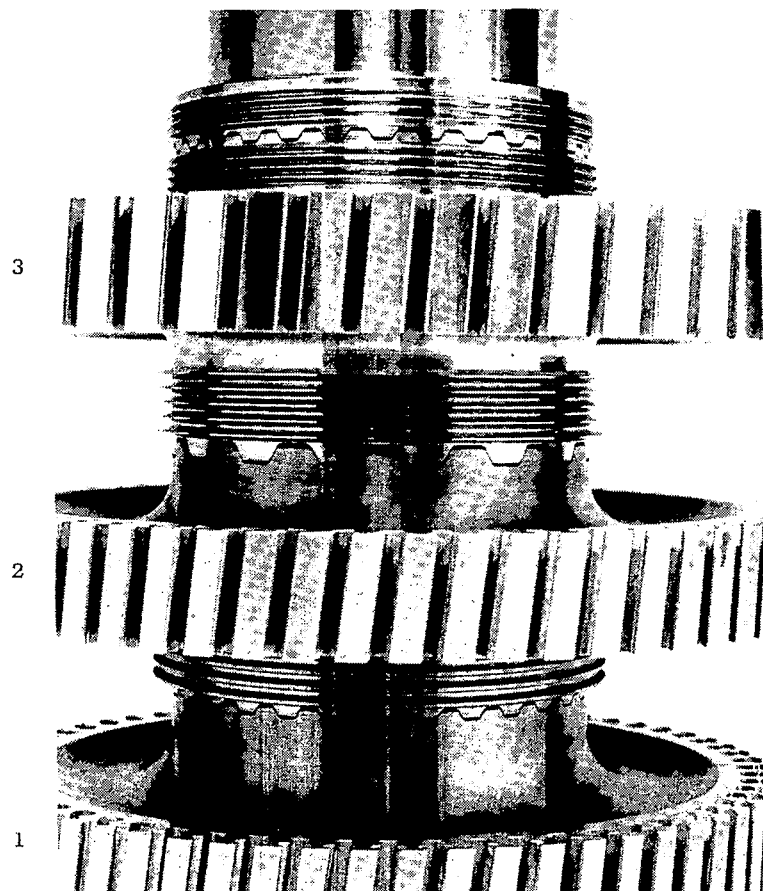
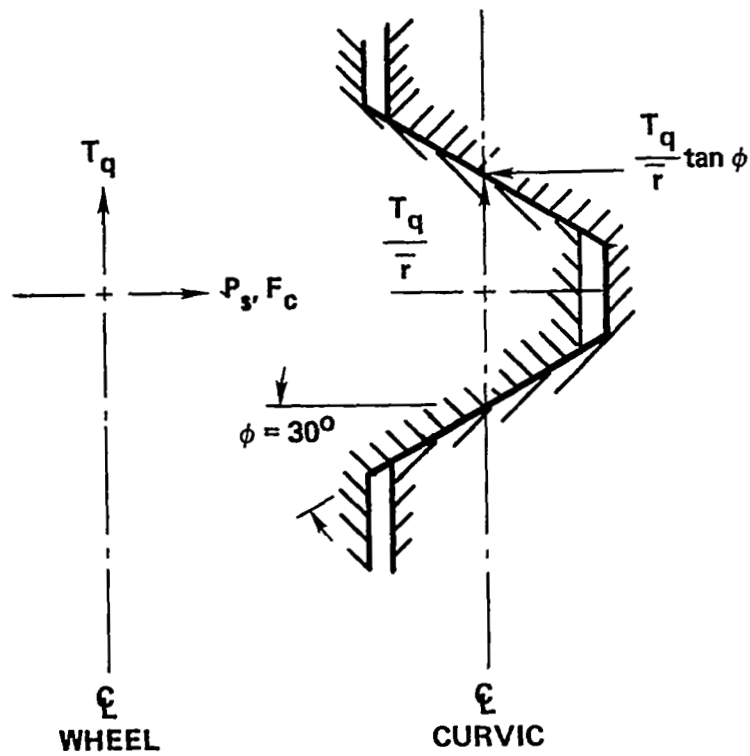


Figure 5.4-1. Curvic Coupling Rotor Assembly.



$$F_c = \frac{T_q}{r} \tan \phi + \frac{1 F_{CB} \ell_{tw}}{2r} - P_s$$

Required tiebolt force = torque separating force  
+ moment separating force  
- thrust

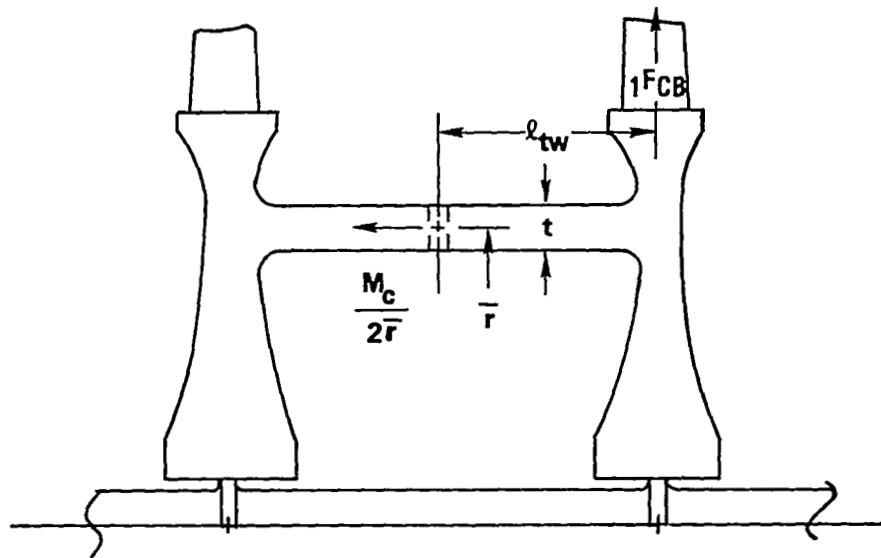
Figure 5.4-2. Curvic Coupling Forces.

- The allowable surface stress, estimated conservatively as 25 percent of the three-year allowable 0.1 percent creep stress, divided by the torque force acting on the total interference area between male and female teeth.
- The three-year 0.1 percent creep stress divided by the surface equivalent stress, a combination of torque, thrust, and tie bolt axial force components.
- The available tie bolt axial force, estimated to be after three years 65 percent of the initial tie bolt force, divided by the combined separating force due to components of thrust, torque, and moment.

The separating moment is calculated by the rotor response computer program to be uninterestingly small under most operating conditions. A criteria was developed which would produce moments of appreciable magnitude. For this purpose, the loss of one rotor blade was assumed to produce a moment equal to the blade centrifugal force times the distance between the centers of the curvic coupling and the wheel. This situation is illustrated by Figure 5.4-3 with a synopsis of parameters relevant to curvic coupling design.

Stage zero refers to the curvic between the tie bolt head plate and the stage one wheel, stage 1 - 7 refers to the curvics downstream (aft) of stages 1 - 7, stage 7.9 refers to the curvic joining stage eight and a conical stub shaft, stage 8 - 11 refers to the curvics downstream (fwd) of stages 8 - 11, and stage 11.5 refers to the curvic between the forward turbine bearing journal and the conical stub shaft adjacent to stage eleven.





Stage	$\bar{r}$ , in.	$t$ , in.	No. of Teeth —	Whole Depth, in.	Contact Depth, in.	Ded. + Clearance, in.	Shear Stress F.S.	Surface Stress F.S.	Surface Eq. Stress F.S.	Clamping Force F.S.
0	1.35	0.50	30	0.066	0.045	0.069	20.0	1.5	2.1(.5)	$\infty$
1	1.55	↓	↓	0.074	0.050	0.073	38.6	9.3	1.2	↓
2	1.88	0.34	↓	0.084	0.057	0.078	23.5	6.2	1.2	↓
3	2.00	0.26	32	0.082	0.056	0.078	15.6	4.8	1.3	↓
4	2.05	0.18	↓	↓	↓	↓	9.6	3.5	1.8	↓
5	↓	↓	↓	↓	↓	↓	8.3	3.6	2.3	↓
6	↓	↓	↓	↓	↓	↓	6.9	3.5	2.7	↓
7	↓	↓	↓	↓	↓	↓	6.0	3.3	3.2	↓
7.9	2.90	↓	60	0.061	0.042	0.066	12.5	7.4	4.0	↓
8	↓	↓	↓	↓	↓	↓	7.2	4.3	4.2	↓
9	↓	↓	↓	↓	↓	↓	8.0	4.8	3.9	↓
10	↓	↓	↓	↓	↓	↓	9.5	5.9	4.2	↓
11	↓	↓	↓	↓	↓	↓	11.3	7.3	4.5	↓
11.5	1.07	0.26	24	↓	↓	↓	2.6	1.8	2.5	↓

Figure 5.4-3. Curvic Coupling Summary.

The entry of "Dedendum + Clearance" is a measure of the closest allowable axial approach of any point on a wheel, for instance the hub, to the center of the curvic joint if clearance for milling the curvic teeth is to be provided.

The shear and surface stress factors of safety are quite acceptable, even though conservative allowable material property estimates were used. The surface equivalent stresses are acceptable, but the allowable three-year 0.1 percent creep stress is exceeded in stage one. An acceptable factor of safety results when the 0.5 percent creep stress is allowed. The clamping force factor of safety is infinite, because aerodynamic thrust is greater than the torque and moment separating components. A negative tie bolt force is required for equilibrium, while a positive tie bolt force is always available. The turbine could be held together by axial thrust alone once operating conditions are reached. Table 5.4-1 lists the magnitude of thrust developed per stage and thrust summation through the selected turbine design.

#### Torque Tubes

The rotor torque tubes must also withstand torque (small on the first stage and progressively higher aft), axial compression due to thrust and tie bolt force, centrifugal forces due to rotation, thermal stresses, and the end loads required to match wheel and torque tube deflection.

The analysis assumes a mean radius and thickness for a torque tube and calculates its expansion as a free hoop under the influence of centrifugal forces only. The deformation of the wheel at the

TABLE 5.4-1

THRUST IN 7+4 TURBINE

<u>Stage</u>	<u>Stage Thrust lb (1)</u>	<u>Thrust Summation lb</u>
1	1705	1705
2	284	1989
3	128	2117
4	15	2132
5	37	2169
6	56	2225
7	<u>-256</u>	1969
Total H.P. Turbine	1969	
11	98	2067
10	-55	2012
9	-81	1931
8	<u>-714</u>	1217
Total L.P. Turbine	<u><u>-752</u></u>	
Total Turbine	1217	

NOTES: (1) Positive aft

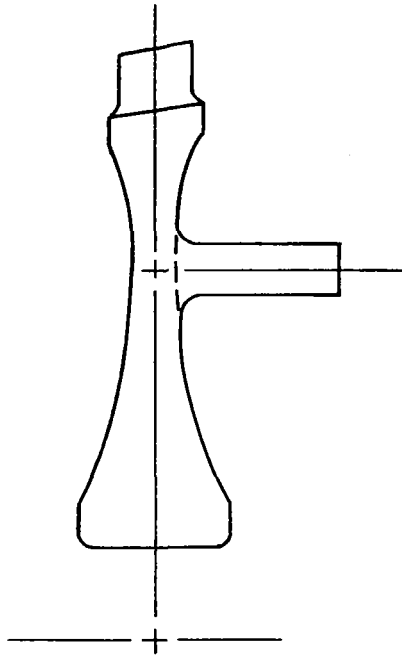
torque tube mean radius is extracted from the ELASTIC DISK computer output. The end force required to mate the wheel and torque tube end is calculated by the TORQUE Data Net computer program, using a beam on elastic foundation approach. An effective stress is calculated which considers the stresses due to the end force, torque, thrust, tie bolt load, and centrifugal force, assuming generous fillet radii at the juncture of torque tube and wheel. The allowable three-year 0.1 percent creep stress is compared to the calculated effective stress, and iterations are made until an acceptable solution is reached. The changes in wheel stress and deformation are calculated. Figure 5.4-4 summarizes the torque tube analysis results.

The major problem areas are the first four stages, where the effective stresses exceed the allowable 0.1 percent creep stress and the 0.5 percent creep stresses had to be used in order to obtain a factor of safety above unity. The magnitude of the required end loads is listed as  $P_{max}$ .

The analysis used to develop these figures can be checked by analyzing wheels and torque tubes together, using the ROTOR finite-element computer program. The close check obtained from this type of analysis of stage one, as previously reported, confirms the approach.

#### Tie Bolt

The tie bolt loading is influenced by elastic strain, change in modulus of elasticity with temperature, differential thermal expansion, stress relaxation, and the thread form. The design problem is to determine the assembly tie bolt load which gives the initial hot



Stage No.	R, in.	r, in.	Lg, in.	T, °F	$\sigma_{0.1Cr}$ , ksi	$\sigma_e$ , ksi	FS <sub>0.1Cr</sub> —	P <sub>max</sub> , lb/in.
1	1.55	1.05	0.66	2075	13.5*	10.2	1.32	332
2	1.97	1.63	0.74	1960	23.0*	16.1	1.43	—64
3	2.13	1.87	0.86	1890	28.1*	19.2	1.46	89
4	2.14	1.96	0.91	1825	32.5*	21.1	1.54	214
5	↓	↓	0.93	1755	25.6	21.5	1.19	352
6	↓	↓	0.95	1680	33.3	21.9	1.52	443
7	↓	↓	↓	1505	45.5	22.0	2.07	506
8	2.99	2.81	1.33	1415	50.0	37.8	1.32	582
9	↓	↓	1.57	1385	51.3	40.9	1.25	1354
10	↓	↓	2.01	1305	54.8	40.1	1.37	1121

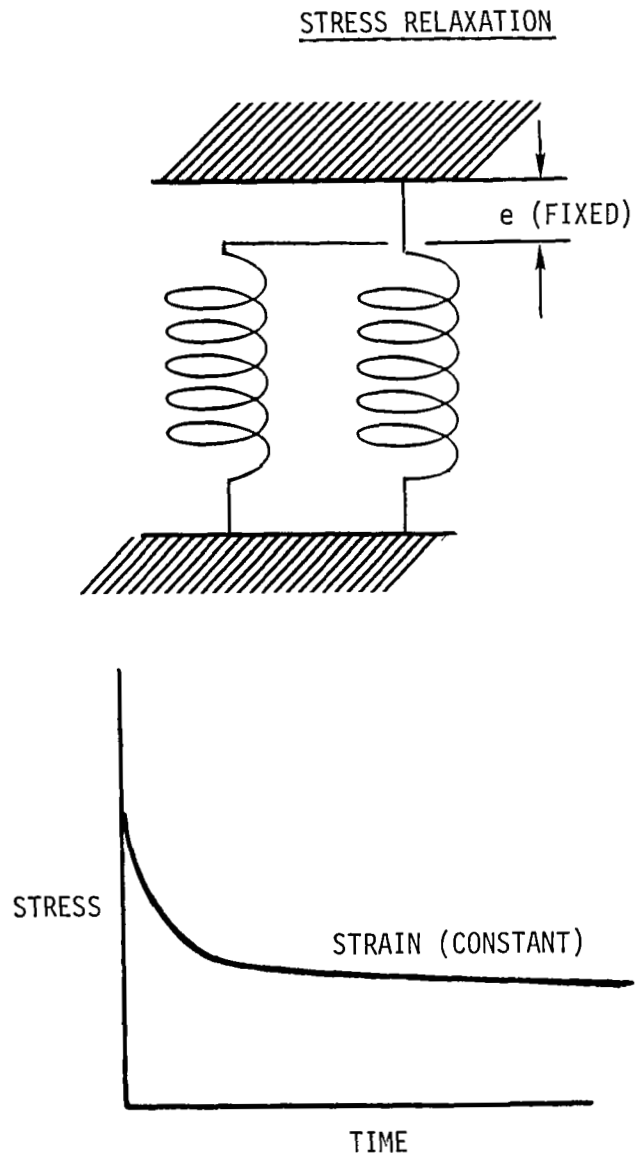
\* = 3 year 0.5% creep

Figure 5.4-4. Torque Tube Analysis - 7+4 Turbine.

tie bolt load for maintaining a minimum acceptable axial force after three years of relaxation. The tie bolt diameter must be varied throughout its length in order to hold the axial stress and its related elastic deformation high, even though the environmental temperature decreases from forward to aft. When this is done, the effect of creep in the hot section on the tie bolt axial force is minimized.

The worst operation conditions for a tie bolt can occur in a split spool, counterflow turbine if the two thrusts place the tie bolt in tension and no diminishment of load occurs when the bolt plastically deforms. With the 7+4 design, however, the net thrust effect is to diminish the tie bolt load. The difference between stress relaxation and creep is illustrated by Figure 5.4-5. An initial strain applied to a body is held constant. The stress decreases suddenly, then more gradually as the material plastically deforms and reduces the magnitude of the force required to produce an increment of strain equal to the original strain minus the plastic strain (assuming no decrease in material cross-sectional area). An unchanging equilibrium position is reached, and the process is called stress relaxation. With creep, however, if a constant load on a body is large enough to produce plastic strain, necking of the material occurs with increased strain until the body traverses through stages I, II, and III of creep, finally leading to rupture if the time period is long enough.

Stress relaxation in the tie bolt is obviously more desirable than creep which proceeds to catastrophic failure because the tensile loads are undiminished during the design life. Relaxation will occur



VS

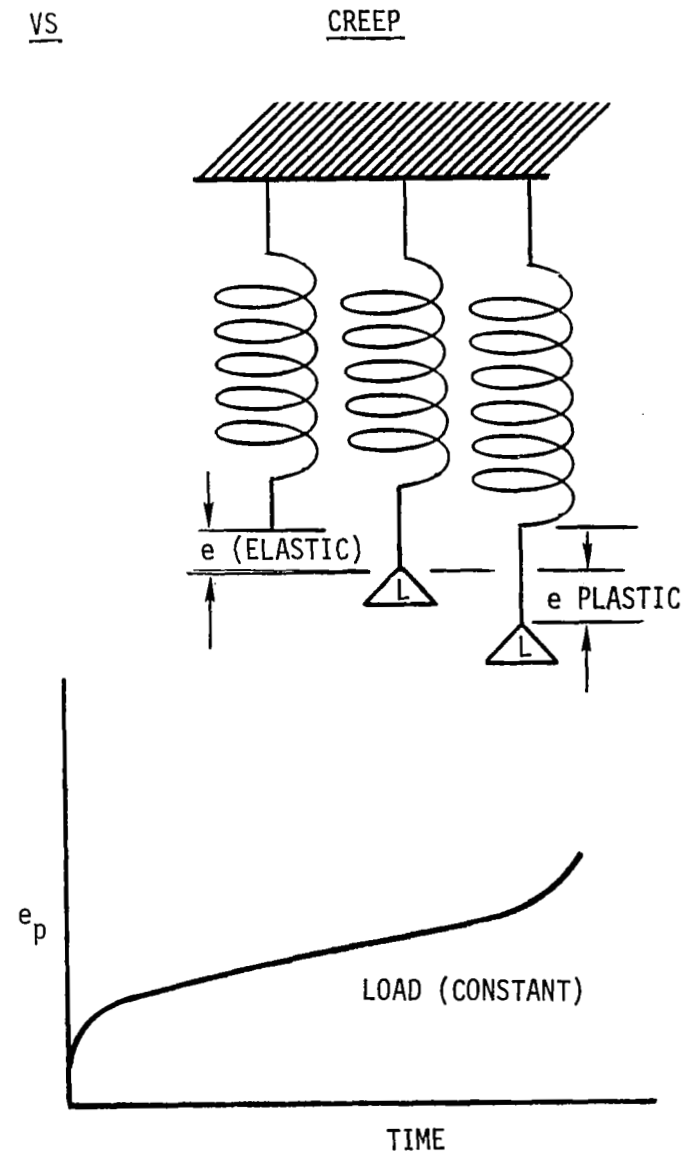


Figure 5.4-5. Material Plastic Deformations.

because the tie bolt experiences the constant strain developed by the controlled elongation of the tie bolt with respect to the total length between the forward side of the tie bolt head plate and the aft end of the rotor shaft. The thrust, which always acts aft, tends to unload the tie bolt.

The temperature distribution through the tie bolt is shown in Figure 5.4-6. It is based upon the THTD transient heat transfer computer calculation equilibrium condition, with 700°F bearing lubricant temperatures. The same temperatures would occur with 900°F lubricant except for slightly higher values immediately beneath and adjacent to the bearings and seals. The modulus of elasticity and allowable stress of the tie bolt material vary inversely. An attempt to hold the tie bolt at a constant high stress (high three-year creep rate) throughout its length by selective variation of its diameter will be difficult to achieve because of the higher allowable creep stresses beneath the forward bearing.

The stress distribution which can be achieved in the tie bolt by diameter variation is shown in Figure 5.4-7. The "hot stress" curve shows that with a compromise for reasonable tie bolt forging geometry, the three year creep stress levels beneath stages one and two are above 0.1 percent, but the 0.1 percent level can be maintained through stage seven. It is allowed to drop to a lower creep rate until 0.1 percent is again reached beneath stage eight, then drops again. The "cold stress" curve shows the stress levels required at room temperature to produce an assembly tie bolt force of 12,880 pounds, which would become 10,000 pounds at operating temperature because of the change in modulus of elasticity alone (differential



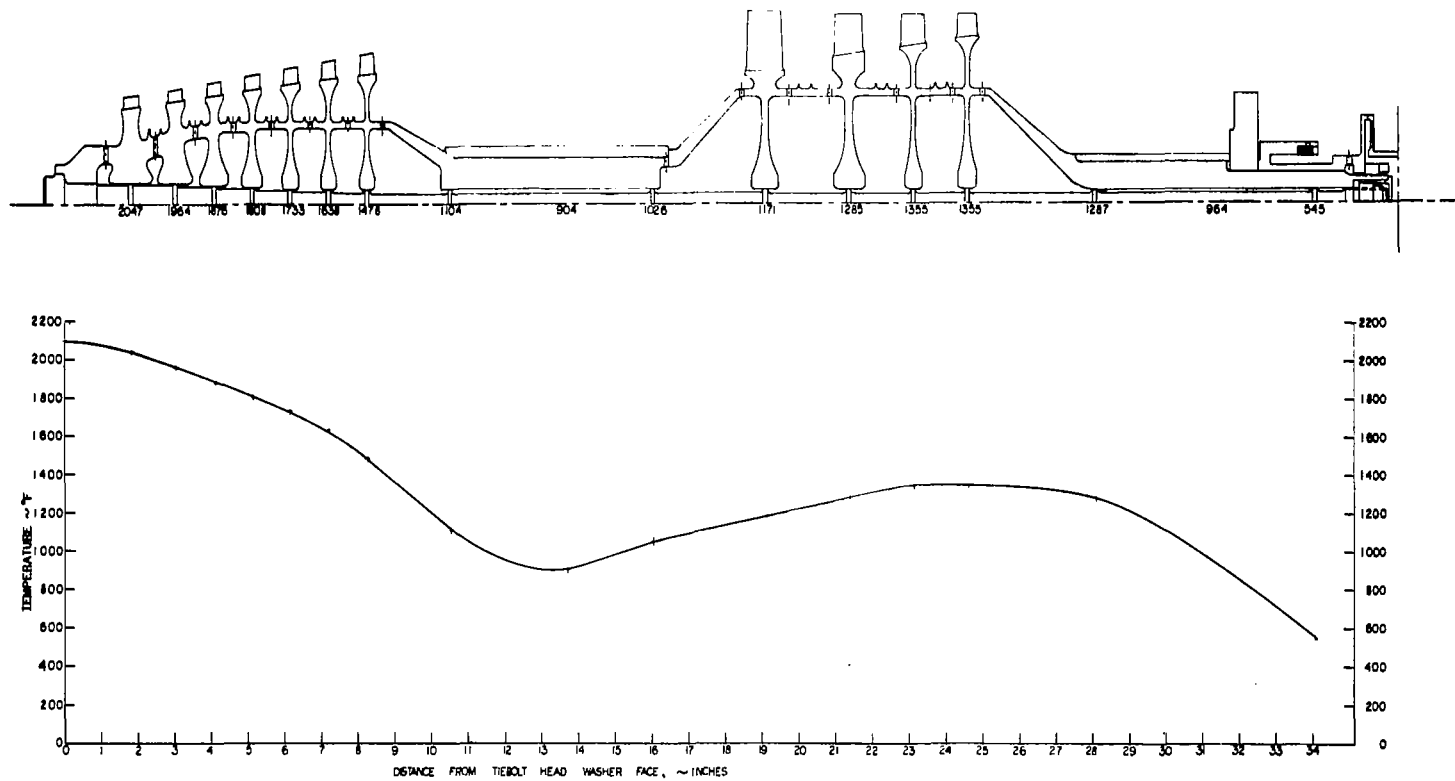


Figure 5.4-6. Tie-Bolt Temperature Distribution for 11 Stage, 19,200 rpm Turbine.

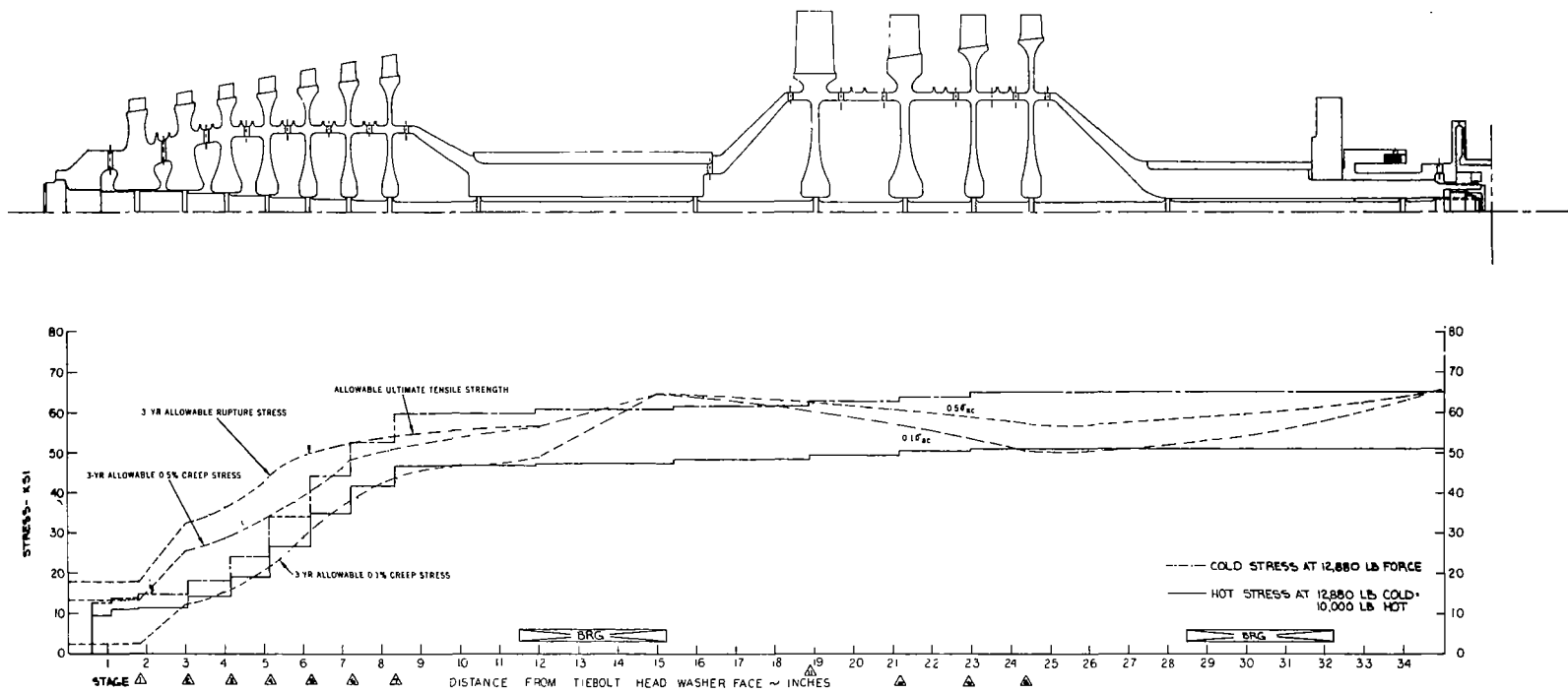


Figure 5.4-7. Tie Bolt Stress Distribution for 11 Stage, 19,200 rpm Turbine.

thermal expansion effects neglected). By holding the creep rate as high as possible throughout while still maintaining an acceptable safety margin, the tie bolt load will decrease less with each increment of strain which occurs. This statement is based upon the shape of a normal stress-strain curve, where small changes of strain cause large changes in stress when the initial stress is low. At high initial stress levels, large strain variations cause small variations in stress. The available tie bolt load is, of course, the tie bolt stress area product.

The effects of differential thermal expansion on the tie bolt load (changes in modulus of elasticity included) is illustrated by Figure 5.4-8. With the rotor length  $l_r$  of 35 inches between tie bolt head and nut, the tie bolt is 0.0110 inch shorter in the room temperature unstressed condition. When the assembly is made (by stretching the tie bolt hydraulically, not by torquing the tie bolt nut), the tie bolt length matches that of the rotor, and a force of 5100 pounds is developed. In the hot condition, the rotor grows 0.1295 inch while the tie bolt grows 0.1035 inch, a difference of 0.0260 inch in length when unstressed. Stretching the tie bolt by this amount produces the desired 10,000 pound force at zero time. The relaxation which occurs over three years will reduce the tie bolt force to approximately 6500 pounds, quite satisfactory since the aerodynamic thrust forces alone more than balance the curvic coupling disassembly forces. The cold unstressed length difference of 0.0110 inch and the hot unstressed length difference of 0.0260 inch do not add up to the 0.0409 inch of hot stretch indicated in the figure. The explanation is that the 0.0110 inch cold stretch produces the same

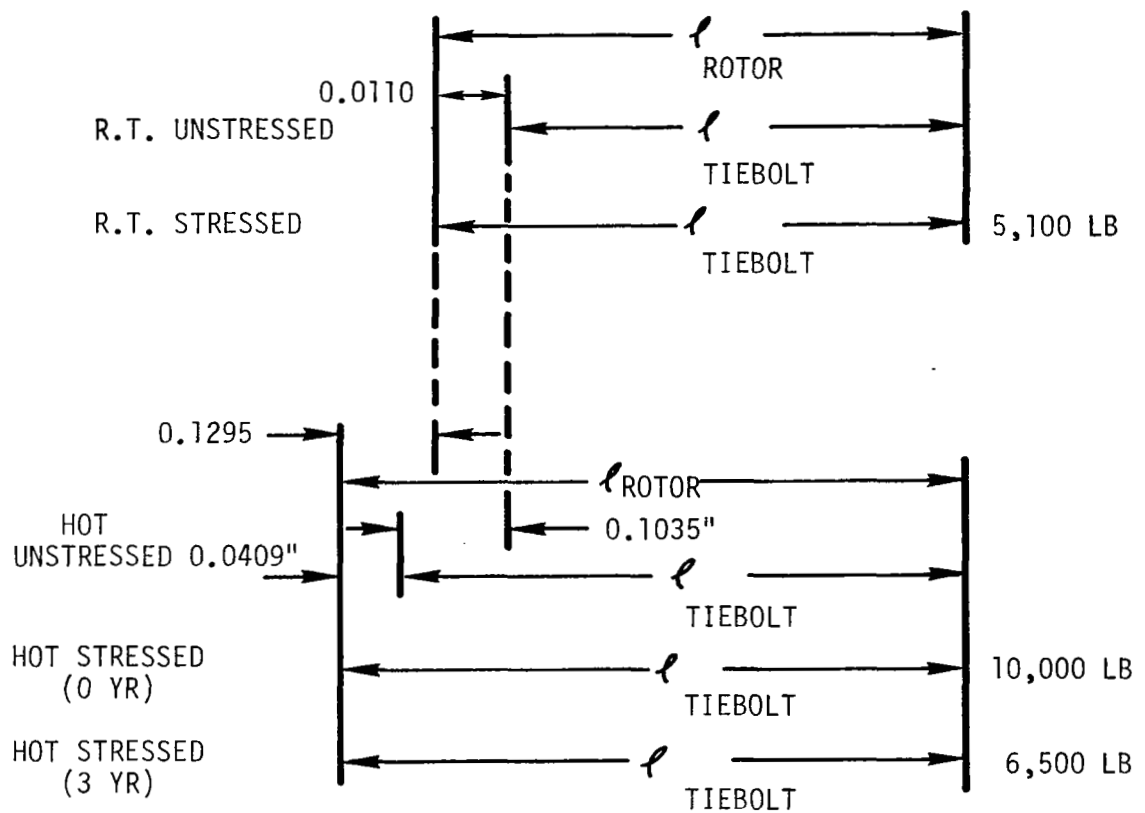


Figure 5.4-8. 7+4 Stage KTA Turbine Tiebolt Elongation.

effect as 0.0150 inch of hot stretch, considering the modulus change. Thus, the differential thermal expansion between rotor and tie bolt, which is caused solely by temperature differences and not by material differences, assists in developing the desired tie bolt load and requires lower assembly stresses.

#### Conical Stub Shafts

The stresses in a typical conical stub shaft and bearing journal are calculated by the ROTOR finite element program. The applied loads, temperature levels, resulting effective stresses, and allowable stresses are shown in Figure 5.4-9. Restraints are imposed upon the TiC + 10% Cb bearing journal to account for the different thermal expansion rates of the two materials. The stress map shows areas of stress concentration at the ends of the carbide journal caused by differences in thermal growth. At no point in the structure, however, do the effective stresses closely approach the allowable three-year 0.1 percent creep stress of the KDTZM-1175 shaft or the ultimate compressive strength of the TiC + 10% Cb journal. The acceptability of this typical conical stub shaft indicates that the remaining conical portions, with lower thermal levels and thermal gradients, present no unacceptable design problems.

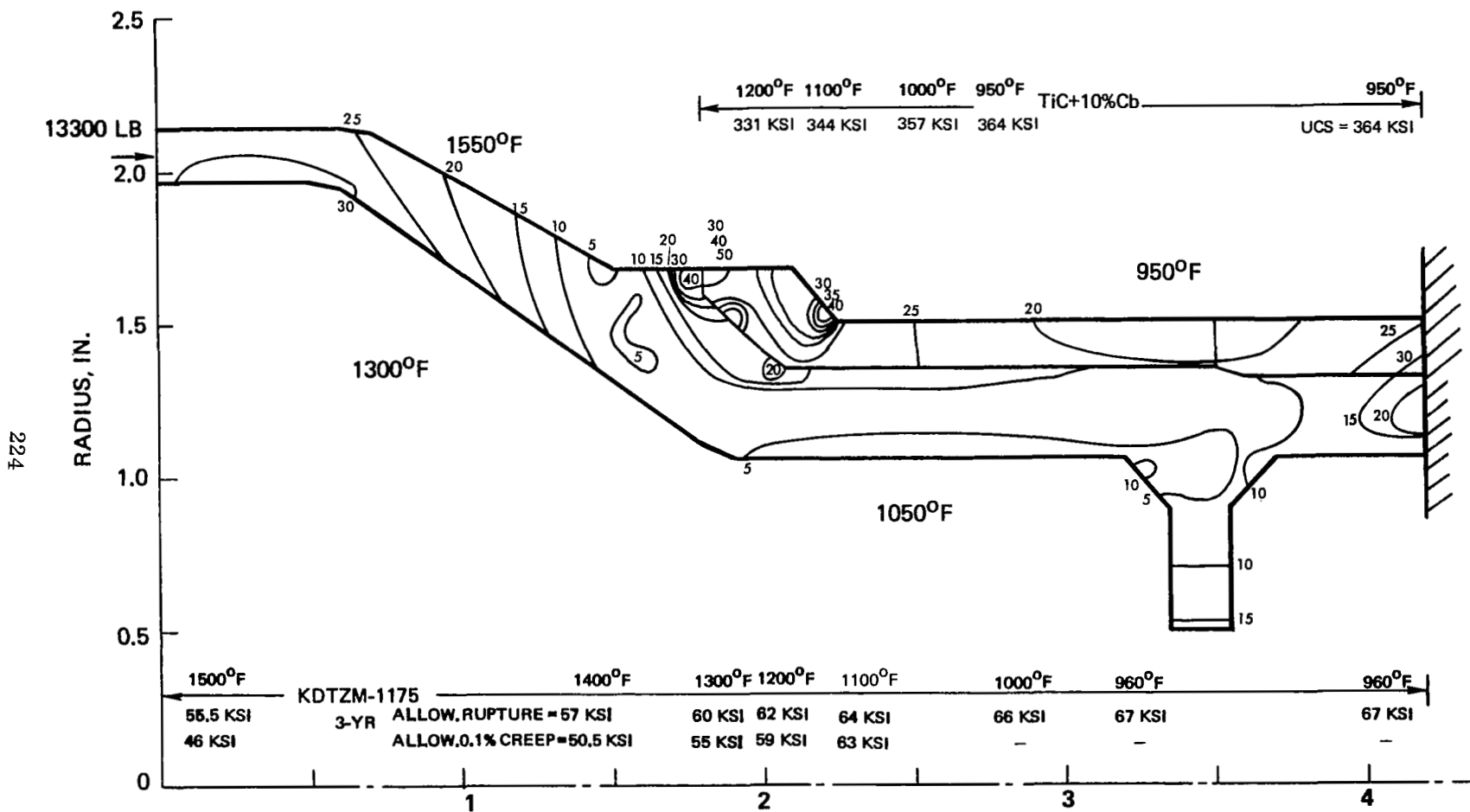


Figure 5.4-9. Effective Stresses in Conical Stubshaft Following Stage 7 of 7+4 Turbine (Typical) at 19,200 rpm with Thrust and Thermal Loads.

## 5.5 CASING AND STATOR

### Nozzle Diaphragms

The ROTOR finite element computer program was used to stress analyze several typical nozzle diaphragms. The stage two diaphragm was selected as typical of the higher temperature diaphragms (stage one is non-typical because it is restrained by the inlet duct bullet-nose). Its computation model and effective stress map is shown by Figure 5.5-1. The model has 63 rectangular "blades" 0.11 inch thick, with the rest of the model being 360° rings. This constitutes a modeling deviation, since the actual diaphragms will be split into two 180° segments. The mechanical design pressures are applied forward and aft. The outer ring is fixed to the casing at its axial centerpoint. An artificial 0.001 inch radially inward casing restraint is imposed all around the outer ring to determine its effect. Note that such a restraint could only be developed in the true case by a temperature difference of 900°F between the casing and ring or by application of a large force at assembly, either of which can easily be avoided. This restraint causes peak stresses which are twice the allowable rupture stress of 7.5 ksi, therefore, such a restraint condition must be avoided. The loads and stresses due to pressure differentials alone will be very low, according to a deflection plot which is produced with the stress calculations.

The stage seven nozzle diaphragm is chosen as another one typical of the high pressure stages. The analysis model is similar to that of stage two, 0.001 inch of radial restraint again imposed requires a temperature differential of 750°F, far higher than is expected.

T-111 AT 2050°F  
 3-YR ALLOWABLE RUPTURE STRESS = 7,500 PSI

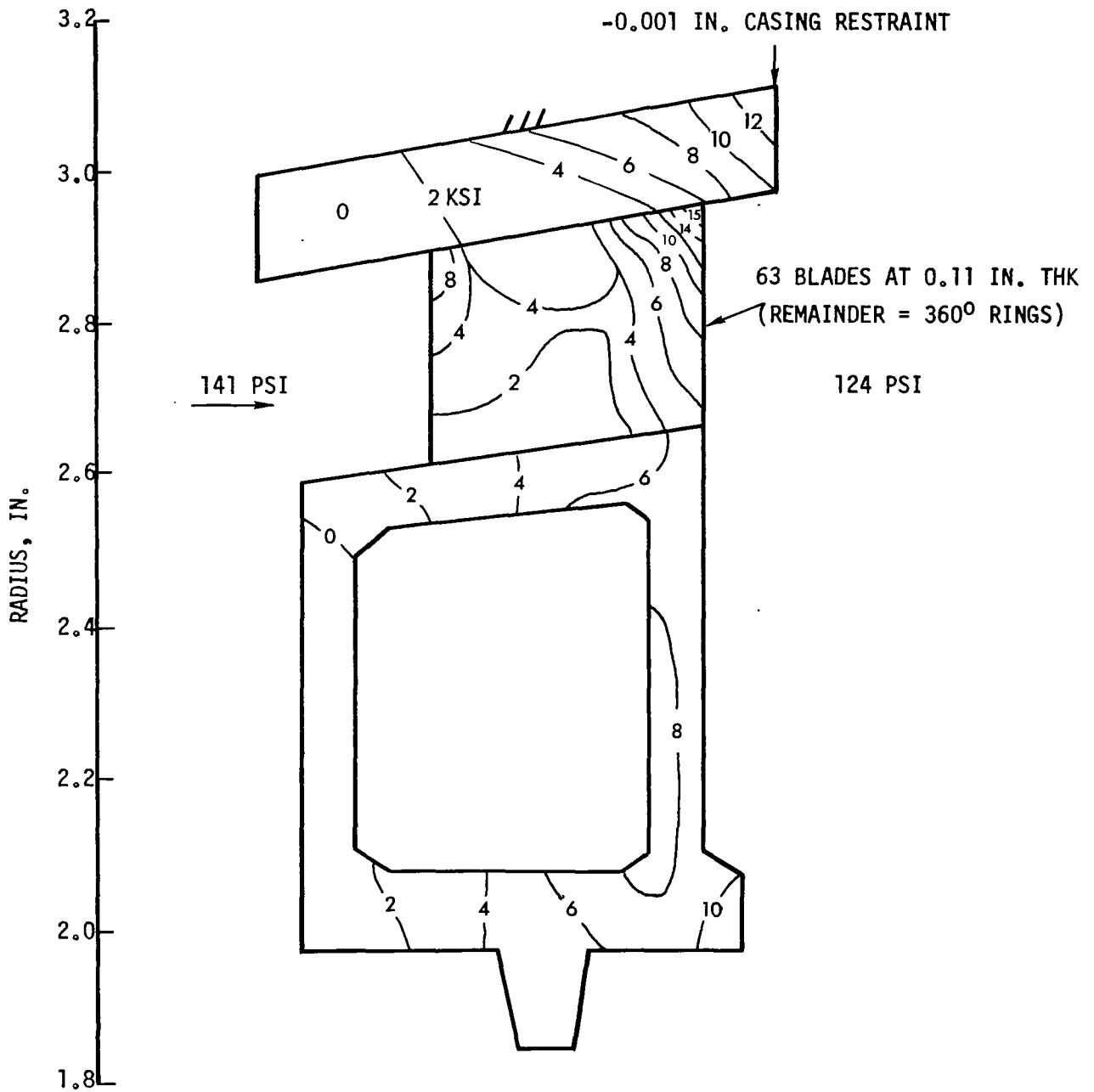


Figure 5.5-1. Effective Stresses in Stage 2 Nozzle Diaphragm of 7+4 Turbine.



The eight psi mechanical pressure differential and 80 vanes of stage seven are used. The maximum predicted stress of 23 ksi shown in Figure 5.5-2 indicates that even the artificial restraint can be tolerated by the T-111 material. However, Cb-1Zr at 1680°F could not do so, nor could it withstand the differential pressure stresses alone. Therefore, T-111 is the recommended casing material for all the high pressure turbine stages. The analysis model of the same diaphragm split into 180° segments is shown in Figure 5.5-3. The thickness perpendicular to the plane of the paper vary as shown in the previous figure. To obtain a maximum of information, artificial radial casing restraints of 0.001 inch and 0.010 inch were applied at two points. The dangers of such restraints are again emphasized by the high stresses predicted, which reach 80 ksi at the 0.010 inch restraint and exceed the allowable rupture stress at the 0.001 inch restraint (probably influenced by the larger restraint). The restraints will be avoided in the actual case.

Having learned the penalties for building restraints into nozzle diaphragm design, the stage 11 nozzle diaphragm was analyzed without restraint as a typical low pressure diaphragm. The model and stress map are shown in Figure 5.5-4. The resultant stresses were exceedingly low, being two ksi maximum - well beneath the allowable rupture stress of 21.5 ksi for Cb-1Zr. This material is recommended as satisfactory for the low pressure stages.

### Casing

The pressure stresses in the casing surrounding each stage of the turbine are calculated, using cylinders of 0.125 inch thickness

T-111 AT 1680°F  
 3-YR ALLOWABLE RUPTURE STRESS = 37,500 PSI

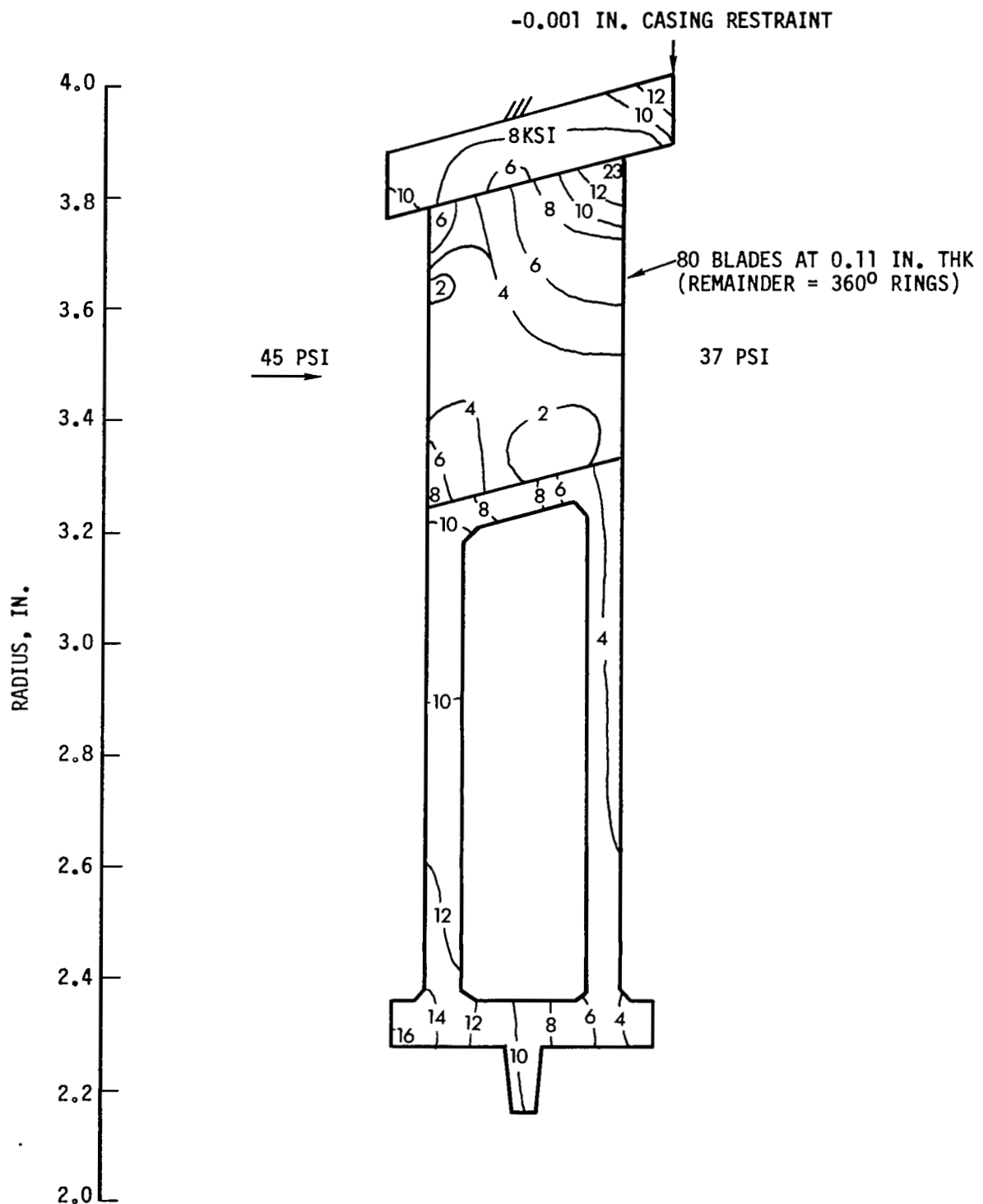


Figure 5.5-2. Effective Stresses in Stage 7 Nozzle Diaphragm of 7+4 Turbine.

T-111 AT 1680°F  
3-YR ALLOWABLE RUPTURE STRESS = 37,500 PSI

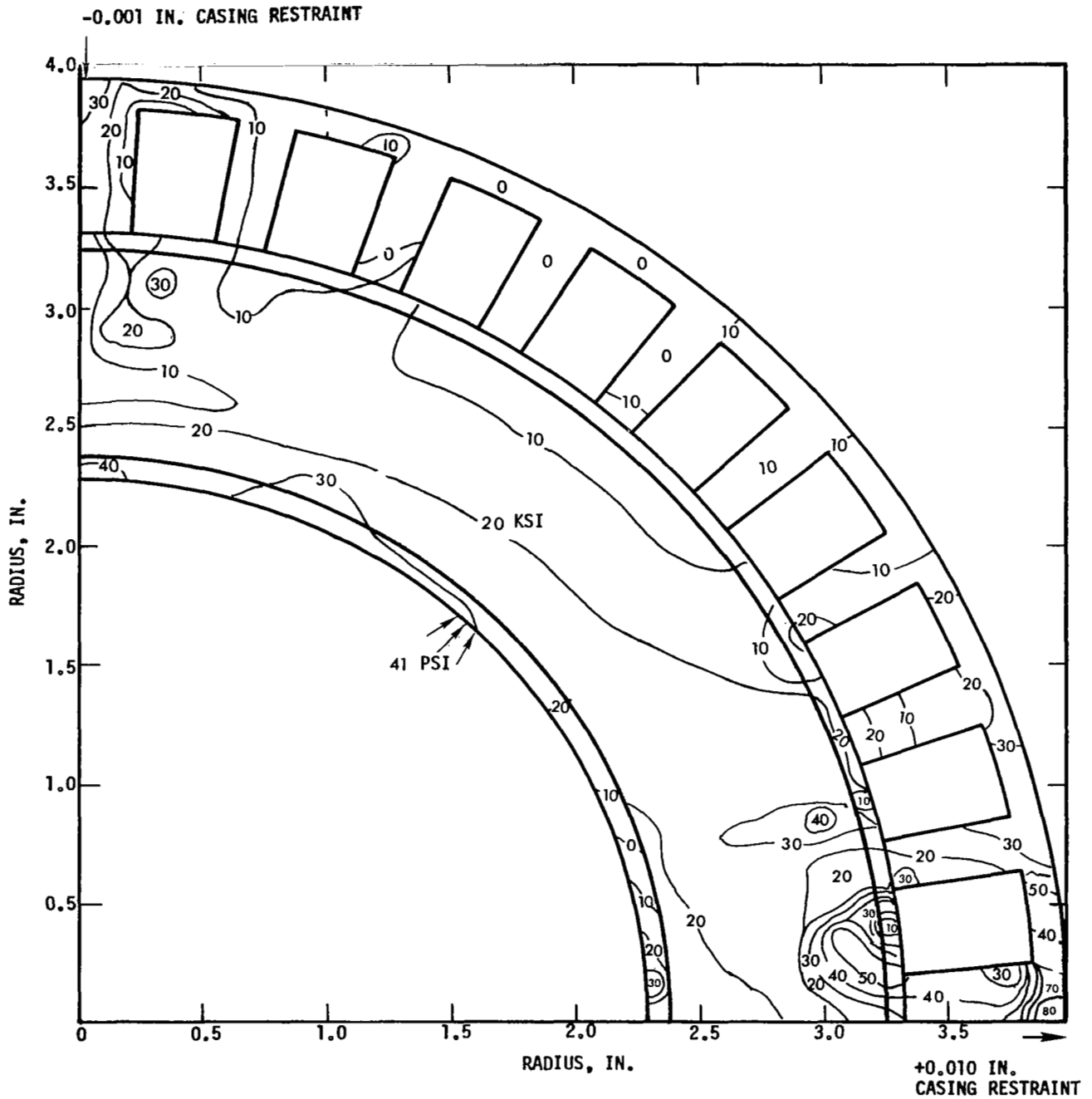


Figure 5.5-3. Effective Stresses in Stage 7 Nozzle Diaphragm of 7+4 Turbine.

Cb-1Zr AT 1310°F  
 3-YR ALLOWABLE RUPTURE STRESS = 21,500 PSI

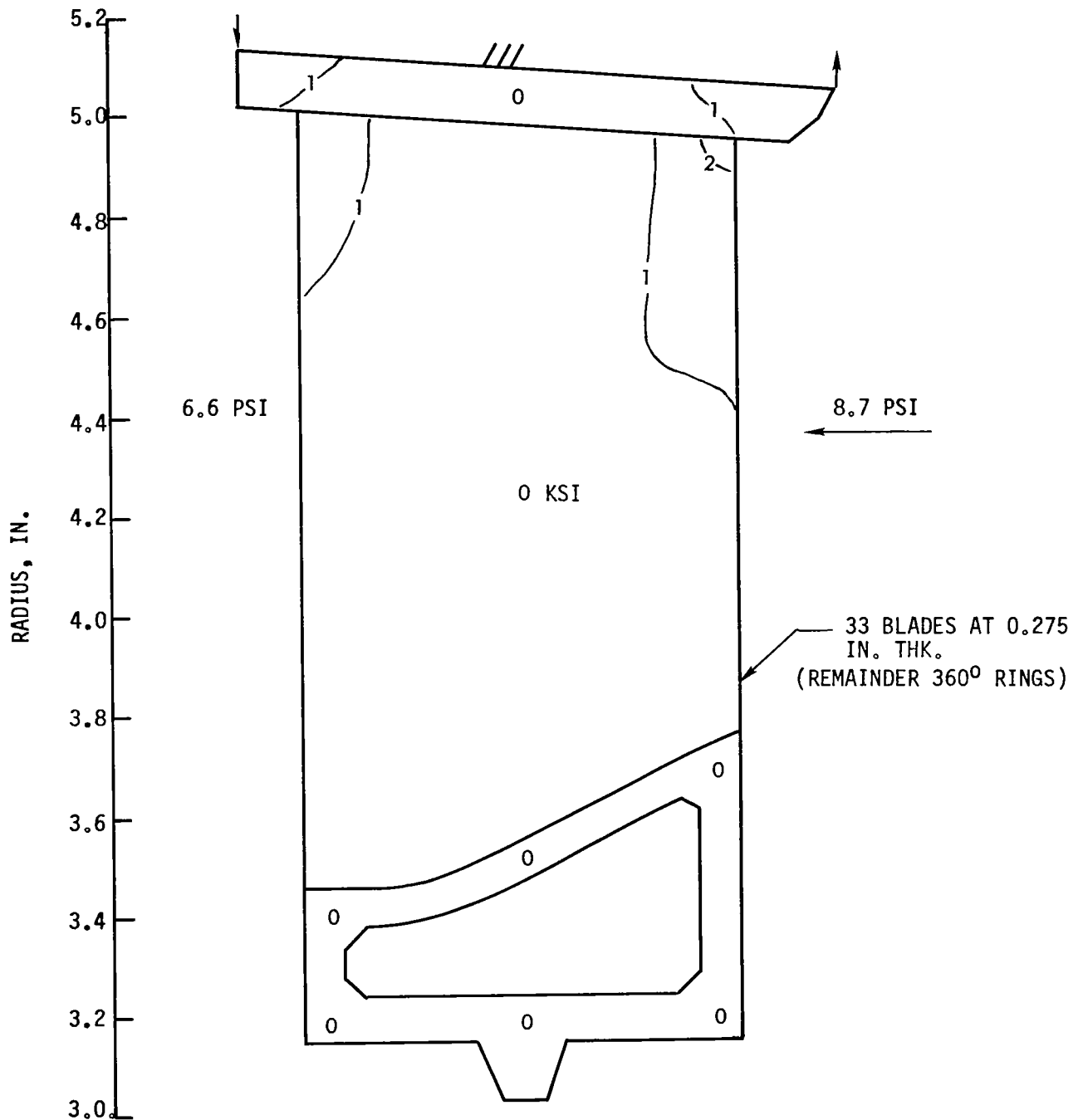


Figure 5.5-4. Effective Stresses in Stage 11 Nozzle Diaphragm of 7+4 Turbine.

as the analysis model. As Table 5.5-1 shows, the effective stresses are well below the allowable three-year 0.1 percent creep stress, with factors of safety from 1.4 - 22.9 in the high pressure T-111 casing and 7.5 - 40.0 in the low pressure Cb-1Zr casing. These results indicate that only the first two or three stages of the turbine are likely to be stress-limited. Therefore, the casing dimensions are determined by deformation considerations.

The most important casing components with respect to deformation are the bearing housing support frames. Their deflection rates can very seriously affect the performance of the bearings because they are a spring in series with the bearing fluid film. If the housing is too soft, the bearing load deflects the housing instead of developing the hydrodynamic pressures in the bearing and the thin fluid film required for good damping. In this case, the dynamic response of the rotor can be very adversely affected, until the rotor deflection exceeds the clearance in the bearing and catastrophic rubbing occurs.

Preliminary calculations indicate that the pierced cone plus webs of the turbine forward bearing support structure is adequately stiff to support the expected loads without excessive deflection. The complexity of the structure, shown in Figure 5.5-5, makes an exact analysis very difficult. By calculating the moment of inertia of the structure about a diameter of the rotor at discrete steps and applying a unit load at the pivot pin of a bearing pad, the response may be estimated. A deflection rate of more than  $10^7$  lb/in. was calculated, which is sufficiently high to cause no significant deterioration of bearing performance. The true performance of the structure would be best determined by fabricating and testing a model.

TABLE 5.5-1  
CASING PRESSURE STRESSES

(0.125 In. Wall Clyinders Assumed)

Stage No. —	Effective Stress, ksi	Material —	Temp., °F	3-Year 0.1% Creep Stress, ksi	FS <sub>e</sub> —
1	3.5	T-111 ↓	2085	5.0	1.4
2	3.3		1975	8.6	2.6
3	3.0		1920	10.8	3.6
4	2.5		1845	13.5	5.4
5	1.9		1755	17.3	9.1
6	1.5		1670	21.1	14.1
7	1.1		1585	25.2	22.9
8	0.8	Cb-1Zr ↓	1440	6.0	7.5
9	0.5		1365	6.8	13.6
10	0.3		1285	7.5	25.0
11	0.2		1205	8.0	40.0

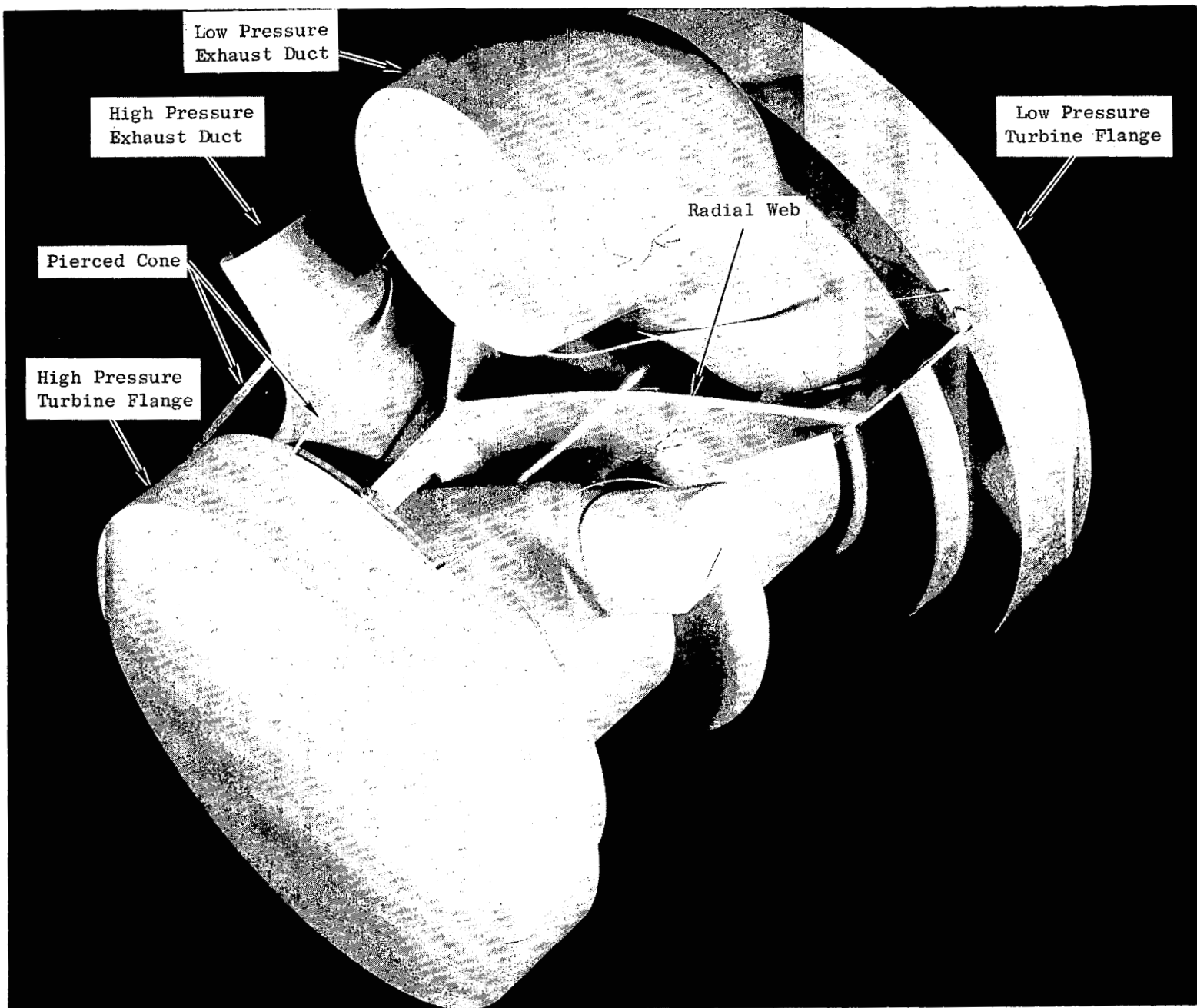


Figure 5.5-5. Forward Turbine Bearing Support Structure.

The stiffness of the alternator end bell bearing support structure, which is similar to the turbine end bell, has been estimated at  $6 \times 10^5$  lb/in. This rate is low enough that its effects on bearing performance can be noted as a decrease in the critical speed of the rotor. The end bells have not yet been redesigned to significantly raise their stiffnesses, but no particularly difficult obstacles would prevent making the required changes, such as termination of the end bell cone directly outboard of the bearing pivot pins to eliminate cantilevered components, use of gussets, and similar approaches.



## 5.6 THERMAL CONSIDERATIONS

### Differential Thermal Expansion

Despite the high temperature levels, the problem of differential thermal expansion between the turbine rotor and stator components is not a serious one, since all the primary materials are refractory metals with very similar coefficients of thermal expansion. These small differences can cause major difficulties when they result in interference of components. Between the static and rotating components, however, relatively generous axial tolerances of 0.060 inch or greater can be provided without seriously affecting the desired flow path. The temperature gradients between the rotor and the casing at a particular axial station are relatively small, and very little radial clearance at blade tips is required for differential thermal expansion.

The steady-state conditions of thermal equilibrium cause less differential thermal expansion problems than do the transient start-up conditions assumed. The transient heat transfer computer program used requires proper thermal properties of the materials involved and surface interface conductance assumptions similar to those successfully used in the three-stage turbine analysis. The turbine was assumed to be slowly preheated to thermal equilibrium at 600°F, then instantaneously subjected to full cycle temperature (all stages at their design temperature). The resulting equilibrium temperatures are shown by Figure 5.6-1. For this model, the bearing lubricant cavities were assumed to be at 700°F and the flexible diaphragm coupling at 400°F, both several hundred degrees cooler than the final assumptions. The primary conclusions of the thermal analysis, for both the transient and steady-state conditions,

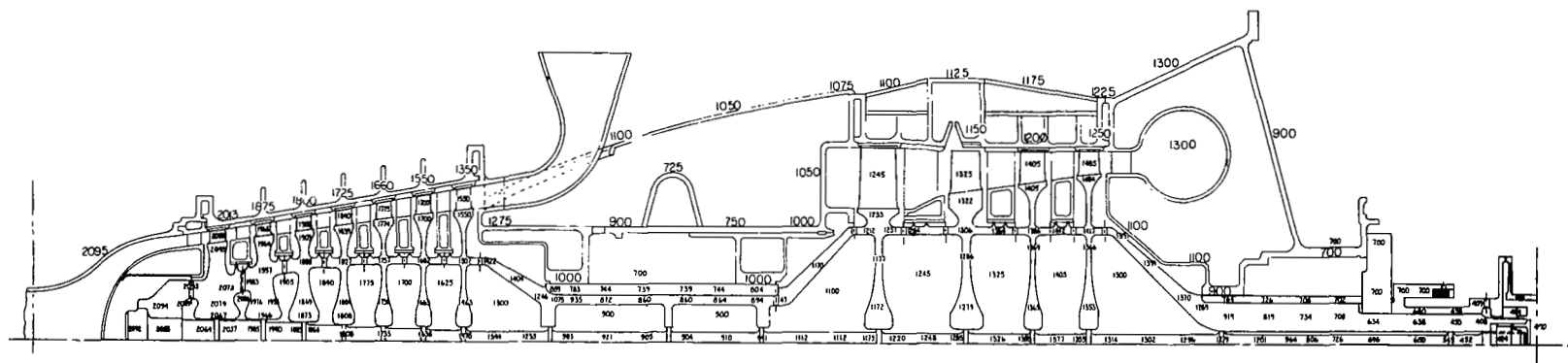


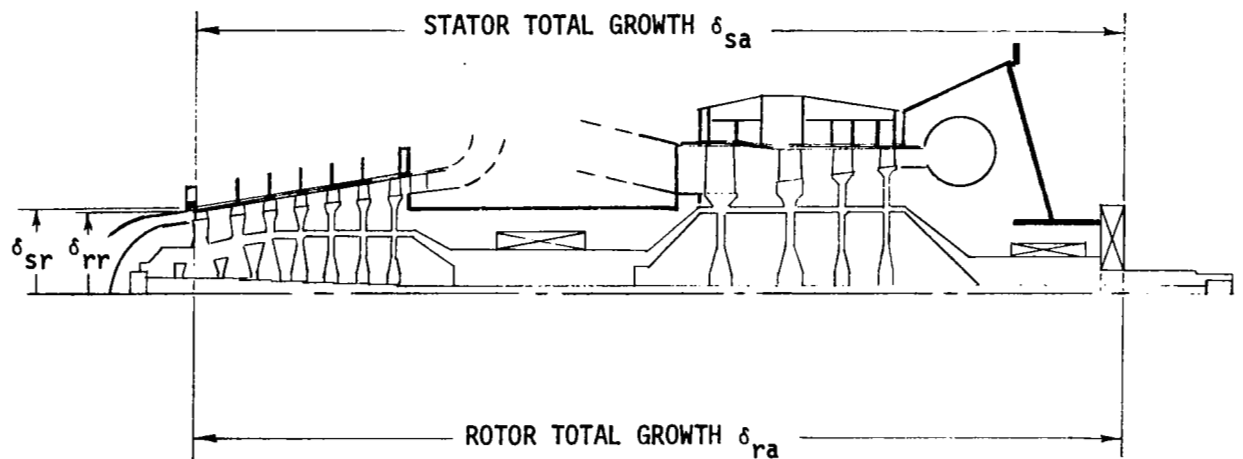
Figure 5.6-1. General Turbine Temperature Distribution.

are shown on Figure 5.6-2. The stator total growth and rotor total growth are both referenced to the common point of the aft face of the thrust bearing runner. The summation of expansions of each element of the casing structure along the most direct path to the forward side of the stage one tip seal and the summation of expansions of each rotor element along the most direct path to the forward side of the stage one wheel were calculated. The difference between these two values indicates the magnitude of the axial thermal expansion problem. Less than 0.030 inch of axial clearance is required, even at start-up, for differential thermal expansion between rotor and stator. The maximum radial differential is less than 0.005 inch. Therefore, an axial clearance of 0.060 inch between rotating and stationary parts is satisfactory, and the achievement of 0.010 inch radial tip clearances at equilibrium is a reasonable goal.

The temperature differences between the tie bolt and the rotor path which includes the torque tubes, the wheel thicknesses at torque tube radii, the conical stub shafts, and the bearing/seal journals help to load the tie bolt. Therefore, less tie bolt deformation is required at assembly to produce a desired axial load at operating conditions. This effect has been previously presented.

### Insulation

The multi-foil insulation selected to reduce the radiation losses from the turbine will surround the entire turbine package instead of individual components, such as the crossover ducts. As shown by Figure 5.6-3, a conical section intimately surrounds the hot inlet duct and high pressure turbine casing, with closed cylinders surrounding



● RESULTS

MAX. AXIAL  $\Delta\delta < 0.030$  IN. (START-UP)  
 MAX. RADIAL  $\Delta\delta < 0.005$  IN. (START-UP)

● CONCLUSIONS

USE 0.060 IN. AXIAL ROTOR-STATOR CLEARANCE  
 0.010 IN. RADIAL CLEARANCE IS SATISFACTORY

Figure 5.6-2. Differential Thermal Expansion Between Rotor and Stator.

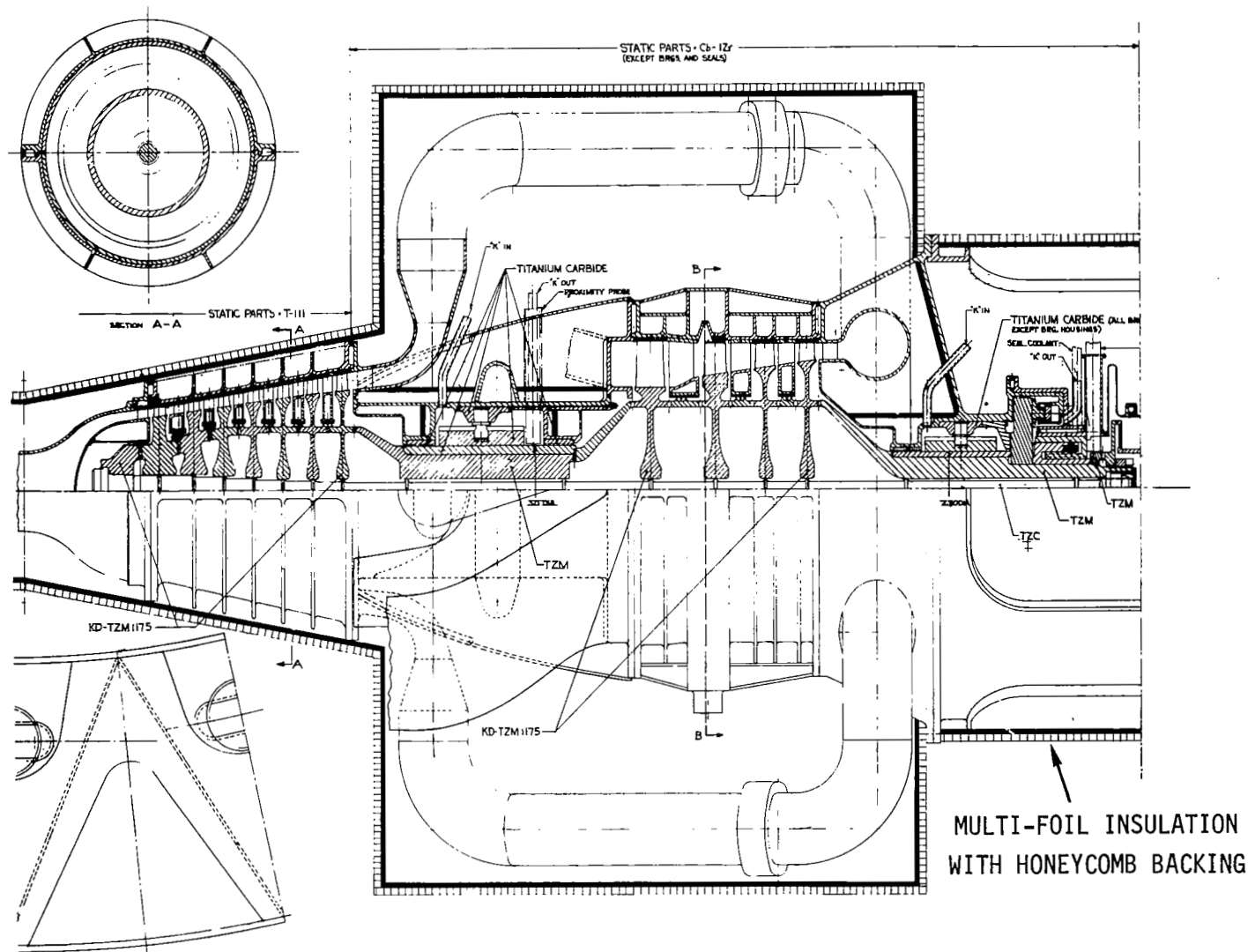


Figure 5.6-3. Thermal Insulation of 7+4 Turbine.

the remainder of the casing and turbine-alternator support structure. The maximum diameter of the insulation is 27 inches.

The insulation is composed of 80 layers of 0.001 inch Mo and Ni foil separated by micron-size  $\text{ZrO}_2$  particles, with a total thickness of 0.125 inch. The layers of foil are backed by 0.250 inch of Cb-1Zr honeycomb for strength. This type of insulation uses technology developed for the Brayton Cycle Heat Receiver program. With a total weight of 40 pounds, the total heat loss of the turbine at normal operating temperatures is held to 0.2 kw, which is considered acceptable. Approximately 50 percent of this loss occurs at the joints between different geometries, where the insulating efficiency of the multi-foils cannot be maintained despite complicated and expensive fabrication methods.

## 5.7 TURBINE-ALTERNATOR COUPLING

The turbine-alternator coupling is analyzed by the methods presented in the Phase I discussion. With a total torque of 1,385 in.-lb to be transmitted in steady-state operation, the torque imposed on the design was 3,632 in.-lb for steady state and 10,895 in.-lb for overload stress computations. A cyclic torque of ten percent of the continuous torque was assumed. The combined conditions of  $\pm 0.0125$ -inch axial misalignment, 0.3 deg. misalignment of the centerlines of the turbine and alternator shafts, and 0.003 inch parallel offset misalignment of shafts were assumed. The fabrication material chosen was 18 percent Ni maraging steel, which is compatible with the assumed temperature limit of 800°F in the coupling zone.

The physical dimensions of the coupling selected are shown by Figure 5.7-1. The 1.5 inch floating shaft length is considerably shorter than the length assumed in the Phase I studies, but the design is satisfactory. The coupling is joined to the turbine by a half-barrel curvic coupling, which allows the different thermal expansions of the TZM turbine rotor and the 18 percent Ni to occur without adverse alignment or stress effects. A TZM shaft nut retains engagement of the curvic coupling teeth. A similar curvic coupling on the alternator end of the flexible diaphragm coupling completes the assembly. In this case, however, the axial retention force is provided by multiple small bolts. Since the coupling assembly is the final rotor assembly operation, it is necessary for the aft coupling joint to be made with bolts which are externally accessible. The curvic flanges of both shafts are joined to the shafts with low stress concentration - especially desirable for the brittle material.

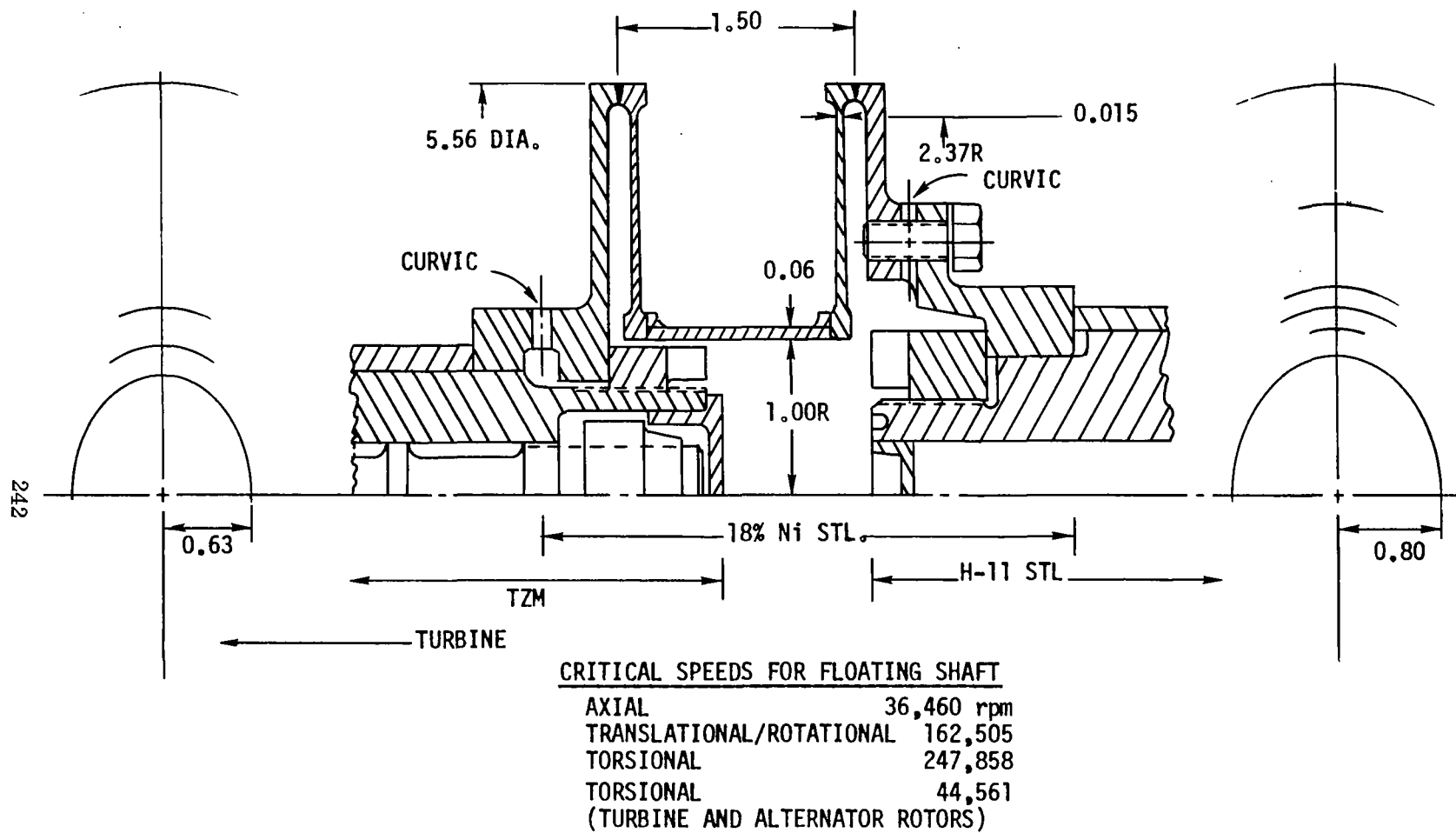


Figure 5.7-1. Flexible Diaphragm Coupling Connecting KTA Turbine to Alternator.



The critical speeds of the floating shaft dictated some of the flexible coupling design decisions. The axial critical speed of 36,460 rpm is 1.9 times the operating speed of 19,200 rpm. The translational/rotational and torsional critical speeds (with only the inertia of the floating shaft considered) are much higher. The torsional critical speed with the inertia of the turbine and alternator rotors considered is 44,561 rpm ( $2.3 N_D$ ). It is believed that these margins are acceptable.

The operating experience of GE-NSP with flexible diaphragm couplings is represented by the one used as a part of the three-stage potassium turbine drive train, and which has operated satisfactorily for 1500 hours of testing. This coupling is shown by Figure 5.7-2. Misalignments similar to or even less than those assumed for this study were achieved at assembly.

The safety of the selected flexible diaphragm coupling design with respect to torsional shear stress is illustrated by Figure 5.7-3. The design condition will produce stresses significantly below those allowable for fracture, buckling, continuous duty. Using the high torque values previously cited, the factor of safety with respect to buckling exceeds 21 for steady-state operation and exceeds five for the maximum torque.

Safety of the coupling design with respect to the effective bending stresses caused by the shafts' misalignments is indicated by Figure 5.7-4. Again, the design point condition is appreciably below the allowable failure or continuous duty stresses. The factor of safety with respect to the continuous duty allowable stress, itself a quite conservative number, is 2.4. The significance of this margin upon the assumed misalignments is illustrated by Figure 5.7-5, which maps the

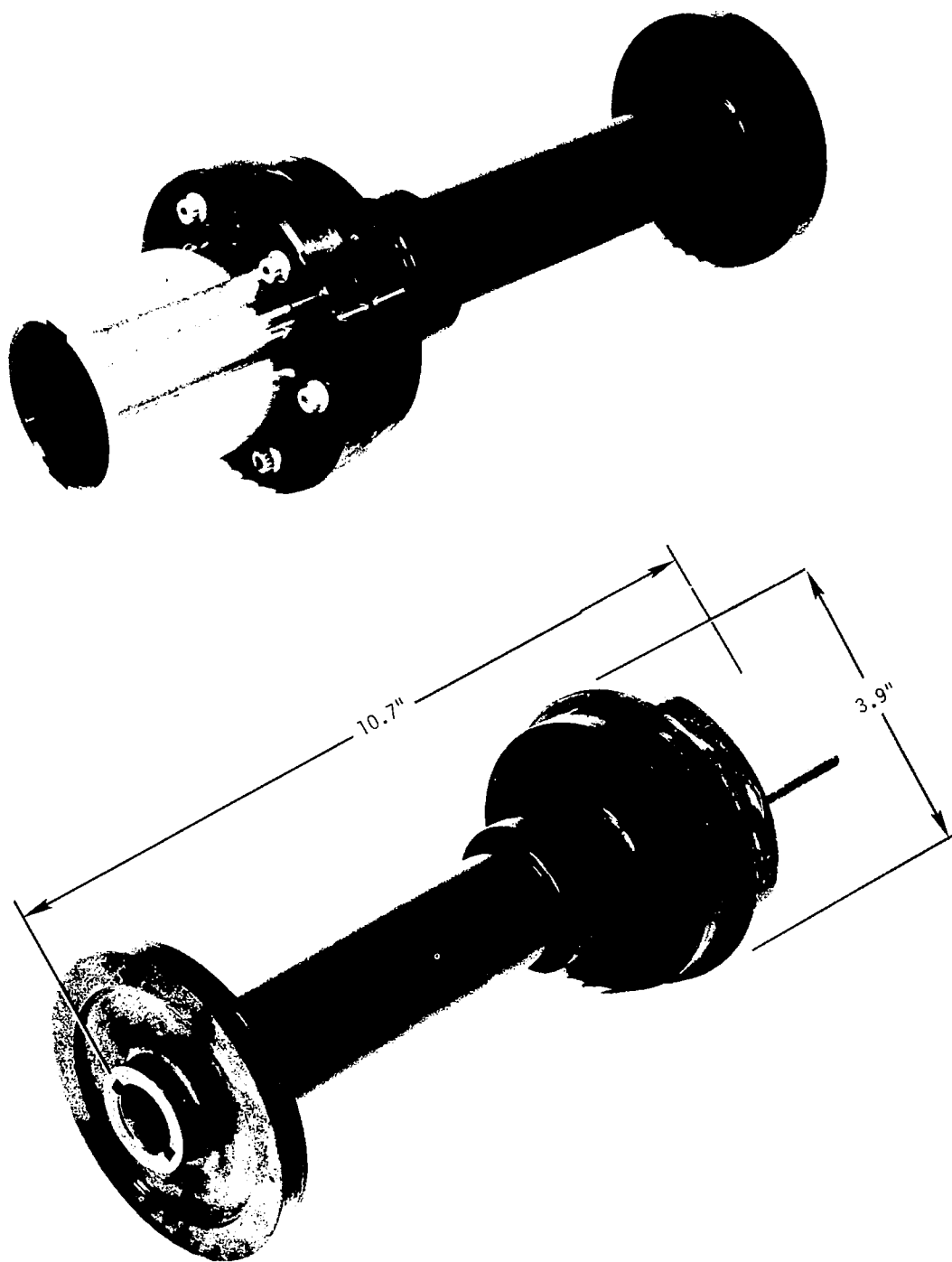


Figure 5.7-2. Flexible Diaphragm Coupling.

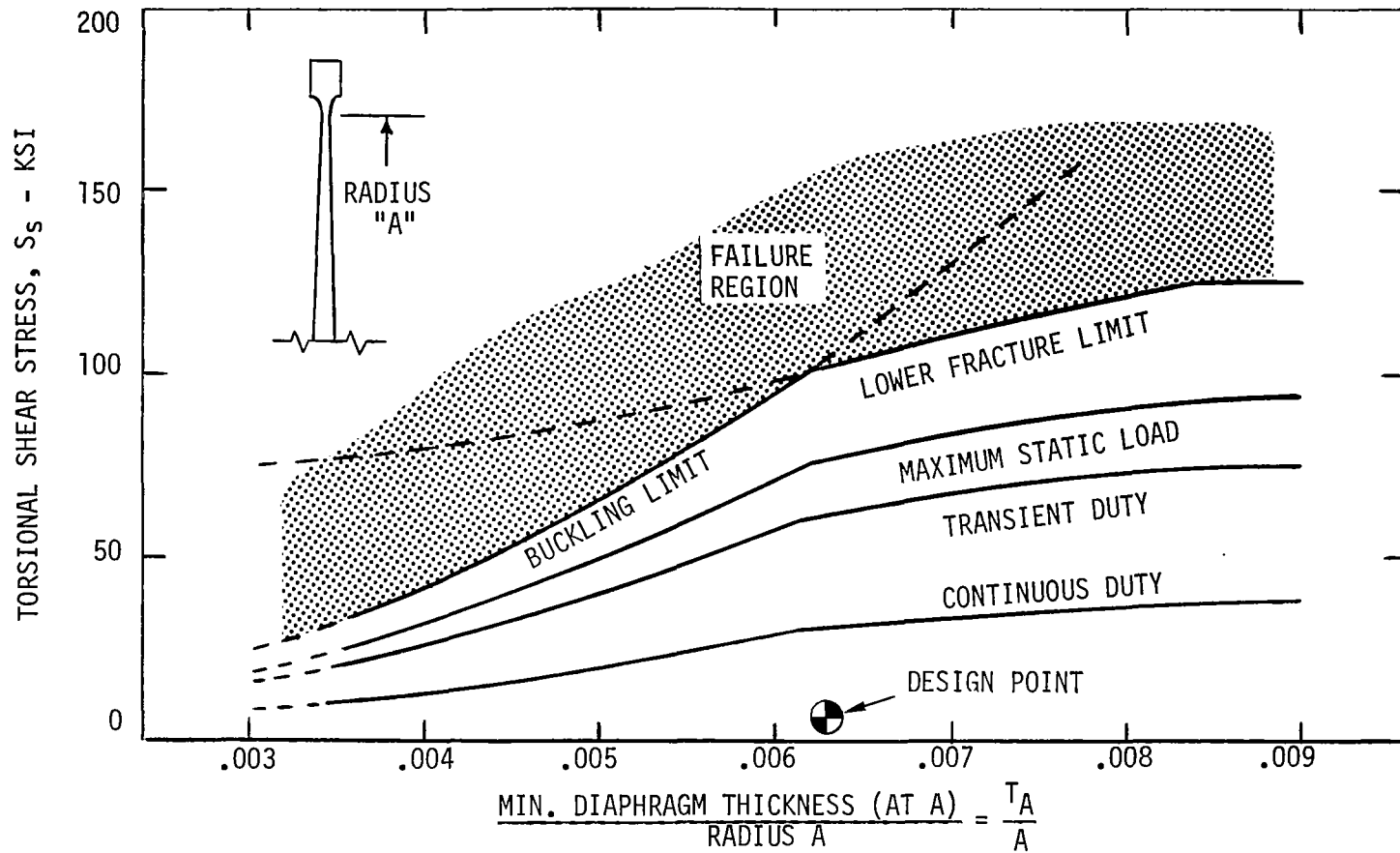


Figure 5.7-3. Maximum Allowable Diaphragm Torsional Stress Levels.

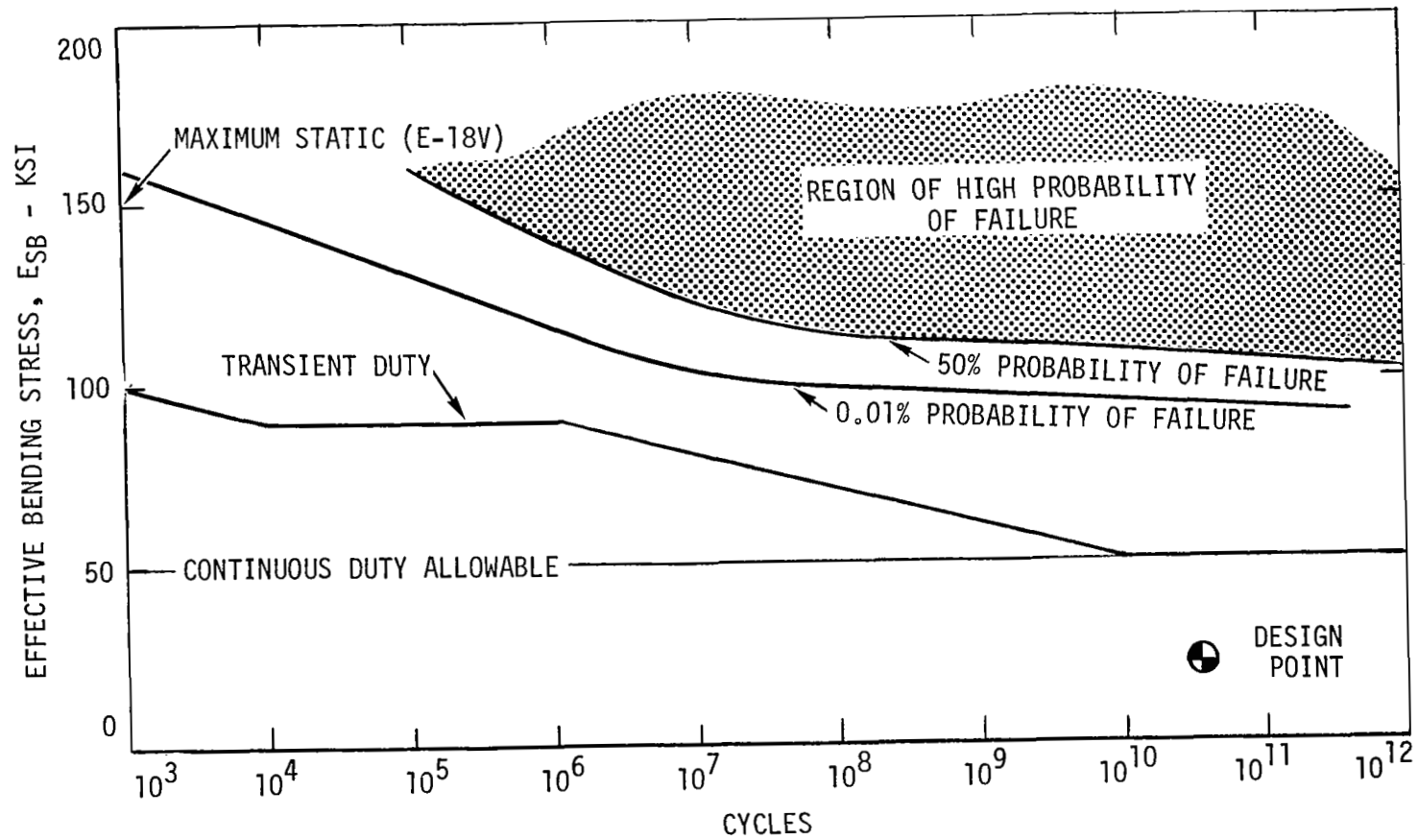


Figure 5.7-4. Maximum Allowable Diaphragm Effective Bending Stress Levels.

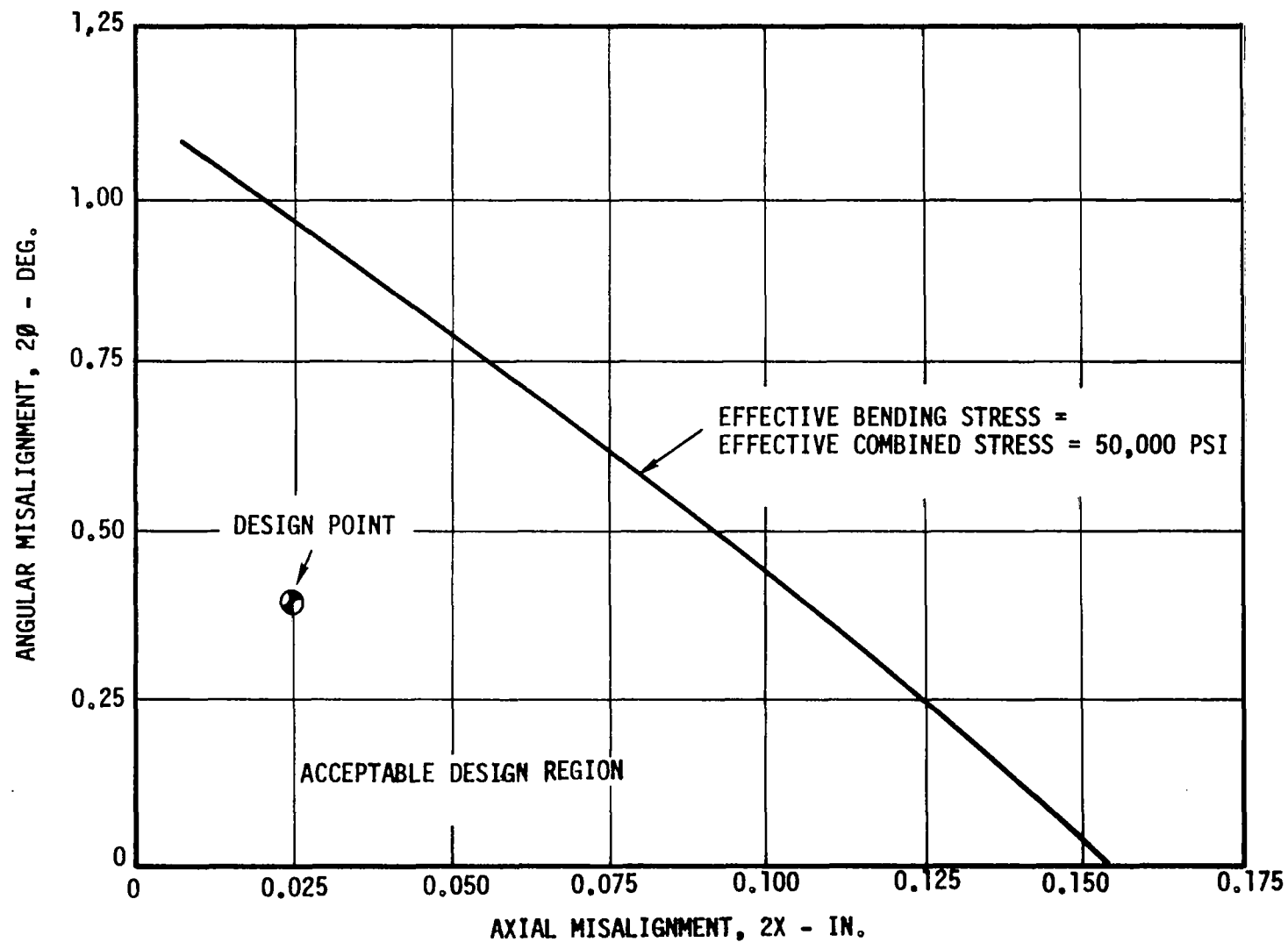


Figure 5.7-5. Allowable Combined Angular and Axial Misalignments for Flexible Diaphragm Coupling.

region of misalignments which are allowable in order to have an effective bending stress or effective combined stress (torsional shear stress included) of less than 50 ksi. These misalignments must not be exceeded at operating conditions, which could require that entirely different misalignment conditions be met at assembly. The primary source of changes in misalignments is the thermal expansion of all components in the loop: flexible coupling, turbine shaft, aft turbine bearing and housing, turbine casing, turbine-alternator connecting frame, alternator housing, fwd alternator bearing and housing, alternator shaft, flexible coupling. With reasonable similar temperatures and coefficients of thermal expansion through this loop, the selective assembly misalignments of the flexible diaphragms can be made to compensate for differential thermal expansions. For instance, if operating conditions produce more deformation in the rotor thermal loop than in the stator thermal loop, the diaphragm centers would be deflected toward each other, producing bending stresses. However, the diaphragm could be assembled with their centers deflected away from each other so that the bending stresses during operation are largely eliminated. The high allowable static and transient effective bending stresses allow compensation for appreciable differential thermal expansion.

## 5.8 INSTRUMENTATION

The instrumentation required for properly monitoring the turbine operation must be included in the design from its inception because of the extreme difficulties likely to be encountered in penetrating the complex casing.

Total temperature should be measured by eight thermocouples in four planes - two T/C in the inlet duct well forward of the bullet-nose, two T/C in the exhaust duct immediately aft of stage seven, one T/C in each of two crossover ducts before exit into the low pressure turbine inlet scroll, and two T/C in the exhaust duct immediately aft of stage 11. These are the minimum total temperature measurements which will describe the turbine thermodynamic performance. Their locations are denoted on Figure 5.8-1. The thermocouples will be 0.005 inch bare-wire W3%Re-W25%Re insulated with  $Al_2O_3$  beads, inside refractory metal wells. The output of these thermocouples is relatively high, being approximately 11 microvolts per °F. By keeping them outside the planes of the nozzle vanes, flow disturbances are minimized.

The static temperature measurements will be made by monitoring the outside temperatures of the casing with two thermocouples aft of the stage seven rotor, spot-welded to the casing outer surface.

Total pressure will be monitored by probes at the same locations as the total temperature wells.

Static pressure measurements will be made by two probes in the inlet duct forward of the inlet nozzle vanes, two aft of the inlet nozzle vanes, two aft of the stage seven rotor, two aft of the stage eight inlet nozzle vanes, and two in the turbine exhaust duct aft of stage 11.

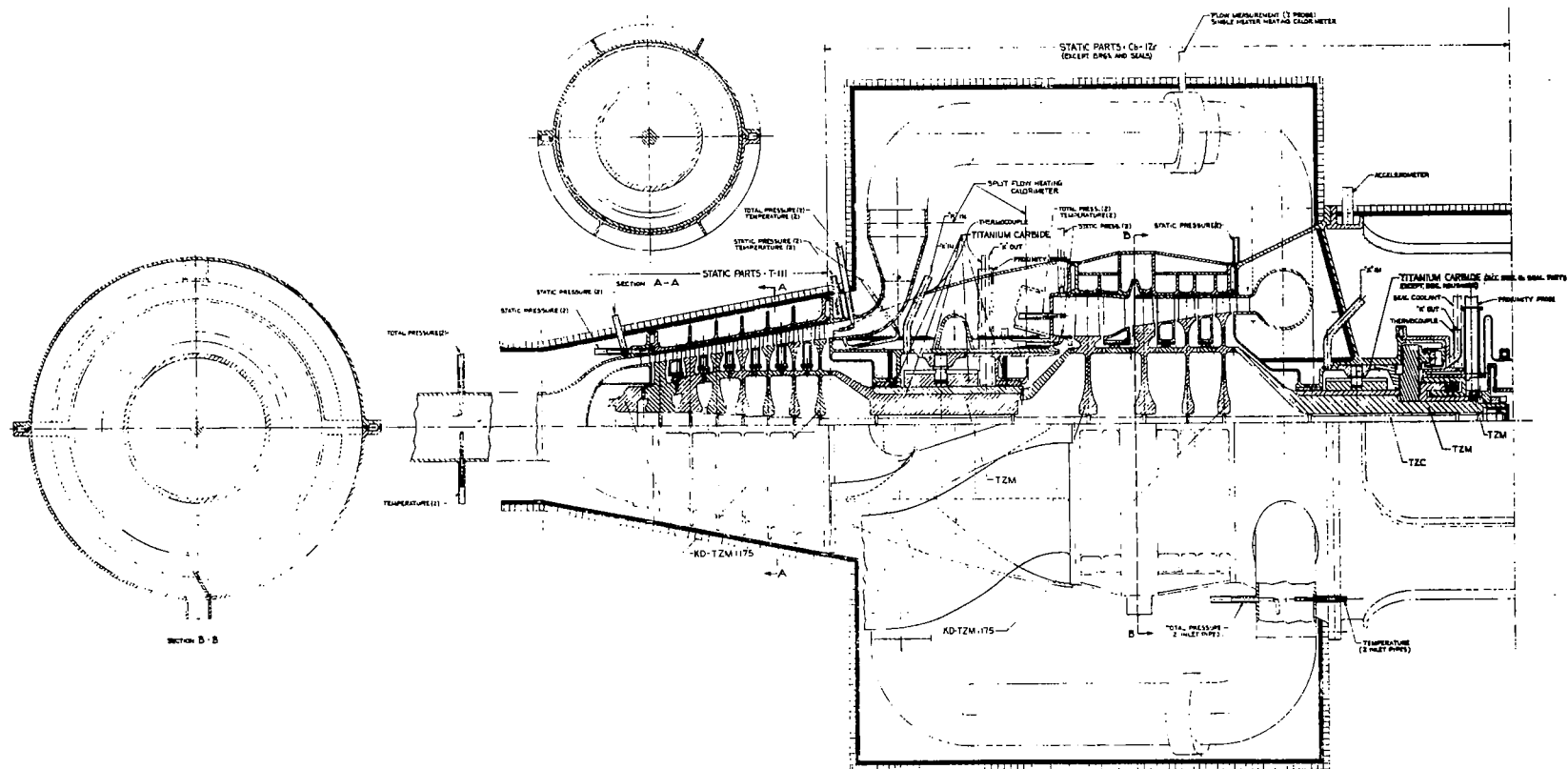


Figure 5.8-1. Instrumentation for 7+4 Turbine.



The pressure measurements will be made with Taylor Gage slack - diaphragm pressure transducers which are maintained at a uniform temperature. These transducers have exhibited excellent zero-shift stability - typically less than three percent per year shift at transducer operation temperatures of 500 - 1500°F on the three-stage turbine program. The high operating temperatures which can be used avoid the problems of coupling tube freezing. The construction material would be T-111 alloy for material compatibility, although stainless steel would perform satisfactorily. An arrangement similar to that used successfully for the Potassium Corrosion Test Loop Program (NAS3-2547) will be used, where 0.375-inch OD x 0.062-inch wall thickness T-111 coupling tubes 12-inches long were arranged so that a liquid leg of loop fluid isolates the transducers from direct contact with the high temperature vapor. Such a configuration allows the transducer operating temperature to be controlled at 700°F even though system vapor temperatures reach 2200°F. For maximum accuracy, each transducer will be installed in an oven which automatically controls the temperature at 700°F.

A differential pressure transducer having a 50 psi full-scale pressure range and backed by accurately measured argon gas pressure will be used to measure the absolute pressure at the turbine exit. Automatic balancing of the argon pressure permits readout on a digital data acquisition system.

The vapor flow measurements will be made using the pressure taps forward and aft of the first-stage nozzle. The nozzle will be calibrated before installation for this purpose.

Bearing lubricant flow rates will be measured by permanent magnet flow meters. All flow meters will have thermocouples attached to the

magnets and the ducts, so that variations in flow rates can be calibrated and used for making corrections to the readings during service.

Rotor displacement measurements will be made by two opposed proximity probes at 90° to two other opposed proximity probes, located within the bearing housings of the forward turbine bearing and the aft alternator bearing - a total of eight proximity probes. Each pair of opposed probes will have matched electrical output to cancel the effect of differential thermal expansion between rotor and casing. The development of such a proximity probe system for use with liquid metals has been underway at GE-NSP for several years. In this system, the sensing head views the rotating shaft through an aluminum oxide window. Shaft radial motion is sensed by measuring the change in fluid film thicknesses up to 0.004 inch. Beyond this distance, probe output drops rapidly and becomes non-linear. It is intended to increase the range of these probes to at least 12 mils. Rotor displacement measurements can be made using state-of-the-art systems with high accuracy at the turbine aft bearing and the alternator forward bearing, since it is possible to locate the probes outside of the liquid metal lubricant containment area.

Vibration pickups usually measure either displacement, velocity, or acceleration, the latter being recommended because it provides the most meaningful information concerning system performance. This type of pickup contains a light mass and stiff spring, with the relative displacement between the mass and its housing being proportional to the acceleration force. Because of a temperature limitation of approximately 450°F for the piezoelectric accelerometers, this instrument could not be directly mounted on the turbine or alternator casing. It

would require mounting on a pedestal outside of the hottest zones. Even so, NaK cooling of the accelerometer would be needed because the ambient temperature surrounding the turbine would be 500 - 800°F. The NaK coolant requires a separate loop.

To obtain the mechanical efficiency of the turbine, its thermal input and mechanical output must be known. Since the alternator, a power absorber, would always be present, it would be desirable to use the alternator output parameters of voltage, current, and phase angle, to measure turbine performance. To do so implies accurate knowledge of both electrical and mechanical alternator losses. However, electrical losses change with load, and bearing and seal losses are affected by clearance and temperature changes. Therefore, it would be most desirable to measure the torque transmitted from the coupling to the alternator. The twist of the flexible diaphragm coupling could be utilized for this purpose, except that the coupling is so torsionally stiff that its deflection is only about 0.30° at full power. Only with an optical enlargement system, such as is used on D'Arsonval galvanometers, could meaningful measurements be obtained. This would involve viewing the coupling through a hermetically sealed  $\text{Al}_2\text{O}_3$  window. No such system is known at the present, and the cost of developing it would be high.

## 5.9 TURBINE SUMMARY

The weight of the Phase II turbine design selected was calculated, based upon the design shown previously and including the exhaust ducts to their inlet into the condenser. The weights are summarized in Table 5.9-1. The total stator weight of 344 pounds and rotor weight of 106 pounds give a turbine weight of 450 pounds. When the frame weight of 28 pounds is added, the total weight is 478 pounds.

Because of the low available strength of KDTZM-1175 in the vicinity of 2200°F and reasonable geometrical limitations, it is necessary to exceed the 0.1 percent creep stress allowable for three years of operation in the stage one wheel and torque tube curvic coupling, in the torque tubes of stages 1 - 4, and in the tie bolt beneath stages one and two. In the remainder of the wheels, the peak hub stresses exceed the 0.1 percent creep stresses allowable at their lower operating temperatures. Most, but not all, of these problems can be decreased by further iterations which were not possible within the contract period. Exceeding the allowable 0.1 percent creep stress does not constitute failure, of course, but is a warning signal which pinpoints areas to which particular care must be given in later design efforts, both in stress and deformation analyses.

The 2100°F inlet temperature is feasible for 19,200 rpm within the assumptions of allowable creep strength and yield strength, with 20 percent overspeed for short periods only. For long-term overspeed, the inlet temperature would have to be decreased by an amount which can only be determined by detailed life-used-up calculations. Such calculations require geometry and stress calculations equivalent to a complete rotor redesign for each assumption of overspeed duration. Since each rotor

TABLE 5.9-1  
TURBINE WEIGHT SUMMARY

● STATOR

HIGH-PRESSURE CASING	53 LB	
LOW-PRESSURE CASING	54	
CROSSOVER DUCTS	35	
AFT SCROLL, CONE, & BRG. HSG.	42	
CASING CONNECTOR	46	
INSULATION	40	
EXHAUST DUCTS	74	
		<hr/> 344 LB

● ROTOR

108

● TURBINE WEIGHT

450

● FRAME

28

TOTAL

---

478 LB

redesign itself requires many iterations on wheel and torque tube geometry and stress, the life-used-up investigation was not possible in the available time. The chances of achieving geometrically feasible solutions in the early stages of the rotor for long-term overspeed duration appear small, considering the loss of available rotor material strength which occurred between the Phase I and Phase II investigations, and the peak hub stresses which became apparent when the detailed stress analyses of Phase II were performed.

The initial hot blade tip radial clearances must be 0.019 inch to 0.010 inch to obtain 0.010 inch minimum tip clearances after three years of operation. The clearance requirements are based upon the creep which will occur in the wheels and blades, and are greater at stage one and less as the operating temperatures decrease.

By using the overhung turbine design, the requirement for turbine forward bearings and seals to operate within a region of 2100°F vapor temperature are avoided. This is most desirable from the standpoint of thermal losses which occur from the vapor to the 900°F lubricant, and to avoid the complexity of the many connectors required to gradually decrease the vapor temperatures within the labyrinth vapor seal. Without the latter, high thermal gradients are expected within the rotor shaft which lead to undesirable thermal stresses.

Buckets with shrouds and dovetails for moisture extraction from the rotor are not generally feasible. Condensate extraction from the stator would be more desirable than from the rotor. Only in certain stages of the rotor is a dovetail solution likely to be possible, and even in these an extensive design effort is required to provide prudent margins of safety.

The tie bolt plus curvic coupling rotor joining method allows an unwelded rotor, which is required by the characteristics of the rotor material which is available for use at the system inlet temperature.

Differential thermal expansion between the rotor and the stator, both radially and axially, is not a major problem because of the similar coefficients of thermal expansion of the materials to be used. The axial clearances required do not require that the vapor flow path be lengthened to an undesirable extent.

The flexible diaphragm coupling between the turbine and alternator will tolerate the axial and radial misalignments which can be held in service, without producing adverse dynamic conditions or requiring lubrication.

The turbine casing is stress limited in the portion surrounding the first two turbine stages and its deflection characteristics must be ascertained in detail, especially in the regions which support the bearings. Because of the complex geometry of the casing, which is necessitated by the crossover and outlet ducting and by the splitting of the casing at each nozzle for rotor moisture extraction, neither hand nor machine computation methods can give highly accurate predictions. Scale model testing is required to supplement thermal, stress, and deflection analyses.

## 5.10 REFERENCES

- 5.2-1 Frank, R.G. and Moor, B.L., "Materials for Potassium Lubricated Journal Bearings, Final Report, Volume V - Friction and Wear Studies," Report No. GESP-100, NASA-LRC Contract No. NAS3-2534, 1969.
- 5.3-1 Kamadoli, B.A., "A Preliminary Design Method for Gas Turbine Wheels and Buckets," General Electric Report No. DF-55-TG-322, August 11, 1955, p.12.
- 5.3-2 Kamp, R.H., Hirschberg, M.H., and Morgan, W.C., "Theoretical and Experimental Analysis of the Reduction of Rotor Blade Vibration in Turbomachinery Through the Use of Modified Stator Vane Spacing," NACA TN 4373, September 1958.



## 6.0 TURBINE FABRICATION

### 6.1 FABRICATION AND JOINING

#### Joining Considerations

Since all the materials in the turbine which must be joined are weldable, this method of joining will be used wherever possible. Appropriate inert atmosphere chambers for TIG welding and vacuum electron beam welding equipment will be used where applicable. In the buildup of components from subassemblies, from individual parts, and from various forms of raw stock, a postweld annealing treatment will be performed immediately prior to finish machining principally for purposes of stress relief but also as a protection against subsequent aging and loss of ductility or corrosion resistance. In the final assembly of the turbine, it will be impossible to stress relieve the welds for fear of distortion and binding of internal parts, or of structural damage to some of the other bearing and seal materials in the turbine. The absence of a final anneal after assembly welding should not be detrimental as indicated in Table 6.1-1; manual welds using Cb-1Zr filler wire appear to have acceptable strain capacity for this application even without a postweld anneal.

Brazes will be used only where they are needed to act as liquid or vapor seals or where welding has been tried and cannot be used. Typical base alloy compositions which might be of direct application to the turbine are shown in Table 6.1-2. In the few instances where brazing may be necessary, some static capsule corrosion tests of the braze alloys in

TABLE 6.1-1  
BEND DUCTILITY IN Cb-1Zr AND T-111 WELDS

T.I.G. WELD		Post Weld Anneal	Post Weld Aging	Bend Test	
<u>T.I.G. Weld</u>	<u>Filler Wire</u>			<u>RT</u>	<u>-100° F</u>
Automatic	None	None	1550° F-50 hr	(70-90°)	
Automatic	None	2200° F-1 Hr	1550° F-50 Hr	105° *	(70-90°)
Automatic	None	2200° F-2 Hr	1550° F-50 Hr	105°	105°
Manual	T-111	None	1550° F-50 Hr	(5-10°)	
Manual	T-111	2400° F-1 Hr	1550° F-50 Hr	(10-20°)	
Manual	Cb-1Zr	None	1550° F-50 Hr	(30-40°)**	

---

\* Maximum bend deflection with bend fixtures used

\*\* Acceptable Strain Capacity for Final Assembly Welds.

TABLE 6.1-2

POTENTIAL BRAZE ALLOYS

<u>Designation</u>	<u>Composition</u>	<u>Brazing Temperature</u>	<u>Prior Use</u>
AS 501	Ti-30V	3000°F	Mo-0.5Ti to 316 SS Brazed Joints
- Carboloy 907 to Cb-1Zr Joints Made.			Carboloy 907 to Cb-1Zr Joints
AS 514	V-35Cb	3400°F	Brazed FS-85 Cb Alloy
AS 537	56Zr-28Ti-16V	2150°F	Al <sub>2</sub> O <sub>3</sub> to Cb-1Zr Joints
Pd-Co	38Co-Bal Pd	2300°F	Al <sub>2</sub> O <sub>3</sub> -Kovar Seals in 800°F K

liquid potassium would be required to verify the expected corrosion resistance of one or more of the alloys.

As a preliminary to the assembly of the turbine components themselves, the various joining methods would be certified by the preparation of simple joints intended to reproduce the actual hardware joint configuration as closely as possible.

## 6.2 FABRICATION AND ASSEMBLY

The following outlines the procedures for the final assembly of the turbine and then discusses, briefly, the method of producing each of the principal components.

### Final Assembly

Refer, first, to Figure 6.2-1 for a view of the turbine assembly. The wheels of the high-pressure stage are first stacked on the tie bolt with the latter in a vertical position. The forward bearing housing is then installed, and the assembly is suspended inlet end down from the upper (aft) part of the tie bolt. The high-pressure stage turbine casing halves and the turbine inlet duct are next clamped in place. As mentioned above, all welding is done in a vacuum-purged, argon-filled TIG welding chamber qualified for welding of refractory alloys. The circumferential welds are made first and then the longitudinal welds. Back stepping weld techniques similar to those used successfully in weld assembling the two-stage and three-stage potassium vapor turbines, Reference 4.3-1, will be used to prevent distortion.

After the high-pressure stage is weld assembled, the turbine will be removed from the chamber, the turbine shafts, wheels and interstage

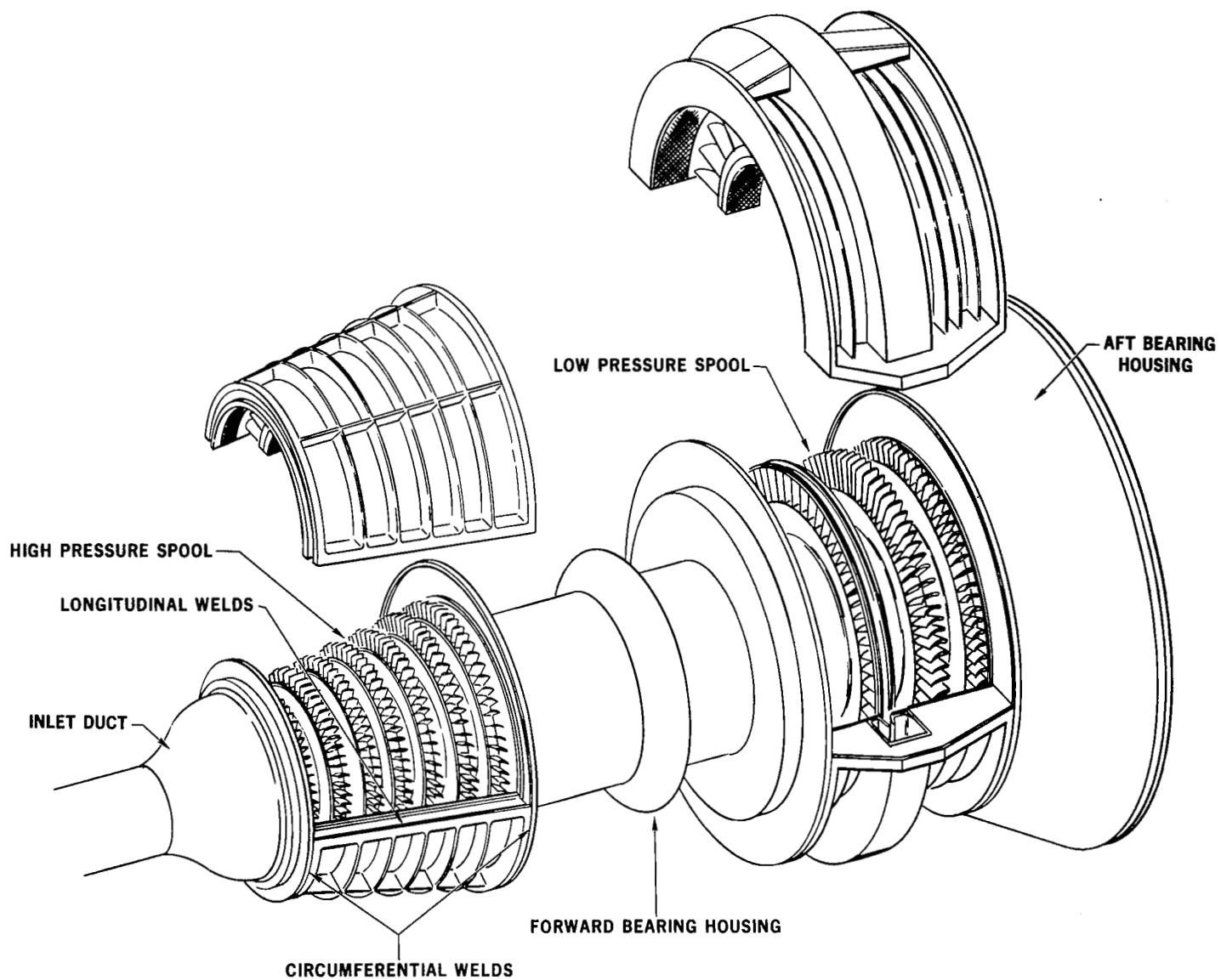


Figure 6.2-1. Turbine Casing Assembly.

connections of the low-pressure stage will be stacked on their curvic coupling surfaces, the low-pressure casings installed, and the aft bearing housing added. Once these components are securely clamped in place, the turbine will again be placed in the weld chamber, and the low-pressure casing assembly welds will be made in a distortion-free manner similar to those of the high-pressure stage.

For simplicity in presentation, the crossover ducting is not shown on the bearing housing in Figure 6.2-1. Only short projections of this ducting would be fabricated integrally with the housing; no ducting would overhang the circumferential welds at the forward and aft ends of the bearing housing. Full ducting connections would be added after final turbine assembly.

#### Turbine Wheels

Figure 6.2-2 shows an integrally machined KDTZM-1175-type molybdenum turbine wheel with integral blades and curvic coupling. The wheel blank will be rough machined from the forging, stress relieved, and finish machined except for curvic coupling and blades. The curvic coupling will then be ground. The last machining operations will be the eloxing of the integral blades in the wheel and final polishing of the eloxed surfaces to meet final airfoil dimensions and to remove the eloxed "recast" surface which will have very small surface irregularities which might otherwise propagate cracks. A final stress relief will be performed on the part. Needless to say, dimensional inspections and nondestructive testing will be used both in-process and at completion of the parts to assure the quality of these critical parts.

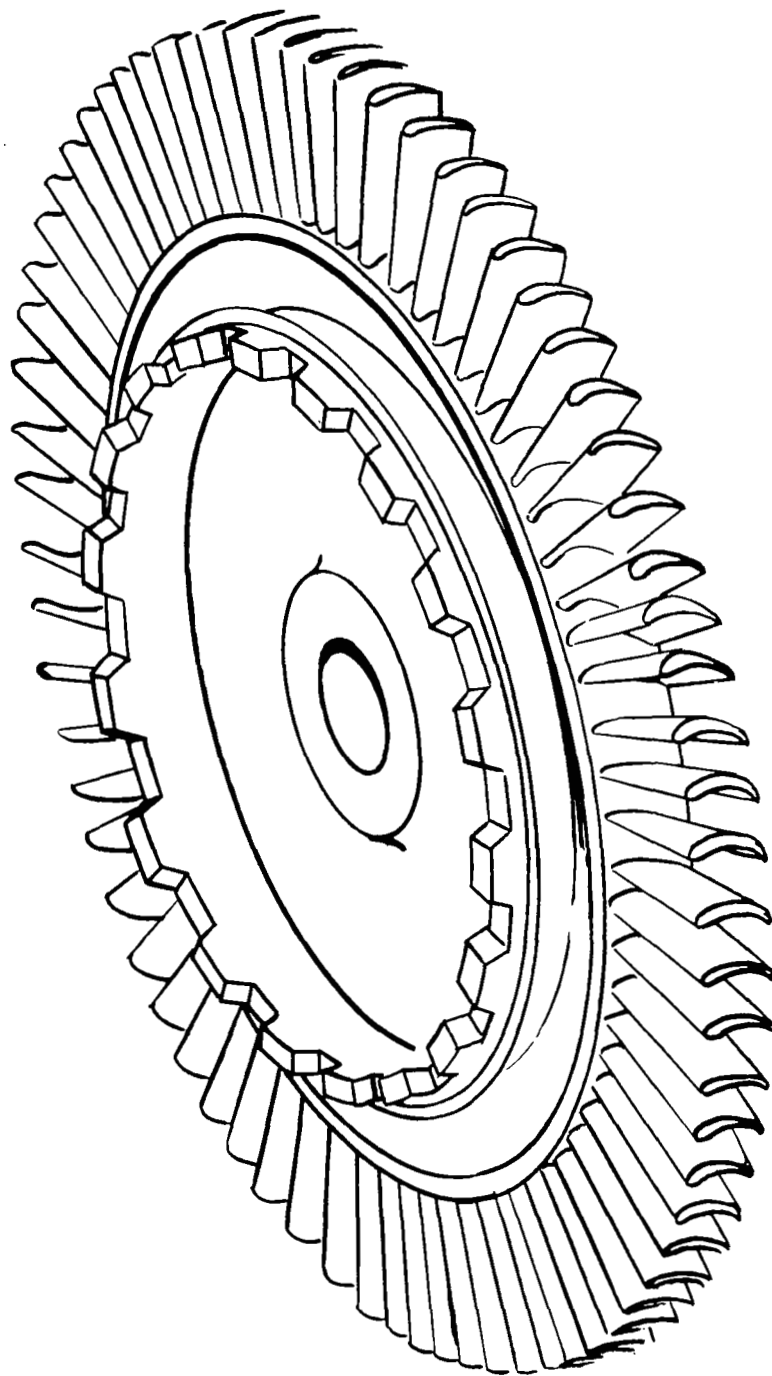


Figure 6.2-2. Integrally Machined Turbine Wheel - KDTZM Molybdenum Alloy.

### Turbine Casings

The assembly of the nozzle diaphragms and tip shrouds into the high-pressure stage casing halves is shown in Figure 6.2-3. Cylindrical rabbited sections are machined into the conical casing halves. This permits the precise axial location and diametrical fitup of each diaphragm and tip shroud. The nozzle diaphragm and shroud rings are installed one at a time beginning at stage one. Each diaphragm or ring is electron beam welded into place from its aft side such that a leak tight seal is produced; this weld can be benched out for later removal of these parts, if necessary.

Assembly of the nozzle diaphragms and tip shrouds in the low-pressure casing is only slightly different, as seen in Figure 6.2-4. The nozzle diaphragm and shroud rings are inserted radially into right cylindrical grooves and electron beam welded in place with the beam entering in the radial direction.

### Nozzle Diaphragm Assembly

The nozzle diaphragms are assembled from machined ring sections and from contour machined and polished vane pieces by electron beam welding as shown in a self-explanatory way in Figure 6.2-5. The interstage honeycomb seals at the ID of the diaphragms and the turbine blade tip seals are installed as shown in Figure 6.2-6. The honeycomb seals fit the ID surface of the appropriate part and are electron beam welded along the forward and aft edges.

### Seal Fabrication

The turbine tip and interstage seals are made from T-111 or Cb-1Zr



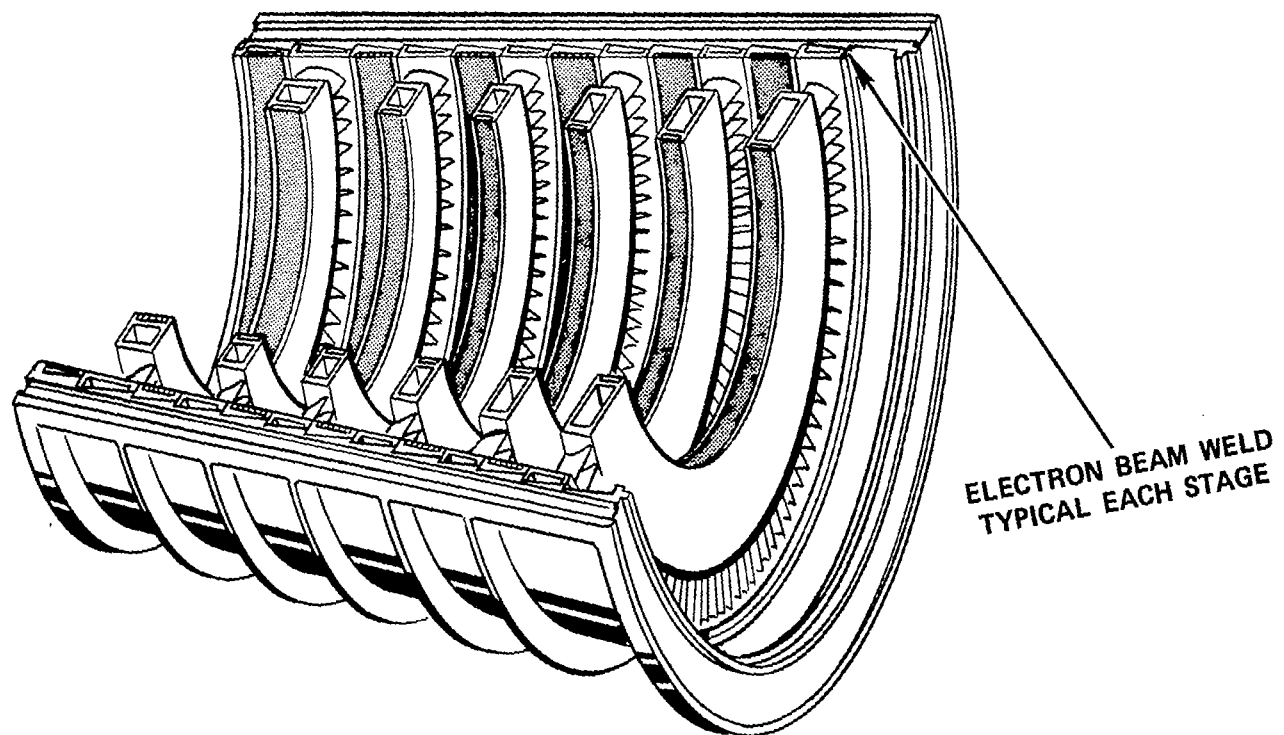


Figure 6.2-3. High Pressure Casing Assembly.

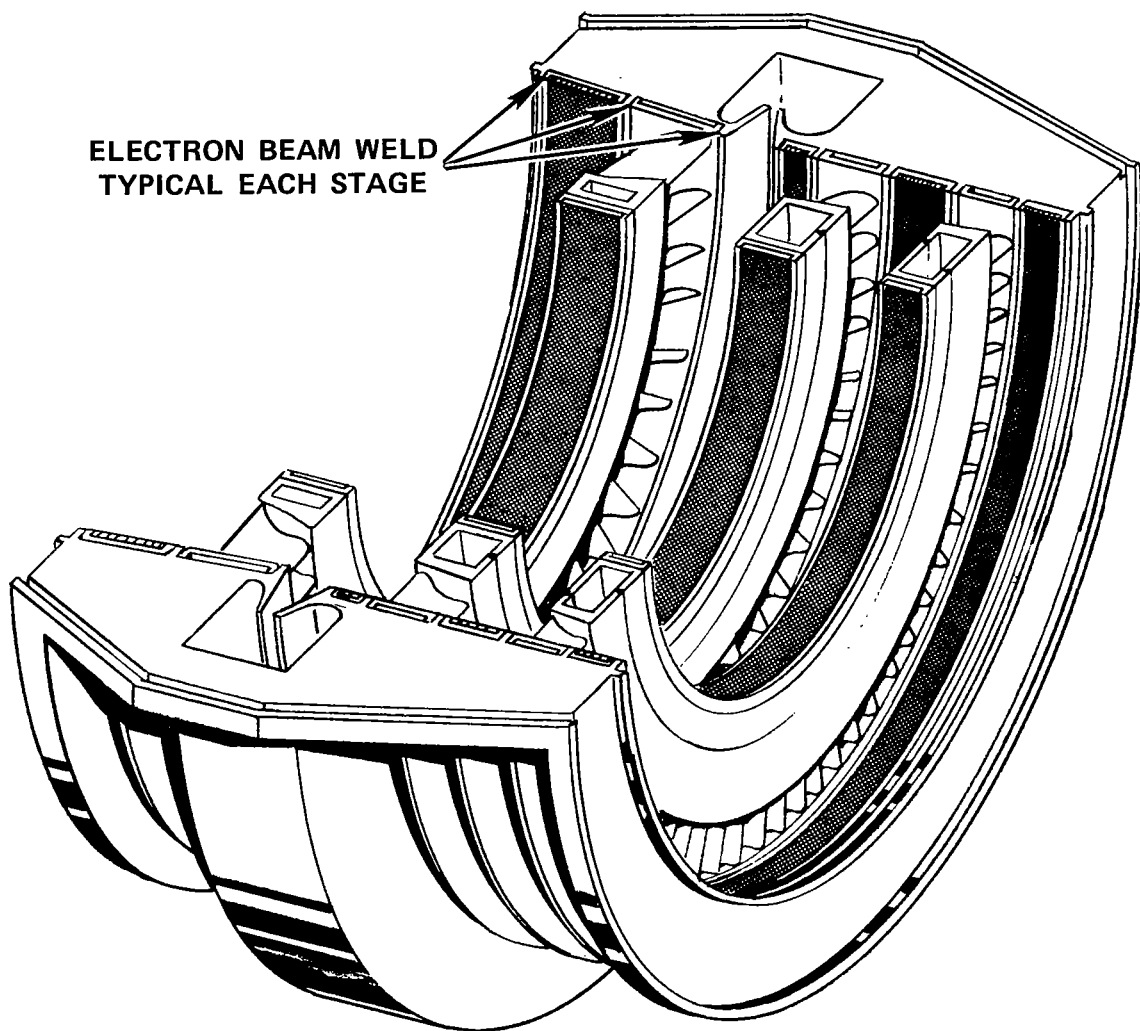


Figure 6.2-4. Low Pressure Casing Assembly.

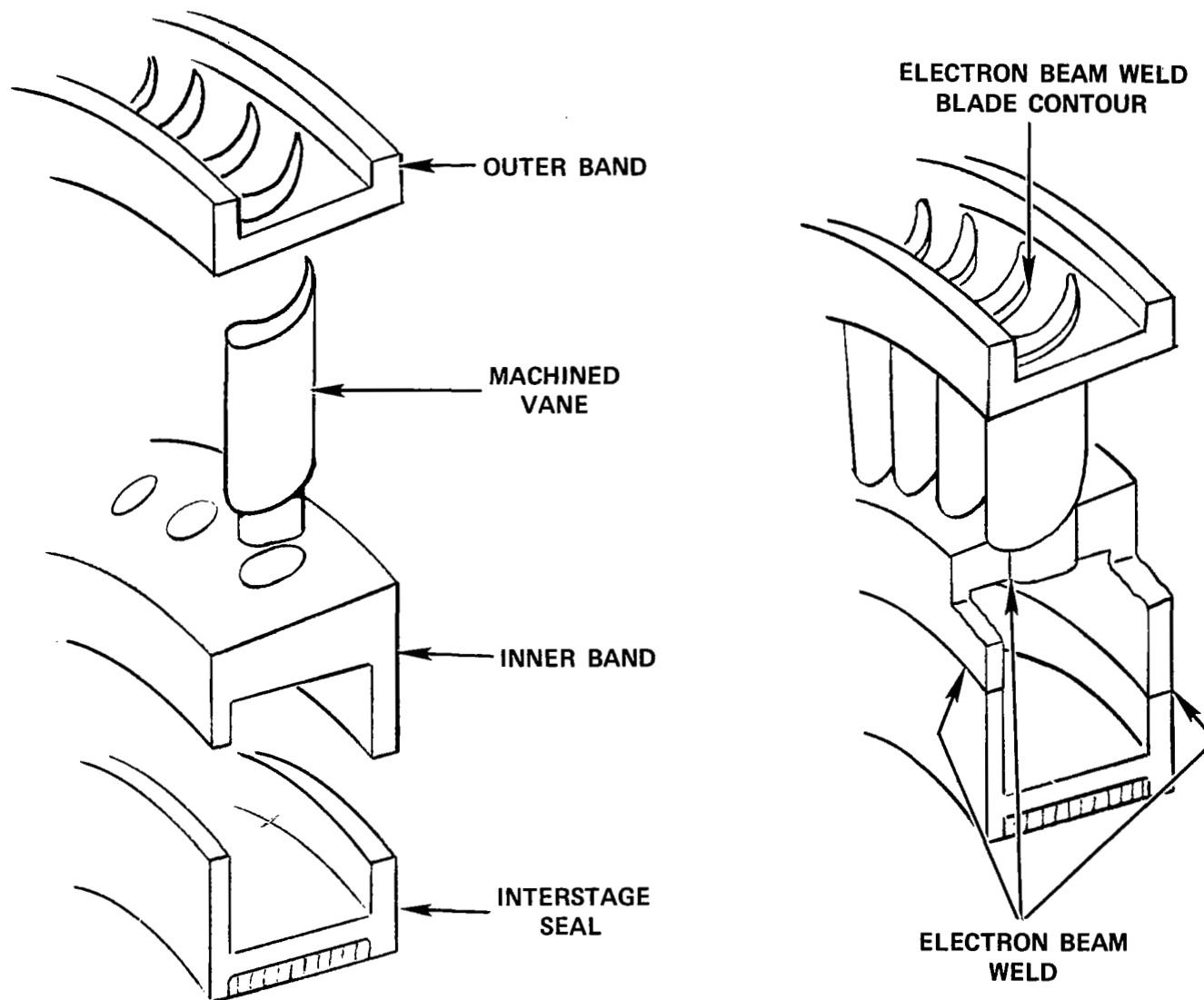


Figure 6.2-5. Nozzle Diaphragm Assembly.

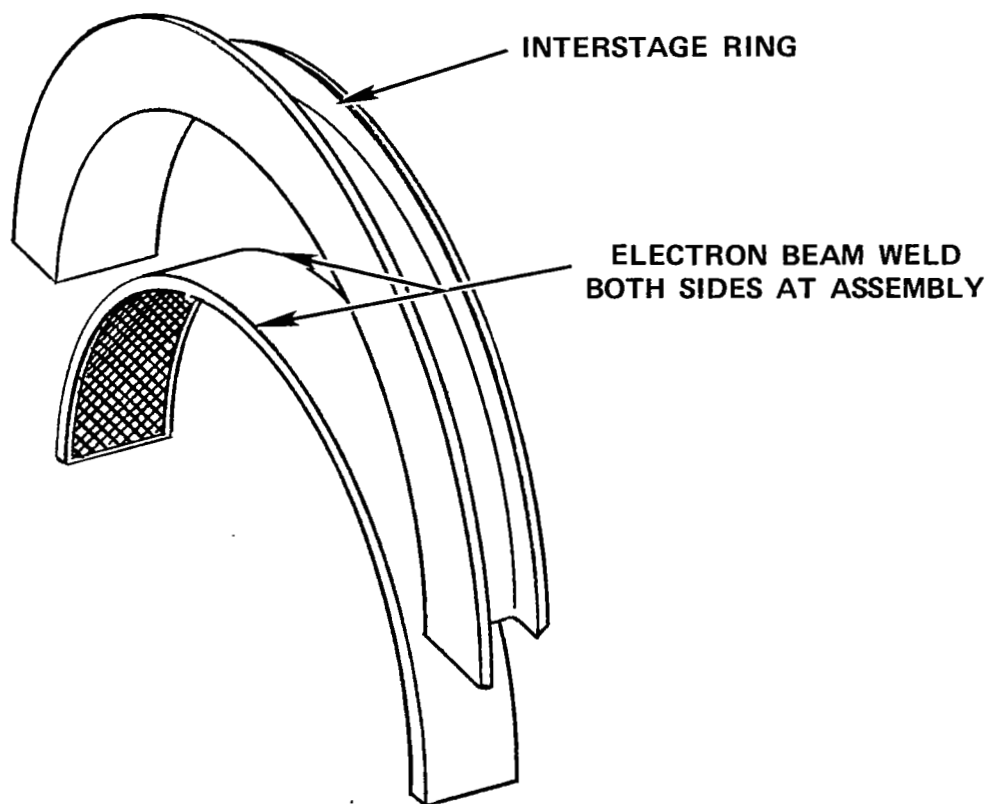


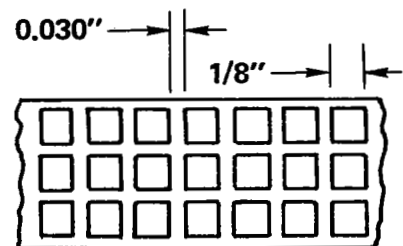
Figure 6.2-6. Interstage Honeycomb Seal Assembly.

as shown in Figure 6.2-7. The T-111 or Cb-1Zr foil honeycomb inserts are formed into curved sections and then attached to its circular T-111 or Cb-1Zr ring by electron beam plug welds. Accurate dimensions can be achieved by a final machining operation.

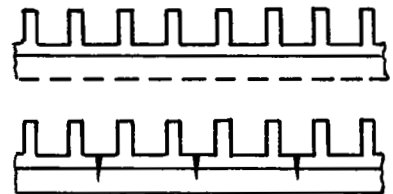
### 6.3 JOINING SUMMARY

The weldability of the principal structural materials in the turbine are good, but each joint configuration must be certified in simulated joints in order to optimize processes and to disclose any need to modify joint design configurations prior to fabrication of hardware.

– BACK EXTRUDE (COIN) INTO HONEYCOMB



- REMOVE EXCESS BACKING
- STRESS RELIEVE
- FORM INTO RING
- EB PLUG WELD TO INSERT RING
- POST WELD STRESS RELIEVE



– FINISH MACHINE

Figure 6.2-7. Honeycomb Seal Fabrication.

## 7. VISCO SEALS AND BEARINGS

### 7.1 VISCO SEALS

The basic requirements which are desired of the turbine seals in order that they satisfactorily contain the potassium bearing lubricant are:

- To maintain the bearing cavity pressure approximately ten psi above the adjacent vapor pressure and high enough to suppress cavitation (20 - 30 psia).
- To contain the bearing lubricant during start-up (40 percent of design speed and approximately 20 psi pressure differential).
- To operate with minimum parasitic power consumption.
- To seal against vacuum with leakage rate not exceeding 1 - 2 pounds in 10,000 hours. This criteria applies only to the bearing (and alternator) seals where leakage does not return to the main potassium loop.

The seal capacity is a function of sealing length, seal diameter, operating speed, lubricant viscosity, and diametral clearance for a screw seal which creates a pressure differential directed from the vapor region to the lubricant chamber. It may be expressed as the seal length required to create a ten psi sealing pressure, as shown by Figure 7.1-1. Shown are the sealing capabilities for the design speed of 19,200 rpm and 40 percent of design speed, which equals 7,680 rpm. Typical selected seal configurations are noted. The pressure capabilities

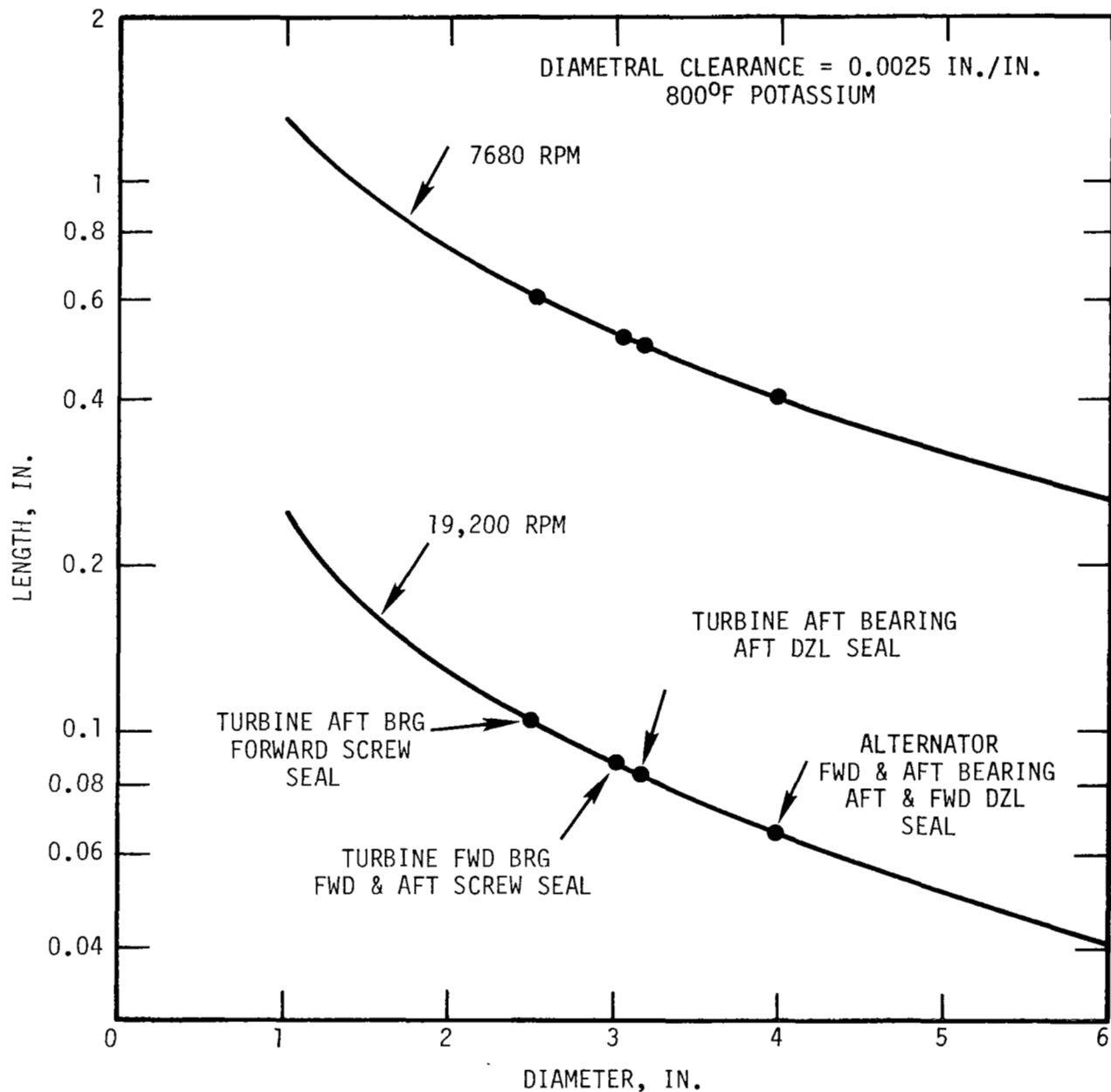


Figure 7.1-1. Screw Seal Length Versus Diameter for 10 psi Sealing Pressure.

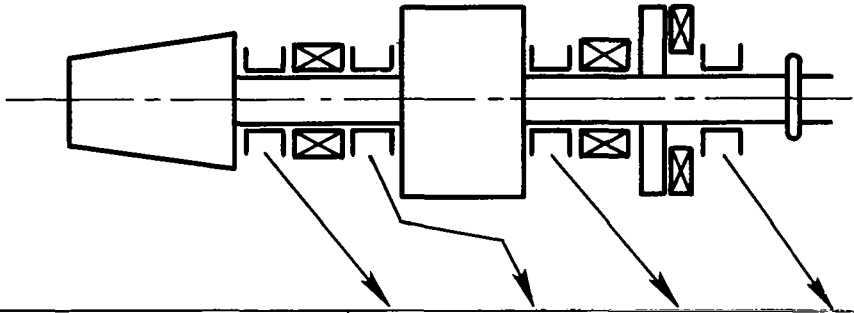


$\Delta P_c$  are determined by the formula:

$$\Delta P_c = \left( \frac{10 \text{ psi}}{L} \right) L_{\text{actual}}$$

Using the above criteria, the capacities of the selected turbine seals are derived for the start-up and operating speeds. These are synopsized in Figure 7.1-2. Note that the designation of a DZL (Dynamic Zero Leakage) seal is used for the aft bearing aft seal, where leakage would leave the main potassium loop. This seal differs from the simple screw seals in that the normal leakage through the screw is collected and recycled into the screw to further reduce leakage. This design was developed and tested by the General Electric Company for such a long term, low leakage space requirement using liquid potassium.

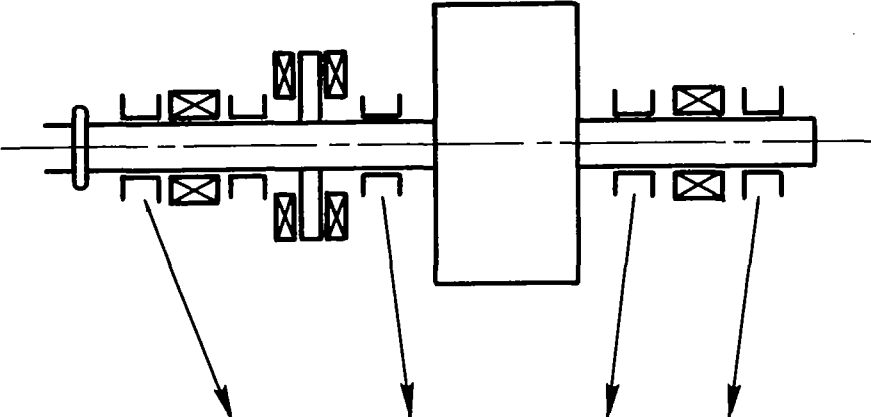
With 900° potassium lubricant and the listed seal geometries, the imposed pressure differentials  $\Delta P_i$  are compared to the seal capabilities  $\Delta P_c$  for the design speed and 40 percent of design speed. If the lubricant cavity is pressurized to 30 psi during the start-up period, the selected seal lengths are unable to completely contain the lubricant and some leakage is predicted. The leakage may be accepted or the lubricant cavity pressure may be decreased. Also, the length of the three screw seals may be doubled, but it is not desirable to allow the system length and weight to increase unless this be the only solution. At operating speed and pressure capability of all the seals greatly exceeds the imposed pressure differentials, and increased seal lengths would provide very much greater capability than needed as well as increasing the parasitic losses which would be present during the entire operating life of the turboalternator. The recommended compromise is to slightly decrease the lubricant supply pressure and accept some leakage during start-up.



	TURBINE			
	FORWARD BEARING		AFT BEARING	
	SCREW SEAL FORWARD	SCREW SEAL AFT	SCREW SEAL FORWARD	DZL SEAL AFT
K LUBE TEMP., °F	900	900	900	900
DIAMETER, IN.	3.00	3.00	2.50	3.10
LENGTH, IN.	1.00	1.00	1.00	1.25
THREAD DEPTH, IN.	0.035	0.035	0.030	0.037
DIAMETRICAL CLEARANCE, IN.	0.0075	0.0075	0.0063	0.0078
NO. OF THREAD STARTS	6	6	5	6
$\Delta P_i$ AT 7680 RPM, PSI	30	30	30	30
$\Delta P_c$ AT 7680 RPM, PSI	18.5	18.5	15.5	26
$\Delta P_i$ AT 19200 RPM, PSI	-3.5	24.63	-2	30
$\Delta P_c$ AT 19200 RPM, PSI	107	132	83	136
MATERIAL	TITANIUM CARBIDE			

Figure 7.1-2. 7+4 Turbine Seals.

With the same basic criteria as those of the turbine seals, except for a different bearing lubricant temperature, the alternator seals listed in Figure 7.1-3 were chosen. Since leakage outside the potassium loop can occur at both ends of the forward bearing and at the forward end of the aft bearing, the Dynamic Zero Leakage seals are used in these locations. The 700°F potassium lubricant temperature and seal geometrical parameters are shown. The imposed lubricant cavity pressure differentials  $\Delta P_i$  of 25 psi, at 40 percent or full operating speed, are met by these seals at 40 percent speed and greatly exceeded by the seal capability pressure differentials  $\Delta P_c$ .



	ALTERNATOR			
	FORWARD BEARING		AFT BEARING	
	DZL SEAL FORWARD	DZL SEAL AFT	DZL SEAL FORWARD	SCREWSEAL AFT
K LUBE TEMP., °F	700	700	700	700
DIAMETER, IN.	3.40	4.00	4.00	2.30
LENGTH, IN.	1.00	0.95	0.95	1.60
THREAD DEPTH, IN.	0.040	0.047	0.047	0.027
DIAMETRAL CLEARANCE, IN.	0.0085	0.010	0.010	0.0058
NO. OF THREAD STARTS	6	6	6	4
$\Delta P_i$ AT 7680 RPM, PSI	25	25	25	25
$\Delta P_c$ AT 7680 RPM, PSI	26	25	25	25
$\Delta P_i$ AT 19200 RPM, PSI	25	25	25	25
$\Delta P_c$ AT 19200 RPM, PSI	110	105	105	123
MATERIAL	STELLITE 6B			

Figure 7.1-3. 7+4 Alternator Seals - H-11 Steel Stubshafts.

## 7.2 BEARINGS - GENERAL

The Phase I KTA preliminary design study of various bearing types indicated that tilting pad journal and thrust bearings were the best choices because of their inherent self-aligning and stability characteristics. Furthermore, the background of theoretical and experimental experience with tilting pad bearings in similar applications insures the adequacy of the analysis and gives confidence that development problems will be minimal. Accordingly, only the tilting pad type bearing has been considered in the Phase II design studies.

Also during Phase I, both oil and potassium lubrication was considered and it was determined that potassium lubricated hydrodynamic bearings have, in all cases, more than adequate load capacity, stiffness, and damping. Furthermore, the potassium lubricated components were less complex and had superior vibrational characteristics. For these and other reasons discussed earlier, the Phase II study was limited to potassium lubrication.

During Phase II, the journal and thrust bearings for each of the final turbine and alternator configurations were sized and detailed performance calculations were made. The results of these calculations along with a discussion of the pivot configuration are presented in this section. The reader is referred to the Phase I report for the discussions of bearing selection and theoretical background.

Also during Phase II, the problem of KTA start-up was considered along with the possibility of reducing the starting torque by incorporating hydrostatic jacking. Two different jacking designs were evaluated and detailed hydrodynamic performance calculations of the designs were made.

### 7.3 JOURNAL BEARINGS

It was indicated in the Phase I KTA study report that the journal bearings were initially sized to support a 1g plus nominal rotating load with an eccentricity ratio less than 0.5 at design speed. This criteria leads to a conservative design, since the specified operating acceleration and shock loads can be taken without the eccentricity ratio exceeding 0.85. The shaft stiffness and other mechanical design requirements usually caused the journal bearings to be larger in diameter than necessary to satisfy the loading criteria.

For the final machine concepts considered in Phase II, all of the journal bearings were also larger than necessary to simply support the radial loads imposed by the rotors. Bearing diameters, in all cases, were established to achieve the rotor rigidity or the bearing stiffness necessary to obtain the desired rotor dynamic behavior. For the purposes of the study, the following bearing geometric relationships were employed:

$$\text{Machined clearance ratio } \left(\frac{C_p}{R}\right) = 0.00214$$

$$\text{Assembled clearance ratio } \left(\frac{C_b}{R}\right) = 0.0015$$

$$\text{Pivot position } (\theta/\beta) = 0.55$$

Where:  $C_p$  = (radius of pad - radius of shaft)

$C_b$  = Distance from bearing center to pad at pivot point

$\theta$  = Angular distance from pad leading edge to pivot

$\beta$  = Pad arc length ( $80^\circ$  for a four pad bearing)

The geometric preload resulting from the clearance relationships is 0.3, which is sufficient to insure stable operation (freedom from half frequency whirl). These clearances are small enough to produce

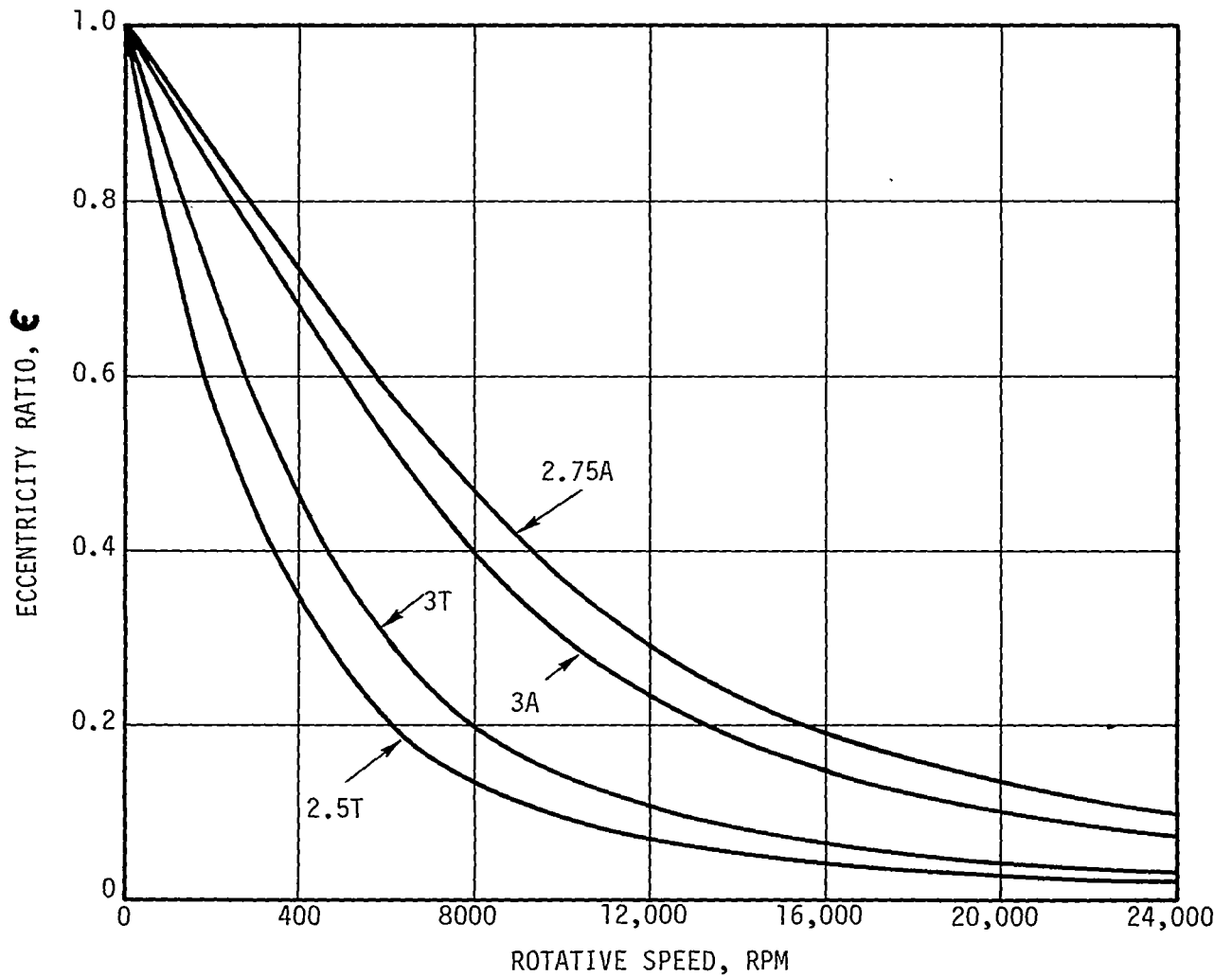
ample fluid film stiffness and damping without consuming undue power or becoming sensitive to normally expected foreign particles.

The manufacturing tolerances are not overly critical, since large variations in the machined clearance ratio can be tolerated with only minimal effects on load capacity, stiffness, and damping, as long as the assembled clearance ratio is maintained. Tight control (in the range of 0.0002 inch) of the assembled clearance is relatively easy to achieve since the pivot plate thickness can be adjusted at assembly.

The calculated performance (eccentricity ratio, stiffness, and speed) for each of the turbine and alternator journal bearings under both Og and lg conditions are shown on Figures 7.3-1 through 7.3-5.

For performance calculations, the potassium lubricant was assumed to be at 800°F. From a bearing standpoint, there is no reason why the lubricant temperature could not be significantly raised. The viscosity index of potassium is quite small and an increase in temperature to 950°F would only reduce the stiffness, damping, and load capacity by about 13 percent. A much larger reduction could readily be accepted with no ill effect.

The bearing pads, pivots, and pad retaining rings are of the same materials as the sleeves (TiC + 10% Cb for the turbine and Carboloy 907 for the alternator) which results in no variation in bearing clearance with temperature. Since it is not possible to support a radial temperature gradient in excess of a few degrees within the liquid metal filled bearing cavity, no clearance change allowance or non-rigid pivot arrangement is required.



LEGEND:

CURVE NO.	3T	2.5T	3A	2.75A
COMPONENT	TURBINE	47R199305	ALTERNATOR	263E329
BEARING	FWD	AFT	FWD	AFT
LENGTH, IN.	3.00	2.50	3.00	2.75
DIAMETER, IN.	3.00	2.50	3.00	2.75
LOAD, LB.	80	25	200	200

Figure 7.3-1. Turbine and Alternator Bearing Eccentricity Ratios Versus Rotative Speed. For All Bearings: Assembled Clearance Ratio ( $C_b/R$ ) = 0.0015; Geometric Preload ( $m$ ) = 0.3; Potassium Lubricant at 800°F; Acceleration = 1 g.



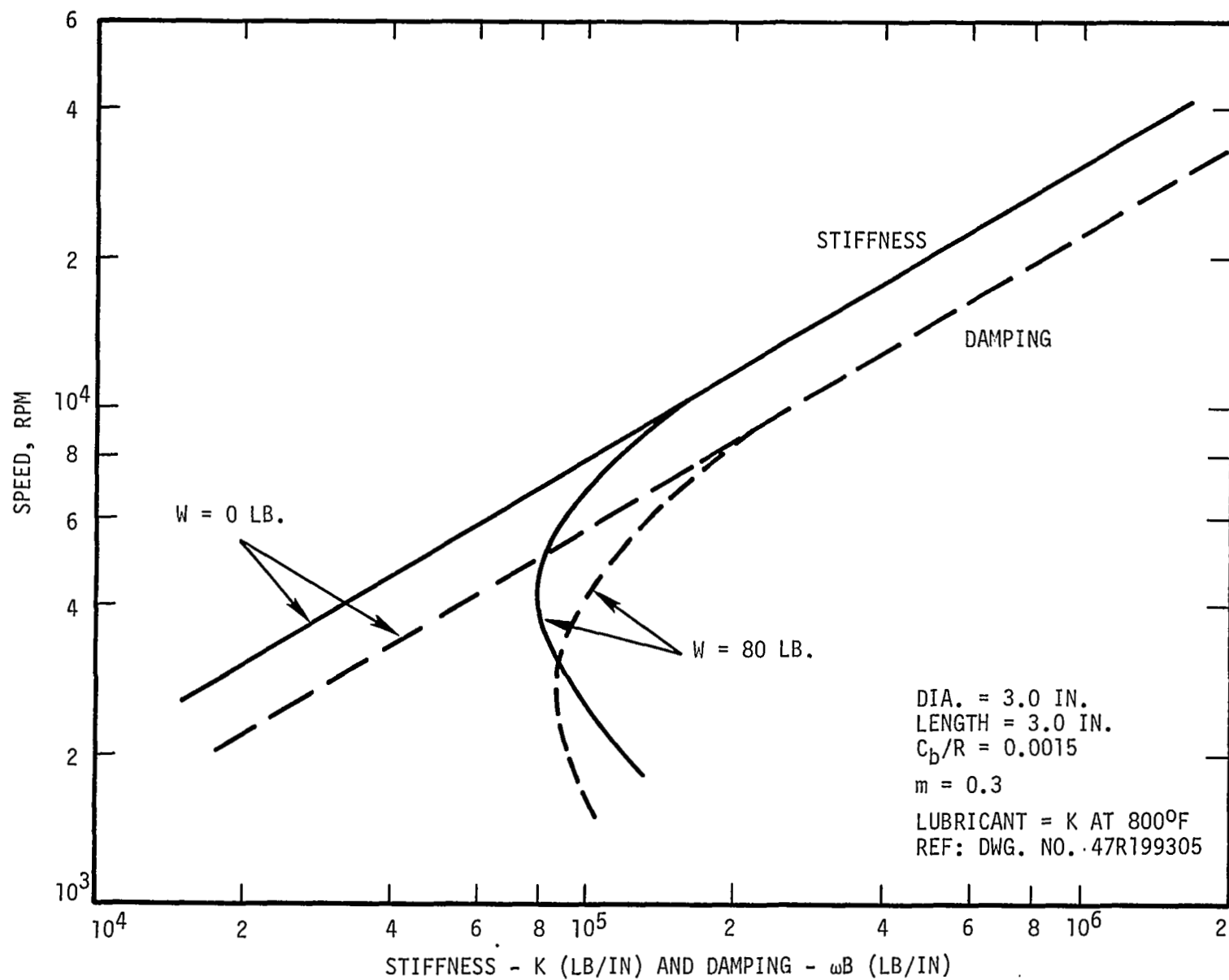


Figure 7.3-2. 3.0 Inch Diameter Turbine Bearing Stiffness and Damping.

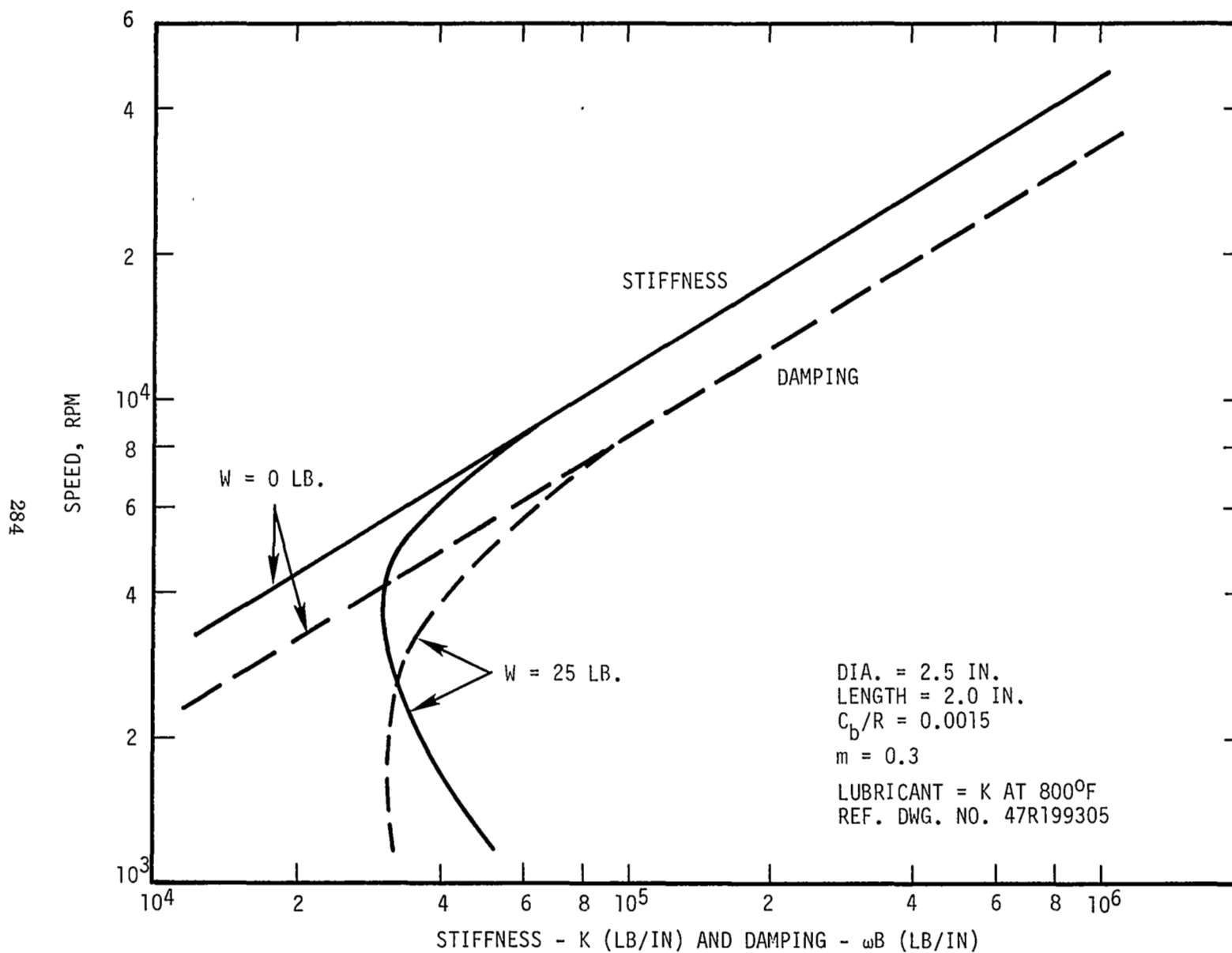


Figure 7.3-3. 2.5 Inch Diameter Turbine Bearing Stiffness and Damping.

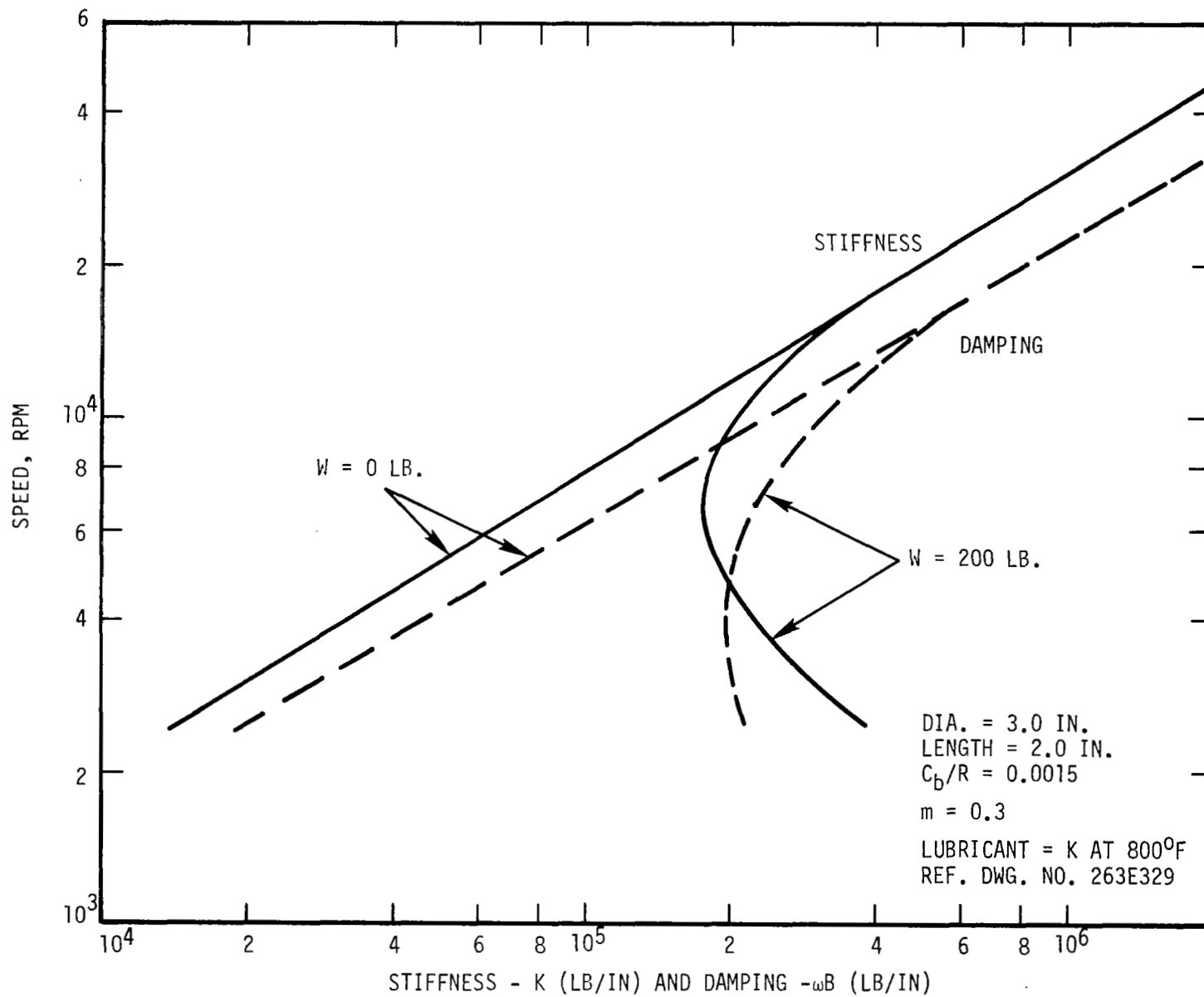


Figure 7.3-4. 3.0 Inch Diameter Alternator Bearing Stiffness and Damping.

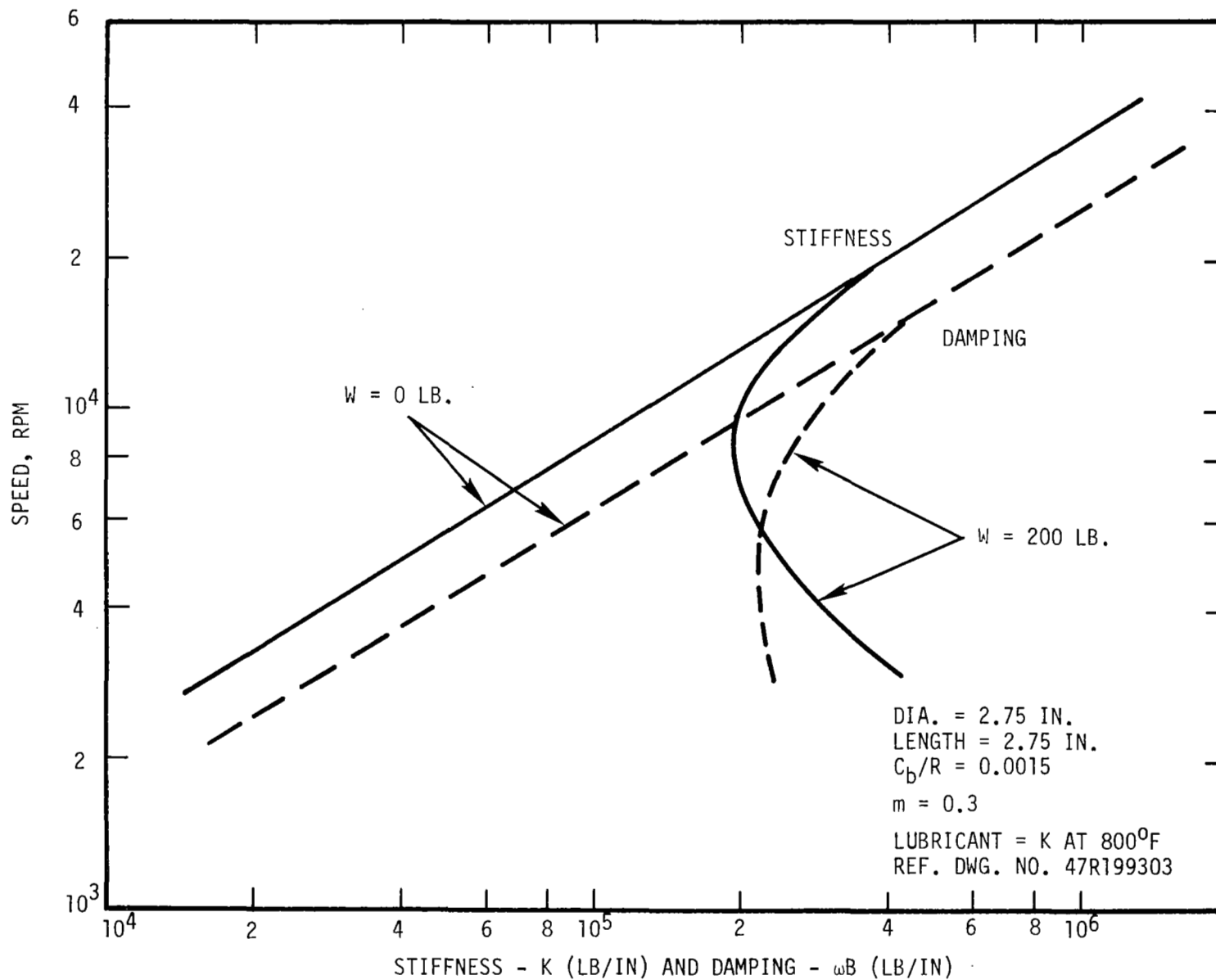


Figure 7.3-5. 2.75 Inch Diameter Alternator Bearing Stiffness and Damping.

The pivot design recommended for the KTA components is a sphere on a flat. This configuration eliminates the sometimes encountered "lock-up" problem in liquid metal lubricated tilting pad bearings, where the high friction coefficient can cause a pivot wedging action upon start-up. When one of the pivot members is a flat, no ramp is provided for wedging.

With the sphere and flat design, a sphere of relatively large radius is required to minimize the contact stress. The maximum contact stress occurs in the alternator journals under the 20g launch condition, where pivot loads could approach 4000 pounds (20 x 200 lb/bearing). To eliminate Brinelling, the pivot spherical radius has been set at eight inches, which results in the following stress levels with a 4000 pound imposed load.

225,000 psi for Carboloy 907 ( $E = 60.1 \times 10^6$  psi)

195,000 psi for TiC + 10% Cb ( $E = 54.3 \times 10^6$  psi)

These stress values are well below the 0.2 percent compressive yield values of 510,000 psi (C907) and > 300,000 psi (TiC) at 800°F. (7.2-1)

Another consideration in the design of the pivot is its stiffness. Since there is measurable deflection at the contact under load, the pivot introduces a compliance into the bearing structure which can have a profound effect on the dynamic behavior of the rotor. However, if the pivot stiffness is maintained about an order of magnitude larger than the bearing fluid film stiffness, only negligible effects on rotor dynamics are usually observed. The minimum pivot stiffness will occur on the aft turbine bearing, the most lightly loaded one, since the stiffness under direct bearing contact is a function of load. The pad load on this bearing under Og operation at 19,200 rpm was calculated to be

82 pounds and it has a fluid film stiffness of  $2.3 \times 10^5$  lb/in.

(Although there is no net bearing load under  $O_g$ , the preload feature causes a positive force on each pad which is balanced within the bearing.) Again taking an eight inch spherical radius pivot, the stiffness under an 82 pound load is:

$1.74 \times 10^6$  lb/in. for TiC + 10% Cb and

$1.98 \times 10^6$  lb/in. for Carboloy 907

Both of these minimum stiffnesses are more than ten times the fluid film stiffness and are considered adequate for rotor dynamic purposes.

#### 7.4 THRUST BEARINGS

Detailed load capacity and power consumption calculations were made on three different thrust bearings which fit within the KTA components and support their imposed axial forces:

47R199305 Turbine	6.25 in. OD x 3.62 in. ID
263E329 Alternator	6.0 in. OD x 4.0 in. ID
47R199303 Alternator	5.75 in. OD x 3.75 in. ID

The inside diameters were set by the requirement of fitting around the bearing cavity seals and the outside diameters were determined by the load requirement. All the bearing calculations were based upon eight tilting pads which, for the diameter ratios used, leads to pads which have a high ratio of circumferential length/width. A more nearly optimum design incorporating 12 pads would result in a 14 percent power saving and a 10 percent increase in film thickness under design load conditions. This performance increase was not felt to be large enough to warrant the complexity of the 50 percent greater number of pads, pivots, and leveling links.

The turbine thrust bearing was sized for an aerodynamic load of 3000 pounds and a design speed pivot film thickness of 0.001 inch. This aerodynamic load results from the mechanical design turbine pressure ratio of 35. If the load were based upon the fluid design turbine pressure ratio of 21.2, the thrust load would be very significantly reduced and considerable power savings could be effected by reducing bearing size.

The alternator thrust bearings were sized for 1600 pound load and a film thickness of 0.0007 - 0.0010 inch. The 1600 pounds was

based upon preliminary rotor weight estimates of 400 pounds in a 4g force field. The actual rotor weight is somewhat lighter, which will result in slightly larger film thicknesses at design conditions.

The load capacity and power consumption for the three KTA thrust bearings are shown on Figures 7.4-1 through 7.4-3. The alternator bearings are double acting (two thrust bearings opposing the same runner), and the performance is shown for three different values of assembly clearance. The clearance should be kept within the values of 0.004 - 0.006. A reduction in clearance will only result in unnecessary power consumption, while an increase will materially reduce the centered position stiffness without significantly reducing power. The turbine thrust bearing is single acting since the aerodynamic thrust is larger than the specified acceleration forces. Therefore, no thrust reversals are anticipated. A small reverse or bumper thrust bearing incorporated to locate the shaft at assembly and to take inadvertent transport shocks. The power consumption shown on these figures are for the pad area of the bearing only, while the total thrust bearing power shown in an earlier section of this report also includes inactive face disk friction and cylinder losses on the runner outer diameter.

The load curves of Figures 7.4-1 through 7.4-3 clearly show the margins offered by the thrust bearings, since alternator bearing loads approaching 4000 pounds and turbine bearing loads approaching 8000 pounds can be imposed without reducing the pivot film thickness below 0.0005 inch.

Figure 7.4-4 summarizes certain important physical parameters of both the journal and thrust bearings of the KTA turbine. The 900°F potassium lubricant inlet temperatures are assumed. The imposed thrust



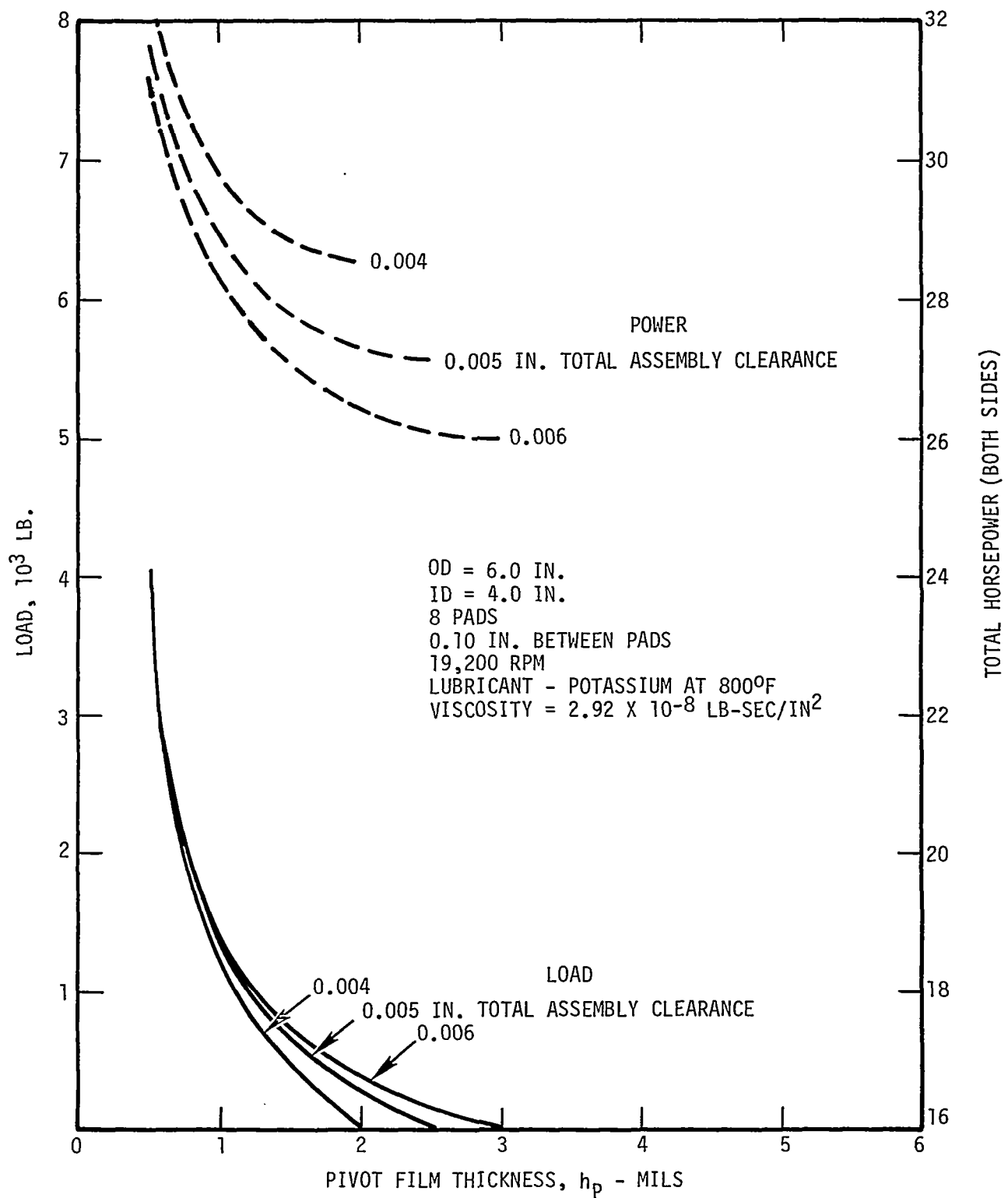


Figure 7.4-1. Alternator Double Acting Tilting Pad Thrust Bearing Load and Power Versus Pivot Film Thickness.

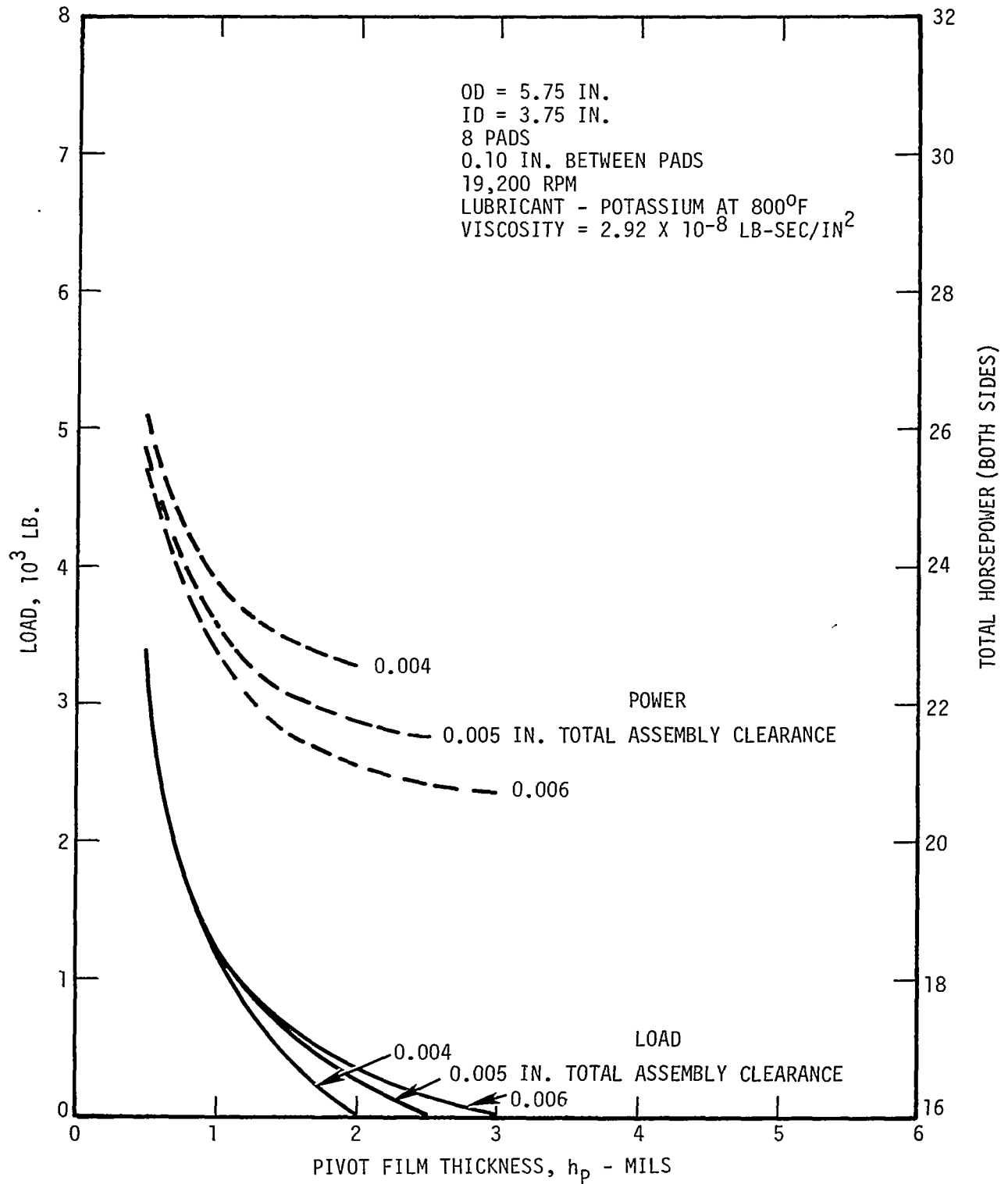


Figure 7.4-2. Alternator Double Acting Tilting Pad Thrust Bearing Load and Power Versus Pivot Film Thickness.

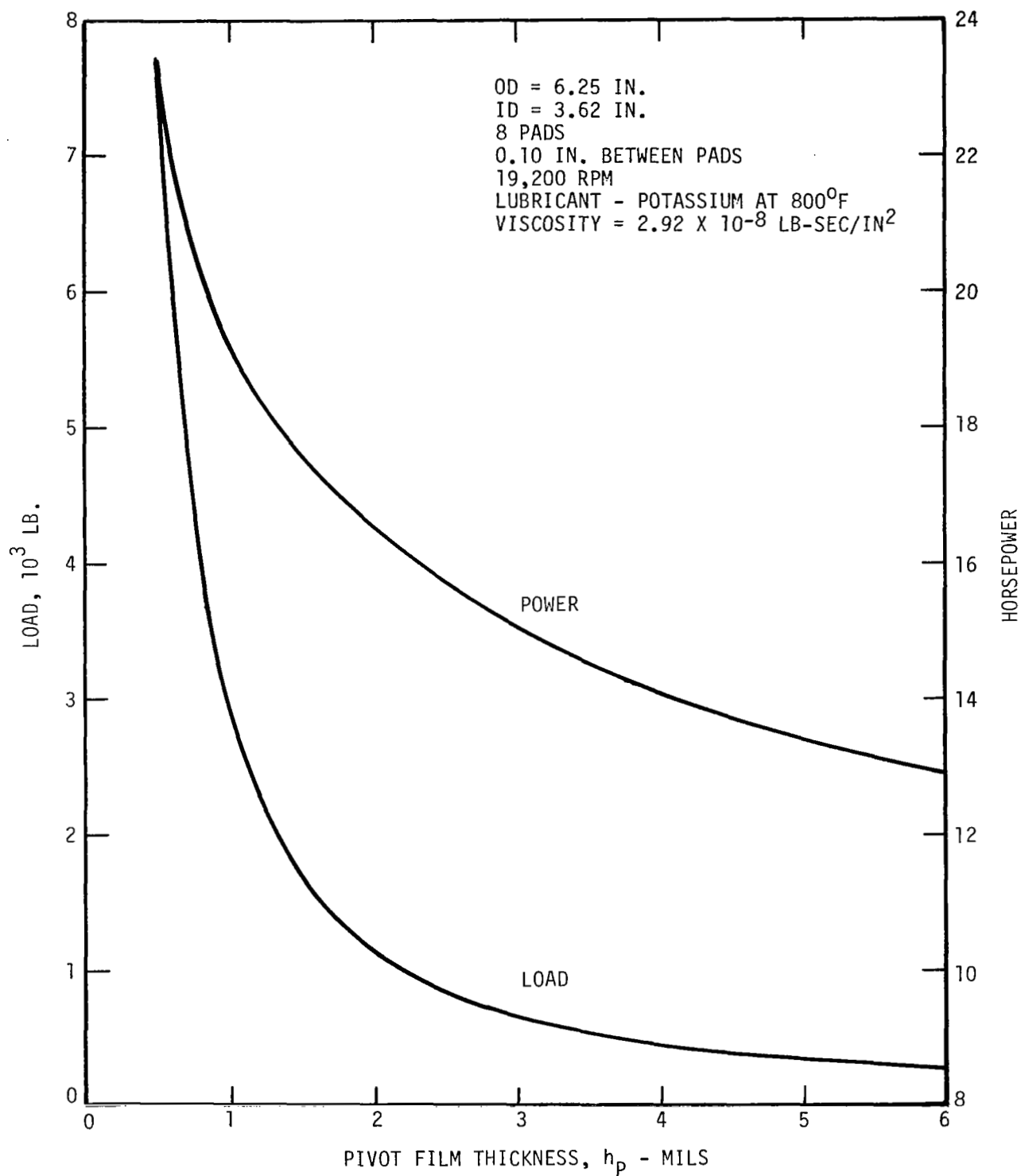
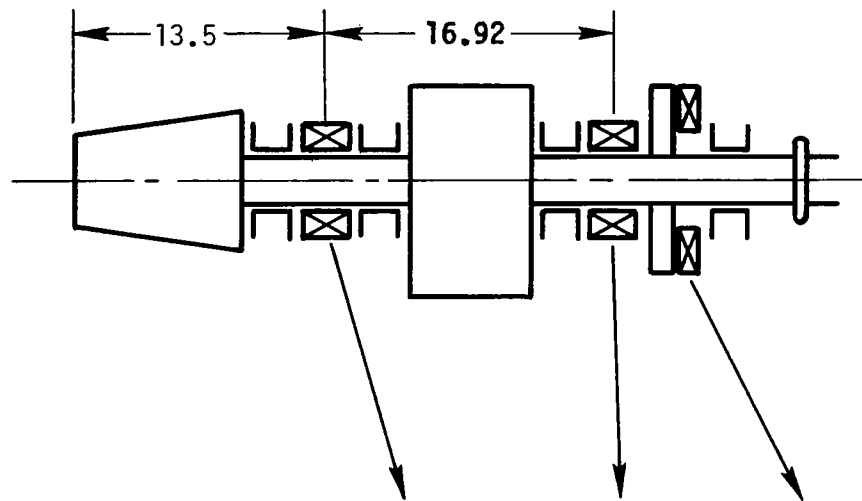


Figure 7.4-3. Turbine Single Acting Tilting Pad Thrust Bearing Load and Power Versus Pivot Film Thickness.



	TURBINE		
	FORWARD JOURNAL BRG.	AFT JOURNAL BRG.	THRUST BEARING
K LUBE TEMP., °F	900	900	900
IMPOSED THRUST LOAD, LBS.	-	-	2120
			1217
DIA., IN.	3.0	2.5	6.0
LENGTH, IN.	3.0	2.0	-
L/D	1	0.8	-
DIAMETRICAL CLEARANCE, IN.	0.0045	0.0038	-
NO. OF PADS	4	4	8
MATERIAL	TITANIUM CARBIDE		
BEARING WEIGHT, LBS	7	3	4

Figure 7.4-4. 7+4 Turbine Bearings.

loads are calculated on the basis of 20g fwd-to-aft acceleration during launch acting on the 160 pound rotor mass, and on the steady-state basis of vapor pressure differentials across rotor components acting upon the areas exposed to them. The selected bearing geometrical parameters are shown with the calculated weights of their static components, based upon TiC + 10% Cb material.

A similar synopsis of the alternator bearings is shown by Figure 7.4-5. The 700°F bearing lubricant temperature is assumed. With the launch acceleration of 20g and steady-state maneuver acceleration of 4g acting on the rotor mass of 353 pounds, thrust loads of 7060 pounds and 1412 pounds are produced. The geometrical parameters are shown for the bearings, with the weights of their static components, based upon Carboloy 907 material.

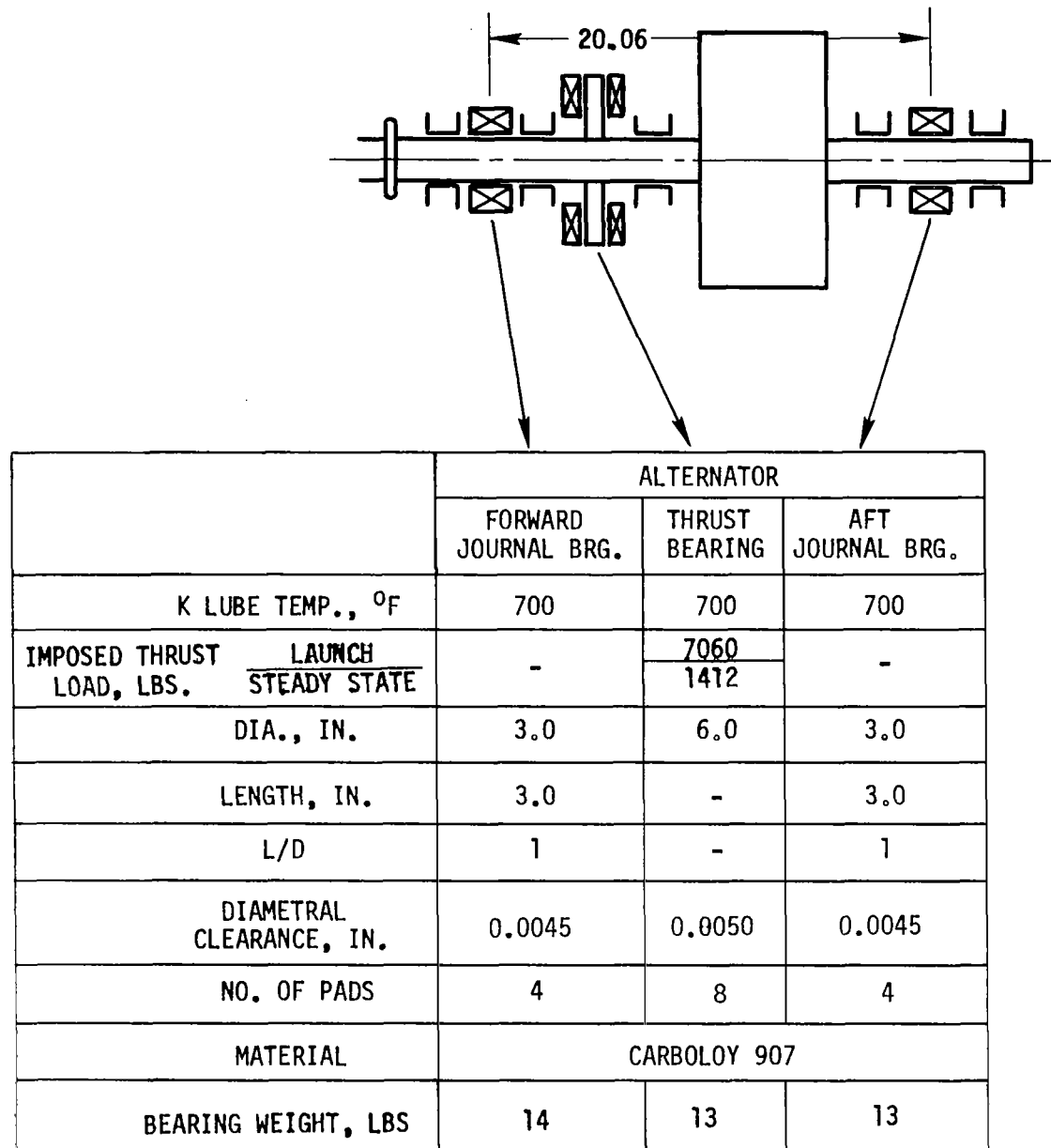


Figure 7.4-5. 7+4 Alternator Bearings - H-11 Steel Stubshafts.

## 7.5 KTA START-UP

In addition to the bearing performance characteristics at design speed under the various loading conditions which have been specified, it is necessary to also consider start-up and low speed operation conditions. These two operating modes are more critical with liquid metal as a lubricant than with oils because the liquid metal, for all practical purposes, offers no boundary lubrication. High starting torques result and, if long periods of rubbing occur, surface damage will occur.

The KTA start-up was evaluated by assuming that the alternator could be utilized as a motoring device before the vapor turbine sustains rotation. The following assumptions were made in the calculation of friction torque:

- The KTA was vertically oriented. This orientation results in the highest starting torque because the thrust bearings are larger in diameter than the journal bearings, giving a larger restive moment for the same weight loading. In calculating friction torque, the thrust bearing outside radius was used as the moment arm.
- The alternator journals were loaded radially by an unbalanced magnetic force of 75 lb/brg from displacing the rotor 0.0045 inch from the centered position. This distance was equal to the displacement of the journal from the bearing center to the pad surface when loaded between pivots.
- The bearing material friction coefficient was 0.5.

The following friction torques were calculated:

Two alternator journal bearings	9.4 ft-lb
Alternator thrust bearing	44.3
Turbine thrust bearing	<u>12.6</u>
Total	66.3 ft-lb

Since there is no radial load on the turbine journal bearings with vertical orientation, no friction torque is developed.

In addition, the film thickness was calculated for each bearing as a function of speed for the assumed gravity and magnetic loads (a typical film thickness vs. speed curve for the alternator thrust bearing is included as Figure 7.5-1). To establish the speed at which dry rubbing friction ceased, a calculated film thickness of 100 microinches was assumed. This is considered a conservative assumption, since coast-down tests of NaK lubricated bearings at MTI have shown that full film lubrication exists to calculated film thicknesses of less than 50 microinches.

Finally, to estimate the time period of bearing rubbing, the minimum calculated alternator motoring speed-torque characteristic was used to calculate rotor acceleration. The results of all of these calculations are summarized on Figure 7.5-2.

Here it is seen that the journals lift (attain a calculated film thickness of 100 microinches) at about 140 rpm and are accelerated to this speed in 0.32 seconds. The thrust bearings, which are more highly loaded, lift at about 240 rpm in 0.73 seconds. Table 7.5-1, which compares the KTA bearing loads, rubbing speeds, and rubbing times with those of applicable cemented carbide rubbing tests in high temperature NaK and potassium, shows that the KTA bearing start-up situation is quite mild. Although all of the tests were successful and only minor polishing



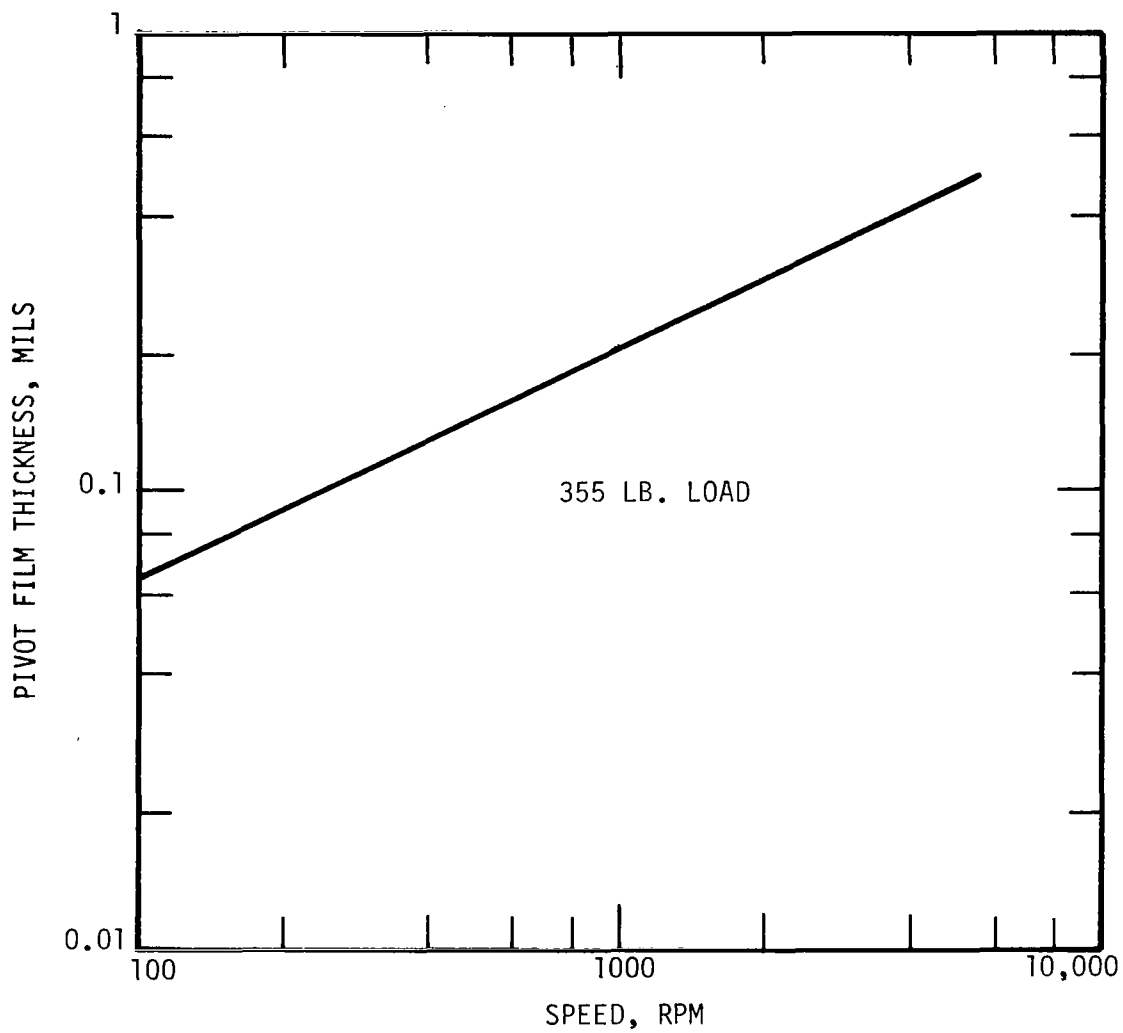


Figure 7.5-1. Thrust Bearing Pivot Film Thickness for 450 KW Alternator.  
(Vertical Shaft)

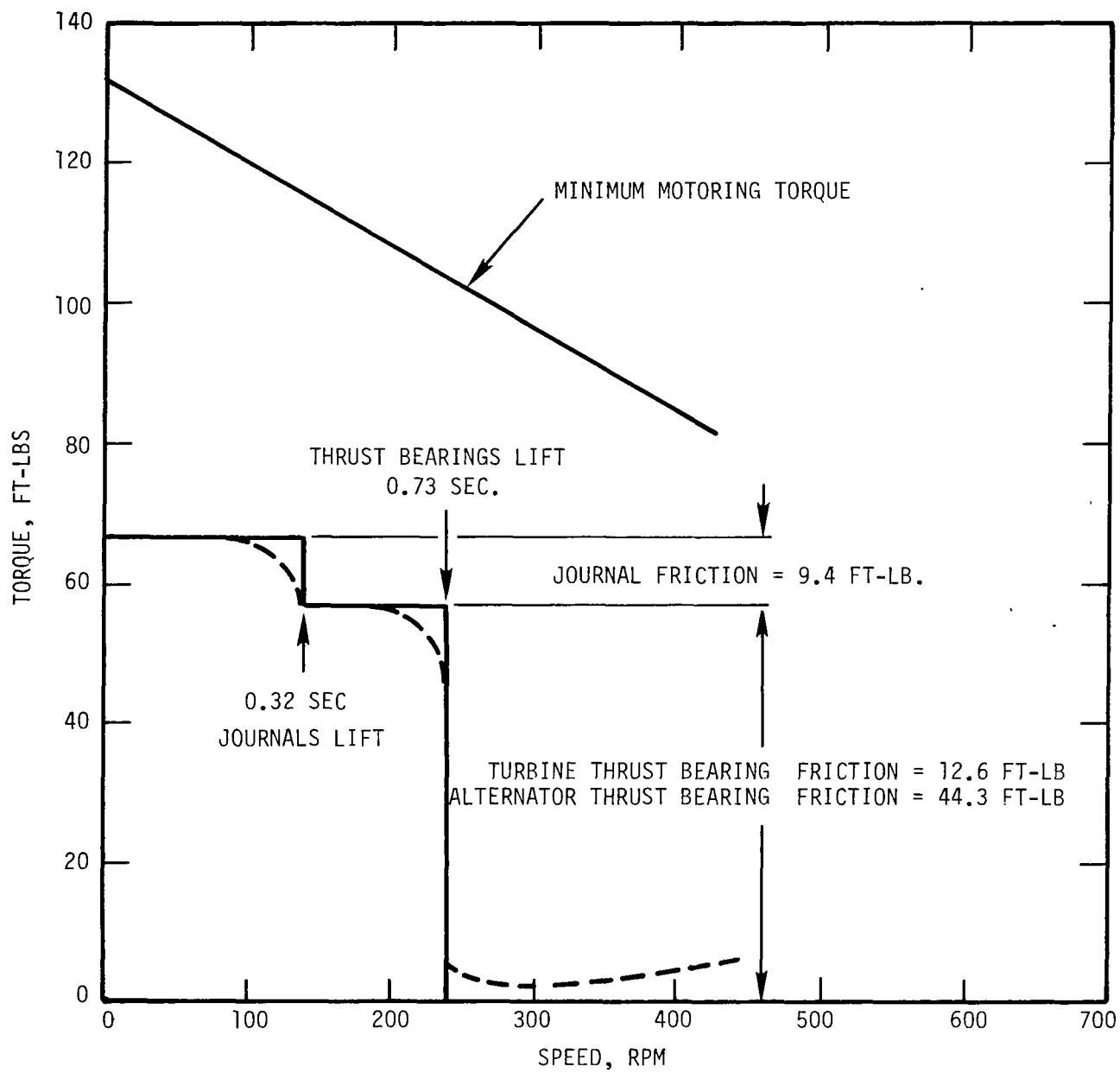


Figure 7.5-2. KTA Start-Up Performance.

TABLE 7.5-1  
COMPARISON OF ALTERNATOR START-UP CONDITIONS WITH  
APPLICABLE CEMENTED CARBIDE MATERIALS TESTS

	Alternator Journal	Alternator Thrust	Vail's Tests	Wallace's Tests	Frank & Moor's Tests
Bearing pressure $\left( \frac{\text{Load}}{\text{Area}} \right) - \text{psi}$	8.3	23.8	—	—	—
Hertz stress — psi	725	319	15000—45000	18100	94000 & 287000
Lift-off speed — rpm	140	240	—	—	—
Max. rubbing velocity — ft/sec	1.9	6.3	7.4	4.5	16.7
Rubbing time — sec	.38	.73	12,300	78,000	3,600
Rubbing distance — ft	.35	1.2	91,000	350,000	60,000
Reference			7.5-1 7.5-2	7.5-3	7.5-4

of the test specimens results, Frank & Moor's tests are the most applicable because they were accomplished in potassium at 400, 800, and 1200°F utilizing both TiC + 10% Cb and a material very similar to Carboloy 907.

Since the KTA bearings are very lightly loaded and the rubbing times based upon the assumed motoring torque available are short, no wear or galling type start-up problems should be anticipated. However, it can be seen on Figure 7.5-2 that the starting torques can be quite high (assuming a friction coefficient of 0.5) and that other starting schemes, such as impingement methods, may not produce the torque required to overcome bearing static friction.

## 7.6 HYDROSTATIC JACKING

If the final system start-up scheme should be deficient in starting torque capability, hydrostatic jacking could be introduced into the system. With hydrostatic jacking, potassium at high pressure would be introduced directly into the bearing pads to separate the bearing surfaces and eliminate the material static friction.

The problem with hydrostatically jacked tilting pad bearings is the physical introduction of the high pressure fluid into the pad. The least complex method is to pipe it through the pivot point and utilize the pivot as the seal. This approach is, however, highly undesirable because, with the pivot center removed to provide a flow path, the characteristic motion of the pivot becomes sliding instead of the preferred rolling. With sliding motion at the pivot, the rate of pivot wear is increased and could lead to premature bearing failure.\* Furthermore, the pad restraint introduced by the sliding pivot friction can be sufficiently large to prevent the pad from tracking the shaft radial motions, which could lead to fractional frequency instabilities.

For these reasons, several arrangements were evaluated to circumvent the pivot area when introducing a hydrostatic feed into the pad. Of these, two showed promise in that they appeared to be reasonably simple, could be made to impose minimum restraint upon the tilting pad, and should not be fatigue limited. One concept, shown on Figure 7.6-1, utilizes long flexible tubes to introduce the fluid to the pad. It has the advantageous ability to incorporate check valves into each pad feed line to prevent back flow of the hydrodynamic pressures into unloaded

---

\* Endurance testing of the NaK lubricated SNAP 8 NaKPMMA has exceeded 10,000 hours with no apparent degradation of the bearing pivots, which were of the rolling design. No similar experience has been accumulated on sliding liquid metal lubricated pivots.

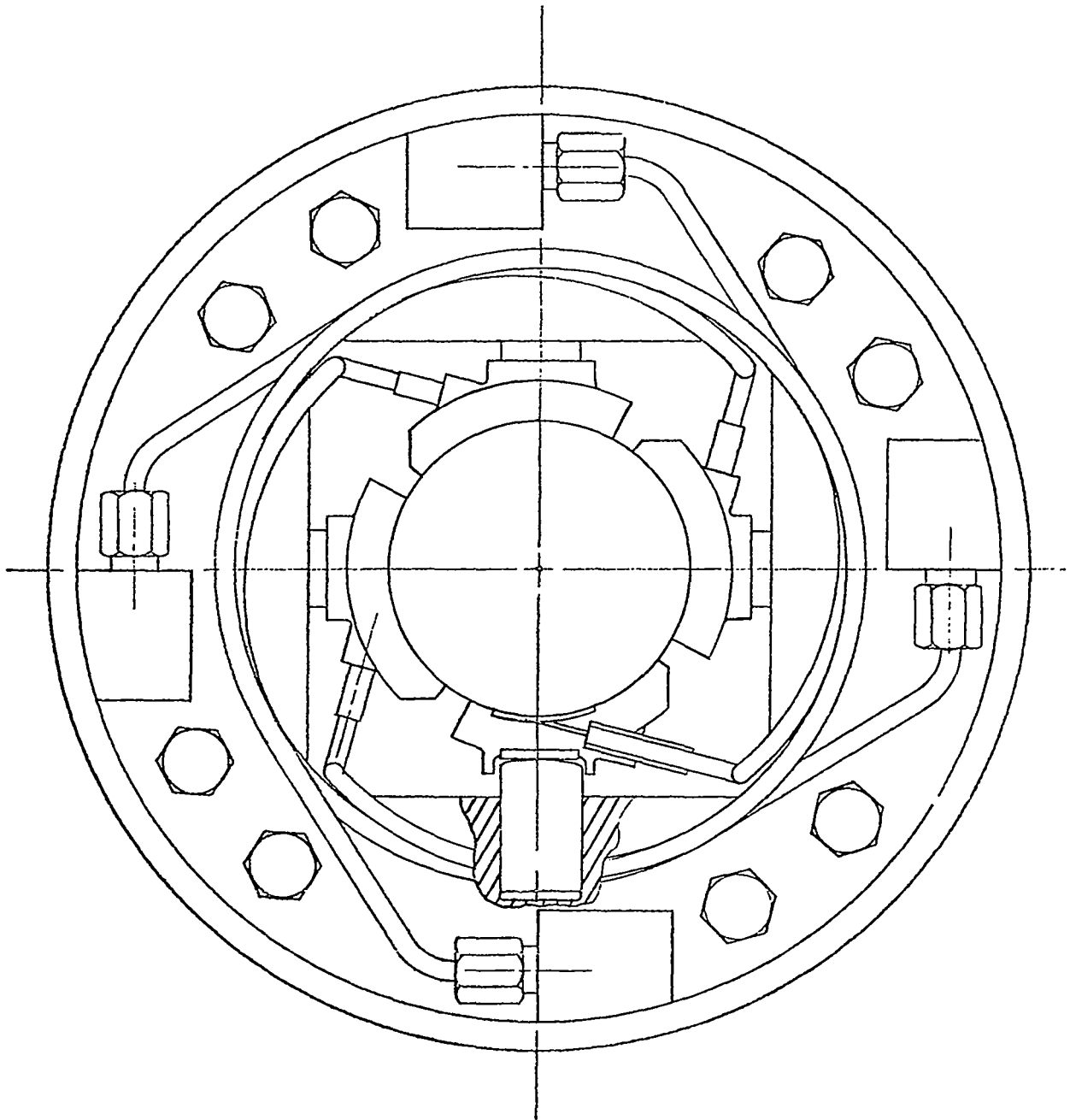


Figure 7.6-1. Concept for Feeding Jacking Fluid Through Long Flexible Tubes.

pads or the hydrostatic system. The disadvantages of this arrangement are the assembly difficulty and the potential for introducing pad restraint by assembly strains.

The other concept is shown on Figure 7.6-2. It avoids the assembly and restraint problem introduced by the supply tubing. In this design, the high pressure hydrostatic lubricant is introduced into a cavity around the pivot, where it discharges through the bearing restrictor into a small hydrostatic supply pressure. After the start-up has been accomplished, the hydrostatic jacking supply is turned off and the diaphragm returns to its normal free position away from the pivot. In this way the pad becomes totally unstrained and the diaphragm seal is not subjected to fatigue stresses in its normal operation mode.

Without a check valve between the pad pocket and the cavity behind the pad, the hydrodynamic pressure generated in the pad during normal operating can leak into the drain cavity and degrade the hydrodynamic performance. Check valves have been built into pads in some gas bearing applications to avoid this problem, but it is felt to be unreliable in a liquid metal bearing because of potential plugging problems.

Preliminary hydrodynamic performance calculations for the concepts shown on Figures 7.6-1 and 7.6-2 were made as a comparison and to establish the practicality of hydrostatic jacking. It was assumed that it would be necessary for a 2.5-inch diameter by 2.5-inch long tilting pad journal to lift 215 pounds and support it at a film thickness of 0.0002 inch, utilizing a 130 psi hydrostatic supply. This approximates the condition of the horizontally oriented KTA alternator. To accomplish this, a 0.75-inch wide by 32° long pocket in the pad would be required

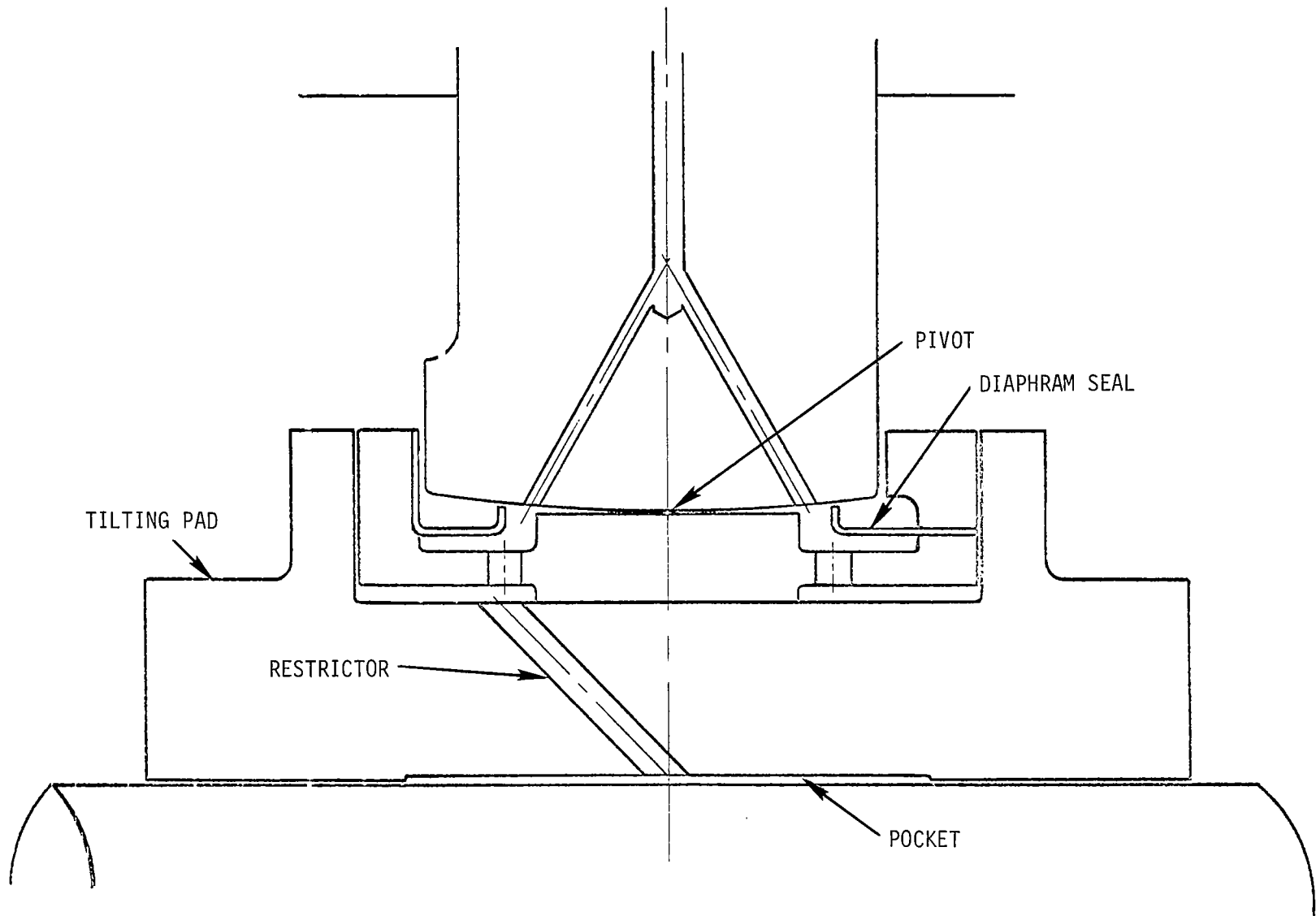


Figure 7.6-2. Concept for Hydrostatic Jacking Utilizing a Diaphragm Seal.



with a 0.0514-inch diameter supply restrictor. These configurations and the assumed requirements of the hydrodynamic evaluation are shown on Figure 7.6-3.

In Table 7.6-1, the hydrodynamic load and stiffness of a plain tilting pad bearing (with no pocket or supply orifice), have been arbitrarily set at 100. The table shows that the presence of the hydrostatic jacking pocket with a blocked orifice (no backflow, as with a check valve) reduces the load by five percent and stiffness by nine percent. This is because the pocket prevents the establishment of the normal peak pressures and flattens the pressure profile over the pocket. If the normal hydrodynamic pressure were allowed to bleed through the 0.0514-inch diameter orifice after the jacking pressure was removed, the resulting load and stiffness would be only 53 percent that of a purely hydrodynamic tilting pad bearing. This is obviously intolerable.

Smaller orifice diameters were assumed, to increase the resistance to flow through the restrictor. The hydrodynamic performance became closer to that which could be achieved with check valves in the pad flow circuit. Orifice diameters of 0.0162 and 0.00514 inch were assumed, and hydrodynamic load capacity and stiffness values were calculated with the reduced backflows. The increased hydrodynamic performance shown in Table 7.6-1 with these smaller orifices is significant, but orifices of such a small diameter present two problems. Not only are they very susceptible to plugging but they require unrealistic supply pressures ( $10^4$  and  $10^6$  psi) to support the load during the hydrostatic jacking mode.

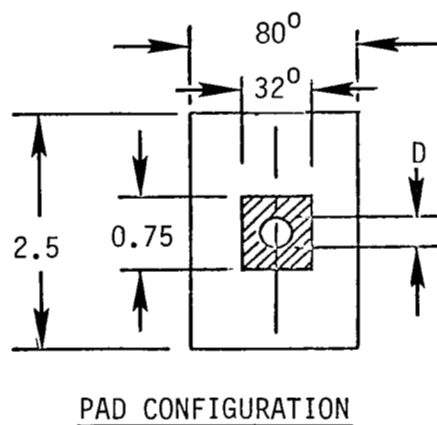
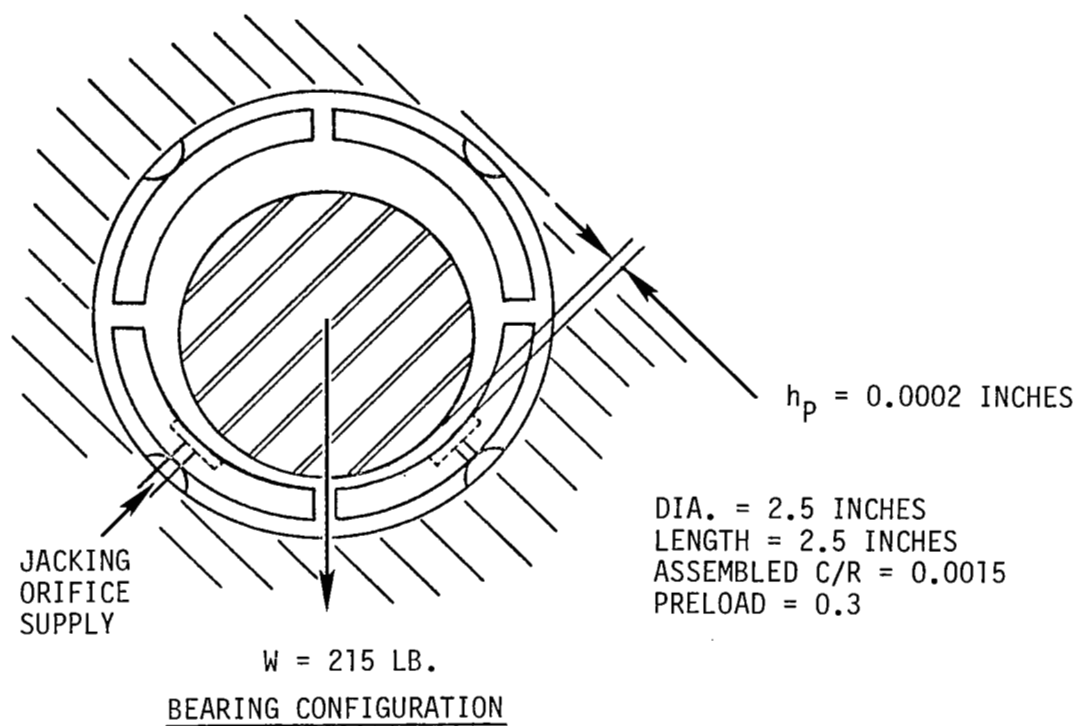



Figure 7.6-3. Hydrostatically Jacked Tilting Pad Journal.

TABLE 7.6-1  
EFFECT OF JACKING PAD ON DESIGN SPEED  
HYDRODYNAMIC PERFORMANCE

Pocket dim.	None	0.75" x 32 <sup>0</sup>	0.75" x 32 <sup>0</sup>	0.75" x 32 <sup>0</sup>	0.75" x 32 <sup>0</sup>
Orifice dia, in.	None	Blocked	0.0514	0.0162	0.00514
Supply pressure, psia	—	—	130	10 <sup>4</sup>	10 <sup>6</sup>
Load rating	100	95	53	75	87
Stiffness rating	100	91	53	70	81

  
 Pocket bleeding to  
 ambient through orifice

From this evaluation it is concluded that, if necessary, hydrostatic jacking of the tilting pad journal bearings could be accomplished. However, in order to avoid undue degradation in hydrodynamic performance under normal operating conditions, it is necessary to incorporate a check valve into each pad circuit.

Similar calculations were not made for the thrust bearing because it was apparent that the introduction of jacking fluid to the eight pads would be intolerably complex. Not only is there less space around the thrust bearing, but the double leveling link rows prevent access to the pads from the rear. If jacking of the thrust bearings should become necessary to minimize the starting torque, a fixed geometry design similar to the step bearing design presented in the Phase I report will be required.

## 7.7 BEARING AND SEAL JOURNAL STRESSES AND MATERIAL CONSIDERATIONS

### General

The question of the effects of differential thermal expansion coefficients arises as a possibly significant factor to be considered when carbide bearing journal materials are to be used on a KDTZM-1175 rotor shaft. Figure 7.7-1 shows the average coefficients of thermal expansion of selected materials from 200 - 900°F. TiC + 10% Cb matches Mo-TZM relatively closely, with its coefficient about  $1 \times 10^{-6}$  in./in.°F higher than that of Mo-TZM. Carboloy 907, on the other hand, a material used in the alternator bearings, matches the coefficient of Mo-TZM almost exactly. Carboloy 907 has a density of 0.531 pci, three times as great as that of TiC + 10% Cb, therefore centrifugal stresses generated in Carboloy 907 will be three times those of TiC + 10% Cb at similar speeds and geometry. .

Both TiC + 10% Cb (0.33 Fe - 0.73 Co - 5.85 WC - 9.54 Cb - bal. TiC) and Carboloy 907 (0.08 Fe - 6 Co - 20 TaC - 0.02 other metals - bal. WC) are carbide materials with high compressive strengths and are expected to have good friction and wear properties in liquid potassium at elevated temperatures (7.7-1).

### Turbine Bearing/Seal Journals

Assuming isothermal steady-state operating conditions, there are still two principal sources of stresses in bearing and seal journals - shrink stresses and centrifugal stresses. The shrink stresses are required, in the absence of mechanical locking devices, to produce a frictional force which prevents relative motion between the shaft and

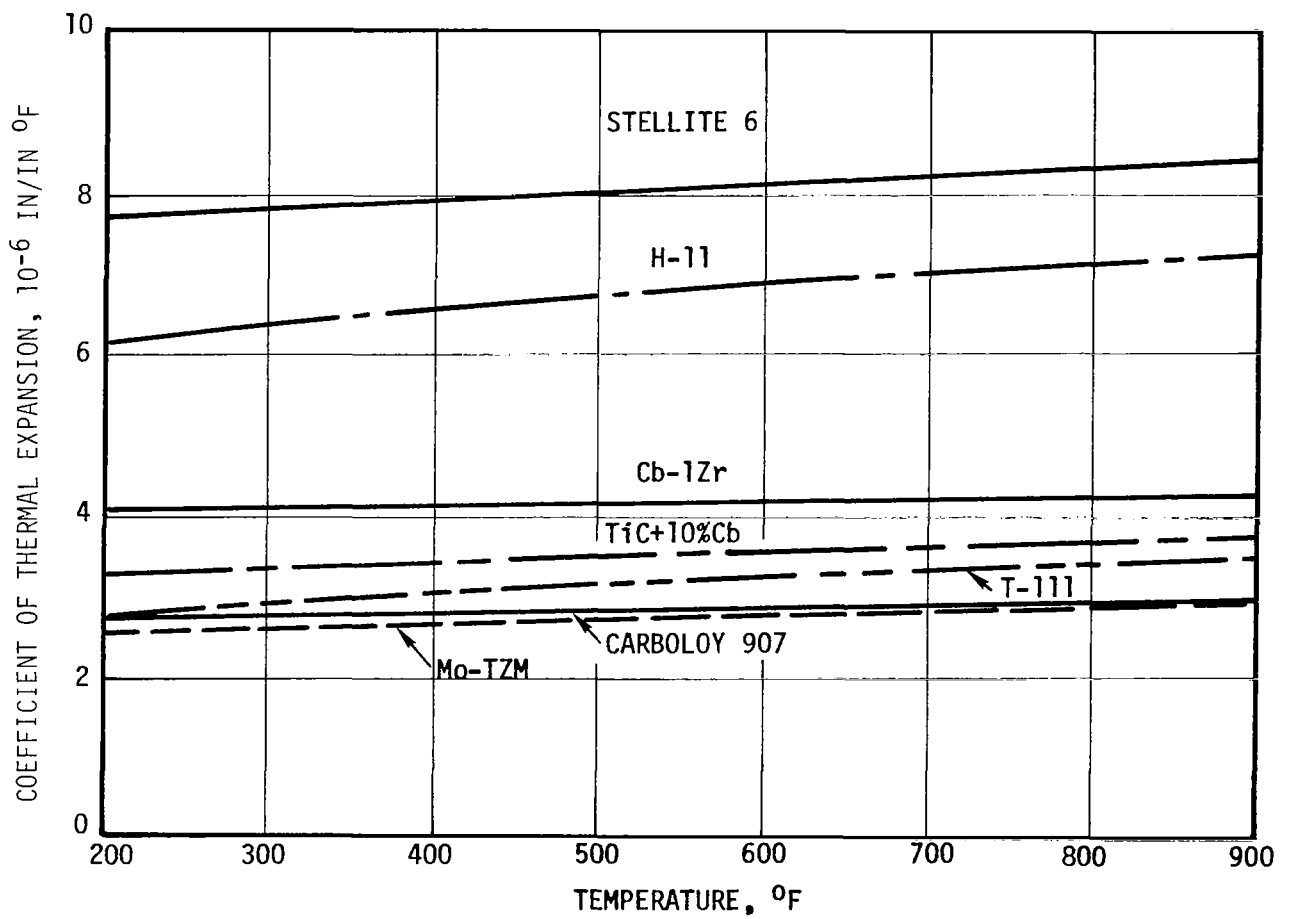


Figure 7.7-1. Average Coefficient of Thermal Expansion of KTA Materials.

journal. For a material combination such as a TZM shaft and TiC + 10% Cb journal, the journal grows away from the shaft at elevated temperatures. Therefore, a relatively large assembly shrink stress is required to produce an operating temperature shrink stress. Also, the greater deformation of the journal than the shaft due to centrifugal stresses adds to the assembly shrink stress requirements.

The relative magnitudes and senses of shrink and centrifugal stresses are shown in Figure 7.7-2. The shrink stresses are derived from a common interface pressure which tries to expand the outer ring and compress the inner one. In the inner ring, compressive shrink stresses combine with tensile centrifugal stresses. In the outer ring, both tangential stresses are tensile, while the radial shrink stress is still compressive but lower in magnitude than for the inner ring. Also, the centrifugal stress levels in the outer ring will be higher than in the inner ring because of larger radii, provided the difference in material densities do not override this consideration (unlikely). This is seen from the terms of material density  $\rho$ , rotating speed  $\omega$ , radius  $r$ , and gravitational constant  $g$  which comprise the centrifugal factor:

$$\frac{\rho \omega^2 r^2}{g}$$

Thus, for the range of present interest, the design approach is to first calculate the interference which exists between the shaft and journal at both room temperature and operating temperature, and at 0 rpm and the maximum speed at which interference is needed. If clearance exists under any condition, that clearance is adjusted to zero and all other interferences rise.

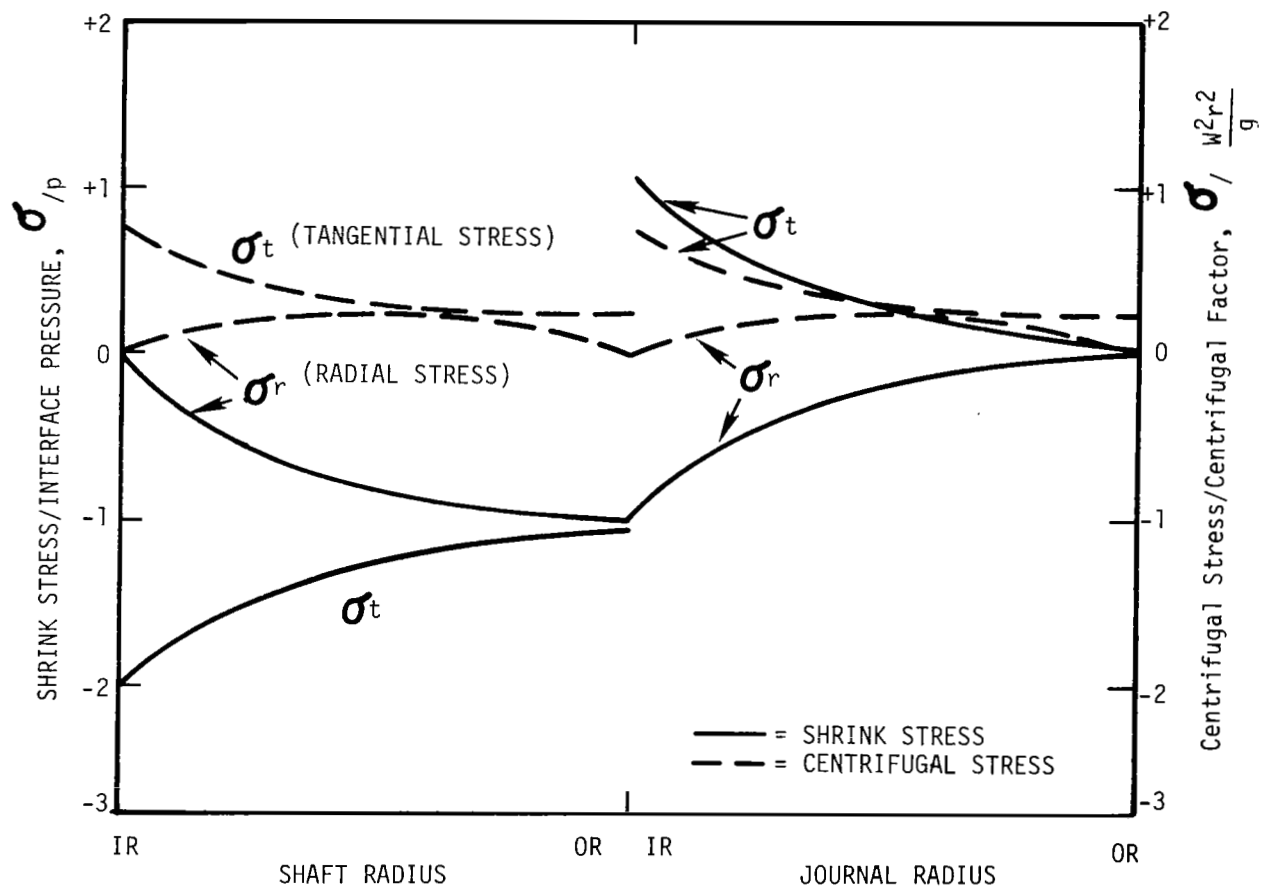


Figure 7.7-2. Stresses in Shrunk-Fit, Rotating, Concentric Shaft and Journal. Tension = +, Compression = -. (Ref. 7.7-1)



The interferences can only exist by deforming the inner ring (shaft) inward and expanding the outer ring (journal) outward, with the sum of the two deformations equalling the interference. By combining the appropriate equations, a mutual interface pressure may be found which produces the required deformations, and from the pressure can be found the shrink stresses. The centrifugal stresses are added to produce the total stresses.

It is assumed that providing positive retention to 30,000 rpm ( $1.56 N_D$ ) is satisfactory. With an assumed operating temperature of 900°F for both shaft and journal, assembly shrink stresses of 18 - 34 ksi are predicted for all the bearing and seal journals and the thrust bearing runner of the turbine. In Figure 7.7-3 the maximum effective stresses (journal inner radius) are shown. As the parts reach 900°F, without rotation, the shrink stresses drop to 3 - 19 ksi. From this point, the shrink stresses drop linearly (on rpm<sup>2</sup> scale) to zero at 30,000 rpm. On the same scale, the centrifugal stresses rise linearly with speed, using the model of a rotating flat disk with central hole for the journals. The total effective stresses plotted, then, are the sums of the shrink stresses and the centrifugal stresses which act at the inner diameter of the carbide pieces. The stresses in the shaft material are of less concern. The bending stresses in the thrust bearing due to the action of the thrust loads which it supports are also of less concern.

The allowable ultimate tensile strength (transverse rupture) of the TiC + 10% Cb material is estimated to be approximately 65 - 75 ksi at room temperature and slightly less at 900°F. This estimate is based upon the best available information from a vendor of this material, and

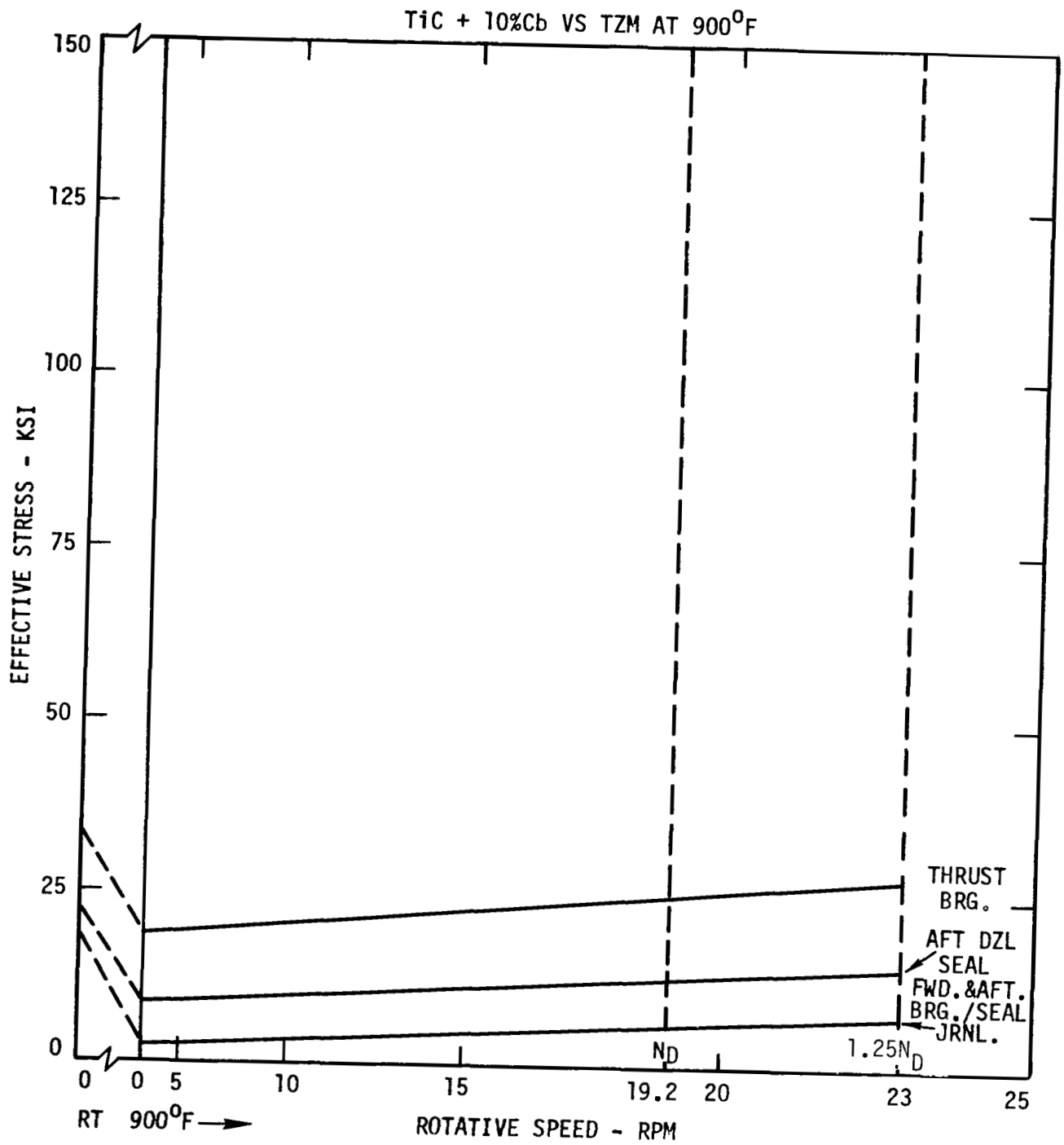


Figure 7.7-3. Effective Stresses in 7+4 Turbine Bearing and Seal Journals.

appears to be realistically low by comparison to the ultimate compressive strength of the materials. However, it is also possible that the transverse rupture strength should be further derated, since the transverse rupture test loads only a line of the specimen, with a limited number of possible flaws, to the maximum tensile stress. Shrink-fitting exposes the full inner surface of the carbide journal to the tensile stress, with a correspondingly much greater number of possible fracture origin sites. From Reference 7.7-3, the average compressive properties are:

Material	Temp. °F	P.L. ksi	0.2% offset ksi	UCS ksi	Total Strain at End of Test
C907	800	255.0	510.0	>608.5	1.9 - 2.5%
C907	1200	270.5	422.0	495.5	
TiC + 10% Cb	800	--	--	383.5	
TiC + 10% Cb	1200	283.0	--	331.0	

The allowable ultimate tensile strength of the materials could be considerably lower than the estimates before close proximity to the calculated stresses exists. However, the existence of such proximity is a very real possibility which must be determined before the bearing and seal journal design is fixed. One preliminary test made at GE-NSP of a TiC + 10% Cb ring shrunk on a TZM shaft indicates that the allowable ultimate tensile strength of TiC + 10% Cb may be so low that the required stresses are not safe. In this case, the conical end scheme of retaining journals could be used (to be discussed later), a lighter shrink fit could be chosen or mechanical pinning could be provided, or the material used in turbine journals must be one which has a thermal expansion coefficient closer to that of the TZM shaft, such as tungsten carbide with refractory binder.

On the other hand, higher allowable ultimate tensile strengths are indicated by some handbooks. From Reference 7.7-4:

	<u>TiC</u>	<u>WC</u>
Tensile Strength, ksi 75F	26-134	130
Transverse Rupture Strength, ksi	122-236	175-460
Compressive Strength, ksi	265-450	518-800
Tensile/Compressive	0.10-0.30	0.25-0.16
Transverse Rupture/Compressive	0.46-0.52	0.34-0.58

If the transverse rupture strengths be estimated from the latter ratio, the allowable strengths estimated from the ultimate compressive stresses of the previous table for C907 and TiC + 10% Cb at 800°F are:

TiC + 10% Cb -	383.5 (0.5)	=	190 ksi
C907 -	608.5 (0.4)	=	240 ksi

The corresponding tensile strengths would be:

TiC + 10% Cb -	383.5 (0.2)	=	80 ksi
C907 -	608.5 (0.2)	=	130 ksi

Shrink fit tests on disks would provide more meaningful data than tensile tests for the design of bearing journals.

Carboloy 907 would be a desirable material for use in the turbine bearing/seal journals because of the close match of its thermal expansion coefficient with that of the TZM shaft, but the cobalt binder is not desirable in the main potassium loop. Because of the high density (0.531 pci), the centrifugal stresses in Carboloy 907 rise rapidly with speed, requiring that its use be limited to parts smaller than the thrust bearing inserts.

### Alternator Conical-End Journal

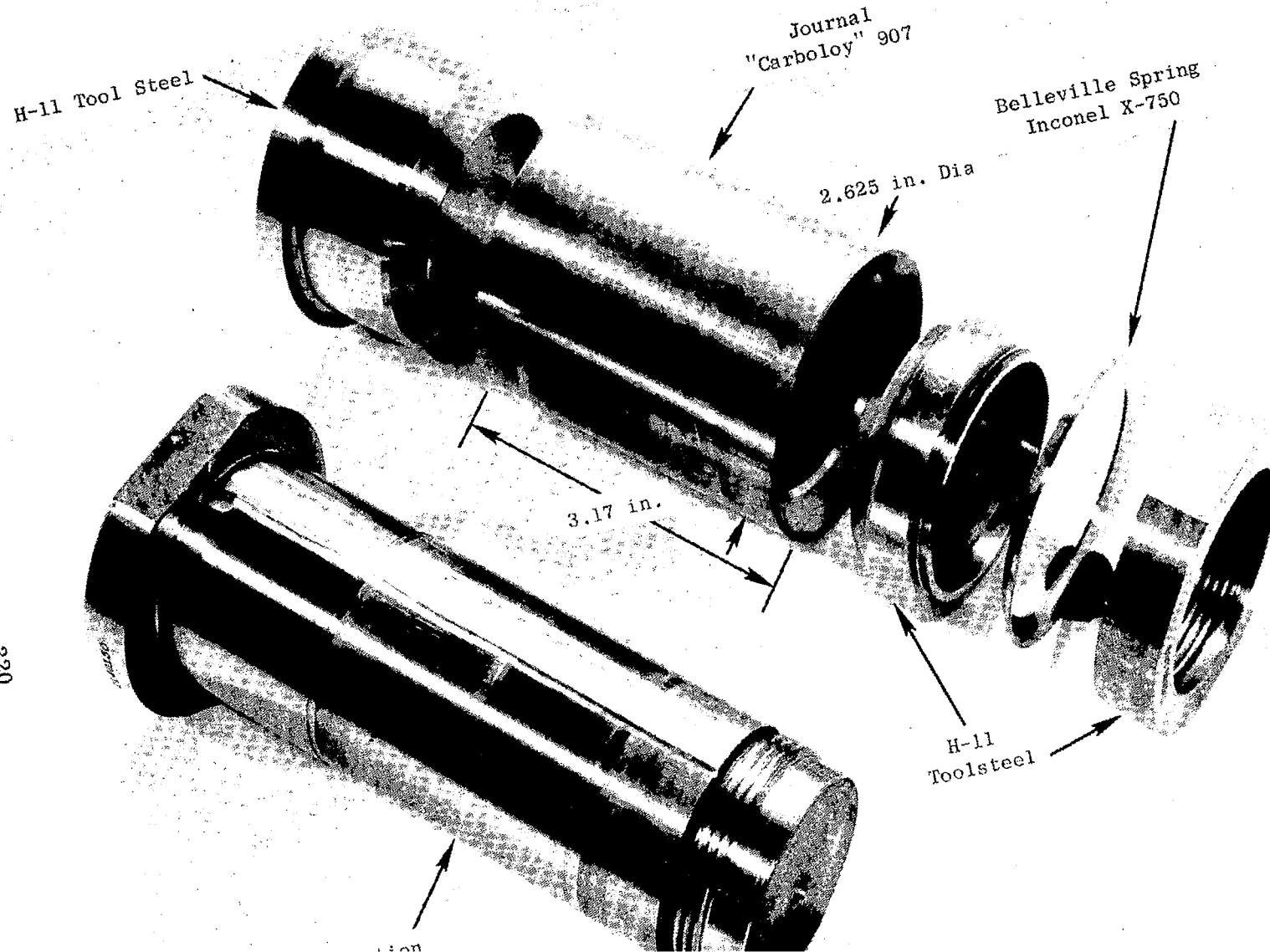
Since the alternator shaft is H-11 steel, with a high coefficient of thermal expansion, and the bearing journals are Carboloy 907, with low coefficient of thermal expansion, special means must be provided for accommodating thermal expansion. A method for doing so is shown on Figure 7.7-4. This device has been built and tested by GE-NSP to prove the principle. The carbide journal has sufficient clearance from the shaft at its ID that the components never contact each other within the design temperature range. Instead, the journal is located axially and radially by two end rings of the same material as the shaft. Axial load restraints is provided by a nut and Belleville spring. The key to this method is the matching cones of the journal and the end rings. If the apexes of the cones terminate at the junction of the centerline of rotation and the axial centerline of the journal, and the journal will slide on the end ring conical surface, the differential thermal expansion will be automatically compensated. This is expressed, for a point on the conical interface located an axial distance  $L$  and a radial distance  $R$  from the apex of the cone having apex angle  $2\beta$ :

$$\tan \beta = \tan \beta'_{H11} = \tan \beta'_{C907}$$

$$\frac{R}{L} = \frac{R(1+\alpha_{H11}\Delta T)}{L(1+\alpha_{H11}\Delta T)} = \frac{R(1+\alpha_{C907}\Delta T)}{L(1+\alpha_{C907}\Delta T)}$$

$$\frac{R}{L} = \frac{R}{L} = \frac{R}{L}$$

The configuration shown or one similar to it has undergone 20 static thermal cycle tests in liquid potassium at temperatures of 250 - 800°F with no galling, seizure, or loss of concentricity. The journal diameter was 2.625 inches and a 600 pound spring preload was used.



Another 20 cycles were run with the end ring conical faces coated with Linde LW-1 tungsten carbide. No ill effects were noted, but it was concluded that the performance of the uncoated rings was satisfactory. In a dynamic Liquid Metal Bearing Test Rig, a similar design was rotated to 20,000 rpm while loaded to 100 lb/bearing in 800°F potassium. No slippage, galling, or loss of concentricity was noted.

## 7.8 SUMMARY AND CONCLUSIONS

The journal bearings were sized to meet the requirements of the KTA rotor dynamics, which results in bearings that are overdesigned from a load capacity standpoint. This has the advantage, however, of allowing the KTA to operate for long periods of time and with reasonable thick films ( $\epsilon < 0.85$ ) in a lg environment at speeds as low as 2000 rpm. The thrust bearings were sized to meet the long-term operating requirement of 4g's and have somewhat less load margin than do the journals because of the desire to minimize the power consumption of the thrust bearing, the largest contributor to the total bearing seal parasitic power. The alternator thrust bearing, however, will operate at 2000 rpm with a lg load at a film thickness of 0.3 mils (see Figure 7.5-1), which is sufficiently large to tolerate long-term operation.

The recommended pivot configuration for all bearings is a sphere on a flat, which will eliminate the possibility of lock-up upon starting. With a spherical pivot radius of eight inches, the contact stresses are low enough to eliminate the possibility of Brinelling the pivots under the 20g launch condition.

The problem of KTA start-up was considered and it is concluded that bearing friction does not present a problem if the alternator is used as a motor starter. Bearing loads and rubbing times are very low and the bearings should not be susceptible to galling or wear upon start-up. If a lower torque source than the alternator is utilized for start-up, hydrostatic jacking could be incorporated to eliminate bearing friction torque.



Hydrostatically jacked tilting pad journal bearings where the hydrostatic supply was circumvented around the pivot were evaluated. It is concluded that such bearing types are feasible, but check valves are required in each pad circuit to eliminate backflow of the hydrodynamic pressure under normal operation. Hydrostatically jacked thrust bearings were deemed impractical because of the complexity of introducing the high pressure fluid to the pads. If hydrostatically jacked thrust bearings are required, a solid geometry design is recommended.

## 7.9 REFERENCES

- 7.5-1 Vail, D.B., "Compatibility of Materials in Liquid Metal," USAEC Report KAPL-589, August 1951.
- 7.5-2 Vail, D.B., "Compatibility of Materials in Liquid Metal," USAEC Report KAPL-1021, January 1954.
- 7.5-3 Wallace, M.J., "Summary of Potential Liquid Metal Bearing Materials for SNAP-50/SPUR Pumps," PWAC-468, November 1965, Pratt & Whitney Aircraft - CANEL.
- 7.5-4 Frank, R.G. and Moor, B.L., "Friction and Wear of Materials in Sliding Contact at Room Temperature to 1200°F in Potassium and in High Vacuum," presented at 1967 ASME Symposium on Lubrication in Nuclear Applications, June 5 - 7, 1967, Miami Beach, Florida.
- 7.7-1 Frank, R.G. and Moor, B.L., "Materials for Potassium Lubricated Journal Bearings - Final Report - Volume V - Friction and Wear Studies," Report No. GESP-100, NASA-LRC Contract No. NAS3-2534, 1969.
- 7.7-2 Den Hartog, J.P., Advanced Strength of Materials, McGraw-Hill, N.Y., 1952, pp.49-59.
- 7.7-3 Hendrixson, W.H. and Frank, R.G., "Materials for Potassium Lubricated Journal Bearings - Final Report - Volume IV - Thermal Expansion, Hot Hardness, and Compression Properties," Report No. GESP-100, NASA-LRC Contract No. NAS3-2534, 1969.
- 7.7-4 "Materials Selector Issue of Materials Engineering," October 1968, p.299.

## 8. BEARING ROTOR RESPONSE

During Phase II, the eleven stage turbine and 450 KW alternator concepts were subjected to a number of critical speed and bearing-rotor response analyses such that the rotor designs could be optimized from a vibrational standpoint. The results of these analyses for the final rotor configurations are presented in this section of the report.

The final KTA rotors are all very well behaved in that the synchronous vibration amplitudes are small - no where do they exceed 0.4 mils in the speed range to 24,000 rpm, and all potential lateral resonances are near critically damped. A potential torsional critical speed exists at about 7250 rpm, but if it is not necessary to dwell near ( $\pm 20\%$ ) this speed, it should be sufficiently well damped as to be of little consequence.

The radial compliance of the KTA structure was neglected in the Phase II response analyses because the housing designs were deferred until late in the program. However, the effect of housing stiffness on the alternator rotor vibrational behavior was evaluated and found to be a significant factor. If the final housing designs reveal excessive compliance, very simple stiffening ribs or small increases in wall thickness can be incorporated to eliminate any resonance problems.

## 8.1 BEARING COEFFICIENTS AND EXCITING FORCES

For the purpose of calculating the rotor critical speeds and actual rotor vibration amplitudes, the bearing stiffness and damping coefficients as a function of speed described in the preceeding section were used.

The source of synchronous lateral vibration driving force is mechanical unbalance and a value of 100 micro-inches of rotor mass displacement was assumed in Phase II. This, as shown in Table 8.1-1, is about an order of magnitude larger than that assumed in Phase I and relatively larger vibration amplitudes could have been expected. However, as a result of the optimization of the rotor design accomplished during Phase II, the actual vibration amplitudes of the Phase II rotors have been minimized.

The larger unbalance assumed during Phase II is considered to be realistic for rotors of the KTA mass. Most balancing machines capable of handling rotors weighing in the order of 100 to 400 pounds have a minimum sensitivity of 25 micro-inches, and allowing another 25 micro-inches for operator tolerance and repeatability, an initial assembly balance within 50 micro-inches is reasonable. Since the bearing and seal sleeves must be removed at assembly, an additional 50 micro-inches was allowed for assembly repeatability tolerance, resulting in a total assumed unbalance of 100 micro-inches.

In the case of the alternators, this unbalance was assumed to be equally distributed at the rotor pole piece ends. In the case of the turbine, the unbalance was distributed proportional to the rotor mass distribution at the spool end stages (1st and 8th).

TABLE 8.1-1

ROTOR UNBALANCE

PHASE I

$$\text{UNBALANCE} = \frac{4W}{N} = \text{in-oz.}$$

$\approx .020$  in-oz. Total for Turbines

$\approx .080$  in-oz. Total for Alternators

PHASE II

UNBALANCE = 100 micro-inches total

= .176 in-oz. Total for Turbine

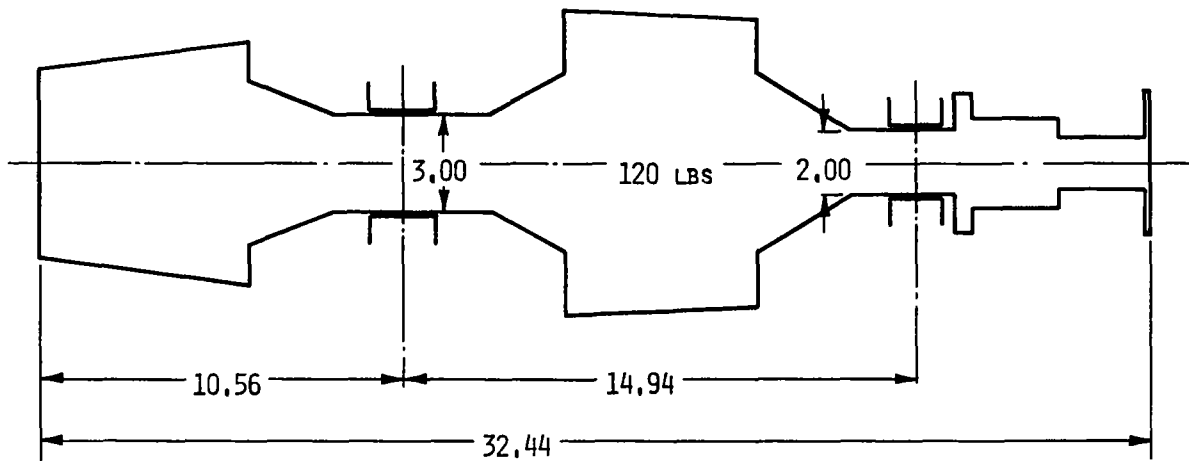
$\approx .57$  in-oz. Total for Alternators

Since the rotor response analysis is a linear analysis (stiffness and damping coefficients are independent of amplitude), the amplitudes for larger (or smaller) values of unbalance can readily be estimated from the results included in this report by simply multiplying the reported amplitudes by the desired unbalance ratio. This approximation is reasonably valid if the amplitudes are less than 30 percent of the bearing radial clearance. For larger amplitudes, the approximation begins to break down because of the increased bearing stiffness and damping resulting from non-linearity in the fluid film.

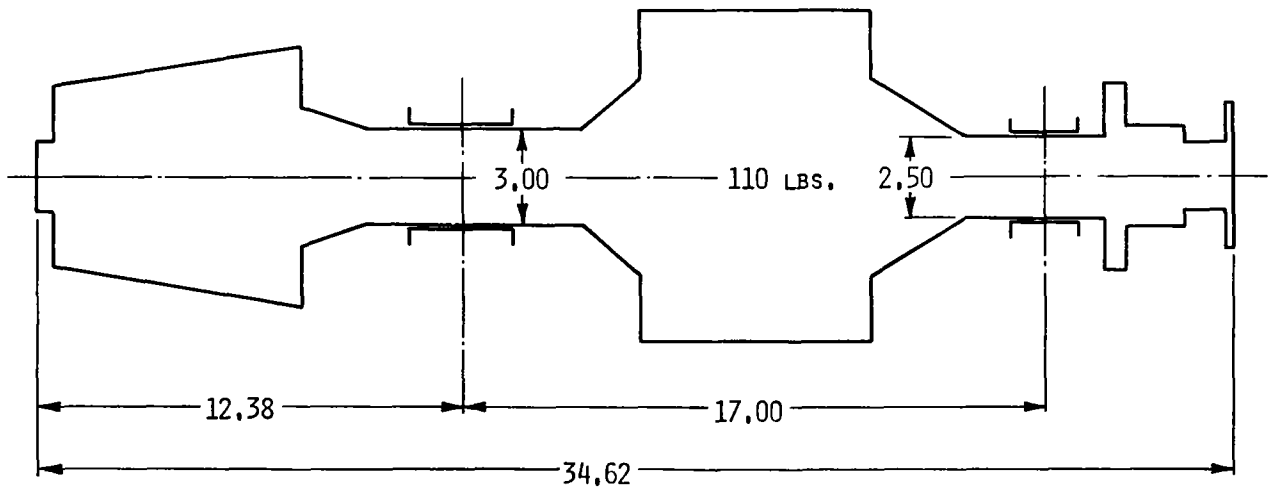
For example, in the case of the eleven stage turbine discussed later, the amplitude in the 2.5 inch diameter bearing at design speed was about 6.7 percent ( $\frac{.125}{1.88} \times 100$ ) of the bearing clearance. Since the analysis is valid to about 30 percent, an unbalance up to approximately 450 micro-inches could be validly considered with the present analysis. The effect of such an increase in unbalance will be discussed in more detail in the following section.

## 8.2 ELEVEN STAGE TURBINE (47R199305)

A comparison of the Phase I and Phase II split spool turbines subjected to detailed rotor dynamics analyses is shown on Figure 8.2-1. The Phase II design (47R199305), although a little over two inches longer, is 10 pounds lighter than the Phase I design because the latter was fabricated from the denser ASTAR and FS85 materials as opposed to the lighter TZM used in the Phase II study. In addition, the Phase II turbine rotor was effectively stiffer than the Phase I rotor because of the larger diameter coupling and stub end shaft (2.5 inches versus 2.0 inches diameter journals), a shorter (approximately 2.5 inches) coupling overhand, and a higher rotor material elastic modulus.



47R199271 TURBINE  
(9 STAGES, 5 OVERHUNG)



47R199305 TURBINE  
(11 STAGES, 7 OVERHUNG)

Figure 8.2-1. Phase I and Phase II Split Spool Turbines.

All of these factors plus some redesign of the turbine wheel to bearing journal transition pieces has resulted in a rotor design where the undamped third critical speed is well above operating speed (in excess of 30,000 rpm) as is shown on Figure 8.2-2. The reader will recall that the Phase I split spool turbine had a third critical at about 20,000 rpm which resulted in a minor resonance near design speed. The bearing stiffness characteristics for both horizontal (lg) and a vertical (0g) operation are also plotted on the critical speed curve in Figure 8.2-2 where it can be seen that undamped resonances could be expected at 5000 rpm and/or 8000 rpm depending upon the operation.

The response plots for horizontal operation with 100 micro-inches of unbalance both in and out of phase are shown on Figures 8.2-3 and 8.2-4. Neither of these plots reveal any resonance peaks as is typical of highly damped rotor systems where the bearings are properly displaced from the resonances nodes. The out-of-phase unbalance relationship tends to have slightly higher vibration amplitudes as would be expected since it tends to accentuate the second critical mode which is conical in nature.

Although both the horizontal and vertical rotor cases were analyzed, only the horizontal case is presented as it is the most interesting and significant. It can be seen on Figure 8.2-2 that, within the speed range studied (2000 rpm to 30,000 rpm), the vertical or zero bearing load case intersects only the second critical (at about 5000 rpm). On the other hand, the horizontal case could be troubled by both the first critical (also about 5000 rpm) and the second critical (8000 rpm). Furthermore, the horizontal operation



(REF. G.E. DWG. 47R199305)  
 (2.5 IN. DIA. DRIVE END BEARING)

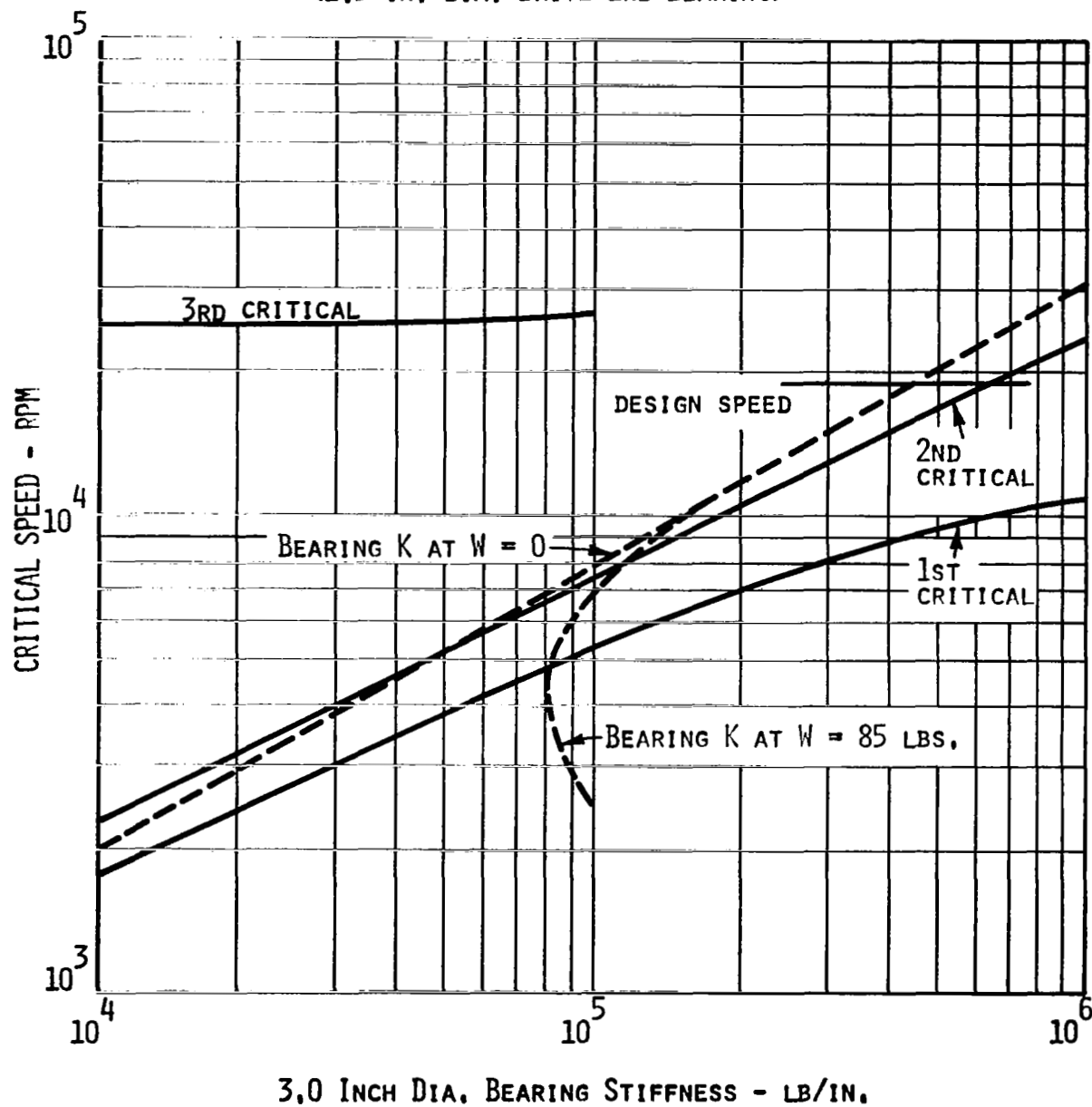


Figure 8.2-2. Eleven Stage (7+4) Turbine (Rev. 1).  
 Critical Speed

(REF. G.E. DWG. 47R199305)

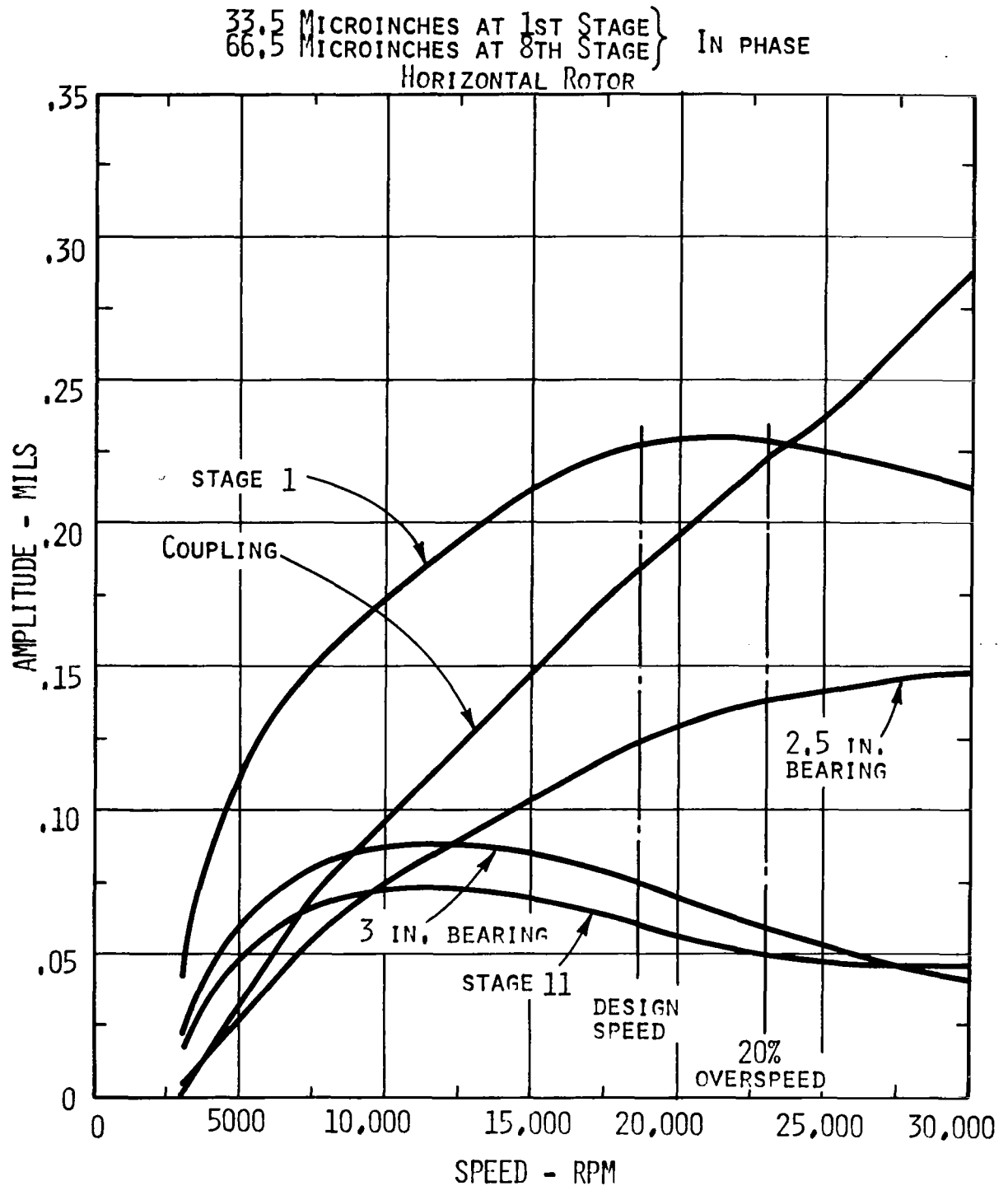


Figure 8.2-3. Eleven Stage Turbine Response to 100 Microinches.  
Total Unbalance

(REF. G.E. DWG. 47R199305)

33.5 MICROINCHES AT 1ST STAGE }  
66.5 MICROINCHES AT 8TH STAGE } OUT OF PHASE  
HORIZONTAL ROTOR

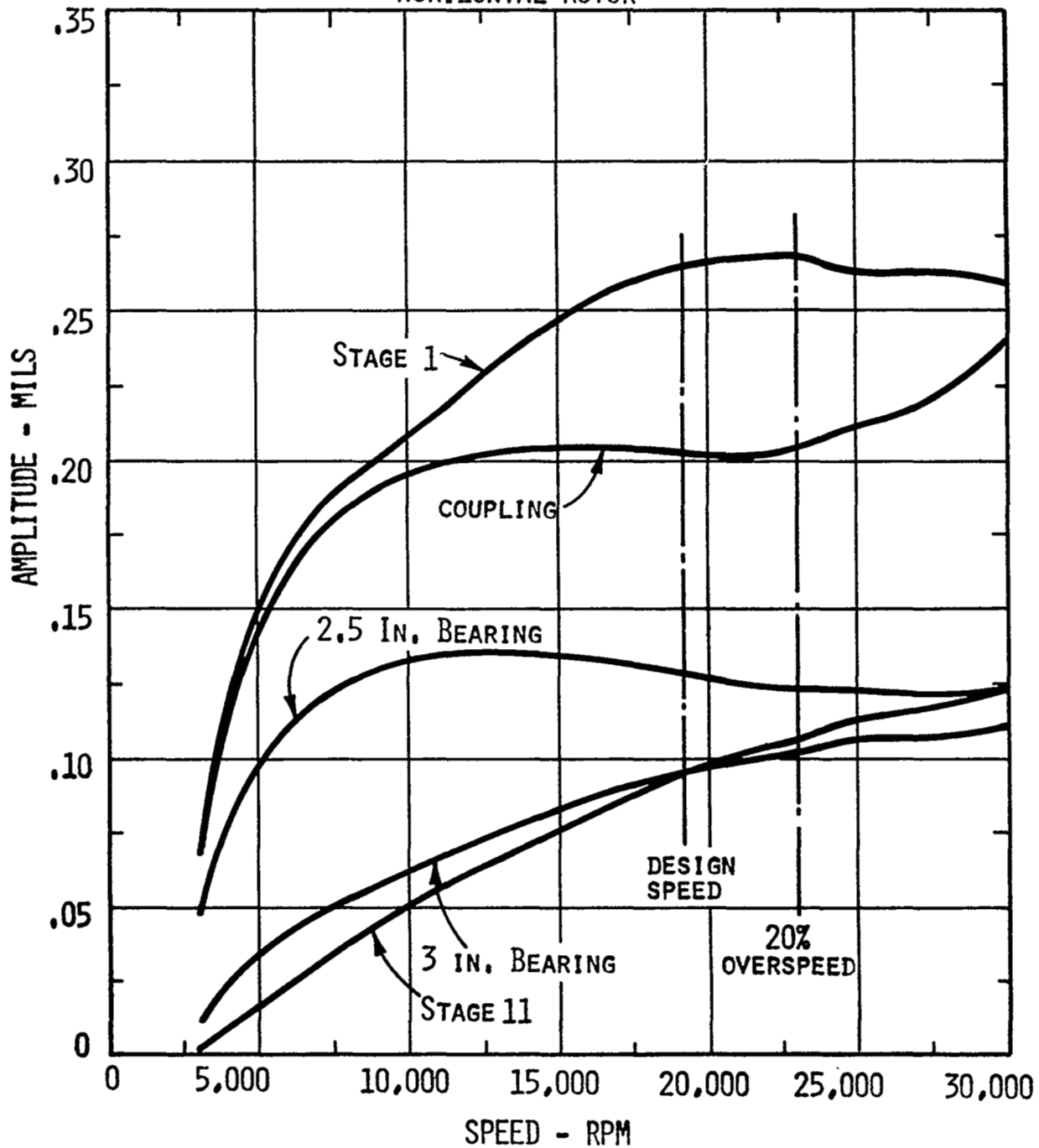


Figure 8.2-4. Eleven Stage Turbine Response to 100 Microinches.  
Total Unbalance

case might be expected to have larger amplitudes at the second because of the higher speed at which it is encountered. In actual fact it was found that the amplitudes for both operations were within 20 micro-inches of one another at speeds below 10,000 rpm. For speeds in excess of 10,000 rpm the amplitudes for the two operations are identical because, as can be seen on Figure 8.2-2, the bearing stiffnesses are identical. This is because the bearings, even under lg, are very lightly loaded and at speeds over 10,000 rpm run so close to the centered position as to have, for all practical purposes, zero load stiffness characteristics.

The amplitudes calculated for the 100 micro-inches (.176 in-oz) of unbalance were quite small - never exceeding 0.3 mils. As was indicated earlier, the analysis is valid for amplitudes approaching 30 percent of the bearing clearance before the assumption of fluid film linearity begins to break down, and it is possible to estimate from the results presented herein the effect of larger values of unbalance. Taking the more severe out-of-phase unbalance case, the 2.5 inch diameter bearing amplitude at design speed is 0.125 mils (see Figure 8.2-4), and as pointed out before, approximately 450 micro-inches (.791 in-oz) could be imposed before the limit of the theory was reached. If this unbalance were distributed as originally assumed (33.5 percent at the first stage and 66.5 percent at the eighth stage) a piece of material weighing 0.097 oz. and 0.111 oz. at these two respective stages could be removed. This is equivalent to a piece of TZM 0.1 inches square and 1.64 inches long at stage 1 and 1.87 inches long at stage eight. This certainly represents a sizable piece of a blade (or pieces) that could be broken or erroded away and still have confidence in the analysis.

Furthermore, with such a large unbalance force, the bearing amplitudes are still quite tolerable (30 percent of the clearance) and the maximum shaft amplitude (Stage 1) would be only about 0.001 inches. Based upon these numbers it can be concluded that the turbine rotor amplitudes even under extreme cases of unbalance are quite tolerable and that the analysis technique used is applicable for very large values of unbalance.

The turbine rotor is built up of the turbine disks and torque tubes held together by curvic couplings and a tie bolt. For the purpose of the dynamic analysis it was assumed that the tie bolt always provided enough compressive force on the curvic couplings to prevent tooth separation on the tensile side. To verify this assumption, the moments at the curvic's were calculated under the influence of the 100 micro-inch unbalance condition and found to be more than an order of magnitude less than the moment provided by the tie bolt. It is possible for the curvic's to introduce some unaccounted for compliance into the rotor system since the teeth are in Hertzian contact. However, because of the large number of teeth (which results in a parallel spring arrangement) and the high bolt load (large Hertz stress) the joint should be very stiff and neglecting of this compliance is not considered significant. During the final design of the turbine rotor when the exact number of teeth and tooth geometry is established, the effect of coupling compliance should be checked.

### 8.3 450 KW ALTERNATORS

As will be recalled from the Phase I study, the alternator tended to have resonance problems usually associated with the third critical

and these problems were a result of the relatively compliant stub shafts which were required to support the massive rotor. Furthermore, it was not possible to move the bearings to a position far enough displaced from the nodes to be able to realize their full damping potential.

The alternator considered in Phase II was about seventy pounds lighter (see Figure 8.3-1) than the Phase I alternator because of the reduced rating (from 550 kw to 450 kw) and lower coolant temperature. Furthermore, as indicated on Figure 8.3-1, the design effort resulted in a significant reduction of both coupling overhang and bearing span.

These changes, all in the direction of stiffening the rotor, made it possible to raise the third critical speed to in excess of 40,000 rpm where it has no effect on the vibration characteristics of the rotor within its normal speed range (to 24,000 rpm). This rotor stiffening also had the beneficial effect of raising the second critical to above operating speed as can be seen on Figure 8.3-2. (It will be recalled that the Phase I alternators were also troubled with the second critical).

The results of the response analyses for 100 micro-inches of unbalance - both in and out of phase - are shown on Figures 8.3-3 and 8.3-4. Again only the horizontal rotor case is shown for the same reasons as explained for the turbine above. The response for the alternator with in-phase unbalance is quite typical for a symmetrical critically damped system with one natural frequency in that the amplitudes increase with frequency to the vicinity of the first natural frequency and then flatten out as the center of rotation shifts from the geometrical to the mass center. In this case, the in-phase

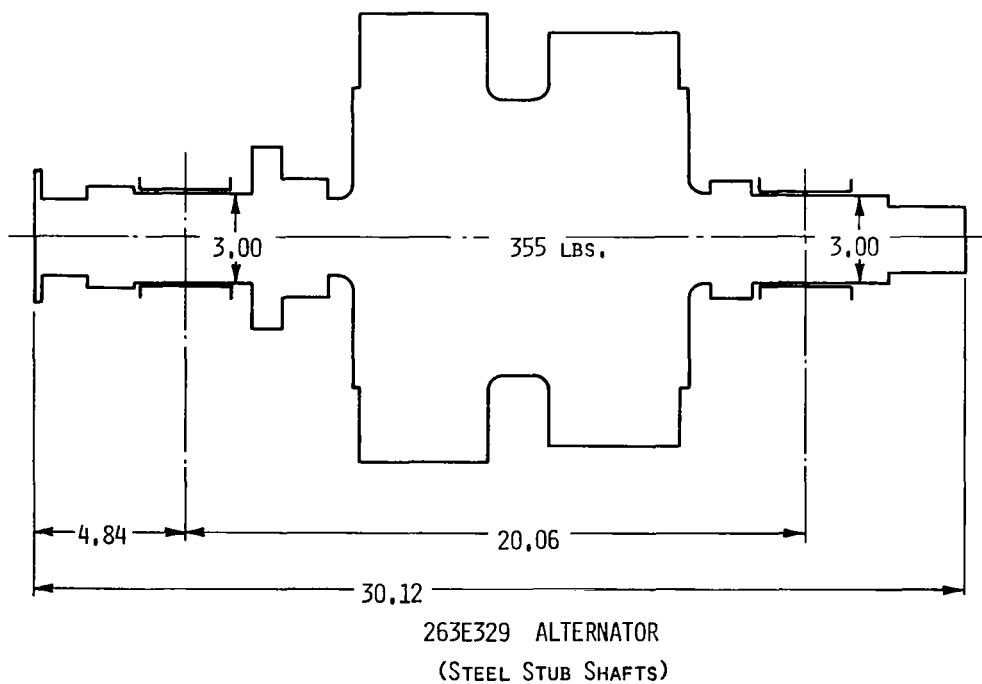
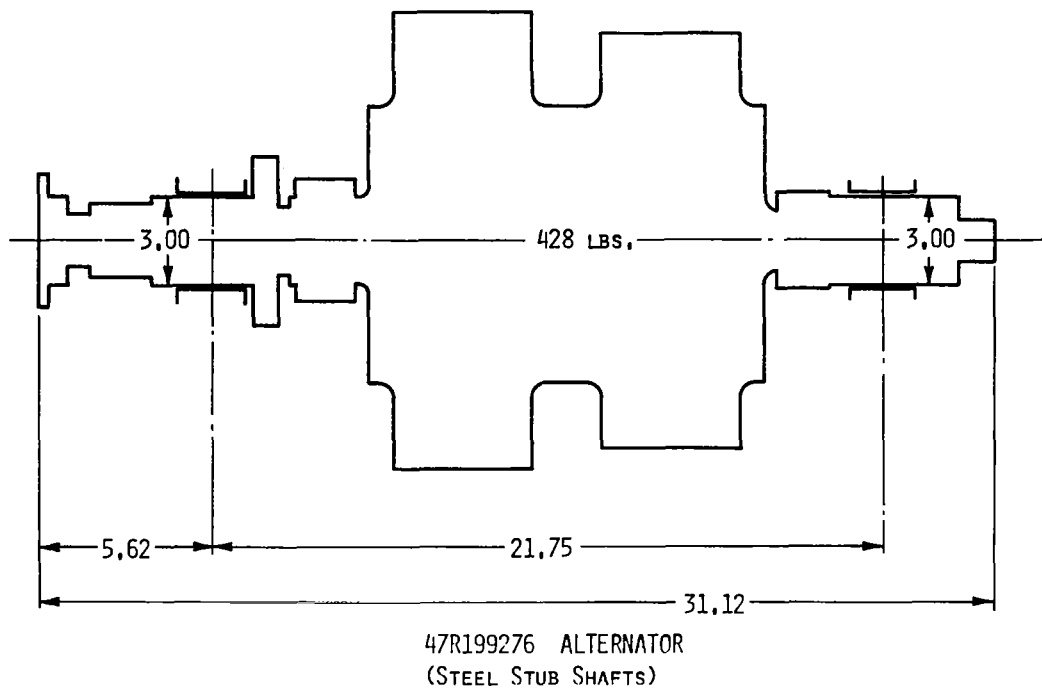


Figure 8.3-1. Phase I and Phase II Alternators.

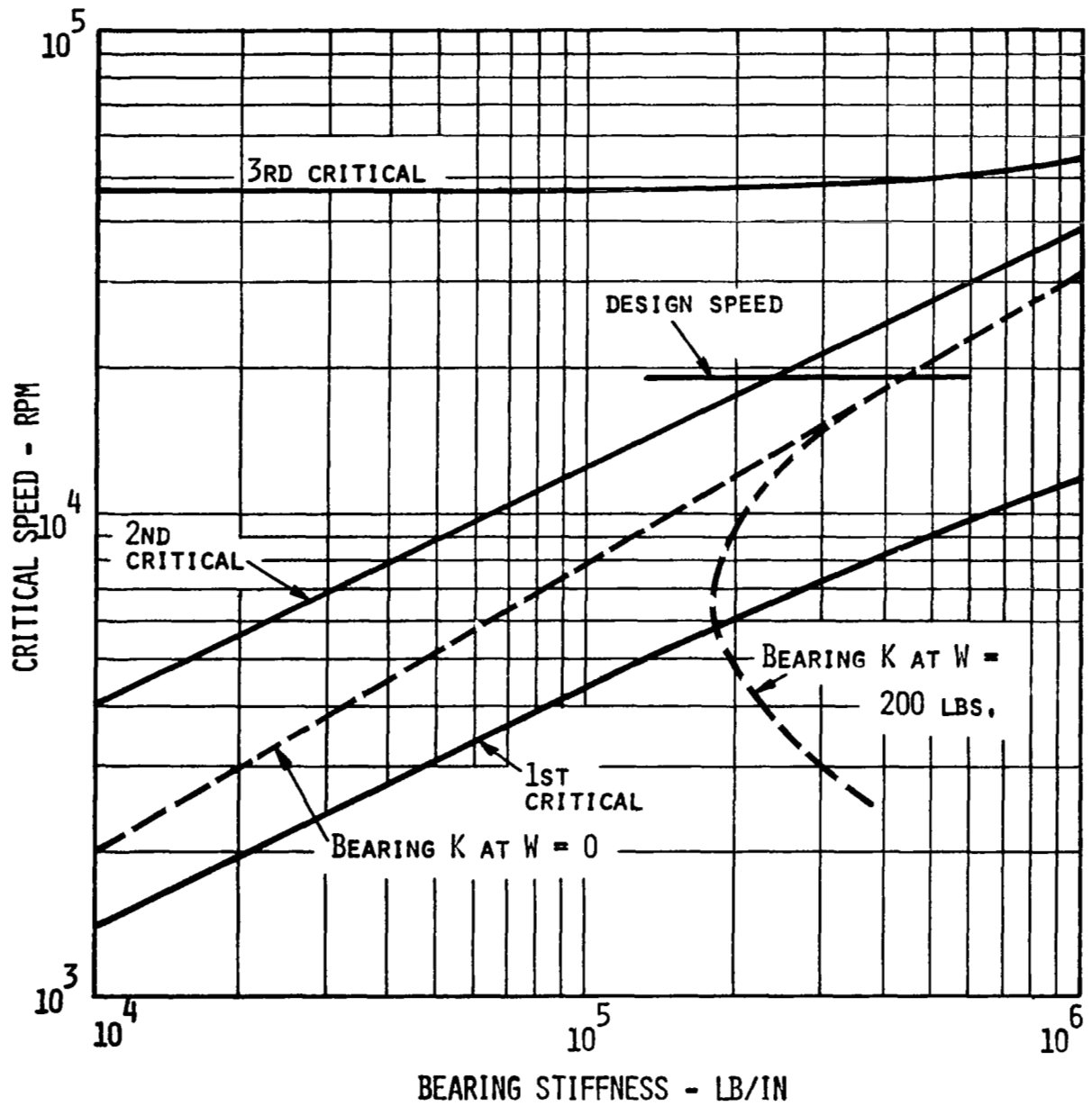


Figure 8.3-2. 450 KW Alternator Integral Steel Stub Shafts.  
Critical Speed



(REF. G.E. DWG. 263E329)  
 50 MICROINCHES AT ROTOR ENDS - IN PHASE  
 HORIZONTAL ROTOR

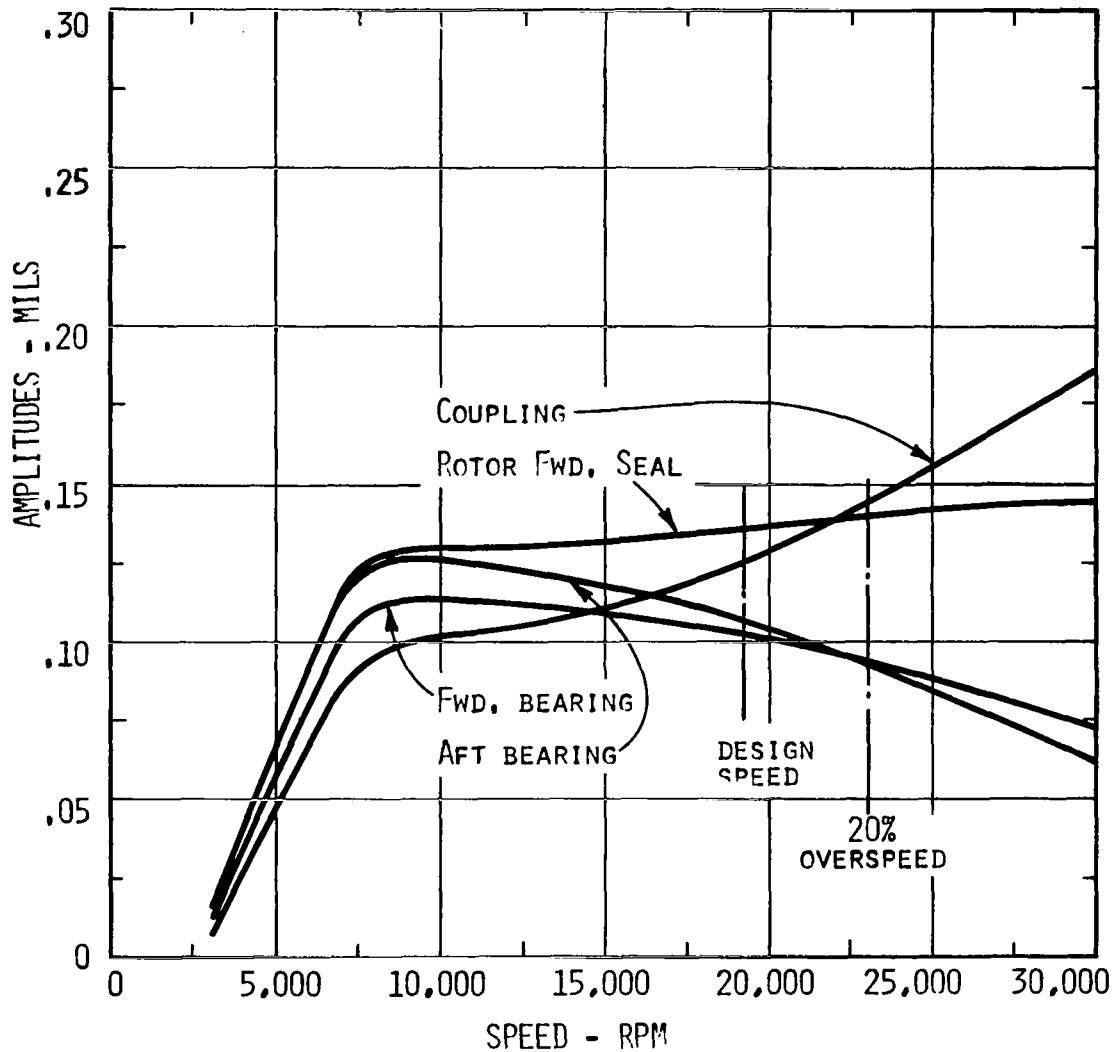


Figure 8.3-3. 450 KW Alternator - Response to 100 Microinches.  
 Total Unbalance

(REF. G.E. DWG. 263E329)

50 MICROINCHES AT ROTOR ENDS - OUT OF PHASE

HORIZONTAL ROTOR

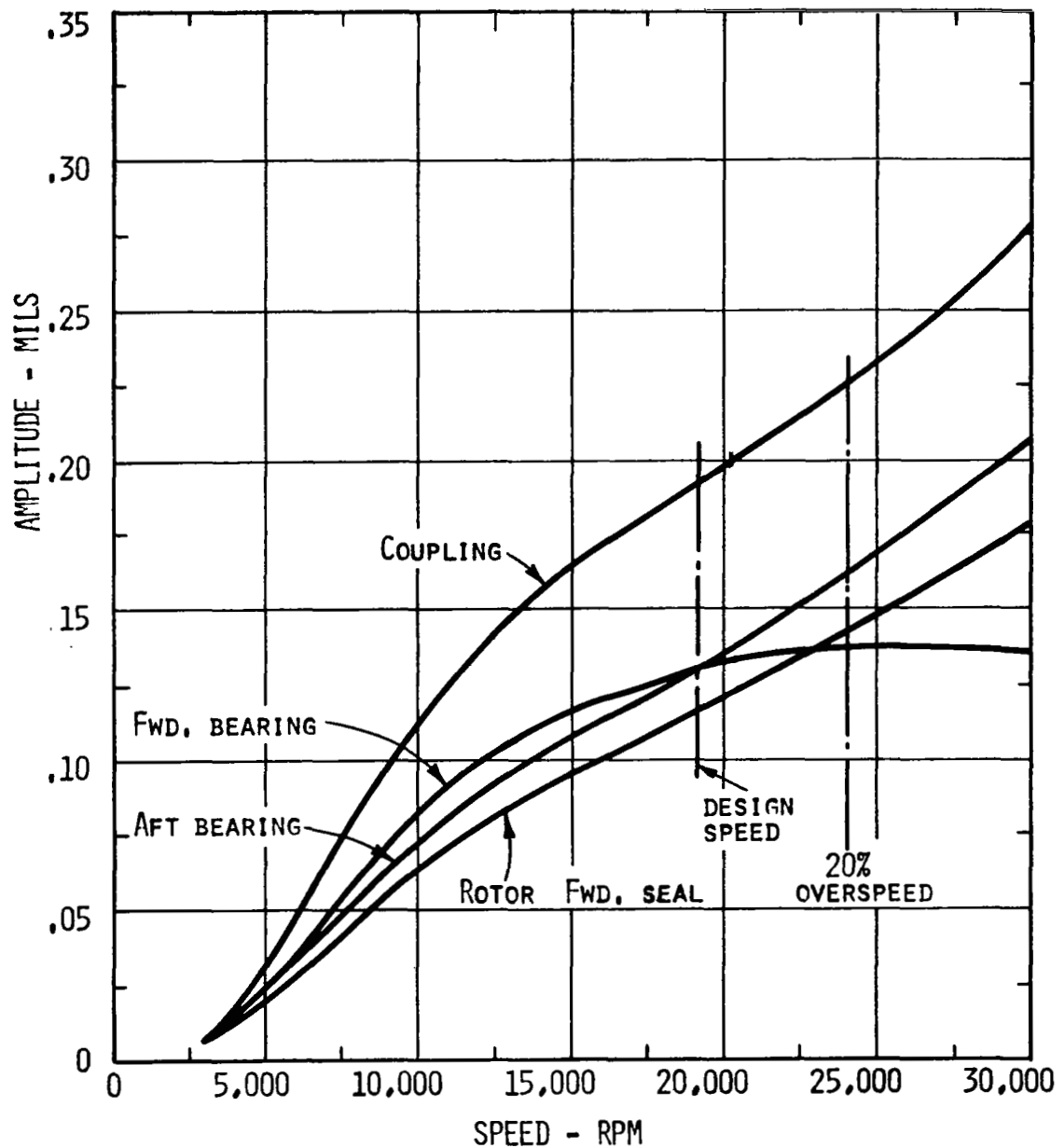


Figure 8.3-4. 450 KW Alternator - Response to 100 Microinches.  
Total Unbalance

unbalance accentuates the first critical, which is translatory, and the vibrating modes are easy to visualize.

In the case of out-of-phase unbalance (see Figure 8.3-4) the unbalance forces tend to force the rotor into a conical mode and the first critical is not as evident. The second critical dominates the vibration mode as would be expected since operation at speeds over 10,000 rpm is closer to the second than the first critical and the unbalance phase accentuates the second which, in this case, is conical. As can be seen from Figure 8.3-3 and -4, the vibration amplitudes with 100 micro-inches (.569 in-oz) never exceed 0.225 mils at the 20 percent overspeed condition and that considerably more unbalance could be tolerated before the amplitudes become excessive. (The same procedure here as was described for the turbine can be used to estimate amplitudes and test the limits of the analysis for larger values of unbalance.)

Although the alternator has excellent dynamic characteristics, it has a relatively large bearing power consumption because of the large diameter stub shafts required to achieve the required rotor rigidity. The bearing losses are summarized on Table 8.3-1 and are indicative for the price paid for the combination of refractory bearings, steel shafts and housings and acceptable rotor response.

#### 8.4 HOUSING COMPLIANCE

For all of the critical speed and rotor response analyses accomplished during the study, it was assumed that the bearing was rigidly attached to ground (or a sizable mass). Actually, the bearings are attached to the main machine housing mass by means of a structural member (i.e. alternator end bell) which is not infinitely stiff. The

TABLE 8.3-1

ALTERNATOR BEARING POWER LOSSES

Thrust Bearing (1 Double Acting)

Size (OD x ID) - Inches	6.0 x 4.0
Total Clearance - Inches	.005
Power Loss at 1 g - Horsepower	27.4

Journal Bearings (2)

Size (Dia. x Length) - Inches	3.0 x 3.0
Assembled Clear. (Diametral) - Inches	.0045
Power Loss at 0 g - Horsepower	11.0
Seals & Misc. Fluid Friction - HP	<u>8.8</u>
Total Alternator Bearing Power - HP	47.2

compliance of this structural member can be considered as a spring in series with the bearing film as is depicted on Figure 8.4-1.

The effect of two different arbitrary alternator end bell stiffnesses on the alternator rotor vibrational characteristics was evaluated to determine the significance of this compliance. One stiffness ( $6.2 \times 10^5$  lb/in) was approximately equivalent to that of the end bell shown on 263E329 while the other stiffness ( $1.5 \times 10^6$  lb/in) was a value considered easily attainable by minor gusseting of the more compliant end bell components.

The equivalent stiffness of the bearings and these two housing stiffness assumptions are shown on Figure 8.4-2 by non-solid lines. It can be seen that the housing compliance has the same lowering effect on critical speed as reducing the bearing stiffness and that the second critical is moved closer to design speed. The response curves for these two cases are shown on Figures 8.4-3 and -4. Figure 8.4-3 which is the coupling amplitude, graphically demonstrates the degrading effect on the vibrational characteristics introduced by the soft bearing mounts. As would be expected from the critical speed plot, the softer mount ( $6.2 \times 10^5$  lb/in) shows a definite resonance peak in the area between 20,000 rpm and 25,000 rpm and is rather poorly damped. Since the bearing stiffness at 20,000 rpm is of the same order ( $4 \times 10^5$  lb/in) as the assumed support stiffness ( $6.2 \times 10^5$ ), about the same order of radial motion occurs in the housing as in the bearing. Since radial motions in the housings do not produce any significant damping forces, the pronounced resonance peak would be expected. Housing and shaft motions are shown on Figure 8.4-4 where it can be seen that for the lower housing stiffness case the housing amplitude is actually larger

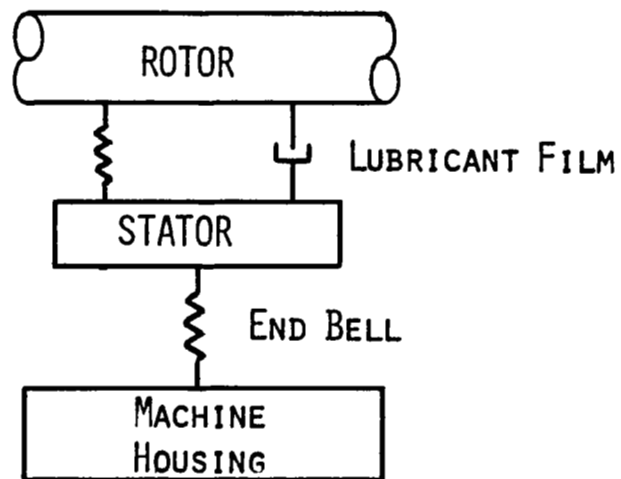


Figure 8.4-1. Effect of Housing Stiffness.

(REF, 263E329 ROTOR)

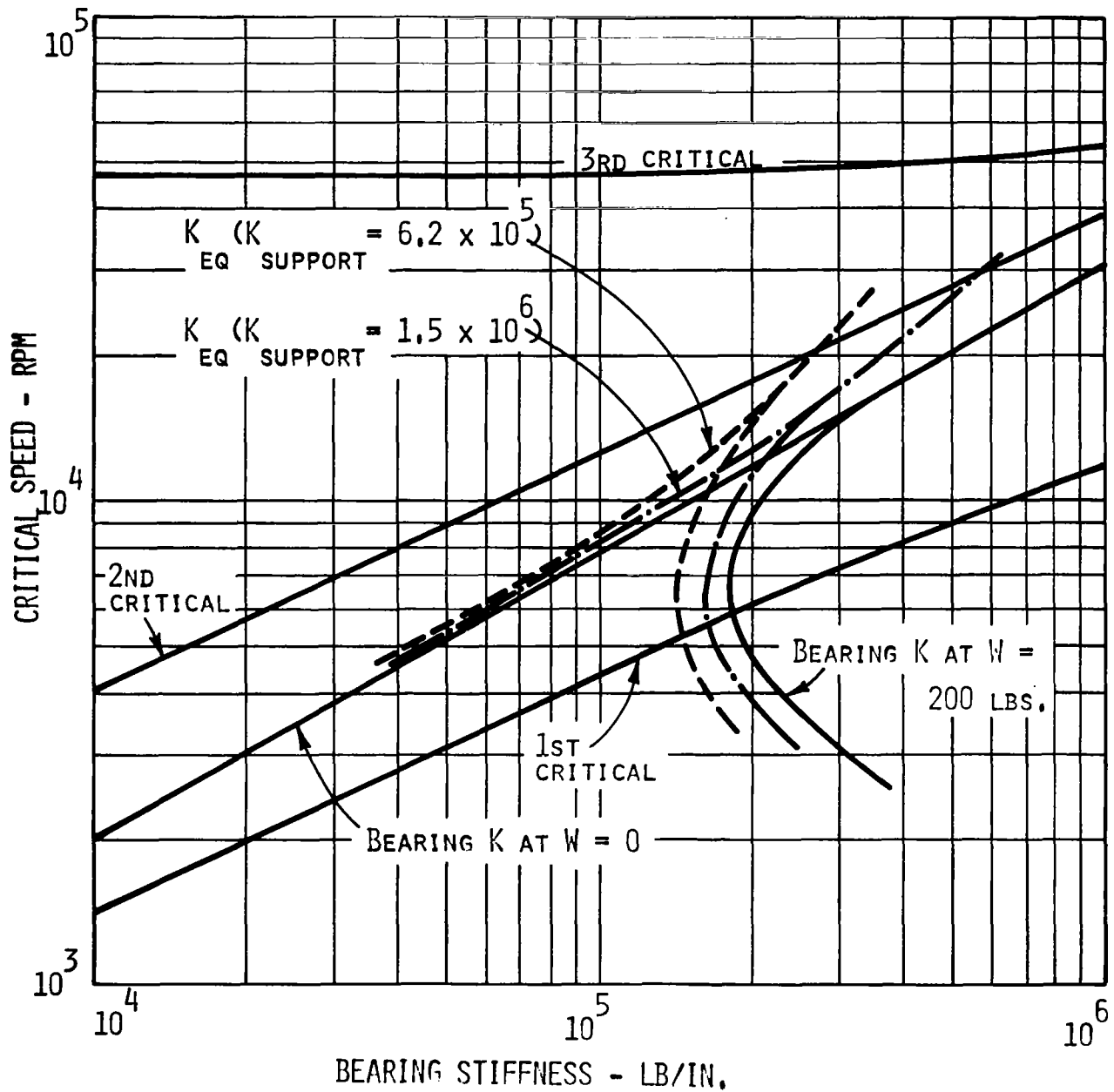


Figure 8.4-2. Effect of End-Bell Stiffness on Alternator.  
Critical Speed

(REF. G.E.DWG. 263E329)  
50 MICROINCHES PER PLANE - OUT OF PHASE

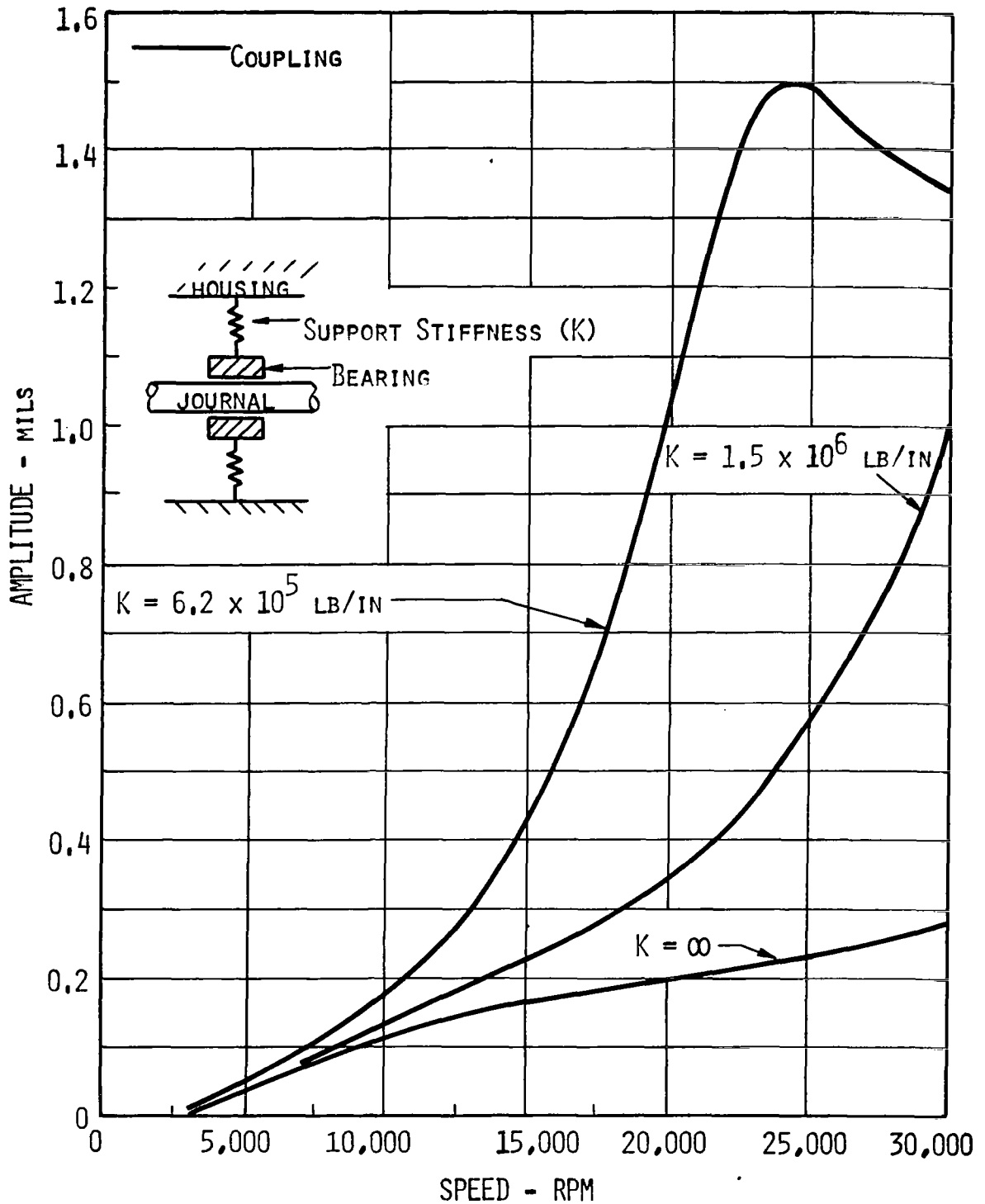


Figure 8.4-3. Effect of Housing Stiffness on Alternator Response.



(REF. G.E. DWG. 263E329)

50 MICROINCHES PER PLANE - OUT OF PHASE

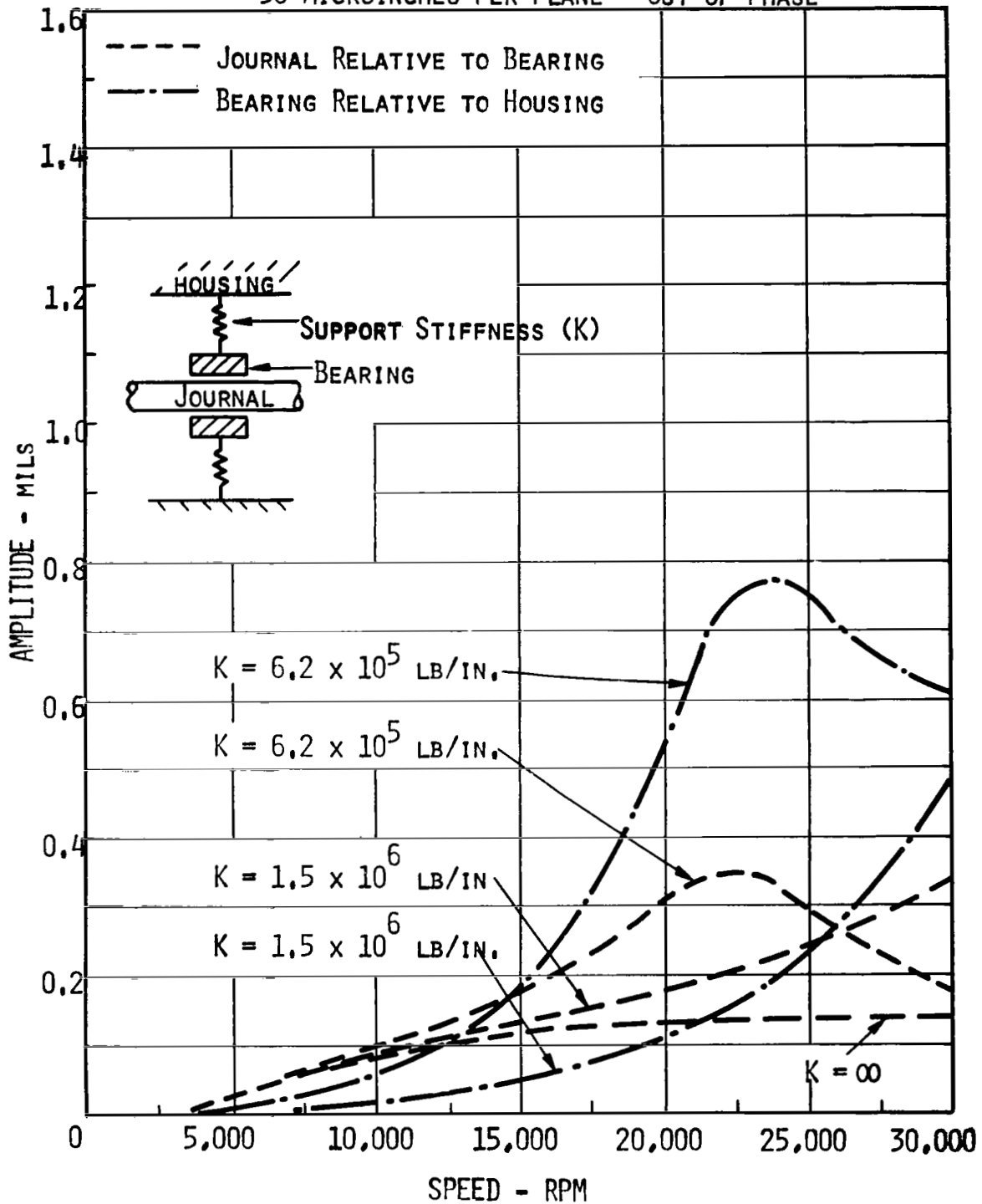


Figure 8.4-4. Effect of Housing Stiffness on Alternator Response.

than the amplitude of the journal within the bearing. (Although the bearing stiffness is lower than the housing stiffness, the bearing damping forces restrain the motion of the shaft within the bearing.) It should also be noted on Figure 8.4-4 that, depending upon the speed and stiffness, the housing amplitudes can be sizable (up to about 0.8 mils) and the question of support structure fatigue must be addressed.

These analysis show that the supporting structure compliance must be seriously considered at the time of the detailed design of the end bells. It should, without much difficulty, be possible to raise the structure radial stiffness to above  $1.5 \times 10^6$  lb/in. which would practically eliminate the problems introduced by a more compliant structure.

It should be pointed out that in the case of the turbine, the problem is far less severe because the turbine operates above the second critical speed (maximum second critical is 8000 rpm). Compliance introduced into the turbine bearing support structures will have the tendency to move the second critical even further away from the operating speed which will eliminate the problem of operating near a poorly damped resonance. Care must be taken, however, to avoid the third critical and the actual housing structure amplitudes should be checked in the final design to assure that no fatigue problem exists.

#### 8.5 COUPLED TURBINE AND ALTERNATOR (KTA)

The KTA consisting of the 47R199305 turbine and the 263E329 alternator was subjected to a lateral rotor dynamics analysis and a torsional critical speed analysis. The results of the lateral rotor response analysis are summarized on Figure 8.5-1 which shows the

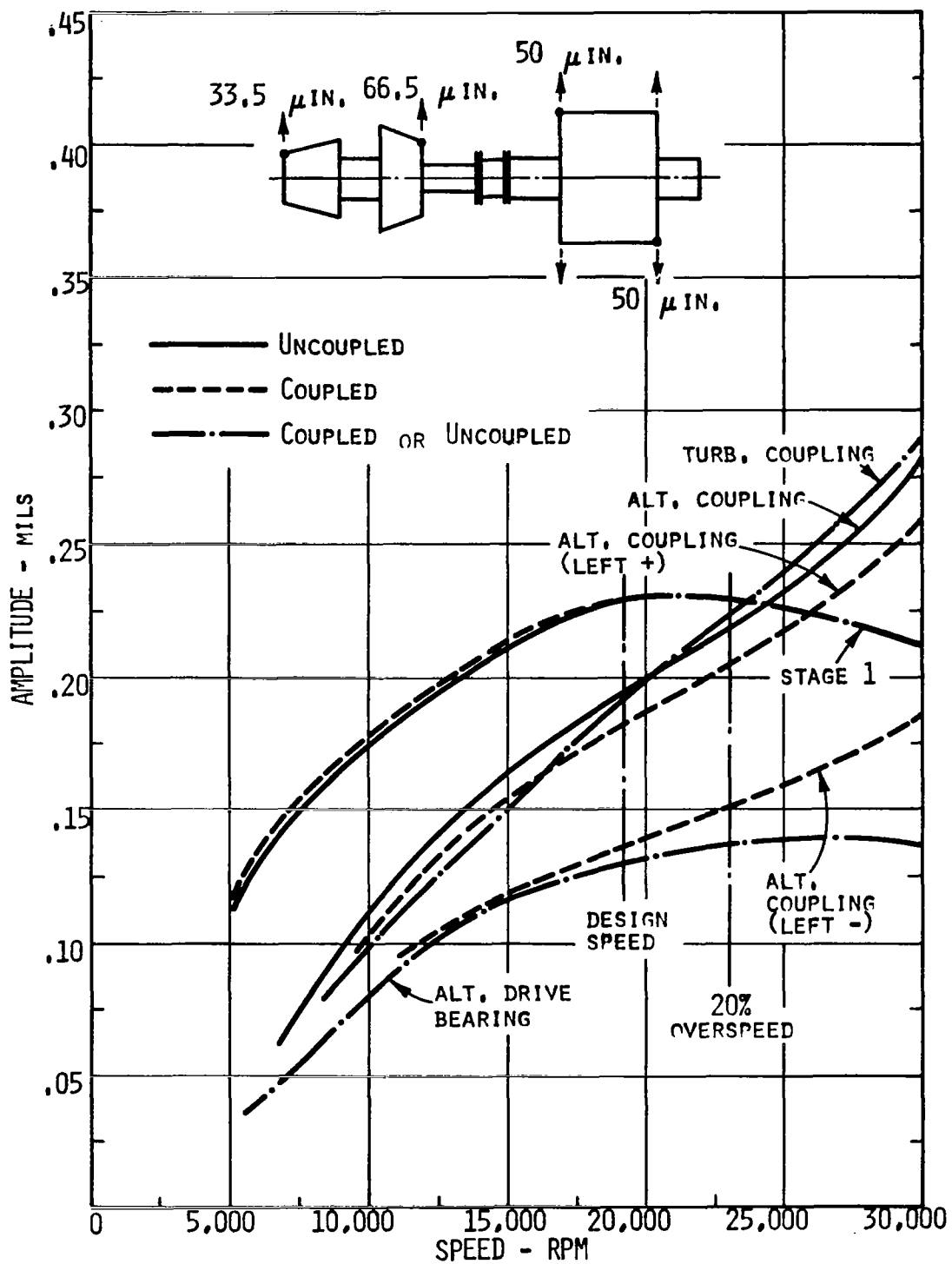


Figure 8.5-1. Comparison of Coupled and Uncoupled Response.

amplitudes of the alternator drive end bearing and coupling, and the turbine coupling and first stage.

The solid lines show the amplitudes of vibration of the individual components (not coupled) and the dashed lines show the amplitudes at the same locations (if different) with the turbine and alternator connected together by the diaphragm coupling. Those cases where the amplitudes were identical, whether coupled or uncoupled, are shown with a dashed-dotted line. The results of two cases are shown and both have the turbine unbalance in phase and the alternator unbalance out-of-phase. The two cases differ in that in one, the alternator left end unbalance is in phase with the turbine unbalance (left +, right -) and in the other case the alternator left end unbalance is out of phase with the turbine unbalance (left -, right +).

As can be seen from these curves, the KTA components respond to unbalance forces when coupled together almost exactly the same as when independent and the change in balance orientation between the two components has a measurable effect on only the coupling end of the alternator. This demonstrates the effectiveness of the diaphragm coupling as a vibration isolator as there appears to be only negligible interaction between the components. This feature can be invaluable during the detailed design and development testing of the components as their vibrational characteristics can be evaluated independently.

The results of the KTA torsional critical speed analysis are shown on Figure 8.5-2 which is an angular mode shape plot of the first torsional critical (7248 rpm). No other torsional criticals exist below 30,000 rpm. From the plot on Figure 8.5-2 it can be seen that the first critical is the mode where the turbine and alternator masses

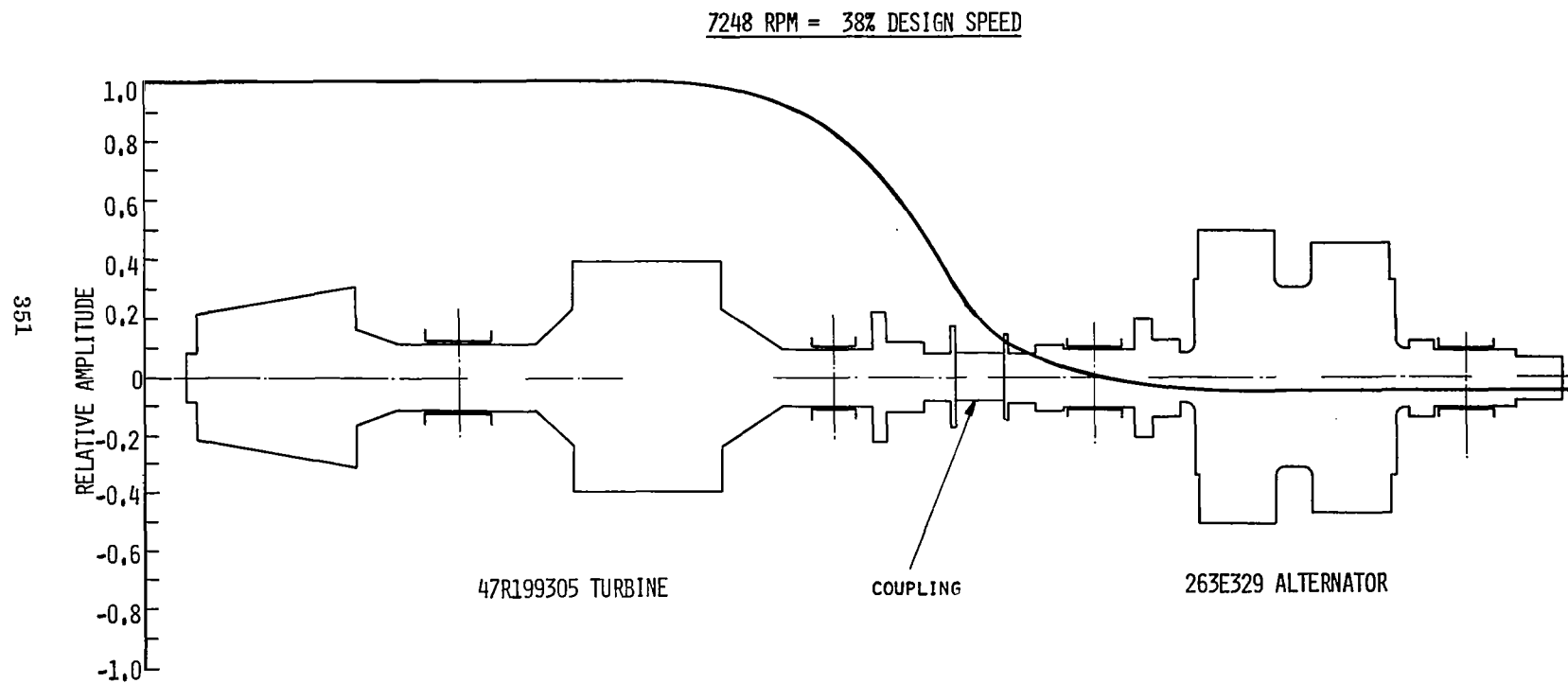


Figure 8.5-2. First Torsional Critical Speed Mode Shape.

rotate out-of-phase with each other with most of the twist occurring in the two stub shafts. Although no estimate of torsional damping was made, the friction between the stub shafts and bearing and seal sleeves should provide sufficient damping to allow driving through this resonance with negligible torsional amplitudes. It is cautioned, however, that prolonged operation in the vicinity ( $\pm 20\%$ ) of this critical should be avoided as the motion between the sleeves and stub shaft could eventually loosen the sleeves. This would not only eliminate the source of torsional damping but could also lead to lateral vibration problems.

If the start-up sequence requires prolonged operation in the vicinity of 7200 rpm, the resonance point should be changed. This could probably be most easily accomplished by introducing more torsional compliance in the section between the coupling diaphragms and thus lower the torsional critical.

## 8.6 SUMMARY AND CONCLUSIONS

During Phase II, the turbine and alternator rotors were subjected to several critical speed and rotor response analyses which led to sufficient design improvements to rid the rotors of any perceptible resonance peaks. With reasonably large values of unbalance (100 micro-inches) the rotor maximum vibration amplitudes never exceed 0.4 mils at the 20 percent overspeed case. It has been estimated that turbine balance degradation equivalent to removing about 0.1 oz. of material from each of the first and eighth stages could be tolerated with the resulting maximum amplitude being less than 1.0 mils at the critical first stage. With such an unbalance condition, the bearing orbits would be a tolerable 30 percent of the clearance.

The turbine and alternator when coupled together have dynamic characteristics almost identical to the components when operated independently. This is because the diaphragm coupling has a very low angular stiffness and cannot transfer any significant moment from one rotor to the other. This is an extremely desirable feature as each of the components can be analyzed and tested independently with the assurance, that when assembled together, they will be effectively dynamically decoupled.

The KTA has one torsional critical speed in the range between 0 and 30,000 rpm occurring near 7250 rpm. This first torsional critical, however, should be of little consequence since sufficient friction damping should be afforded by the stub shaft bearing sleeves to enable accelerating through the critical with a minimum of amplification. Dwelling near this critical speed should be avoided since the relative twisting motion between the sleeves and stub shaft may eventually loosen the sleeves and both eliminate the source of torsional damping and lead to lateral vibration problems.

The effect of housing flexibility on the alternator rotor vibrational characteristics was evaluated and found to be a significant factor. It was determined that the radial stiffness of the end bells should exceed 1.5 million lb/in in order to minimize the effect of housing flexibility and that stiffness values approaching  $10^7$  lb/in should not be difficult to obtain with proper reinforcement of the more compliant housing structural elements. Housing flexibility is not as critical a concern in the turbine because it operates above the second critical and additional system compliance further removes the operating speed from the area of the critical.

## 9. CONCLUSIONS AND RECOMMENDATIONS

The overall outcome of the design study is an extremely positive one. It has been shown that almost all the design problems involved can be resolved by established engineering methods. The materials incorporated are known and understood to a considerable extent and it appears that those manufacturing processes not yet established can be resolved within a reasonable time period. The alternator especially appears to be designed to a point where it could be converted into hardware with a high probability of success.

The NASA specification of 700°F for the potassium lubricant and coolant was highly beneficial to the whole alternator design. It helped in reducing electric losses and it completely eliminated creep as a problem in the alternator rotor design. The hot spot temperatures resulting from 700°F coolant are entirely modest at 900°F and pose no uncontrollable problems in the alternator stator design. The 700°F coolant for the rotor made it possible to use slotted pole faces which also are an established and reliable method. The development problem posed by the ceramic bore seal and its intermetallic connections has been considerably reduced and narrowed down by the Phase II design effort.

The turbine also appears to pose no extraordinary design and manufacturing problems. The proper forging of molybdenum wheels will require an extension of established methods and a certain amount of learning, but there is little doubt that this process will be established. The curvic coupling tiebolt connection of the rotor employs the technology of the three stage potassium test turbine (Contract NAS3-8520). The welding of casing and



stator has been discussed in considerable detail and it may be concluded that the existing welding techniques are entirely adequate to build up stator and casing as a welded assembly.

For the bimetallic joint between T-111 and Cb-1Zr, sample welds are available today which indicate that this joint poses no major problems. The learning process required in fabricating T-111 is continuing under current contracts and it is anticipated that T-111 technology will be fully established within several years. It may be concluded that from a material joining and stress point of view the turbine also could be designed and manufactured within a reasonably short time span.

Some intangibles and a number of recognized problems remain which require close attention and additional development effort. The greatest unknown in wet vapor turbine design remains the turbine resistance to erosion. The present design was based on the assumption that at tip speeds not exceeding 850 ft/sec, 8 to 10 percent moisture could be tolerated in a turbine stage without creating severe permanent damage. The results from the three-stage potassium test turbine (Contract NAS3-10606) so far have not been conclusive on this point. Under a contract addendum, which continues three stage turbine testing, erosion damage on molybdenum as well as Rene'77 blades will be studied further. Under contract NAS3-12977, for investigating condensate removal, the different potential methods of removing potassium condensate from the turbine rotor, from the turbine stator and through vortex separators arranged in cross-over ducting, will be studied further by design, analysis and test. These results will permit the turbine design to be finalized.

## 9.1 REMAINING PROBLEM AREAS

Table 9.1-1 presents a listing of the remaining problem areas to be considered in the turboalternator components. Long term creep data on KDTZM needs to be acquired to confirm turbine rotor, stages one and two as well as the pretensioned tie bolt head designs. The creep data used in the KTA design are based on extreme extrapolations of short term creep data. Long term creep and stress rupture information should be acquired before a turbine life of 3 to 5 years can be predicted in a reliable manner.

Design stresses are high in turbine stage 10 because of design conditions resulting from the NASA request for condensate removal from the rotor. The tip shrouds and dovetail connections between the stage 10 wheel and the blades, which are considered necessary for condensate removal from the rotor, could be eliminated by adopting condensate removal from the stator. This would reduce stress levels considerably in the turbine rotor. Stress levels are also high in the alternator rotor due to the combination of temperature and tip speed. Attention to high quality in forging, machining and heat treating this large H-11 piece should produce a satisfactory rotor.

Fretting is recognized as a problem in the pivoting points of pad bearings, radial as well as axial. It also is a problem in thermal cycling of bearing expansion cones in the alternator and in curvic couplings, especially when bimetallic. Selection of appropriate materials and designs at contact points should eliminate fretting as a serious problem. The use of flexible pad suspension should eliminate fretting of bearing pivot points.

Leakage within a wet vapor turbine could lead to "wire-drawing" erosion and consequently loss of efficiency. To avert this, stator vane assemblies should be welded into the casing and carbide seals should be connected to the casing by brazing.

TABLE 9.1-1

REMAINING PROBLEM AREAS

Creep	Turbine Stage 1 & 2 Tie Bolt Head
Stress	Turbine Stage 10 Alternator Thrust Bearing Alternator Rotor
Welding	T-111 Casing and Rotor
Fretting	Bearing Pivot Points Bearing Expansion Cones Curvic Couplings
Leakage	Carbide Seals to Casing Stator Vanes to Casing
Thermal Fatigue	Turbine Shaft Cones Bore Seal
Vibration Fatigue	Bearing Support Frames Front Bearing Turbine Radial Bearings Alternator
Erosion	Turbine Blades Stage 7 & 10 Honeycomb Tip Seals, Open Bearing Surfaces
Rubbing	Blade Tip Seals Interstage Seals Screw Seals

Thermal fatigue is a potential problem in rotor as well as stator wherever alternating stresses are created by rotor unbalance. Particular attention must be applied to the proper design of bearing support frames in alternator and turbine.

Rubbing between rotor and stator can be created by rotor unbalance, by operation in or close to critical speeds, and by thermal distortion. The places where rubbing most likely will take place are the blade tip seals, the interstage labyrinth seals and the screw seals adjacent to bearings. In all these seals material combinations must be chosen to avoid seizing and galling.

## 9.2 RECOMMENDATIONS

Based on the discussion of Problem Areas, the following recommendations are made:

Establish reliable long-term creep and stress-rupture information for KDTZM, the material to be used in turbine stages 1 and 2.

Avoid condensate removal from the rotor, instead develop and use condensate removal from the stator.

Fully establish welding and heat-treatment specifications for T-111.

Use flexible bearing-pad supports instead of pivot point contacts.

Develop the technique required to braze carbide seals in the casing.

Establish erosion tolerance limits permissible in wet-potassium turbines.

Avoid honeycomb tip seals in wet stages and establish erosion resistant refractory tip seal design.

Establish non-galling pairs of materials to be used in the presence of potassium for blade tip seals, interstage seals and screw seals.

Attack processing and technology problems by fabricating components such as turbine wheels, turbine stator, alternator bore seals, alternator stator.

## 10. ALTERNATE DESIGN STUDIES

### 10.1 MULTISTAGE MOISTURE REMOVAL

During the KTA study, an attempt was made to identify ways to minimize the amount of condensed moisture in the turbine to reduce the probability of erosion. One way is to remove liquid in each stage, beginning with the fourth stage where the liquid fraction becomes significant. Shown in Figure 10.1-1 is the variation of moisture fraction for several values of extraction effectiveness. For 25 percent effectiveness, the level of moisture fraction will exceed 8 percent in the latter stages. An effectiveness of 50 percent in each stage is required to keep the moisture fraction below 5 percent; this is an optimistic level of effectiveness for interstage moisture extraction.

A preliminary design of an eleven-stage turbine was made with stator extraction in stages 4 through 7 and rotor and stator extraction in stages 8 through 10. The moisture level is shown in Figure 10.1-2 for two levels of extraction effectiveness. The effectiveness is expected to be greater for the latter stages because there are rotor and stator devices and because rotor extraction is more effective at lower pressure levels. The lower line with effectiveness values of 25 and 50 percent may be optimistic and the middle line with values of

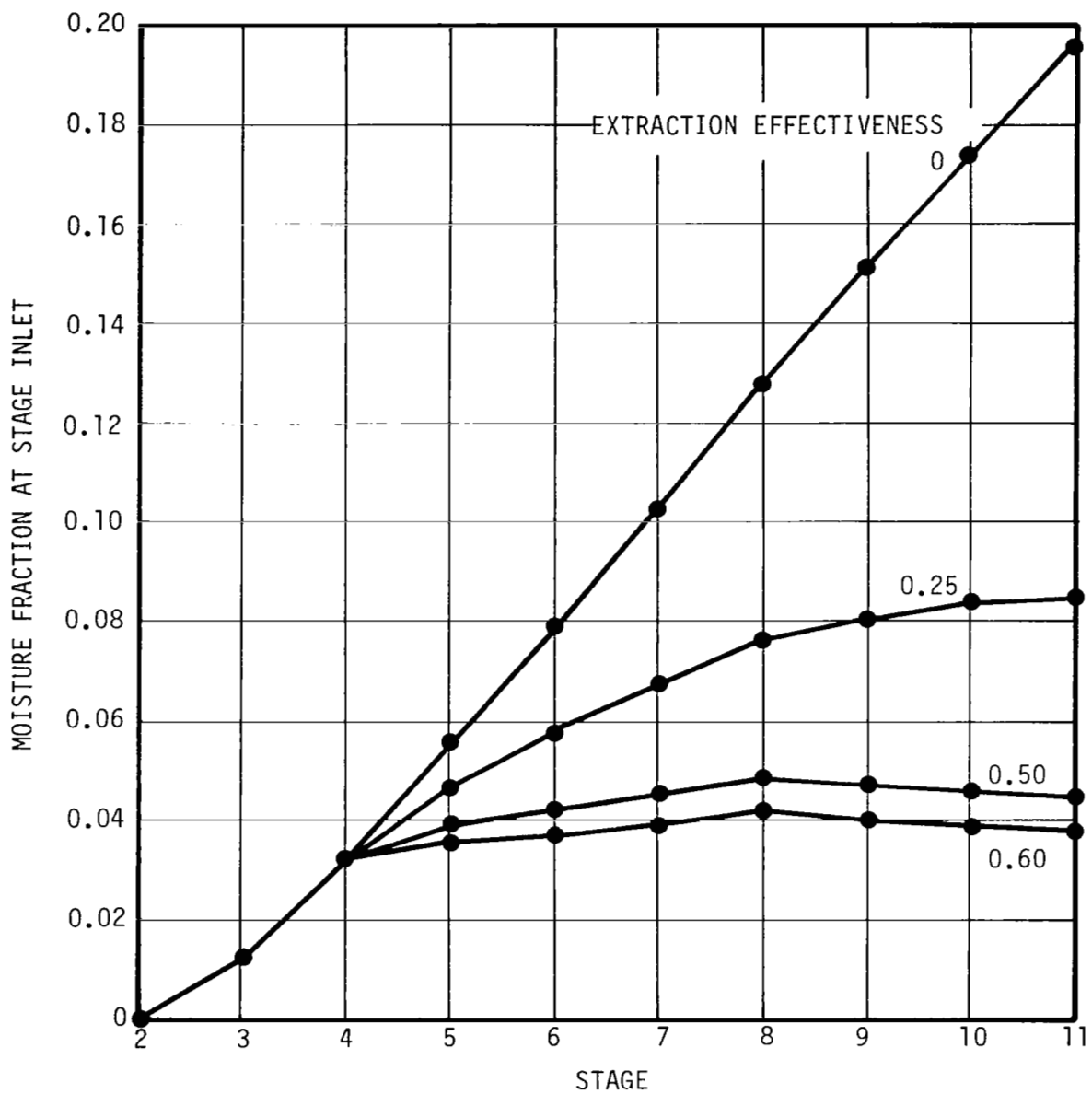


Figure 10.1-1. 11 Stage Turbine with Moisture Extraction in Stages 4 Through 10.

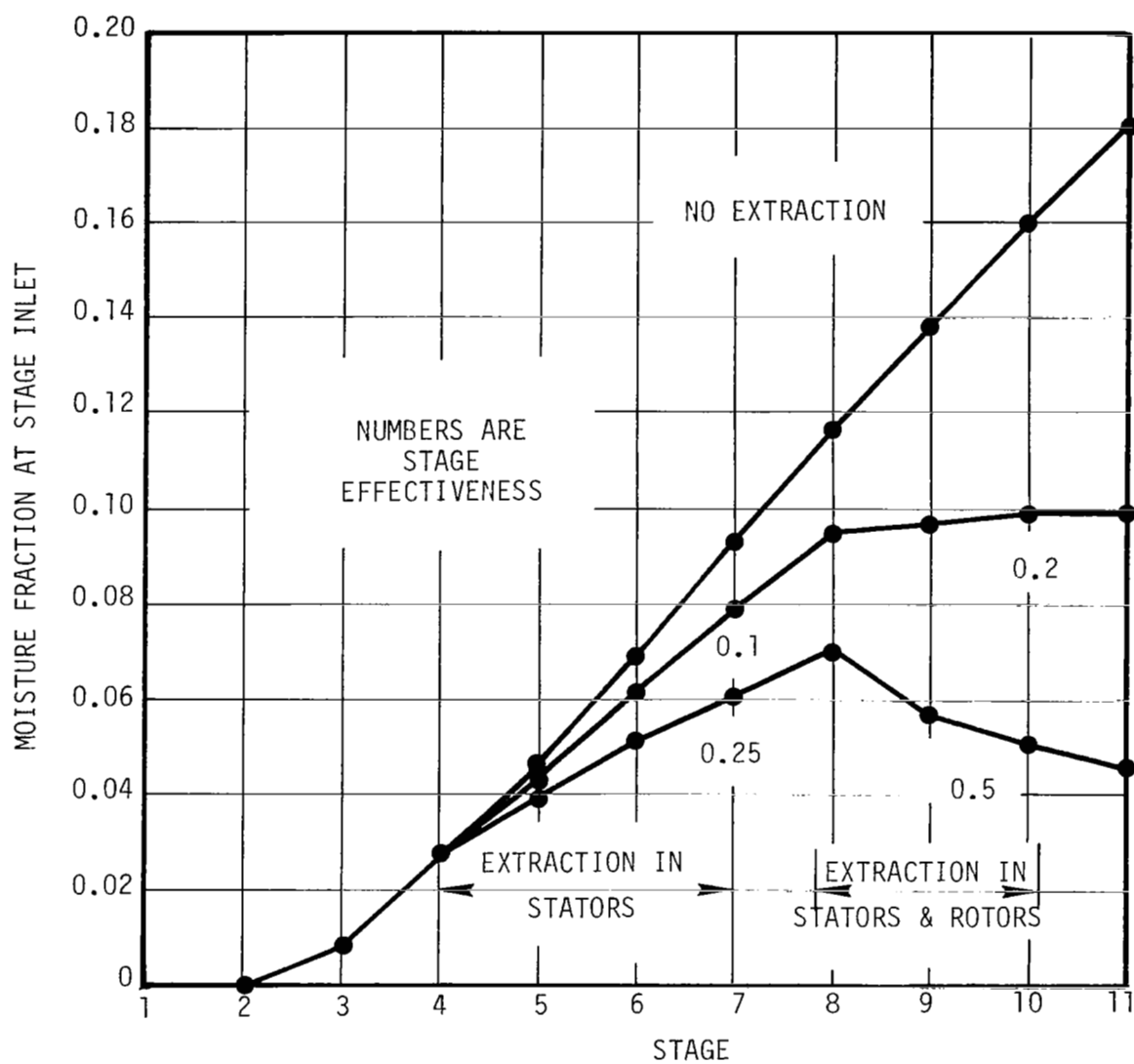


Figure 10.1-2. 11 Stage Turbine with Moisture Extraction in Stages 4 Through 10.



10 and 20 percent is probably conservative. A maximum moisture fraction of about 8 percent appears to be feasible for this design.

Another way to minimize the liquid fraction is to remove liquid both in interstage as well as interspool extraction devices. Shown in Figure 10.1-3 is the variation of moisture fraction in a turbine that has interstage extraction and a vortex separator between the seventh and eighth stages. The effectiveness of interstage extraction was assumed to vary from 16 to 28 percent as the pressure decreased. The change in slope of the line in the last four stages is due to the fact that the low pressure turbine is not limited in wheel speed by small blade height as is the high pressure turbine. Therefore, more work can be done and more moisture condensed in each stage. A maximum of 8 percent liquid is possible compared with about 10 percent for interstage extraction only. Using two schemes instead of one does not double the effectiveness because the liquid removed by one device is not available to the other.

## 10.2 STATOR CONDENSATE REMOVAL

A scheme that is particularly attractive is moisture removal from the trailing edge of the stator vanes. The accepted theory of turbine bucket erosion is that large liquid drops are formed by coagulation of condensed moisture on stationary surfaces. These drops are swept off of the vanes by the vapor stream and are struck by the rotating blades which have a much greater velocity than the large drops. Condensate removal from rotor blades requires the impact of drops upon at least one rotor blade row, with the resulting erosion damage. The advantage of stator liquid removal is that the large,

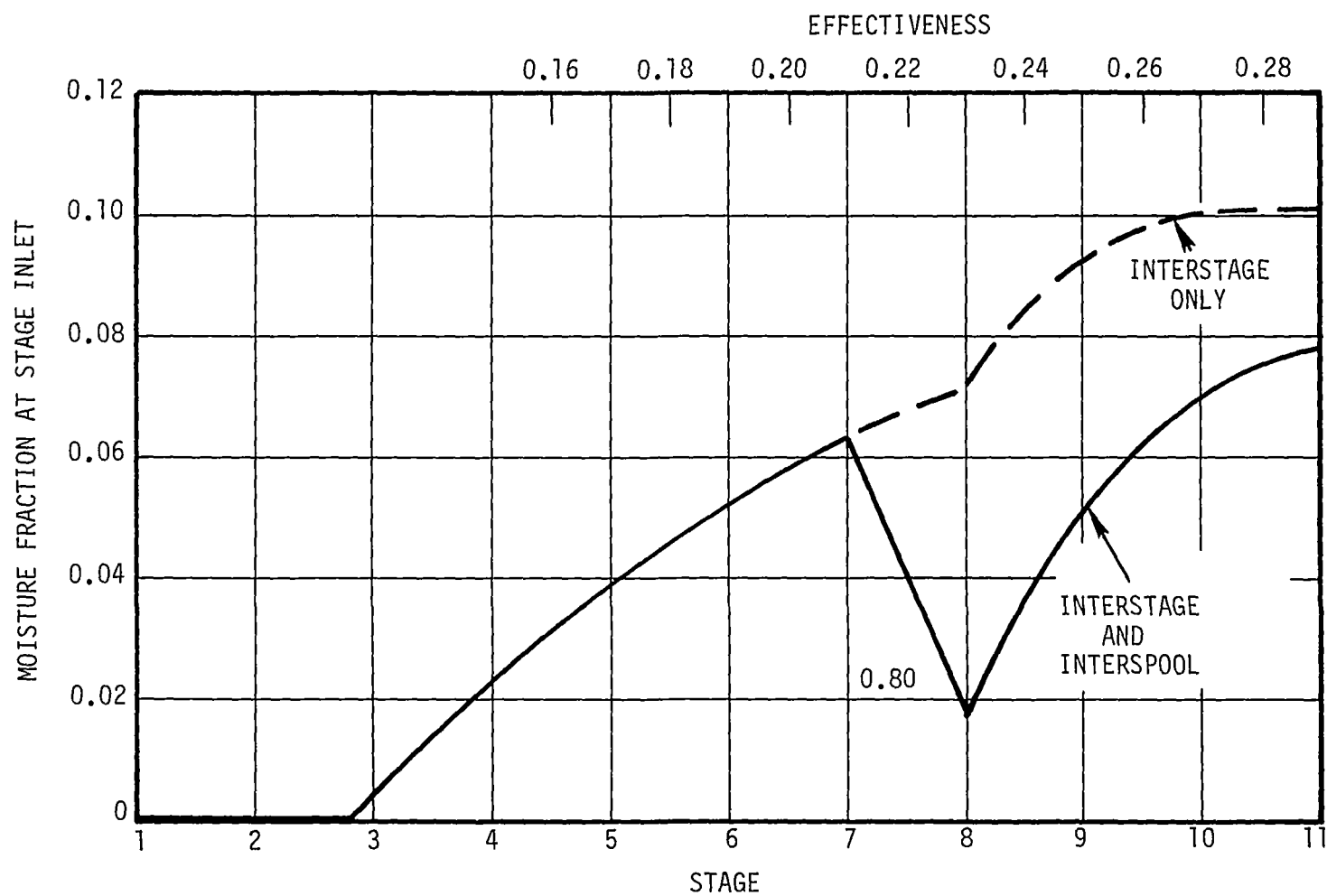
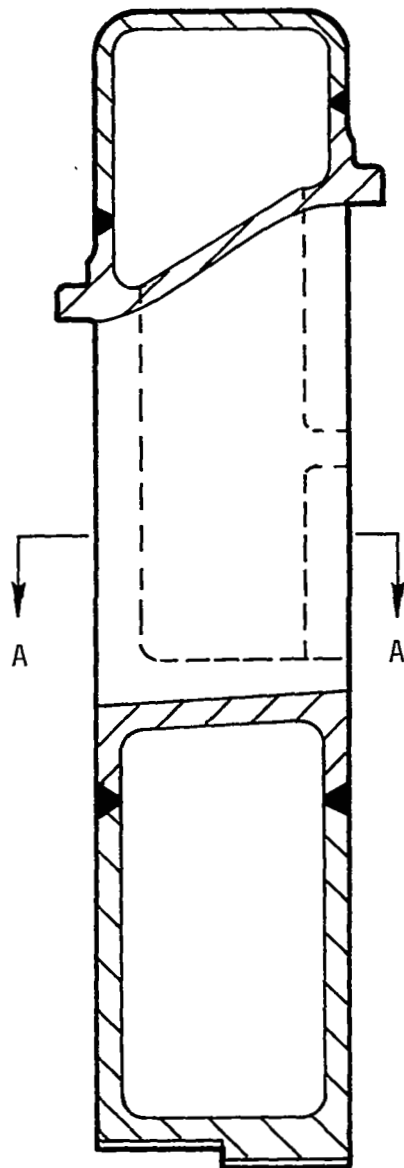


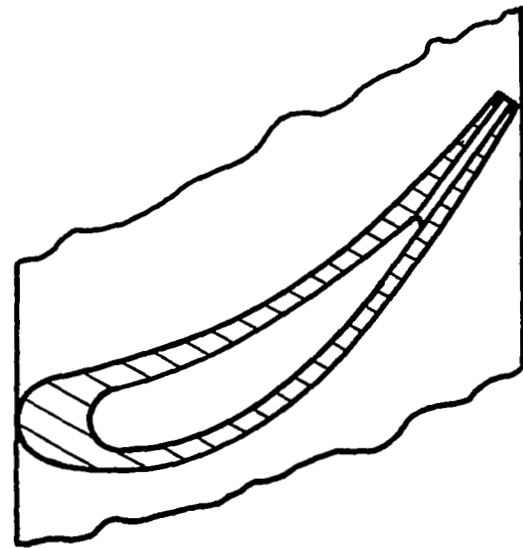
Figure 10.1-3. Moisture in 7+4 Turbine with Interstage and Interspool Extraction Moisture.

potentially damaging liquid drops are removed before they can collide with the rotating blades.

Shown in Figure 10.2-1 is a sketch of a stator vane designed for liquid extraction. The extraction port consists of a slot in the trailing edge of the vane which is connected to a lower pressure, so that liquid can be removed by suction from the trailing edge of the vane. This scheme has been tested using water/air and steam/air in a cascade flow test shown in Figure 10.2-2. Water is injected directly on the surface of the vane slightly aft of the leading edge and is removed by suction from the trailing edge. Visual indication of the extraction effectiveness can be seen in Figure 10.2-3. The upper picture, taken with no suction, shows water blown off the trailing edge by the air stream. The lower picture, with suction applied, indicates that most of the water is removed. Shown in Figures 10.2-4 and 10.2-5 are two plots which are typical of the air cascade test results. Figure 10.2-4 indicates that slot size is a significant parameter but suction differential pressure has only a small effect. Figure 10.2-5 indicates that stream Mach number and the amount of liquid present have some effect on the extraction effectiveness. These preliminary results indicate that under proper combination of parameters, it is possible to remove most of the liquid that is present on the stator vanes. Even if the liquid on the vanes is a small fraction of the total liquid present in a turbine, this is the liquid which collects into large drops and causes erosion damage. This promising scheme is also being developed in the Large Steam Turbine Department.



NOZZLE DIAH. ASSY. DETAIL  
8th STAGE - SCALE 2X



SECTION A-A  
SCALE 4X

Figure 10.2-1. Details of Stator Moisture Extraction.

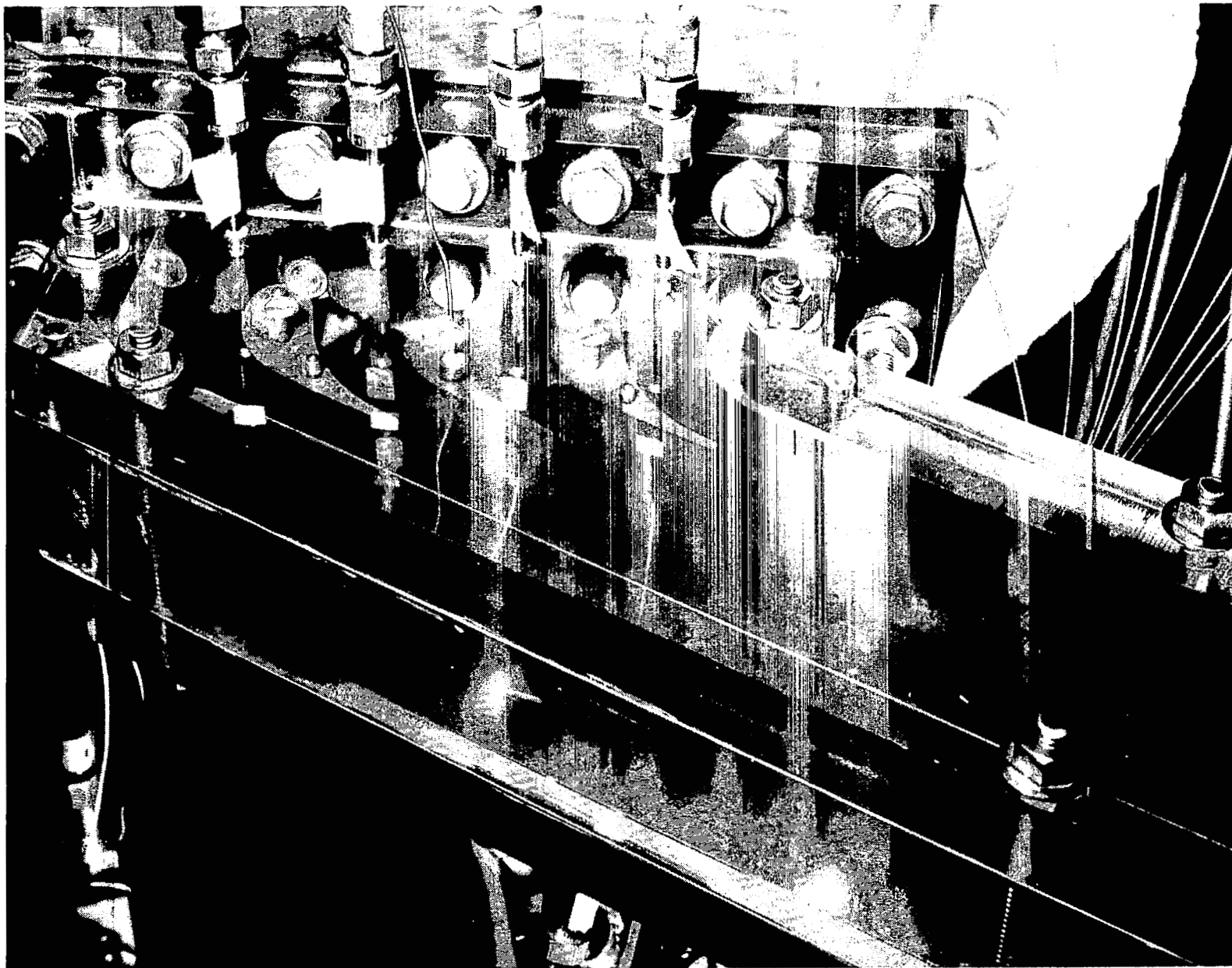


Figure 10.2-2. Trailing Edge Condensate Removal Cascade.



**NO SUCTION**



**SUCTION  $\Delta P$  3.5 PSI**

**Figure 10.2-3. Trailing-Edge Condensate Removal - 20 x 40 Mil Slot, Velocity 500 fps.**

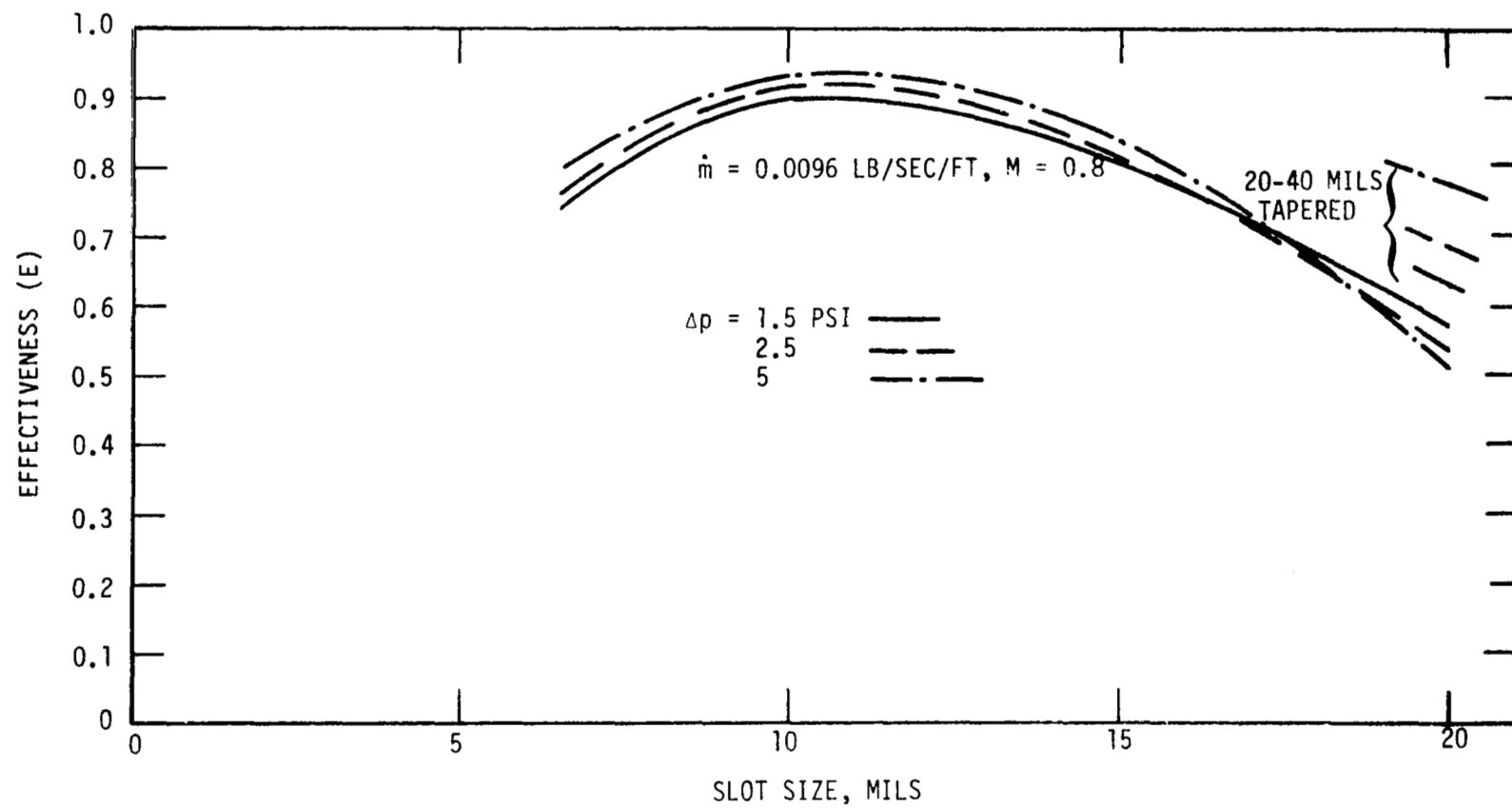


Figure 10.2-4. The Effect of Slot Size.

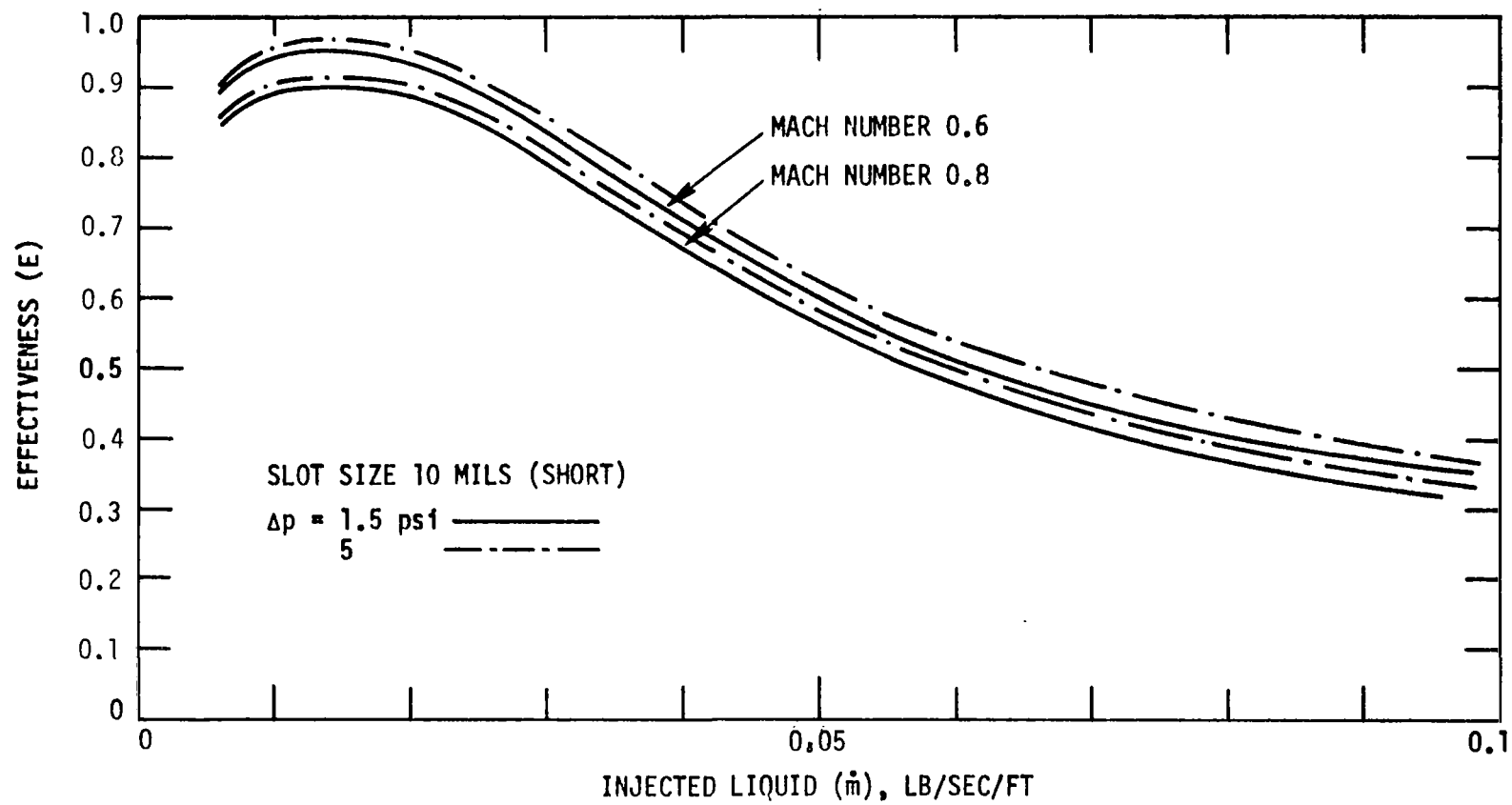


Figure 10.2-5. The Effect of the Amount of Liquid on the Blade.



### 10.3 REHEAT

Another way to minimize moisture is to reheat the working fluid after it has been partially expanded in the turbine. The working fluid may be reheated by the primary fluid but this requires additional high temperature ducting. If the fluid is reheated by condensing potassium vapor, a heat exchanger is required and the maximum reheat temperature must be less than the original saturation temperature. A preliminary reheat scheme was investigated in which the fluid was expanded through five stages, reheated to 2100°F and expanded in a five-stage low pressure turbine. The turbine fluid design looks feasible but no heat exchanger or mechanical design has been done. A sketch of this cycle is shown on a Mollier diagram in Figure 10.3-1 along with the non-reheat turbine expansion. The main attraction of the reheat cycle is the low moisture content as shown in Figure 10.3-2. However, there are several drawbacks in the reheat scheme. First, the high temperature reheater and ducting introduce complexity and weight. Second, the high temperature will cause stress problems not normally present in the low pressure turbine. Third, the flow rate is reduced for a given power output resulting in smaller blades in the high pressure turbine where they are already quite small. The reheat system needs more study for a technical evaluation.

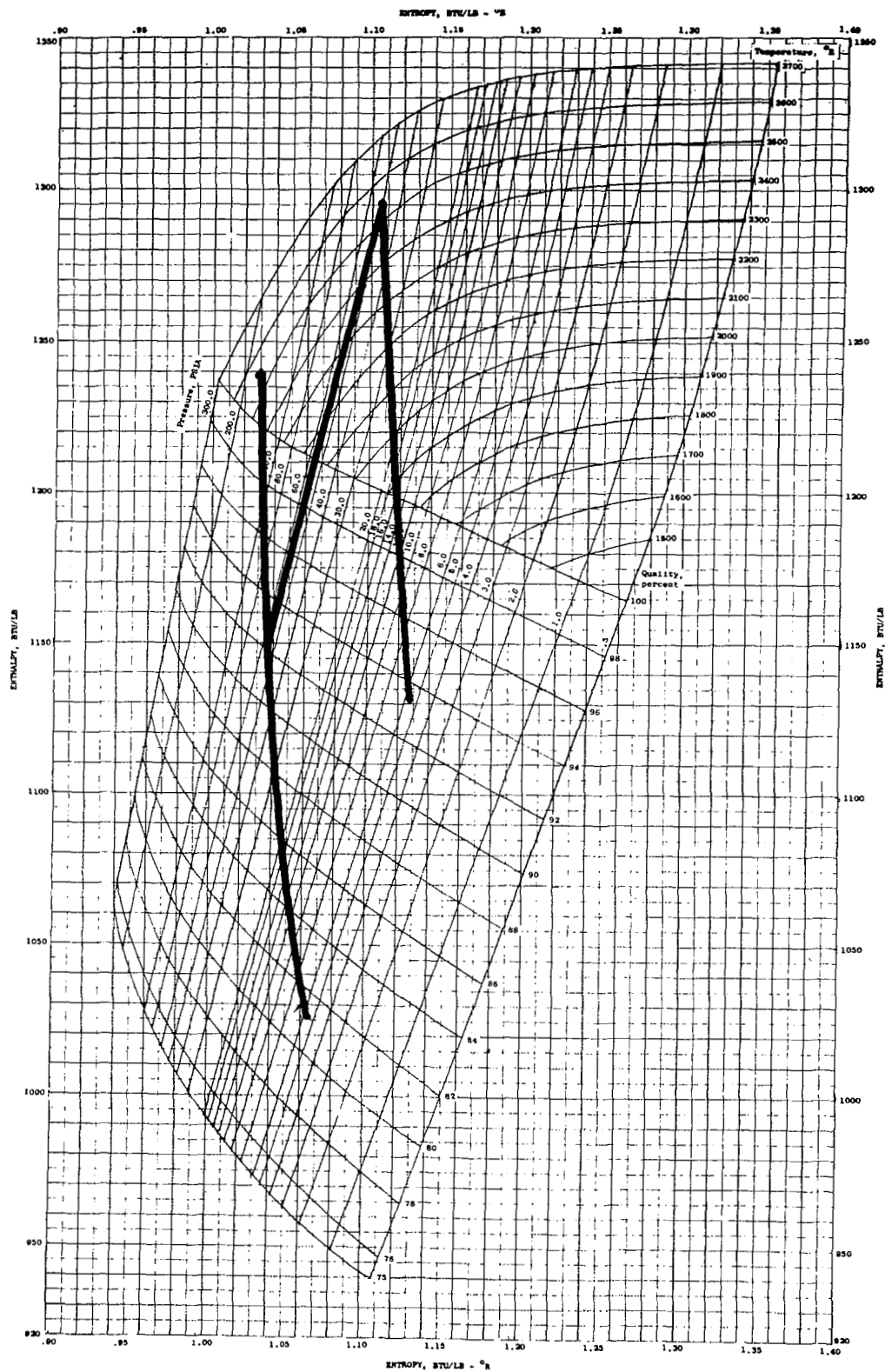


Figure 10.3-1. Mollier Diagram for Potassium Vapor.

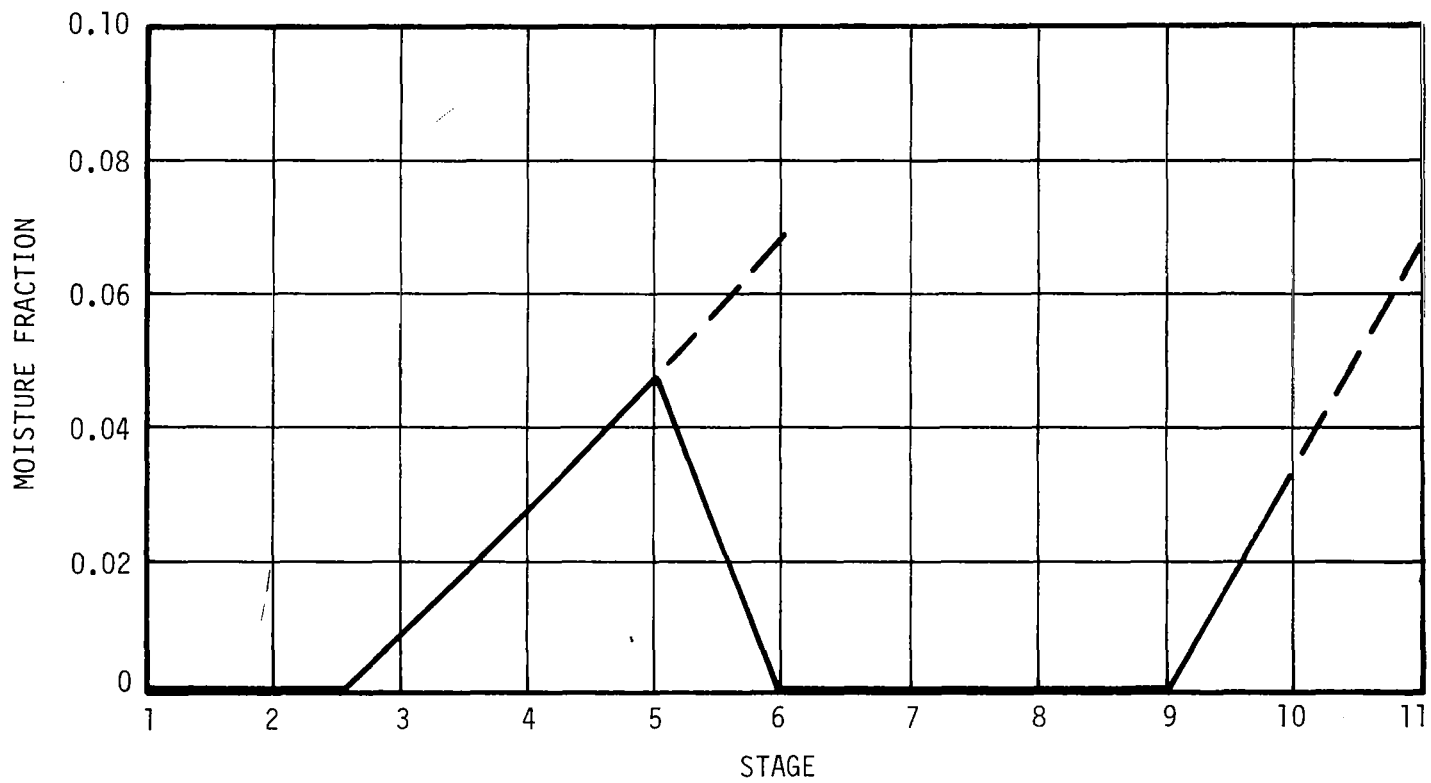


Figure 10.3-2. Moisture in Reheat Turbine - Reheat Temperature 2100°F.